Cathode material for high-performance lithium-sulfur batteries

Zhiyong Pan

A thesis presented for the degree of Doctor of Philosophy

Supervised by

Professor Ivan P. Parkin

Professor Gopinathan Sankar

Department of Chemistry

Mathematical and Physical Sciences Faculty

University College London

2021

Declaration

I, Zhiyong Pan, confirm the work presented in this thesis as my own. Where information has been derived from other sources, I confirm that this has been indicated in this thesis.

Abstract

Since the late 20th century, energy crises have acquired worldwide attention. In the last two decades a lot of renewable energy sources have been fully developed and used, including solar energy, wind energy, tide energy and so on. However, the application of these energy sources are hindered by time and space restrictions. For example, solar energy can only be used at day time with relatively clear whether. To make full use of these energy resources, a variety of energy storage devices have been developed. Among them, lithium-ion batteries (LIBs) are the most successful commercialized energy storage devices and are widely used in our daily life, including phones, computers, electric vehicles and so on. However, the energy density of LIBs is hindered by the theoretical specific capacity of the lithium transition metal oxide cathode. Lithium-sulfur batteries (LSBs) with a theoretical specific capacity of 1675 mA h g^{-1} are regarded as the most promising next generation energy storage devices. But several obstacles, including the low conductivity of S and Li_2S, the big volume change of S during charge and discharge and the notorious shuttle effect, stand in the road of commercialization of LSBs.

In the thesis, two different strategies have been applied to solve these problems. First, ZIF-67, one kind of metal-organic framework (MOF), was used as a template to synthesis porous carbon frameworks. The carbon frameworks were used as a S host to accommodate the volume change of S and improve the conductivity of the electrode. What's more, the Co centres in ZIF-67 transferred into cobalt phosphide and cobalt sulphides, based on the detailed experiment condition. Cobalt phosphide and cobalt sulphides with high catalyst activity accelerate the reactions in the electrodes and alleviated the shuttle effect and thus improved the electrochemical performance.

Second, sulfurized poly acrylonitrile (SPAN) was used as a source of S for LSBs. The covalent C-S bonds in SPAN alleviated the shuttle effect through reducing the formation of lithium polysulfides. Carbon nanotubes (CNTs) and Se-doping further improved the electrochemical performance of SPAN through improving the conductivity and accelerating the reactions. Samples with different levels of Se-doping were synthesized and characterized to find the best conditions. Meanwhile, the structure of the as-synthesized SPAN samples was characterized by a variety of methods to gain some insight about structure of SPAN, which is a subject of debate among researchers.

Through these two strategies, the shuttle effect in LSBs was reduced and the performance of LSBs were improved. A higher specific capacity and a better cyclic stability were achieved. At the same time, a better understanding of the mechanism of LSBs was gained.

Impact statement

The fast development of electric vehicles and other electronic devices urged the development of energy storage devices with higher energy density and longer working life. However, the energy density of the commonly used commercialized LIBs is limited. LSBs with a high specific capacity of 1675 mA h g^{-1}, about 4 times higher than that of LIBS, is the most promising candidate for next generation energy storage devices. This PhD project has solved the most severe problems faced by practical application of LSBs, the shuttle effect, through different strategies. Better electrochemical performance and understanding of the mechanism were achieved.

High lights:

i. ZIF-67, which has been used as template in this project, is easy to prepare and suitable for large scale production.
ii. The low conductivity of ZIF-67 template through carbonization at high temperature to synthesis graphitized carbon framework.
iii. ZIF-8@ZIF-67 core-shell structure was synthesized to reduce the collapse of ZIF-67 during the carbonization process to increase the specific surface area of the products.
iv. The catalyst activity of cobalt sulphides was characterized by different methods and samples with and without cobalt sulphides were synthesized and tested to verified it.
v. SPAN with covalent C-S bonds was used as S source in LSB to alleviate the shuttle effect through reducing the formation of LPSs.
vi. Se-doping improved the conductivity of SPAN thus the electrochemical performance.
vii. The structure of Se-doping SPAN was characterized by different methods, the formation of C-S covalent bonds was confirmed. Besides, S-containing ring structure and –S-C=N- bonds were also formed in the as-synthesized samples. And there was also physically absorbed S particles in SPAN.

Acknowledgements

During my PhD study, I have encountered a lot of problems and challenges. Thanks to all the help that I got from my supervisor, my colleague, my friends and my family, I made it through. I would like to thank them all for their warm heart, helpful guidance, valuable suggestion and so on.

I would like to thank my supervisor Prof Ivan for his help and suggestions in both academic research and daily life. Prof Ivan offered a lot of suggestions in experiment design, data analysis, article writing and so on. Also, Prof Ivan helped a lot in daily life especially during the pandemic of Covid-19.

I would like to thank my colleagues, the energy group. We shared ideas and talked about our projects a lot. Jian Guo helped me with settling down when I arrived at London four years ago for the first time. He also helped me with learning and using the equipment and facilities in the lab and the department. Jianwei Li, or Vince, and I talked a lot about the experiments about both batteries and electronic catalysts. Juntao Li helped me with a lot of experiments and characterizations.

I would like to thank the staff in the chemistry department. Steve helped me with the training for SEM, TEM, TGA, Raman and so on. I got lots of data from all these characterizations. Tony helped a lot with purchasing of equipment, chemicals and consumables. And there are lots of other staff who helped with many other aspects like first safety, Covid safety and so on.

Finally, I would like to thank my parents and all my friends, who supported me a lot during my PhD project. And I would like thank CSC for the funding that made my PhD study at UCL possible.

Contents

List of Figures

Chapter 1

Chapter 2

Chapter 3

Chapter 4

List of Tables

Abbreviation

LIBs	lithium-ion batteries
LSBs	lithium-sulfur batteries
LTMO	lithium transition metal oxide
SEI	solid-electrolyte interface
LPSs	lithium polysulfides
SPAN	sulfurized poly acrylonitrile
MOF	metal-organic framework
ZIF	Zeolite Imidazole Frameworks
CNT	carbon nanotube
SEM	scanning electron microscope
TEM	transition electron microscope
XRD	X-ray diffraction
XPS	X-ray photoelectron spectroscopy
FTIR	Fourier transform infrared spectroscopy
UV-vis	ultraviolet visible spectroscopy
CV	cyclic voltammetry
GCF	graphitic carbon framework
NCF	N-doped carbon framework
CNCF	cobalt supported on N-doped carbon framework
SGCF	sulfurized graphitic carbon framework
SNCF	sulfurized N-doped carbon framework
CSNCF	cobalt sulphides supported on N-doped carbon framework
LDH	layered double hydroxide

Chapter 1

Background and introduction

1.1 Lithium-sulfur batteries (LSBs)

The energy crise is one of the major challenges faced by human beings in the 21st century, as the non-renewable fossil energy is running out.[1–5] Large amounts of CO_2, which is blamed for the greenhouse effect, has been produced by the use of fossil energy. Therefore, renewable energy sources have been explored over the past decades, including wind energy, solar energy, and so on. However, the use of these renewable energy sources is restricted by weather conditions and geographical environments. For example, solar cells transfer solar energy to electricity during daytime, but during night or rainy days, solar cells cannot work effectively. Thus, it is necessary to establish an effective energy storage system that can store the excess electrical energy when the sun shines to power other facilities when sunshine is low or during the night.

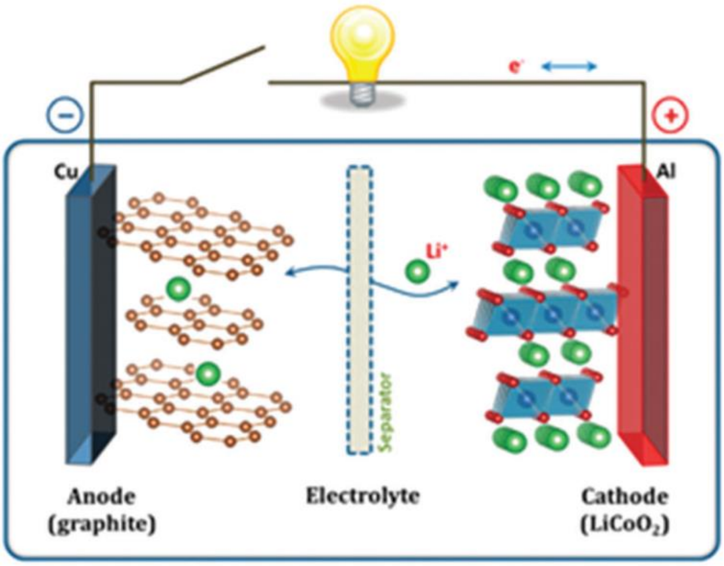

Figure 1.1. Schematic illustration of a lithium-ion battery using graphite and $LiCoO_2$ as anode and cathode, respectively. [6]

Different energy storage systems have been studied, for example, super capacitors[7–9] and batteries[10–13] over the past years. Each has its advantages and disadvantages. Super capacitors have high power density and high cycle stability, but the energy density is very low. Batteries have higher energy density but lower power density. However, batteries, especially lithium-ion batteries (LIBs), stand out ever since the commercialization of LIBs by the Sony company in the 1990s. In a typical battery system, anode and cathode are separated by separators and ions can diffuse through these separators in the electrolytes (**Figure 1.1**).[6] The performance of a battery system is largely affected by the anode and cathode. In commercialized LIBs, graphite and lithium transition metal oxide (LTMO) are used as anode and cathode, respectively. However, the capacity of graphite and LTMO are relatively low, several hundred mA h g^{-1} at the most, which cannot meet the requirements of newly emerged electrical devices. To reach higher energy density, a variety of new materials as well as new battery systems have been studied.[14–17] Among them, lithium-sulfur batteries (LSBs) are the most promising ones.

S have a high theoretical specific capacity of 1675 mA h g^{-1}, which is about four times higher than that of the commercialized LTMO cathode. The high abundance of S on earth results in low price, which is favourable for large scale application. Besides, S has lower toxicity compared with many of the transition metal compounds, which contain Co and Ni, and are used in LIBs. Because of these advantages, LSBs have attracted attentions worldwide over the past decades.

1.1.1 Development history of LSBs

The development can go back the 70s of the 20th century. At that time, the cells operated at high temperature (300 °C) as shown in **Figure 1.2** and the electrodes were in the molten state same as the sodium-sulfur batteries.[18] However, the development of LSBs was slow at that time. First, the commercialization and rapid development of LIBs has drawn most of the research attention. Second, the reversible charging of LSBs was difficult at the beginning, which made it a primary battery system. After about 30 years of development, researchers found suitable organic electrolyte systems that enabled the reversible charge of LSBs and capable of operating at room temperature. Then, in the 21st century, the development of LSBs speeded up. The development of electronic devices requires energy storage devices with high energy density. Besides, the emergence of C/S composite cathode with high performance has now spread. In 2009, Nazar's group reported a cathode made from ordered mesoporous carbon (CMK-3) with a high specific capacity of 1320 mA h g^{-1}. Since then a variety of porous carbon materials and carbon containing composite materials have been applied as host of S in LSBs. Recently, more and more attention is paid to the lithium metal anode. The formation of lithium dendrite will lead to short circuit and safety issues. To prevent this, lithium host, artificial solid-electrolyte-interface (SEI) and solid electrolyte have been proposed and studied.

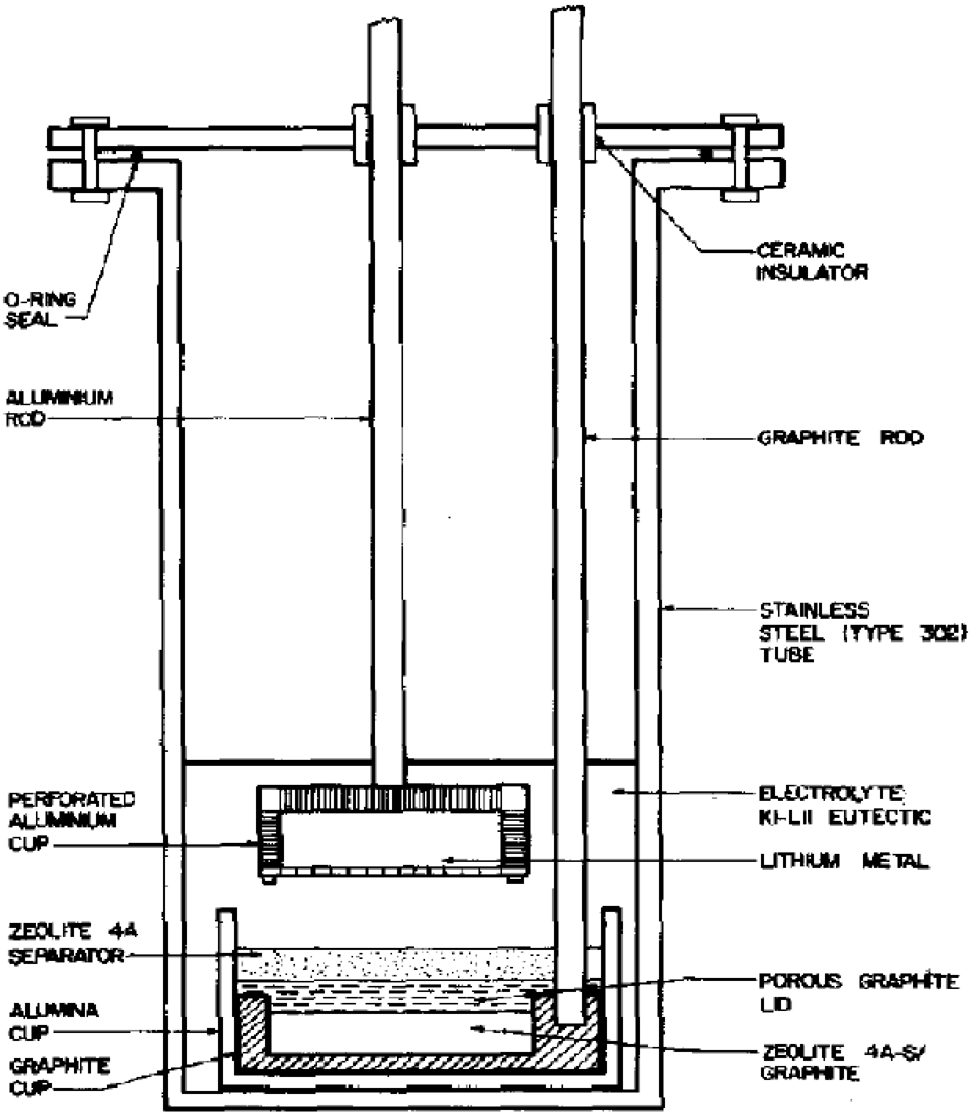

Figure 1.2. Schematic illustration of a lithium-sulfur battery(LSB) operate at 300 °C in molten state.[18]

1.1.2 Mechanism of LSBs

In LSBs, when discharging, Li will be oxide to Li^+ and release electrons to the external circuit (equation 1), and sulfur will receive electrons from the external circuit and be reduced to Li_2S_8 at the beginning, and then be further reduced to Li_2S_6/Li_2S_4 and Li_2S_2/Li_2S (equation 2-5). Thus, two voltage plateau will be found: one at around 2.4 V corresponding to the transfer from sulfur to long chain lithium polysulfide and one at around 2.1 V corresponding to the transfer from long chain lithium polysulfide to short chain and Li_2S/Li_2S_2 (Figure 1.3).[19]

$$Li = Li^+ + e \quad (1)$$

$$2\ \mathrm{Li}^+ + \mathrm{S}_8 + 2\ \mathrm{e} = \mathrm{Li}_2\mathrm{S}_8 \quad (2)$$

$$3\mathrm{Li}_2\mathrm{S}_8 + 2\ \mathrm{Li}^+ + 2\ \mathrm{e} = 4\mathrm{Li}_2\mathrm{S}_6 \quad (3)$$

$$2\mathrm{Li}_2\mathrm{S}_6 + 2\ \mathrm{Li}^+ + 2\ \mathrm{e} = 3\mathrm{Li}_2\mathrm{S}_4 \quad (4)$$

$$\mathrm{Li}_2\mathrm{S}_4 + 2\ \mathrm{Li}^+ + 2\ \mathrm{e} = 2\ \mathrm{Li}_2\mathrm{S}_2 \quad (5)$$

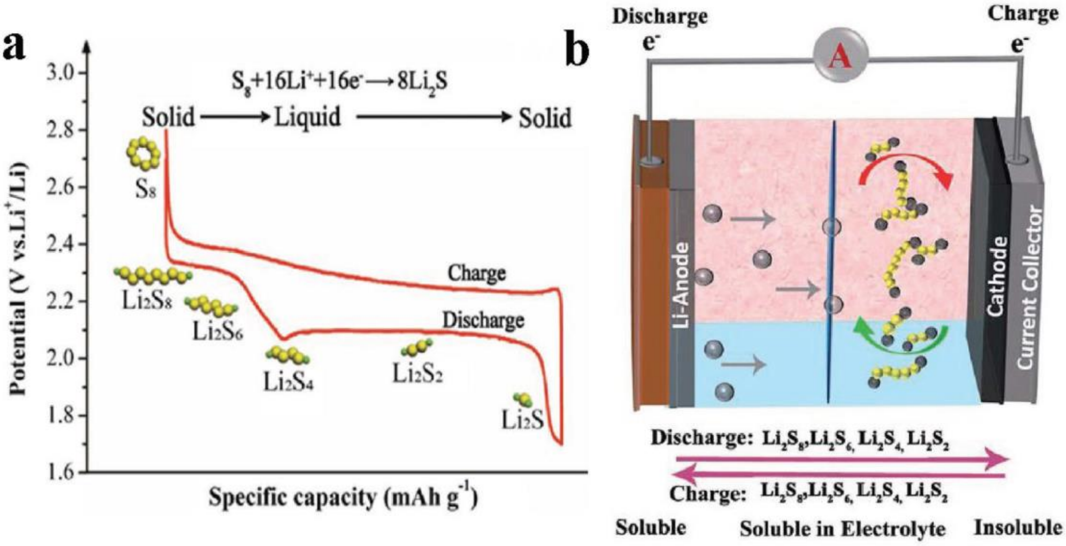

Figure 1.3. a) Charge-discharge curve of lithium-sulfur battery. b) Illustration of charge and discharge process of lithium-sulfur battery. [19]

1.1.3 Challenges of LSBs

However, the application of LSBs is prohibited by several challenges. First, sulfur and the discharge products lithium sulfide ($\mathrm{Li_2S}$) are intrinsically insulating, with a low conductivity of 5×10^{-30} S cm^{-1}.[20] Second volume expansion as high as 78% will happen when sulfur is fully converted to $\mathrm{Li_2S}$.[21] Third, the intermediates, lithium polysulfide (LPSs) ($\mathrm{Li_2S_x}$, $4 \leq x \leq 8$), are soluble in electrolyte, thus these intermediates can diffuse between anode and cathode, known as the shuttle effect.[22][23][24] When lithium polysulfide reaches the surface of lithium, it will react with lithium to form solid $\mathrm{Li_2S}$, leading to the consumption and passivation of lithium. On the sulfur cathode, lithium polysulfide will be electrically or chemically oxidized to $\mathrm{Li_2S_8}$, leading to the consumption of the sulfur.

Except for the above challenges, low volumetric energy density is another obstacle that stands in the road of industrialization of LSBs. The gravimetric energy density of commercialized LIBs can reach 250 to 300 W h kg^{-1} by using Ni-rich oxide cathode. While the gravimetric energy density of the prototype of LSBs produced by some pioneer manufactories can reach 400-600 W h kg^{-1} as shown in **Figure 1.4**, which is almost double of that of LIBs.[25] Though higher gravimetric energy density leads to lower mass ratio of energy storage part in devices like computers, electric vehicles and so on, volumetric energy density must be taken into consideration in devices like smart phones and electric vehicles. The designed space for battery packs in an electric vehicle is about 220 L. The volumetric of commercialized LIBs has already reached 700 W h L^{-1}, while the volumetric energy density of LSBs in pouch cell configuration is limited at 200-400 W h L^{-1}. Thus, using commercialized LIBs can provide higher energy. However, for drones, lower mass of the whole devices to provide the same capacity is of great importance.

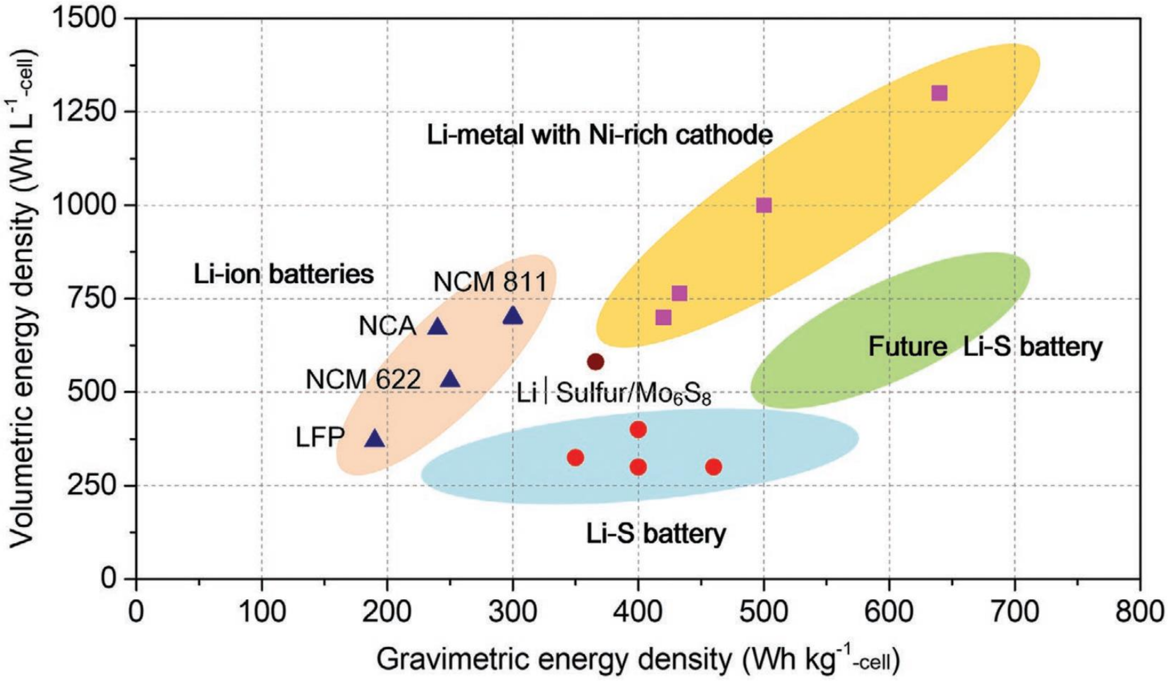

Figure 1.4. Comparation of volumetric energy density and gravimetric energy density of LIBs and LSBs.[25]

1.1.4 Solutions of LSBs

Recently, several solutions have been proposed to solve these challenges, like using functionalized separators[26–28] and solid electrolyte[29–31]. However, most research interest has been devoted into designing and synthesizing nano-sized porous material, which can act as physical confinement, chemical absorption and catalyst, for sulfur in LSBs.

1.1.4.1 Physical confinement

To alleviate the shuttle effect, using a porous host to physically confine sulfur in restricted space could be a possible solution. Mostly, carbon-based porous nanomaterials are used as the host for sulfur. Except from the physical confinement, carbon-based porous nanomaterials can also improve the conductivity of the whole electrode material and the pores in the porous structure can accommodate the volume change of sulfur during charge and discharge. Mesoporous carbon, graphene-based material, carbon nanotube and their composite have been used as host for sulfur in lithium-sulfur battery.

Pure carbon materials like carbon black, CNT with high surface area and porous structure have been studied as S host in LSBs. Though the carbon host improve the conductivity of the electrode and provide physical confinement of LPSs to alleviate the shuttle effect, the performance of pure carbon materials is not satisfactory. Li *et al*. studied the effect of three different kinds of carbon host (porous Ketjen black (ECP), Super P (SP) and CNT) on the electrochemical properties of LSBs.[32] It was found that CNT and ECP had higher initial capacity and better cycling stability than SP as shown in **Figure 1.5**, which could be ascribe to the hierarchical porous structure. However, the nonpolar property hinders the performance of pure carbon materials. Even in the case of CNT, an initial capacity of about 1050 mA h g^{-1} could be reached and about 750 mA h g^{-1} could be maintained at a relatively low current density of 0.2 C (1 C = 1675 mA g^{-1}).

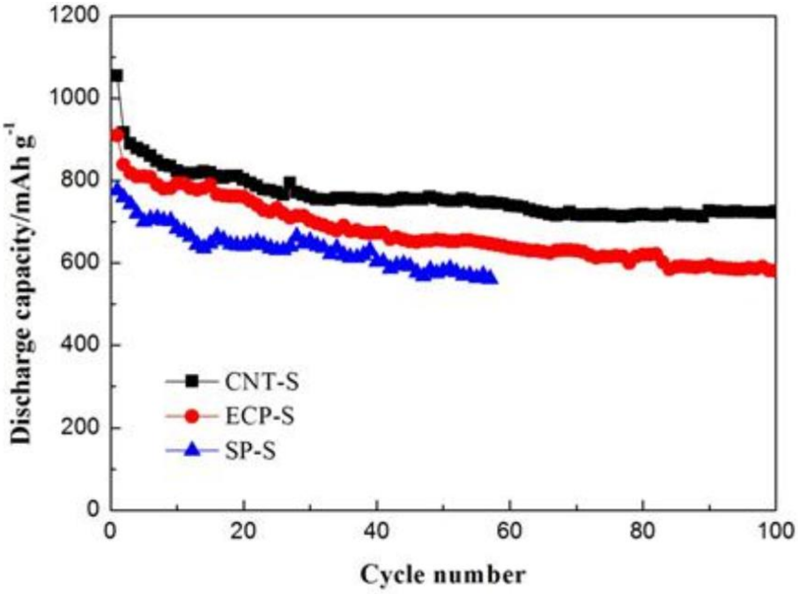

Figure 1.5. Cycling performance of different carbon host at a current density of 0.2 C (1 C = 1675 mA g^{-1}).[32]

Ordered mesoporous carbon is one kind of carbon nanomaterial with mesopores (2-50 nm), and ordered mesoporous carbon has high surface area and large pore volume, which makes it an appropriate host of active materials. In 2009, Nazar's group firstly introduced CMK-3, a well-known member of ordered mesoporous carbon materials, as a host of sulfur in LSBs.[33] Through a melt-diffusion process, sulfur filled into the channels of CMK-3 by capillary force. This structure not only provided close contact between insulating sulfur and conductive CMK-3, but also confines the soluble lithium polysulfide from shuttling between anode and cathode. It's also worth mentioning that the high pore volume enabled the high sulfur content in the as-synthesized CMK-3/S composite (70%). When applied as a cathode in LSBs, this material delivered a discharge specific capacity as high as 1320 mA h g^{-1}, nearly 80% of the theoretical specific capacity of LSBs. Inspired by this work, Nazar's group further studied other ordered mesoporous carbons as host of sulfur. They successfully synthesized a novel kind of ordered mesoporous carbon with extremely high bimodal porosities (6 nm and 3.1 nm). This material had a pore volume as high as 2.32 cm^3 g^{-1}, and a high reversible discharge capacity of 1200 mA h g^{-1} was maintained.

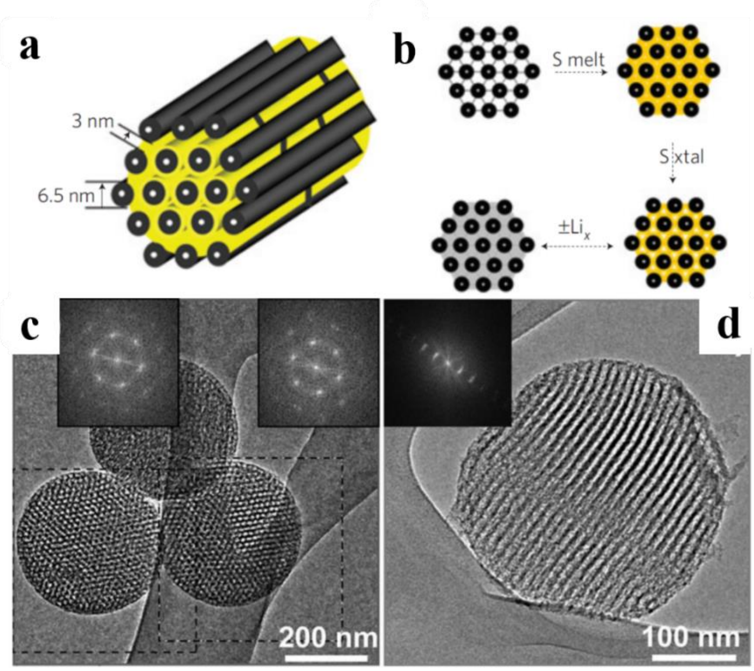

Figure 1.6. a) A diagram of the sulfur confined in CMK-3. b) Illustration of the melt-diffusion process and the charge-discharge process. c-d) Transmission electron microscope images of ordered mesoporous carbon nanoparticles. [33]

Graphene and graphene-based materials have been extensively studied in energy-related areas because of their unique 2D structure, high surface area as well as high structural stability. However, the conductivity of chemically reduced graphene oxide is not satisfied when used as a host of sulfur. Thus, a novel type of N-doped graphene was synthesized to increase the conductivity of graphene (~270 S cm^{-1}). The N-doped graphene/S composite electrode was assembled without carbon black, which resulted in high sulfur content in the electrode and a high specific capacity based on the total mass of the electrode.[34] When used as a cathode in LSBs, this N-doped graphene/S cathode showed high cycle stability, 2000 cycles at 2 C (1 C = 1675 mA g^{-1}) with a with a decreasing rate of 0.028% per cycle.

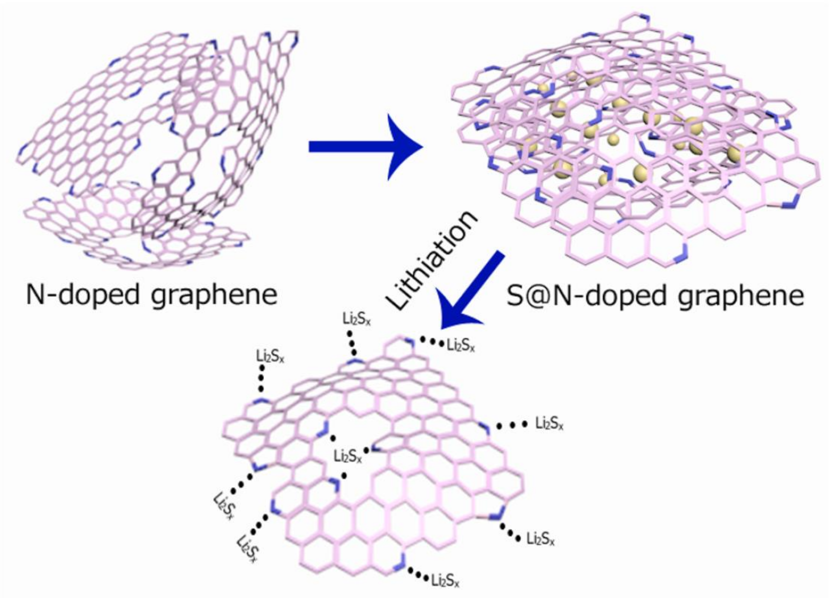

Figure 1.7. The synthesis process of N-doped graphene/S composite and the discharge mechanism. [34]

1.1.4.2 Chemical absorption

Except from physically confining lithium polysulfide in porous nanomaterials, researchers have also used chemicals that have strong intercalations with LPSs to prevent it from diffusing between electrodes, with transition metal-based materials like transition metal oxide, transition metal sulfide, transition metal nitride and so on are the most attractive ones.

The use of transition metal-based material is hindered by its low conductivity, thus finding conductive material or synthesis transition metal-based material/C composite is necessary. Fe_3O_4 is one kind of highly conductive transition metal oxide. Based on this, a yolk-shelled C@Fe_3O_4 nanoboxes was synthesized by Manthiram's group and applied as host for sulfur.[35] The polar Fe_3O_4 provides strong intercalation with LPSs while the carbon shell provides physical confinement, and both Fe_3O_4 and the carbon shell are highly conductive, which favors electron transport. A high sulfur content up to 80% was achieved. This conductive host exhibits a superior rate capability with a discharge capacity of 773 mAh g^{-1} at 2 C and 1286 mA h g^{-1} was recovered at 0.1 C (1 C = 1675 mA g^{-1}).

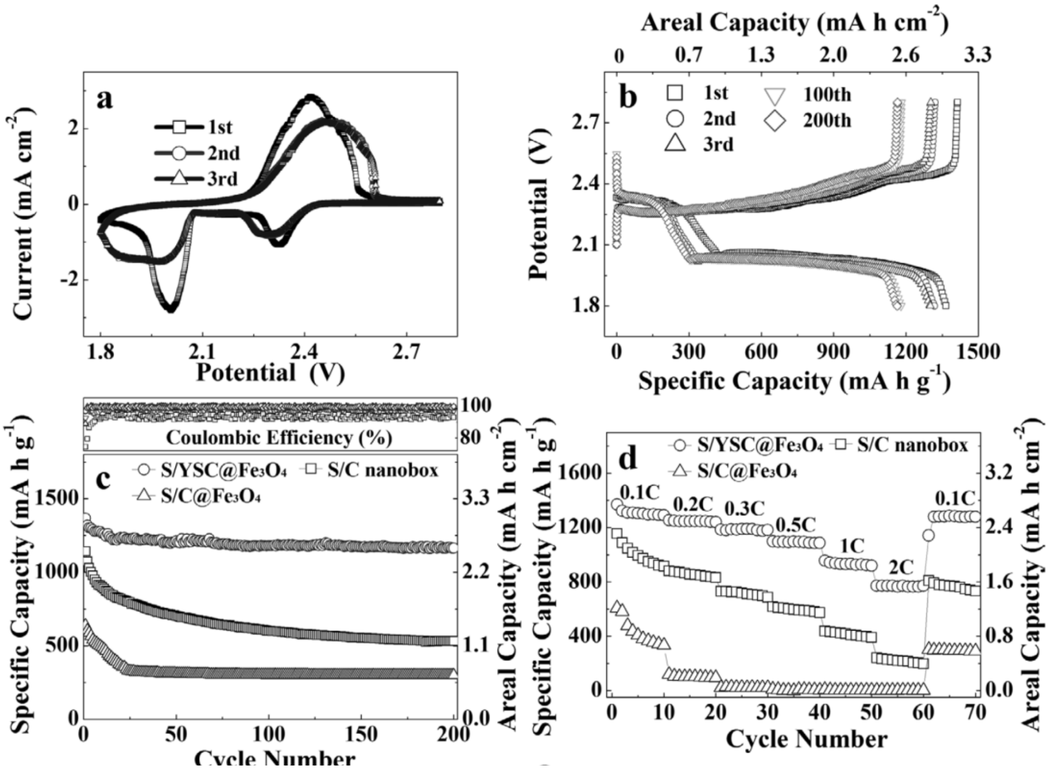

Figure 1.8. Electrochemical performance of yolk-shelled C@Fe_3O_4/S composite. a) cyclic voltammogram (CV) curves. b) charge-discharge curves. c) cycle stability. d) rate performance. [35]

Compared with transition metal oxides, transition metal sulfides have several intrinsic advantages. First, the strong sulfiphilic property to sulfur-containing species. Second, lower lithiation voltage than that of lithium-sulfur batteries. However, when the material is in a planer structure, LPSs that are far from the surface can easily diffuse into the electrolyte. Thus, a novel uniform honeycomb-like Co_9S_8 spheres were synthesized as host for sulfur.[36] The physical confinement of the hollow sphere and the chemical absorption of Co_9S_8 made it hard for the LPSs to shuttle between anode and cathode. A high sulfur content up to 70% was achieved and the initial discharge capacity was 1136 mA h g^{-1} at 0.2 C. The chemical absorption capability of lithium polysulfide of Co_9S_8 was studied by climbing image nudged elastic band and density functional theory.

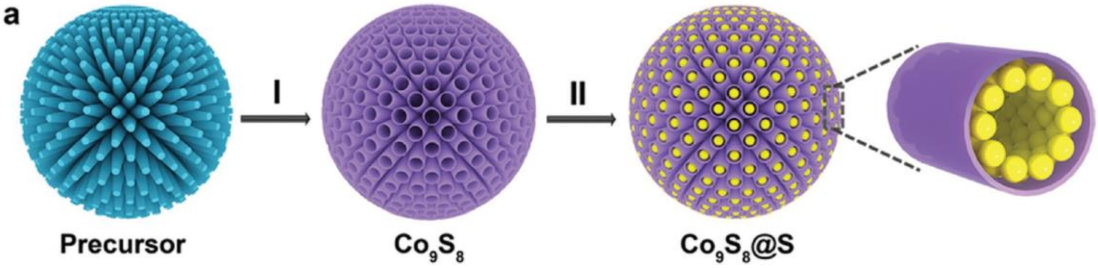

Figure 1.9. Illustration of the synthesis process of the honeycomb-like Co_9S_8 sphere/S composite. [36]

1.1.4.3 Catalyst

Although physical confinement and chemical absorption can mitigate the shuttle effect, as most LPSs are blocked and cannot be reused, this strategy become less effective especially with high sulfur loading and ultra-long cycling. Another effective strategy is using catalyst to alleviate the sluggish reaction, thus the life time of lithium polysulfide will be reduced and the chance that lithium polysulfide can shuttle into electrolyte will decrease. Catalysts like noble metal, metal sulfide, metal phosphide and so on have been recently studied.

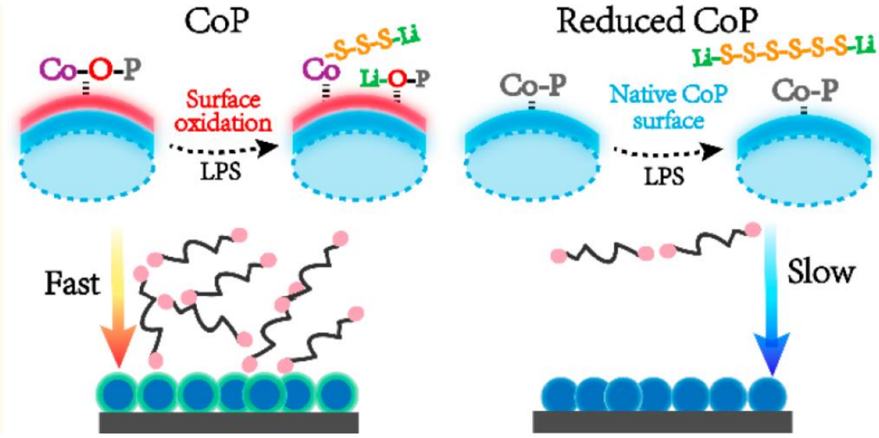

Figure 1.10. Illustration of chemical absorption of lithium polysulfide in CoP and reduced CoP. [37]

Despite the research about these catalysts worldwide, the mechanism of them is still ambiguous. A lithium polysulfide-binding mechanism was proposed for metal phosphide. It was found that the strong intercalation between LPSs and CoP originates from the oxidization layer on the surface under ambient condition, as the samples reduced under H_2 atmosphere showed relatively worse performance.[37] The oxidized Co atoms in Co-O-P groups have stronger absorption of polysulfide anions, resulting in the formation of Co-polysulfide and Li-O-P groups.

1.1.4.4 Organosulfur

Organosulfur compounds with C-S covalent bonds have attracted more and more attention recently because of its inherent properties. The covalent C-S bonds alleviate the shuttle effect by reducing the formation of LPSs. Based on the structure, organosulfur compounds can be classified into three types: small organosulfur molecular, high sulfur content copolymer and sulfurized polymer. Among them, sulfurized poly acrylonitrile (SPAN) is the most promising one because of the high electrochemical performance and facile synthesis process. However, the chemical structure of SPAN and the working mechanism are not clarified though many researchers have proposed some possible models. On the other side, the electrochemical performance of SPAN needs to be improved before its commercialization. First, the conductivity of SPAN is relatively low, which hinders its performance especially at high current density. Second, the cyclic stability of SPAN is far from satisfactory.

Above all, different solutions have been studied to prevent the shuttle effect in LSBs. However, one solution alone is far from enough. In practical applications, physical confinement, chemical absorption and catalyst should be taken into consideration together to assemble a high-performance cathode for LSBs.

1.2 Metal-organic-framework (MOF)-based materials for LSBs

Among all the materials that have been applied in LSBs, metal-organic-frameworks (MOFs) stand out because of their unique properties. MOFs are coordination polymers with metal ions and organic compounds as connectors and linkers, respectively. The special structure endows intrinsic properties, including high porosity, low density, high surface area and tunable pore size.[38–41] Thus, MOFs have been widely studied in areas like sensors, electrochemical catalysts, CO_2 absorption, energy storage and so on.[38–45] In LSBs, the high porosity and high surface area make MOFs an eligible host of S. Besides, the metal ions and organic ligands in MOFs with high polarity can absorb LPSs or provide catalyst activity in LSBs. Except for cathode materials, MOFs have also been used as functional separator and solid-state electrolyte for LSBs. The ion sieving effect of MOFs with tunable mesoscopic channels is suitable for selective ion conductors, which has been used in separators and solid-state electrolytes. However, the low conductivity of MOFs has hindered their application.[46–48] Therefore, carbonized MOFs and MOF-containing hybrid materials with conductive components have been prepared. When treated at high temperature, the organic ligands in MOFs will pyrolysis into carbon material, and the degree of graphitization is related to the temperature. When metal ions like Co^{2+}, Ni^{2+} and Fe^{2+} are used, they will catalysis the graphitization process, and higher conductivity can be achieved. Furthermore, depending on the atmosphere applied during the carbonization process, metal ions will turn into metal oxides/sulphides/nitrides. These metal-based compounds normally have strong chemical absorption of LPSs and catalyst activities. Synthesizing MOF-containing hybrid materials with conductive components is another strategy to improve the conductivity. Carbon nanotube (CNT), graphene or graphene oxide (GO) and MXene and their composites are the most widely used conductive components because of their high conductivity as well as other properties.

1.2.1 MOFs and their derivate as host of S in LSBs.

The energy density of LSBs mainly depends on the capacity of S cathode, when using Li metal as an anode. However, the performance of S cathode is greatly affected by several problems as mentioned above. Recently, MOFs and their derivate have been applied as S host to solve these problems. First, carbonized MOFs normally have better conductivity than pristine MOFs, and MOFs-containing compounds with conductive materials also provide high conductivity. Second, the porous structure of MOFs and their derivate can accommodate the volume change during charge and discharge. Third, the porous structure of MOFs and their derivate can restrict the diffusion of LPSs, and the metal ions or metal oxides/sulphides/nitrides synthesized with high polarity can provide strong chemical absorption of LPSs as well as catalyst activities to accelerate the reactions and alleviate the shuttle effect. Therefore, there has been a variety of research about application of MOFs and their derivate as host of S in LSBs.

1.2.1.1 Pristine MOFs

In 2011, Tarascon *et al*. reported the use of a mesoporous chromium trimesate MOF (MIL-100(Cr)) as host of S in LSBs.[49] The large pore volume (~1 cm^3 g^{-1}) and small windows (5-8.6 Å) provided large pores for S loading and small windows to slow down the diffusion of LPSs. Besides, the surface activity of MIL-100(Cr) also had a trapping function. The X-ray photoelectron spectra (XPS) results before and after S impregnation showed a shift in S peak as well as a decrease of the F peak, indicating the substitution of F by S and the formation of F interactions. However, the conductivity of this material was low, large amount (50 wt%) conductive carbon was needed to provide a satisfactory stability as shown in **Figure 1.11**.

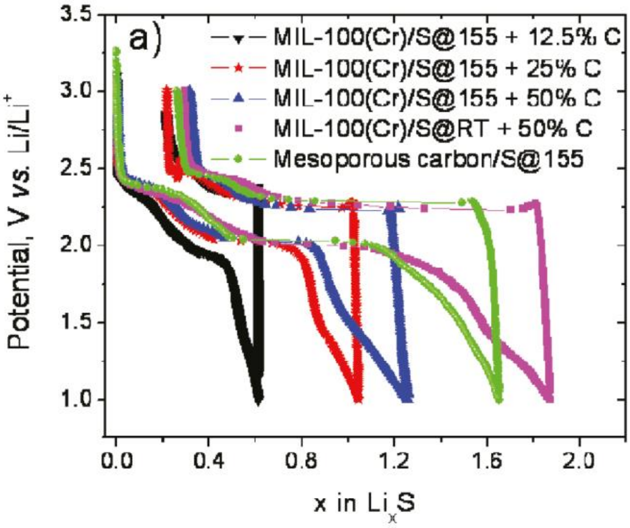

Figure 1.11. The charge-discharge curves of MIL-100(Cr) with different content of conductive carbon additives.[49]

The pore size as well as the particle size of MOFs can be tuned by changing the reaction parameters, including metal ions, organic ligands, reaction time, temperature and so on. To find out how the pore size and particle size affect the performance, Zhou *et al*.[50] used four different kinds of MOFs (ZIF-8, HKUST, MIL-53 and NH2-MIL-53) as host of S to find out how particle size and aperture size affect the performance (**Figure 1.12**). ZIF-8 samples with different particle size (from 150 nm to 3 μm) were tested at 0.5 C (1 C = 1675 mA g^{-1}) for 100 cycles. It was found that ZIF-8 with a particle size of 150 nm had the highest specific capacity of 733 mA h g^{-1}, and those with a particle size of 3 μm only delivered a specific capacity of 491 mA h g^{-1}. What's more, the ratio of Q2/Q1 (Q1 and Q2 are the capacities of the first and second discharge voltage platform, respectively) increased as the particle size decreased. The nano-size shorten the diffusion length and promote the utilization of S. As for aperture, it was found that those with smaller aperture had lower capacity decay rate. It was proposed that the apertures larger than 6.9 Å (the diameter of S_8) had attenuated immobilizing ability of LPSs. Zhou et al.[49] also studied the effect of particle size on the performance. ZIF-8 particles with a wider size rang (from ~15 nm to ~ 2 μm) were synthesized and studied. It turned out that the utilization of S increased monotonically with the decrease of particle size. Particles with a size of ~15 nm had a specific capacity of over 950 mA h g^{-1} at a current density of 0.5 C (1 C = 1675 mA g^{-1}). However, those with a particle size of ~200 nm had the best cyclic stability, 75% capacity retention after 250 cycles at 0.5 C.

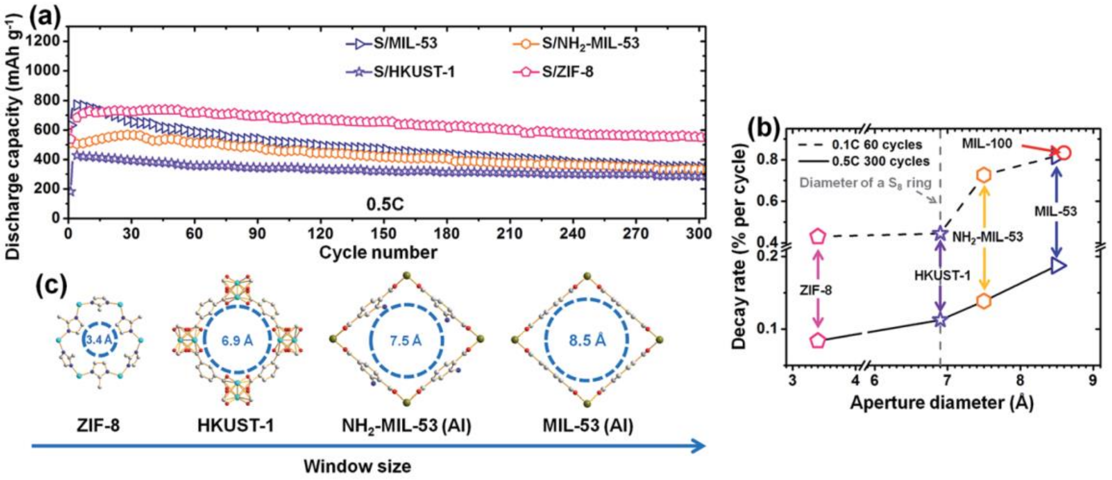

Figure 1.12. Long-term cyclic stability of S/MOFs: (a) discharge capacities at 0.5 C. (b) Average decay rate as a function of the window size of the MOF host. (c) Schematic of the largest apertures of the four MOFs.[50]

Except for pore size and particle size, metal ion centers also affect the performance of MOFs in LSBs. It is widely accepted that metal ions will absorb LPSs through Lewis acid-base interaction, the metal ions and LPSs act as Lewis acid and Lewis base, respectively. Different metal ions have different absorb abilities towards LPSs, and the chemical environment also affects their absorption abilities. Park *et al*.[52] used density functional theory (DFT) to calculate the absorption ability towards S-containing compounds in 16 metal-substituted variants of M_2(dobdc) (MOF-74) as shown in **Figure 1.13a**. It turned out that those with Ti, Ni and Mo metal center had the highest affinities towards Li_2S_4 and Li_2S. Zheng *et al*. also synthesized a Ni-based MOF (Ni-MOF, $Ni_6(BTB)_4(BP)_3$, BTB = benzene-1,3,5-tribenzoate and BP = 4,4'-bipyridyl) and tested the performance of this material as S host (Figure 1.13b).[53] Except for high binding energy calculated from DFT, XPS also showed a shift in Ni peaks, indicating the interaction between Ni center and LPSs. Further, Wang *et al*. studied how the chemical environment of the same metal center affect the performance of MOF-based S hosts.[54] A series of mixed-metal-organic frameworks (MMOF-525(2H), MOF-525(FeCl) and MOF-525(Cu)) with different number of Lewis acid site (LAS) have been synthesized (Figure 1.11c). The metal ions at the centers of MMOF-525 are chelated by four coplanar N atoms with several accessible LAS for the sulphur confinement. While in MMOF-525(2H), MOF-525(FeCl) and MOF-525(Cu), the LAS is zero, one and two, respectively. More LAS enabled higher interaction between metal center and LPSs and thus a more alleviated shuttle effect. As a result, MOF-525(Cu) had the best electrochemical performance, with a specific capacity of 704 mA h g^{-1} after 200 cycles at 0.5 C.

A main drawback of MOFs is the low electrical conductivity, to solve this problem, Cai *et al*. reported a conductive 2D-layered MOF (Ni_3(2,3,6,7,10,11-hexaiminotriphenylene$)_2$, $Ni_3(HITP)_2$) as S host.[55] Due to the 2D structure and π-conjugation, the conductivity of this material can reach 400 S m^{-1}. With such a high conductivity, the use of conductive carbon was reduced, and a high sulfur content of 65.5% in the electrode was achieved. This material delivered a high initial capacity of 1302.9 mA h g^{-1} at 0.2 C (1 C = 1675 mA g^{-1}), and good cyclic stability (629.6 mA h g^{-1} after 300 cycles at 1 C).

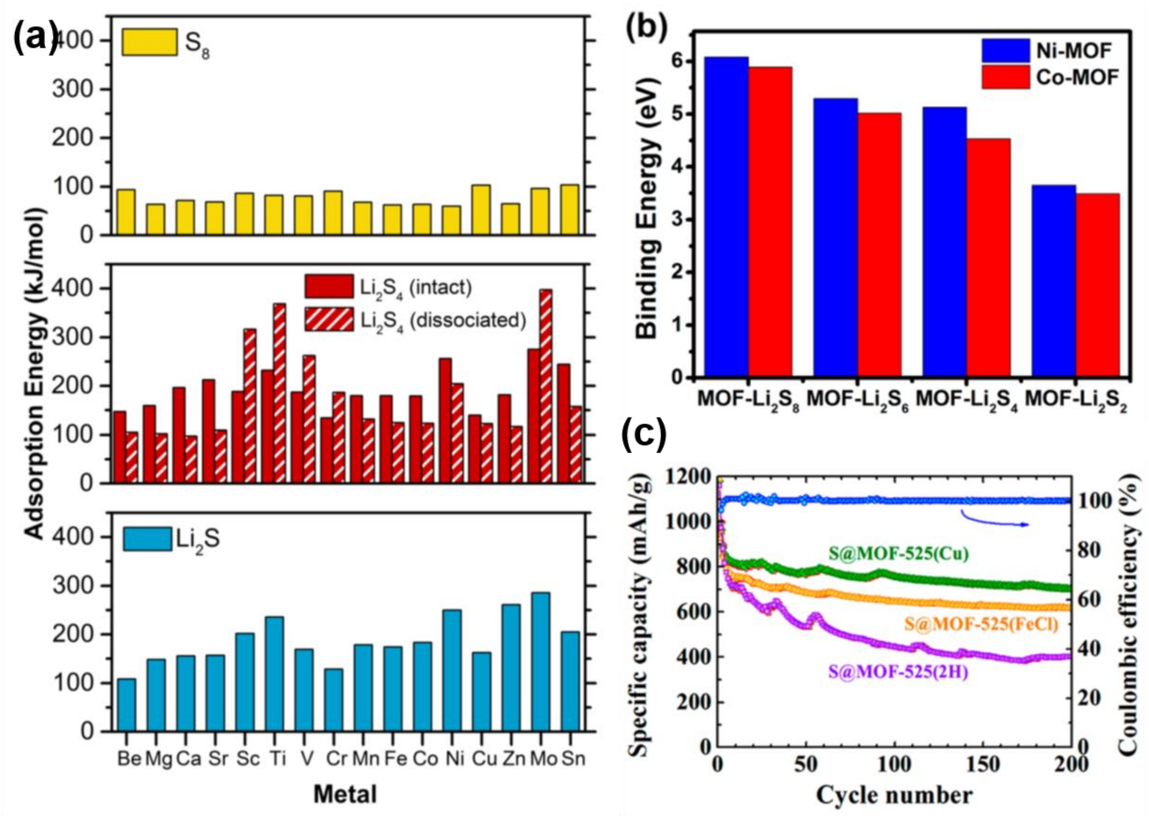

Figure 1.13. (a) Calculated adsorption energies for S_8 (top), Li_2S_4 (middle, differentiating between intact and dissociated geometries), and Li_2S (bottom), as a function of CUS composition, M, within the MOF M_2(dobdc).[52] (b) Comparison of binding energies of lithium polysulfides to Ni-MOF or Co-MOF. (c) Cycle performance of S@MOF-525(2H), S@MOF-525(FeCl), and S@MOF-525(Cu) with the Coulombic efficiency of S@MOF-525(Cu).[54]

1.2.1.2 MOF derivate

The low conductivity of pristine MOFs will be improved after high temperature pyrolysis, meanwhile, porous structure will be created. More importantly, metal centers will transform into metal oxides/sulphides/nitrides and so on, which have high chemical absorption towards LPSs and catalyst activity to promote the reactions. Thus, MOF derivate has been widely synthesized and applied as S host in LSBs. Based on the composition of the derivate, they can be divided into pure carbon, metal oxide-carbon composite, metal sulphide-carbon composite, metal carbide-carbon and so on.

Xu et al. reported a MOF-5 derived hierarchically porous carbon nanoplates (HPCN) as S host.[56] MOF-5 is formed with Zn^{2+} metal center and terephthalic acid as ligands. Zn has a relatively low boiling point of 907 ℃, when MOF-5 is heated to 900 ℃ for 3 hours, the Zn inside will evaporate, and the organic ligands will carbonize into porous carbon material. The as-synthesized HPCN had a very high specific surface area (1645 m^2 g^{-1}) and a large pore volume (1.18 cm^3 g^{-1}), which was suitable for S host (**Figure 1.14a**). The pores could accommodate the volume change of S during charge and discharge and immobilize LPSs, besides they also provided channels for electrolyte diffusion and ion transfer. Cells with the host had a high electrochemical performance. An initial discharge specific capacity up to 1177 mA h g^{-1} can be achieved at a current density of 0.1 C (1 C = 1675 mA g^{-1}). After 50 cycles at 0.5 C, 730 mA h g^{-1} could be maintained (Figure 1.14c-d).

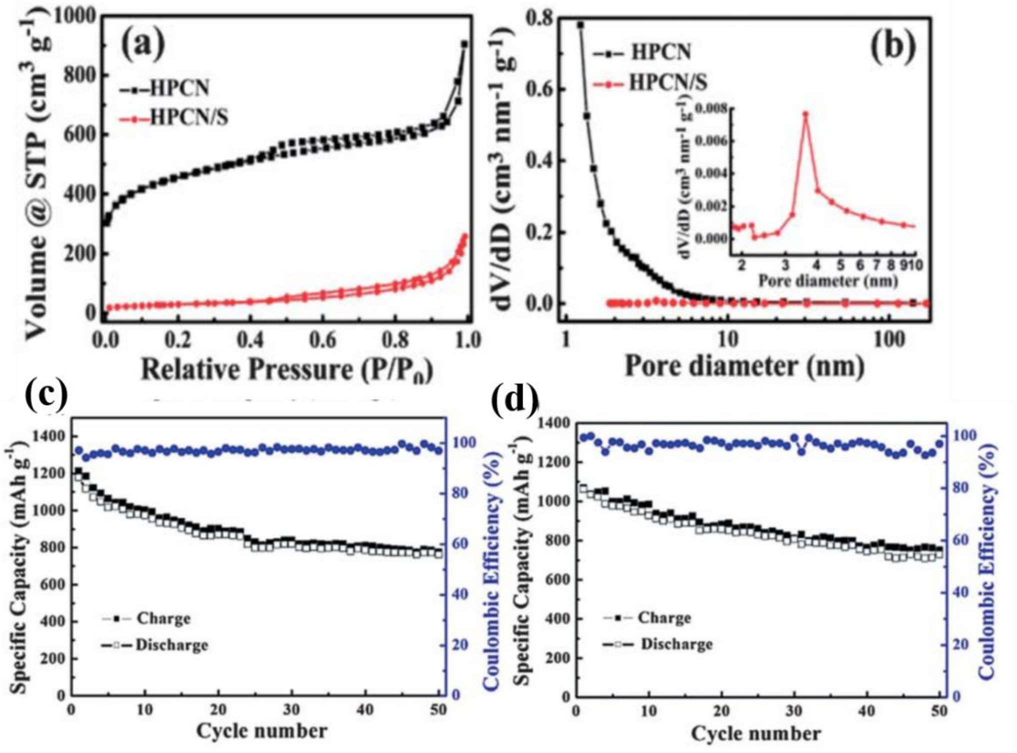

Figure 1.14. (a) N2 adsorption–desorption isotherms at 77 K and (b) pore size distribution of HPCN and HPCN–S composite. Cycling performance of HPCN–S composite electrode at a constant rate of (c) 0.1 C and (d) 0.5 C.[56]

Transition metal carbides, including MXene, Mo_2C and so on, have been widely studied in energy related area because of their high catalyst activity, conductivity and stability. Chen *et al*, reported a MOFs-derived Mo_2C based material as host for LSBs. As shown in **Figure 1.15a**.[55] Cu and Mo based MOF-$[Cu_2(BTC)_{4/3}(H_2O)_2]_6[H_3PMo_{12}O_{40}]$ (NENU-5) was synthesized as precursor. After heated at 800 ℃ for 6 hours, NENU-5 turned into a mixture of Mo_2C and Cu supported on carbon material. Then the Cu particles were etched by $FeCl_3$

solution (0.1 M). The as obtained product was labelled as Mo_2C-C NOs. At a high S content (72.15%), cells with this S host delivered a high initial specific capacity of 1396 mA h g^{-1} at 0.1 C (1 C = 1675 mA g^{-1}). This could be ascribed to the high conductivity and electro catalytic ability of Mo_2C. When tested at 1 C for 600 cycles, a specific capacity of 762 mA h g^{-1} could be maintained with a low-capacity decay rate of 0.0457% per cycle. Zhang et al. synthesized a metal oxide/metal carbide heterostructure with high catalyst activity for LSBs (Figure 1.15b).[58] MIL-47(V) was synthesized through a hydrothermal reaction between VCl_3 and terephthalic acid. By controlling the temperature of pyrolysis process from 800 ℃ to 1000 ℃, V_2O_3, V_2O_3/V_8C_7 and V_8C_7 supported on carbon materials could be synthesized. Among all the samples, V_2O_3/V_8C_7@C showed the best electrochemical performance: 587.6 mA h g^{-1} at high current density of 5 C, and high stability with low-capacity decay rate of 0.017% per cycle after 1000 cycles, which could be ascribed to the synergetic effect of V_2O_3/V_8C_7 heterostructure. A capture and conversion process took place on the surface of V_2O_3/V_8C_7, V_2O_3 had strong absorption ability towards LPSs, while V_8C_7 was an efficient catalyst for the reversible reactions.

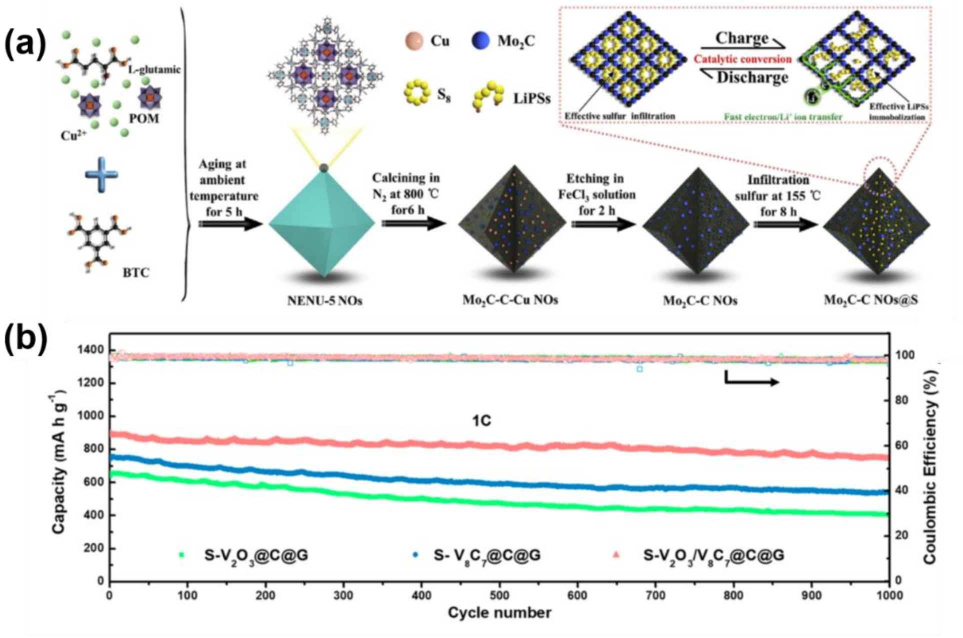

Figure 1.15. (a) Schematic illustration of the sequential preparation strategy for the MoC2–C NOs@S composite.[57] (b) Long-term cycling test at 1 C for S−V_2O_3@C@G, S−V_8C_7@C@G, and S−V_2O_3/V_8C_7@C@G cathodes, respectively.[58]

Cobalt sulphides (CoS, CoS_2, Co_9S_8 and so on) are widely studied in LSBs because of the high catalyst activity. Zhang *et al*. reported a novel method to synthesis MOF-derived CoS_2 supported on carbon framework (S/Z-CoS_2).[59] Previously, ZIFs were carbonized and sulfurized at first to synthesis carbon framework supported metal sulphides, then S is incorporated through a metal-diffusion process. However, in this research, S particles were synthesized at first, then ZIF-67 was in-situ grown on the surface of S. Finally, this composite was heated at 300 ℃ for 7 hours under vacuum to synthesis S/Z-CoS_2. The carbon framework and CoS_2 provided electron and ion transport path. And the in-situ encapsulation of S enabled physical confinement of LPSs. Finally, CoS_2 acted as chemical absorber and catalyst to eliminate shuttle effect.

Layered double hydroxides (LDHs) are a promising LPSs mediator as reported by many research. However, the isolating nature of LDHs hindered their application. Zhang et al. reported a facile method to synthesis ZIF-67 derived $Co(OH)_2$@LDH (CH@LDH) double shelled nanocage as host of S for LSBs (**Figure 1.16a**).[59] The double shelled structure provided enough space for S incorporation and high surface area and active sites for chemical absorption. However, the low conductivity resulted in relatively low electrochemical performance: an initial discharge specific capacity of 1014 mA h g^{-1} at a current density of 0.1 C with 653 mA h g^{-1} maintained after 100 cycles. Furthermore, Chen et al. reported a LDH/Co_9S_8 heterostructure nanocage for LSBs with ultra-long lifespan.[60] Co_9S_8 provided high conductivity, chemical absorption and catalyst activity in this material. A high initial specific capacity of 1339.1 mA h g^{-1} at a current density of 0.1 C could be achieved as well as a high cyclic stability up to 1500 cycles at 1 C with a capacity decay rate of 0.047% per cycle (Figure 1.16b).

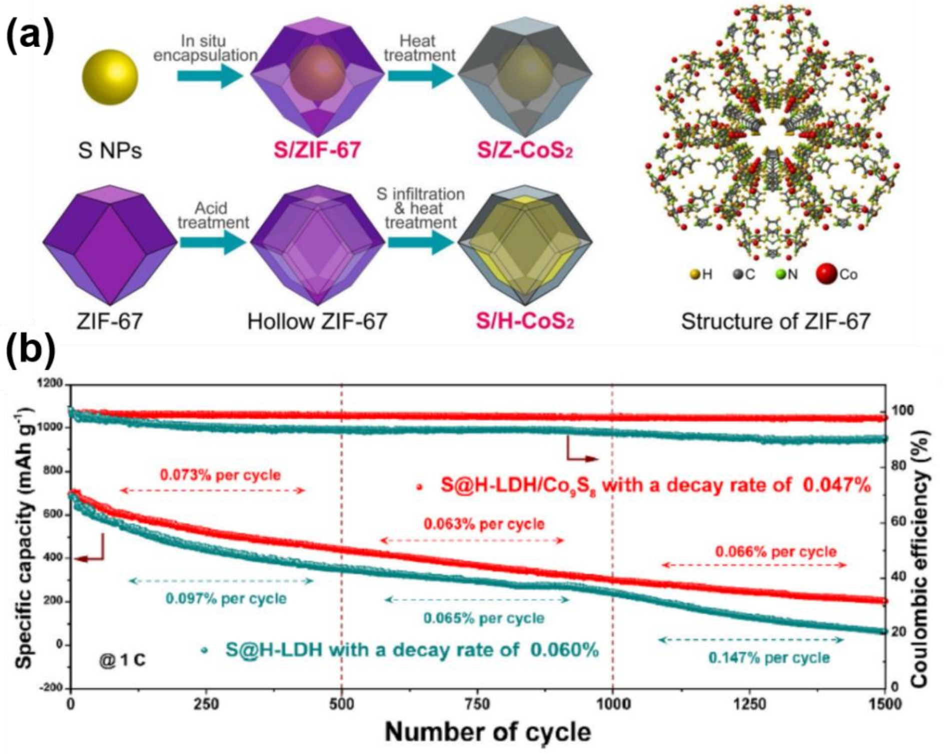

Figure 1.16. (a) Schematic illustration of the synthesis procedures of S/ZIF-67, S/Z-CoS_2 and S/H-CoS_2.[59] (b) long cyclic performance at 1C of S@H-LDH and S@H-LDH/Co_9S_8.[60]

1.2.1.3 MOF composite

Efforts have been devoted into synthesizing MOFs-based composite material with higher conductivity. Jiang *et al*. synthesized a polypyrrole (PPY a commonly used conductive polymer) and MOF composite with 5-7 magnitudes higher conductivity for LSBs.[60] The coating of PPY enabled higher conductivity and provided physical confinement of LPSs. Consequently, ppy-S-in-PSN-224 had an ultra-stable performance: 670 mA h g^{-1} maintained after 200 cycles at ultra-high current density of 10 C.

Carbon nanotubes (CNT) are widely used in energy-related area because of its high conductivity and stability. Cao's group has developed several CNT and MOFs composite as S host for LSBs. In 2018, they reported a 3D porous MOF@CNT sponge for LSBs. CNT sponge formed a 3D porous structure that provided sites for MOFs growth and channels for electrolyte diffusion and electron transportation (**Figure 1.17a**).[61] The size effect was also studied in this report. Unlike pristine MOFs, samples with larger size had higher performance. As the size of MOFs got larger, more CNTs were embedded with more channels for ion and electron transportation. Samples with larger size showed a high initial specific capacity of 1380 mA h g^{-1} at a current density of 0.1 C. Though CNT sponge provided porous structure for S host, there is extensive macropores in this structure resulting in low bulk density and low volumetric capacity. Thus in 2019, they developed drying-shrinking process to prepare dense monolithic MOF and CNT composite (Figure 1.17b).[62] Small MOF nanoparticles could be compacted into dense monolith through solvent evaporation and epitaxial growth. By tailoring the MOF content in the composite, a high volumetric capacity of 676 mA h mL^{-1} could be achieved.

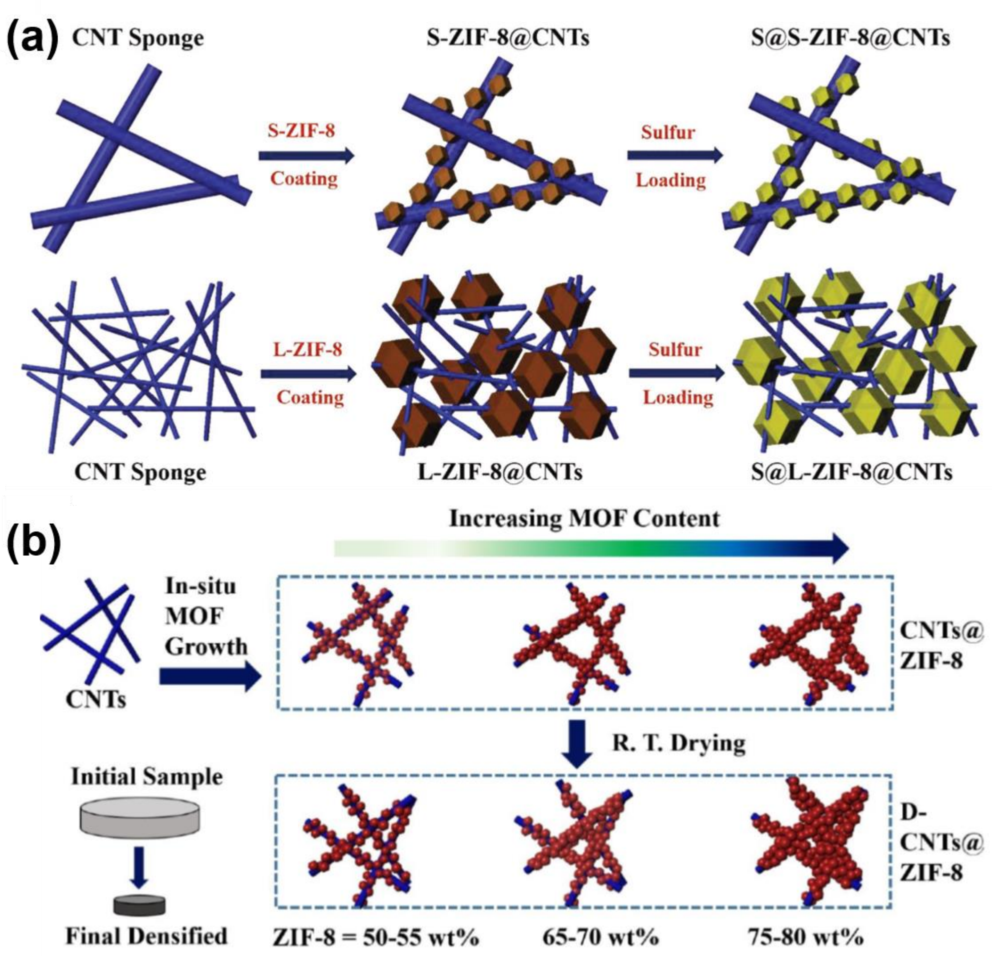

Figure 1.17. (a) Two typical hybrid structures obtained by growing smaller or larger ZIF-8 particles, which maintain the 3D network after sulfur loading, termed as S@S-ZIF-8@CNTs and S@L-ZIF-8@CNTs, respectively.[61] (b) Schematic illustration of the fabrication process including in-situ MOF growth and R.T. drying.[62]

1.2.1.4 MOF derivate composite

Through combining MOF derivate and carbon materials, the conductivity can be further improved or to prepare free-standing electrodes that does not need slurry coating process. Han et al. synthesized a MOF and reduced graphene oxide (rGO) composite (UiO-66-NH_2@rGO, U@rGO, UiO = (1R)-1,5-Anhydro-1-C-[3-[[5-(4-fluorophenyl)-2-thienyl] methyl]-4-methylphenyl]-D-glucitol) and studied how the pyrolysis temperature affect the electrochemical performance.[63] Because of the high conductivity, U@rGO carbonized at 300 ℃ showed superior rate performance: 935.3 mA h g^{-1} at 1 C and 619.1 mA h g^{-1} at 4 C. When using blade-casting process to prepare electrodes, the flexibility of the assembled batteries is not satisfactory, thus developing free-standing electrodes for flexible batteries is necessary. Jin et al. developed a MOF-derived CoP anchored on vertical graphene grown over carbon cloth (CoP@G/CC) freestanding S host for LSBs.[64]

1.2.2 MOFs and their derivate as functional separators in LSBs.

Using functional separators with high ion selectivity and mechanical strength is a promising method to promote the performance of LSBs. Celgard separators commonly used in LIBs and LSBs are polymer-based films with porous structure for electrolyte and ion diffusion. However, in LSBs, this kind of separator has several disadvantages. First, the large pores allow LPSs to diffuse between cathode and anode and lead to the corrosion of Li metal anode. Second, the mechanical strength of this separator is poor, the growth of lithium dendrite will impale the separator and result in a short circuit. Finally, the polarity of this separator is low, with low absorption and catalyst activity for LPSs. Thus, cannot accelerate the reactions and alleviate the shuttle effect.

Using MOFs to decorate separators and endow functionalization is a possible way to develop high performance LSBs. MOFs with controllable pore size and high ion selectivity can be used as ion sieves. Ideally, lithium ions can diffuse through the separators while LPSs are trapped on the cathode side. The screening of lithium ions together with uniform and abundant channels will reduce the growth of lithium dendrite. Besides the coating of MOFs on the separator will improve its mechanical strength. Finally, the metal centers in MOFs have strong chemical absorption towards LPSs and sometimes catalyst activities. Except for pristine MOFs, MOF derivate and MOF-based composites are also studied as separators for LSBs.

1.2.2.1 Pristine MOFs

Chen *et al*. developed a 2D conductive MOFs ($Ni_3(HITP)_2$, HITP = 12,3,6,7,10,11-hexaiminotriphenylene) with high atom utilization, low transport barrier and uniform 1D channels modified separator for LSBs.[65] The uniform pore structure restricted LPSs from diffusing to the anode side (**Figure 1.18a**). The high conductivity boosted the kinetics of the reactions. More importantly, the as-prepared separator was hydrophilic, which had a lower contact angle than an unmodified separator. The hydrophilicity of the separator enabled good affinity for LPSs. Cells with this modified separator had a high initial specific capacity of 1220.1 mA h g^{-1} at a current density of 0.1 C, and maintained 585.4 mA h g^{-1} after 300 cycles at 0.5 C. Though a variety of MOFs have been used to modified separators, some MOFs are sensitive to moisture and components in the electrolyte, which requires harsh environment for preparation. Fan *et al*. reported a stable MOF (UiO-66) modified separator for LSBs.[66] Density functional theory (DFT) revealed a low adsorption energy between UiO-66 and LPSs, the O atoms in UiO-66 had strong Coulomb attraction toward Li^+ in LPSs. Cells with these modified separators had a good cyclic stability, maintained a specific capacity of 586 mA h g^{-1} after 500 cycles at 0.5 C with a Coulombic efficiency of nearly 100% (Figure 1.18b).

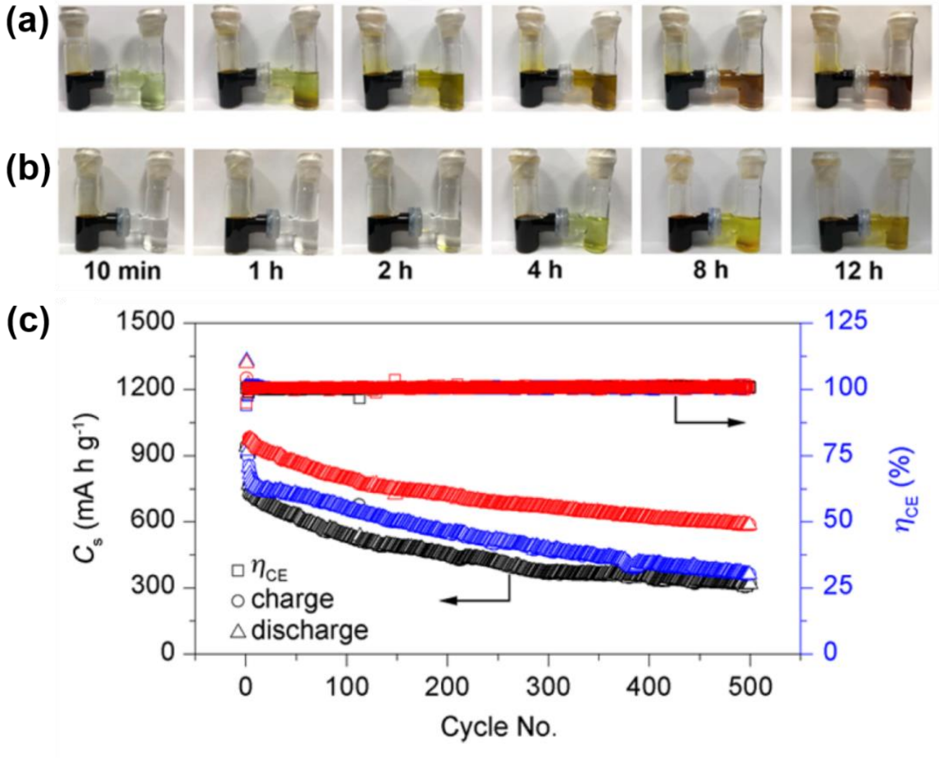

Figure 1.18. Permeation test of Li2S6 with the (a) PP separator and (b) modified separator at different times, respectively.[65] (c) Galvanostatic specific charge/discharge capacity (Cs) and

corresponding Coulombic efficiency (ηCE) of the Li−S cells, red for UiO-PP, blue for SiO_2-PP and black for pristine PP.[66]

1.2.2.2 MOF composite

He *et al*. reported a MOF-based membrane (MOF@PVDF-HFP) with both abilities to suppress shuttle effect and lithium dendrite growth.[67] HKUST-1 particles were coated on the surface of Celgard separator through vacuum filtration process, then PVDF-HFP was added as binder to link the MOFs and fill the void space between MOFs. After being repeated three times, a flexible MOF@PVDF-HFP membrane was prepared. The H-type glass Li-S cells tests showed no obvious color change with MOF@PVDF-HFP separator, indicating that this separator was effective in suppressing shuttle effect. Li//Li symmetric cells were assembled and tested to study the ability of suppress dendrite growth of this separator. It was found that cells with MOF@PVDF-HFP membrane had a lower overpotential of about 45 mV after 1000 cycles, while those with normal separators failed after around 600 cyles. Finally, coin cells with this separator showed improved electrochemical performance. An initial specific capacity of 1322 mA h g^{-1} at a current density of 0.1 C, which was 91 mA h g^{-1} higher than that with an unmodified separator. A high reversible capacity of 802 mA h g^{-1} was seen after 600 cycles at 0.5 C, compared with only 304 mA h g^{-1} in the unmodified separator.

In 2016, Bai *et al*. reported a MOF-based separator made from MOFs and GO, without Celgard separator as substrate.[68] HKUST-1 was grown *in-situ* as first, then GO layer was formed through filtration of diluted GO solution, after repeating for several times, a free-standing separator was prepared. Although GO is conductive, which might cause short circuit in batteries, the isolating property of HKUST-1 enabled the direct application of this membrane as separator. The permeation test showed no color change after 48 hours, indicating that this membrane was a good ionic sieve and suppressed the mitigation of LPSs. Cells with this separator showed a low-capacity decay rate of 0.019% after 1500 cycles.

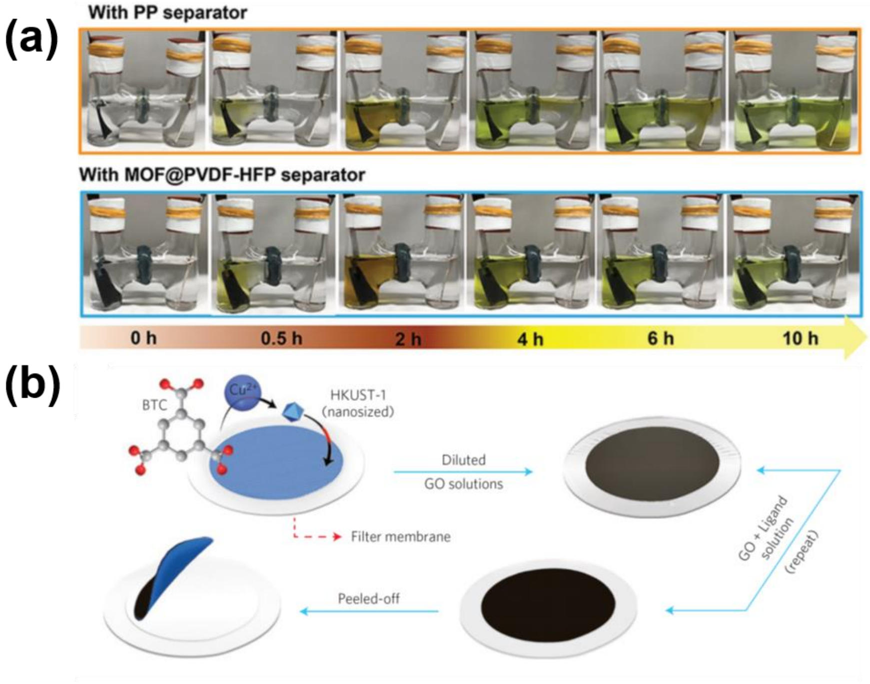

Figure 1.19. (a) Optical images of visible H-type Li–S cells with different separators during a discharging process.[67] (b) Schematic of the fabrication process to produce MOF@GO separators.[68]

1.2.2.3 MOF derivate

MOF modified separators prepared through filtration have several disadvantages. First, the stacked thick layers lead to long length and high resistance for Li^+ diffusion. Second, pristine the trapped LPSs cannot be fully used because of the slow reaction kinetic. To solve these problems, He et al. reported an *in-situ* synthesized MOF-derived Co_9S_8 hollow nanowall arrays on Celgard separator for LSBs (**Figure 1.20**).[69] MOF arrays were grown *in-situ* on the surface of Celgard separator, followed by a sulfurization process though hydrothermal reaction. The porous nanowall arrays structure of MOF template was maintained to provide space and active site for LPSs absorption and catalyst activity. The Co_9S_8 had high conductivity as well as high chemical absorption towards LPSs. Cells with this separator delivered a specific capacity of 530 mA h g^{-1} after 1000 cycles at a current density of 1 C with a low-capacity decay rate of 0.039%.

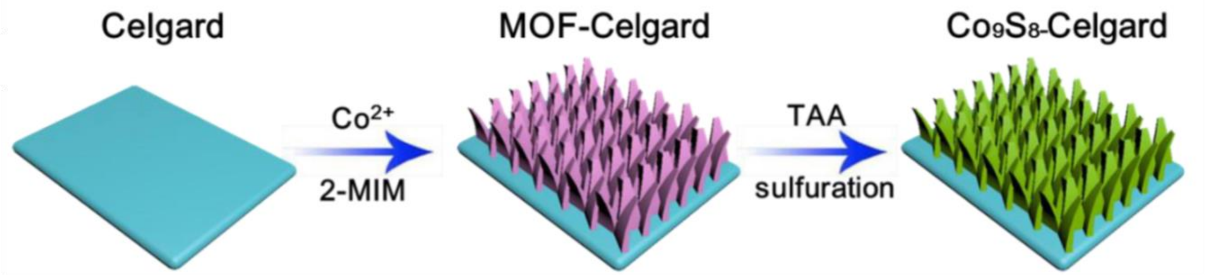

Figure 1.20. Schematic illustration of the synthesis process of Co_9S_8-Celgard.[69]

1.2.3 MOFs as solid-state electrolytes in LSBs

Using solid state electrolyte (SSE) is a possible way to eliminate shuttle effect, suppress lithium dendrite growth and improve cyclic stability of LSBs. However, the low conductivity of SSE and high resistance between interfaces lead to poor electrochemical performance. Chiochan et al. reported a MOF-based SSE with high conductivity for LSBs.[70] UiO was used as template because of its high stability. To improve the ionic conductivity, lithium sulfonates (-SO3Li) were grafted through a two-step process. A lithium ionic liquid (Li-IL) was integrated to further improve Li^+ conductivity, the final product was termed as Li-IL/UiOSLi. Samples with different IL/UiOSLi ratio were prepared and tested. Though the conductivity increased as the ratio of IL increased, the mechanical property became worse. $IL_{1.0}$/$UiOSLi_{1.0}$ reached a good compromise between conductivity and mechanical strength, with a remarkable ionic conductivity of 3.3×10^{-4} S cm^{-1} at room temperature. The suppression of LPSs diffusion and lithium dendrite growth were confirmed by visual tests (**Figure 1.21**) and symmetric cell tests. Cells with this SSE and Li_2S_6 catholyte as source of S showed stable cyclic properties: 84% of the initial capacity was preserved after 250 cycles with a capacity decay rate of 0.06% per cycle.

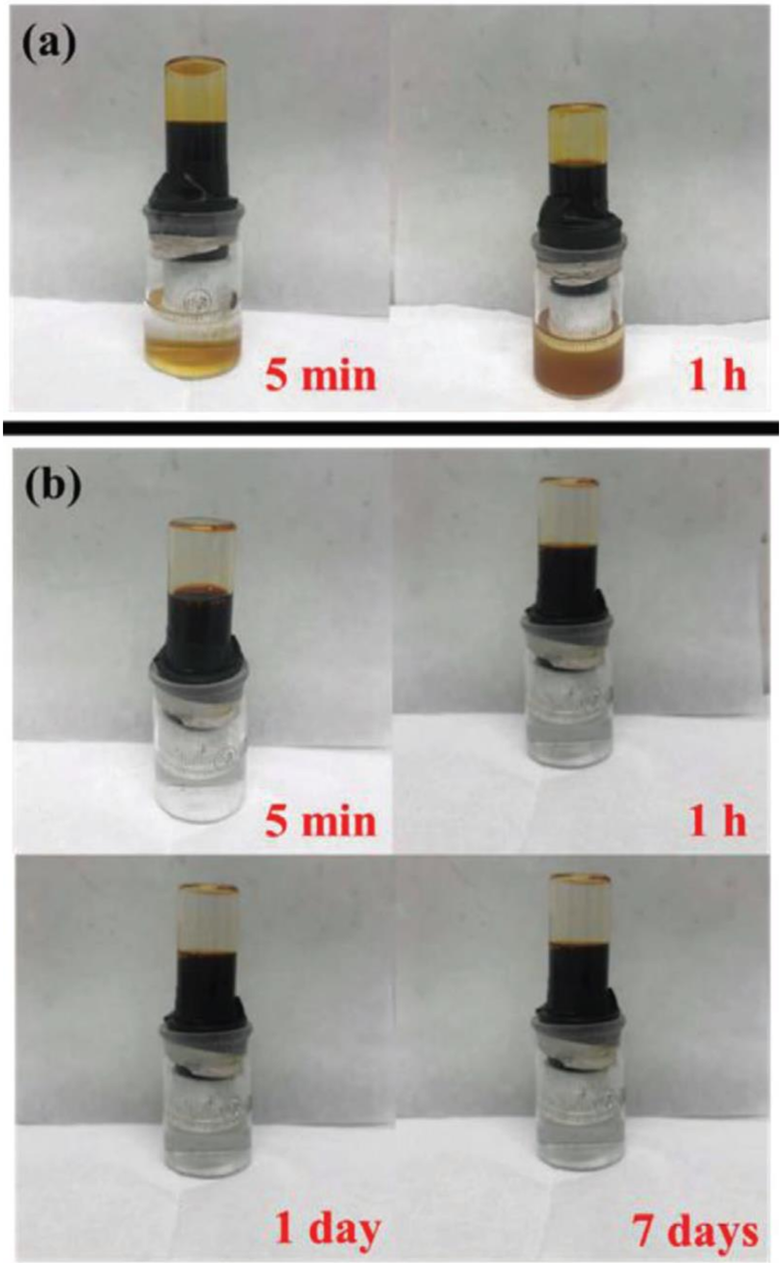

Figure 1.21. Polysulfide (Li_2S_6) penetration test through a) Celgard membrane and b) Li-IL/UIOSLi membrane.[70]

1.3 Organosulfur for LSBs

Organosulfur have been widely studied because of its inherent merits.[71–73] The fabrication of organosulfur compounds is often easier compared with the synthesis of transition metal-based compounds. Organosulfur compounds are inexpensive and environmentally friendly. More importantly, the organosulfur provides a structure to supress shuttle effects. Sulfur is embedded in the framework and covalently bonded with carbon or other heteroatoms.

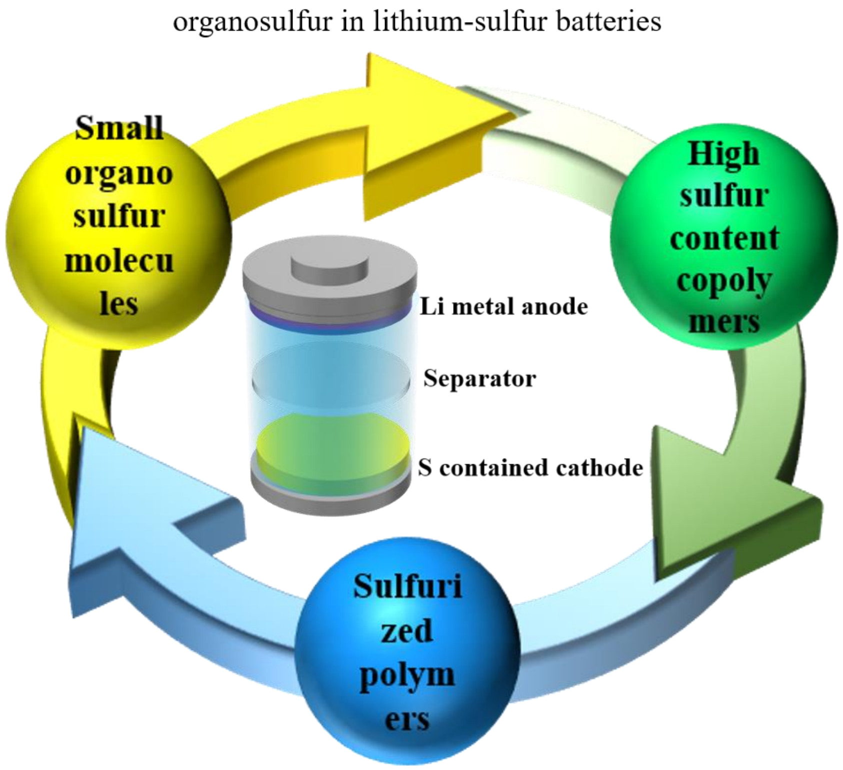

Figure 1.22. Schematic diagram of organosulfur in lithium-sulfur batteries (LSBs).

1.3.1 Organosulfur as cathode materials for LSBs

Cathode materials are crucial for LSBs. The energy density of LSBs mainly depends on the capacity of sulfur cathodes, when lithium metal anode is used. The efficiency and cyclic stability of LSBs mainly depend on whether the sulfur cathodes successfully suppress the shuttle effect. Consequently, there are thousands of research articles about designing and synthesizing cathode materials for high-performance LSBs over the past decades. By optimizing the structure and component of cathode materials, the shuttle effect can be alleviated through the different strategies mentioned above. However, these cathode materials often have a complicated and expensive fabrication process. Meanwhile, organosulfur compounds are easy to synthesize, not poisonous and environmentally friendly, thus drawing more and more recent attention. Organosulfur compounds can be classified into three types based on their structures, synthesis methods and electrochemical performances: small organosulfur molecules, high sulphur content copolymers and sulfurized polymers (**Figure 1.22**). Small organosulfur molecules are organic molecules that have several sulfur atoms. Because of the short sulfur chain, usually less than four sulfur atoms in one molecule, the formation of lithium polysulfides during charge and discharge processes vanishes. This type of organic molecules is usually soluble in the organic electrolyte used in LSBs, which is suitable for use as an electrolyte additive. However, when used as the electrode material, a host is needed to prevent it from dissolving into the electrolytes and reacting with the Li anodes directly. High sulfur content copolymers can be fabricated through the copolymerization of sulfur and unsaturated organic monomers. A cross-linked structure is formed as sulfur is grafted to the main chain of the polymer. The physical and chemical properties of these compounds can be modulated by designing monomers with different structures and controlling the ratio of sulfur and monomer during the copolymerization. Sulfurized polymers are synthesized through a high temperature treatment of a mixture of sulfur and polymers. Polymers with unsaturated groups in their main chain or side chain will react with sulfur to form ring structures or cross-linked structures. All three kinds of organosulfur materials can be used as cathode materials for LSBs. However, the differences in structures between these compounds result in different physical and electrochemical performances.

1.3.1.1 Small organosulfur molecules

In 1988, Visco *et al.* firstly reported a battery system that worked through the chemically reversible oxidation of alkali metal thiol salts to corresponding disulfides ($2\ RS^- \rightleftharpoons RSSR + 2\ e^-$).[74] Since then, small organosulfur molecules have been widely studied in different energy storage systems, including LSBs.

Manthiram's group studied the application of a variety of small organosulfur molecules as electrode materials for batteries. In 2020, they reported the application of Xanthogen polysulfides as the cathode material for the first time. Xanthogen polysulfides have a formula of $R\text{-}O\text{-}C(S)\text{-}S\text{-}S_n\text{-}S\text{-}(S)C\text{-}O\text{-}R$, where R is an alkyl or aryl group, n is the number of sulfur atoms and C(S) is a double bond between C and S (**Figure 1.23a**).[75] The materials with different numbers of sulfur atoms were synthesized and characterized: di-isopropyl xanthogen disulfide (DIXDS) and di-isopropyl xanthogen polysulfide (DIXPS). The number of sulfur atoms affects both physical and electrochemical properties of these compounds. DIXDS with only two sulphur atoms is a light-yellow solid powder, while DIXPS is a yellow liquid; free-standing carbon nanotube (CNT) paper was used to confine the liquid in the batteries. DIXDS showed only one voltage plateau, DIXPS showed three voltage plateaus: 2.61 V, 2.30 V and 2.08 V (Figure 1.23b and 1.23c). The voltage plateaus at 2.30 V and 2.08 V were ascribed to the conversion of linear sulphur to Li_2S, while the highest voltage plateau originated from the disulphide-thiolate redox occurring at the terminal xanthogen groups. The inductive and mesomeric effects of xanthogen groups lead to electron-withdrawal from terminal sulfur atoms, and thus the electrochemical potential is higher than other sulfur atoms; apparently more sulfur atoms means higher specific capacity. An initial capacity of 628 mA h g^{-1} at 0.1 C (1 C = 672 mA g^{-1}) was delivered by DIXPS, about two times higher than that of DIXDS. Meanwhile, a prolonged cycling (1000 cycles) stability at a high rate of 4 C with a low-capacity decay rate of 0.026% was achieved.

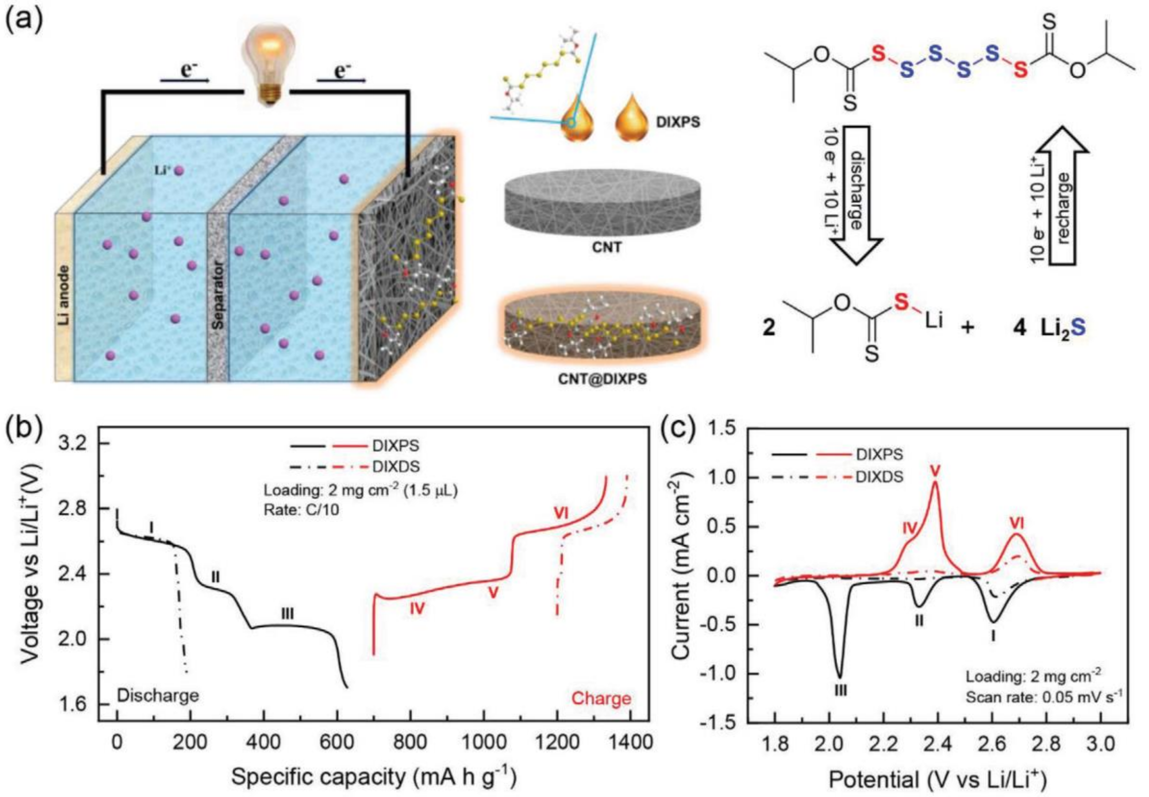

Figure 1.23. a) Schematic of the cell configuration. b) Voltage profiles for di-isopropyl xanthogen polysulfide (DIXPS) and di-isopropyl xanthogen disulfide (DIXDS) when cycled at 0.1 C (1 C = 672 mA g^{-1} for DIXPS; 1 C = 198 mA g^{-1} for DIXDS). c) Cyclic voltammograms

(CV) of the first cycle for DIXPS and DIXDS at a scan rate of 0.05 mV s^{-1}. Reproduced with permission.[75] Copyright 2020 Wiley-VCH.

He *et al*. employed dimethyl trisulfide (DMTS, CH_3SSSCH_3) as a model compound to investigate the capacity fading mechanism of organosulfur materials and proposed a solution.[76] As DMTS is soluble in the electrolyte, three dimensional graphene sponge and those with nitrogen doping and Fe_3O_4 decorating (3DG, 3DNG and 3DFNG) were used as the host for DMTS. It was found that materials with 3DFNG as the host showed the best electrochemical performance: high initial capacity (822 mA h g^{-1} at 0.1 C), better rate performance and superior long cycle stability (500 cycles with a capacity decay rate of 0.09% per cycle). The visual test showed that the cell with 3DFNG had no obvious colour change while those with 3DG and 3DNG turned yellow and brown after working for certain time. This phenomenon suggested that DMTS and the discharge products (CH3-S-Li CH3-S-S-Li and Li_2S) were soluble in the electrolyte, which were the same as lithium polysulfides. As a result, these compounds would diffuse to the anode and passivate lithium metals. Because 3DFNG had the highest adsorption ability of intermediates and prevented side reactions, the batteries with 3DFNG hosts had the best performance. The ^{1}H nuclear magnetic resonance (NMR) also revealed a weaker peak intensity of CH3-S-Li in cell with 3DFNG host.

Thiols are another type of organic compounds that easily react with sulfur to form products with long sulfur chains ($2\ RSH + n\ S = R\text{-}S\text{-}S_{n-1}\text{-}S\text{-}R + H_2S$). Bhargav *et al*. reported a facial and scalable route to synthesize phenyl polysulfides: phenyl tetrasulfide (PTS), phenyl pentasulfide (PPS) and phenyl hexasulfide (PHS), as shown in **Figure 1.24**.[77] The relationship between the length of the sulfur chain in phenyl polysulfides and the volume change of electrode was revealed. In C/S composite electrodes, the volume change can reach 80%, which will lead to the fracture of electrodes and the poor stability. However, when utilizing phenyl polysulfides, the volume change can be reduced to 37%, less than half of that in C/S composites. Phenyl polysulfides had three voltage plateaus during discharging: 2.4 V, 2.2 V and 2.0 V. The highest one corresponded to the breakage of the central S-S bond, the middle one originated from the formation of phenyl persulfide and phenyl sulphide radicals, and the lowest one was caused by the formation of Li_2S and lithium thiophenolate (PhSLi). The electron-withdrawing phenyl group raises the electrochemical potential of sulfur, which was beneficial for cathode materials. Finally, coin cells with phenyl polysulfides as cathode materials, and CNT papers as the host, were assembled and tested. PHS delivered the highest specific capacity of 650 mA h g^{-1} and a capacity retention of 80% in 500 cycles at 1 C (1 C = 774.5 mA g^{-1}).

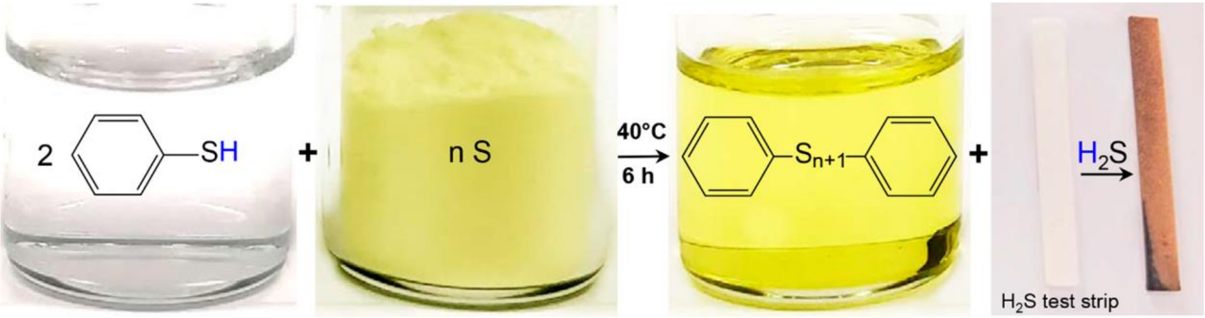

Figure 1.24. Visual representation of the synthesis process of phenyl polysulfide. Reproduced with permission.[77] Copyright 2018, American Chemical Society.

Apart from these, small organic molecules such as thiuram polysulfides[78], organotrisulfides[79], have also been reported as electrode materials for LSBs. Like in C/S composites, multi-step reactions occurred when these organic molecules were utilized as electrode materials, except those with only two sulfur atoms. However, to understand the mechanism of multi-step reactions, advanced characterization technology and computational simulations are needed. The properties of these molecules can be altered by designing the structure: sulfur atoms can bond with different organic groups including alkyl, vinyl, aryl, *etc*. The electrochemical potential, solubility, density, stability as well as many other properties of these molecules can be tuned. It is also worth exploring host materials for small organic molecules, as these compounds may be in the liquid phase or soluble in the electrolyte. CNT papers or aerogels are the most widely used hosts. But the synthesis of CNT is complicated, and CNT is easy to aggregate, which will reduce the available pore structure. Graphene aerogel, which is easier to synthesis has also been reported as host of small organosulfur molecular for LSBs. Transition metal-based compounds can be introduced to further improve the absorption ability of the host. MXene, another type of 2D conductive material might also be suitable for sulfur host. The metal components in MXene, usually Ti and V, have stronger absorption ability towards organosulfur molecular than nonpolar carbon materials. Besides, the high catalyst activity of MXene will promote the dynamics, which is beneficial for high utilization of S and high rate performance.

1.3.1.2 High sulfur content copolymers

High sulfur content copolymers can be easily synthesized through a copolymerization reaction between elemental sulfur and unsaturated monomers. The unique properties of sulfur make this copolymerization reaction possible. Sulfur tends to catenate and form a crown-shaped *cyclo-S8* under ambient conditions. When heated to over 159 ℃, ring-opening polymerization occurs. S_8 turns into linear polysulfane with radical ends, which can react with unsaturated monomers to form high sulfur content copolymers. The lithiation and delithiation route of these copolymers are similar to S_8. Li_2S, together with R-S-Li (or R-Li), are the discharged product.

Pyun's group firstly reported the synthesis of poly(sulfur-random-1,3-diisopropenylbenzene) (poly(S-r-DIB)) through the copolymerization between sulfur and DIB at above 159 ℃, no additional initiators or organic solvents are needed (**Figure 1.25a**).[80] They called it an inverse vulcanization process as a large amount of sulfur was used, which is inverse to conventional vulcanization process where a small amount of sulfur is used to stabilize the polydiene. The sulfur content in this compound can be tuned by adjusting the mass ratio of sulfur and monomers. A series of copolymers with sulfur content ranging from 50% to 90%, corresponding to 10-44 S units per DIB unit, were synthesized. The high sulfur content, which enables high energy density, is beneficial for the practical application of organosulfur compounds. The electrochemical behaviour of these compounds was similar to S_8, two voltage plateaus at ~2.3 V and ~2.1 V were detected. The copolymer delivered an initial specific capacity of 1100 mA h g^{-1} with a capacity retention of 823 mA h g^{-1} at 100 cycles at a current density of 0.1 C (1 C = 1672 mA g^{-1}).

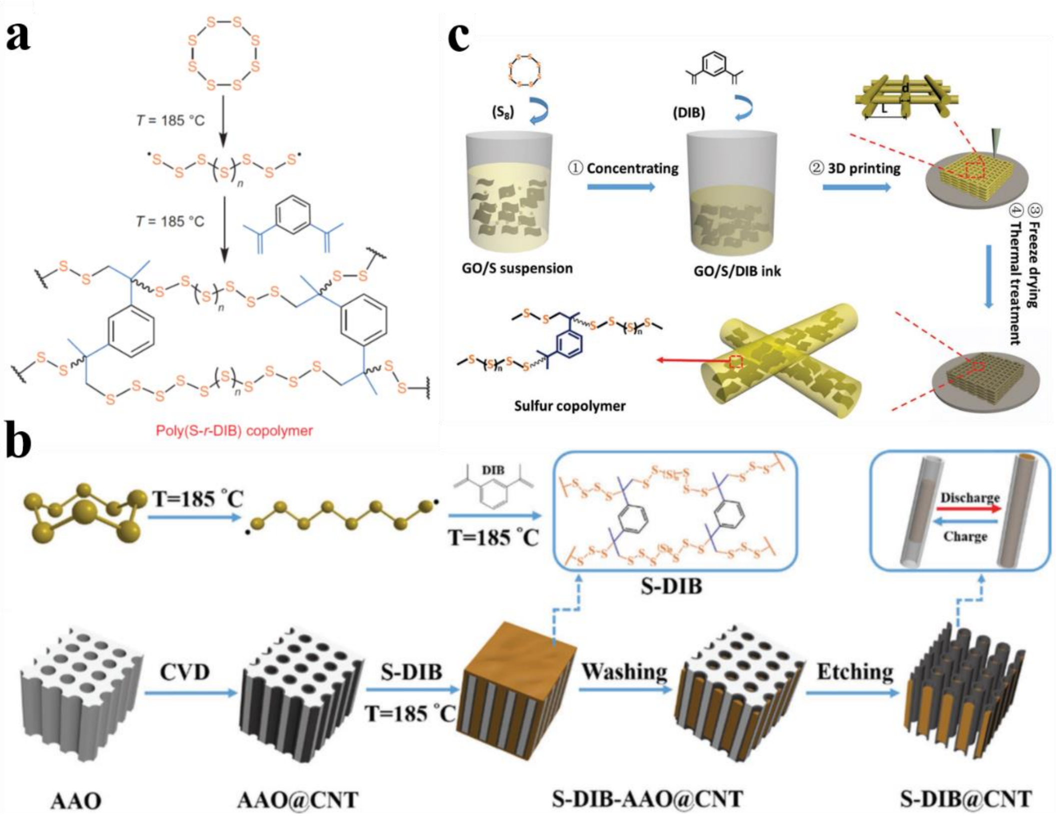

Figure 1.25. a) Synthetic scheme of poly(sulphur-random-1,3-diisopropenylbenzene) (poly(S-r-DIB)). b) Fabrication process of S-DIB@CNT. c) Schematic demonstration of 3D printing sulphur copolymer-graphene (3DP-pSG) architectures. a) Reproduced with permission.[80] Copyright 2013 Springer Nature. b) Reproduced with permission.[81] Copyright 2017 Wiley-VCH. c) Reproduced with permission.[80] Copyright 2018 Wiley-VCH.

Inspired by this work, poly(S-r-DIB) incorporated with CNT and graphene oxide (GO) were reported by others. Hu *et al.* reported a dual-confinement strategy to synthesize high-performance sulfur-copolymers for LSBs as shown in Figure 1.25b.[81] The CNT matrix was synthesized on an anodic aluminium oxide (AAO) template, then S-DIB copolymer was introduced through a melt-diffusion process. The sulfur content was 67%, lower than pure S-DIB copolymers in Pyun's work. But this compound showed higher initial specific capacity and long cycle stability: 1300 mA h g^{-1} at 0.1 C and 880 mA h g^{-1} at 1 C after 100 cycles with a capacity retention of over 98%. The better electrochemical performance was ascribed to the well-designed structure. CNTs framework and C-S covalent bond provided physical and chemical confinement of lithium polysulfides, respectively. Also, CNTs facilitated ion and electron transfer and accommodated the volume change of sulfur during charge and discharge. Shen *et al*. used an extrusion 3D printing strategy to fabricate 3D sulfur copolymer-graphene architecture (3DP-pSG) for the first time (Figure 1.25c).[82] S_8, DIB monomers and graphene oxide were embedded in the 3D architecture. An *in-situ* copolymerization process took place at 200 °C. Similarly, the GO framework provided high electrical conductivity and buffered the volume change. The sulfur content in 3DP-pSG reached 75.0%. This compound delivered a reversible capacity of 812.8 mA h g^{-1} at a current density of 50 mA g^{-1}. However, after 50 cycles, only 43% of the initial capacity was maintained.

Apart from DIB, there are other monomers that have been used to synthesize sulphur-copolymers. Li *et al*. reported a facial two-step process to synthesize high sulphur-containing copolymer (**Figure 1.26a**).[83] The S powder was heated to 180 °C under an Ar atmosphere, then triallyl isocyanurate (TAIC) was added into the molten S at a controlled mass ratio. The mixture was cooled to room temperature after reacting for several hours. Finally, the product was synthesized through heating the samples at 250 °C for 4 h under Ar atmosphere and referred to as S-triallyl isocyanurate organosulfur polymer composite (STI). It was found that STI had a "watermelon-seed" structure, the monoclinic S was the seed and the copolymer is the wrapper. This unique structure had several merits. First, a high sulfur content of 90% can be realized. Second, the superfine distribution of monoclinic S provides transport channels for ions and electrons. Finally, copolymer frameworks and C-S bonds suppress the generation and diffusion of lithium polysulfides. Consequently, STI had a high reversible capacity of 1123 mA h g^{-1} at 0.2 C (1 C = 1675 mA g^{-1}) and a good long-term stability of 827 mA h g^{-1} after 200 cycles at 0.5 C with a decay rate of 0.043% per cycle.

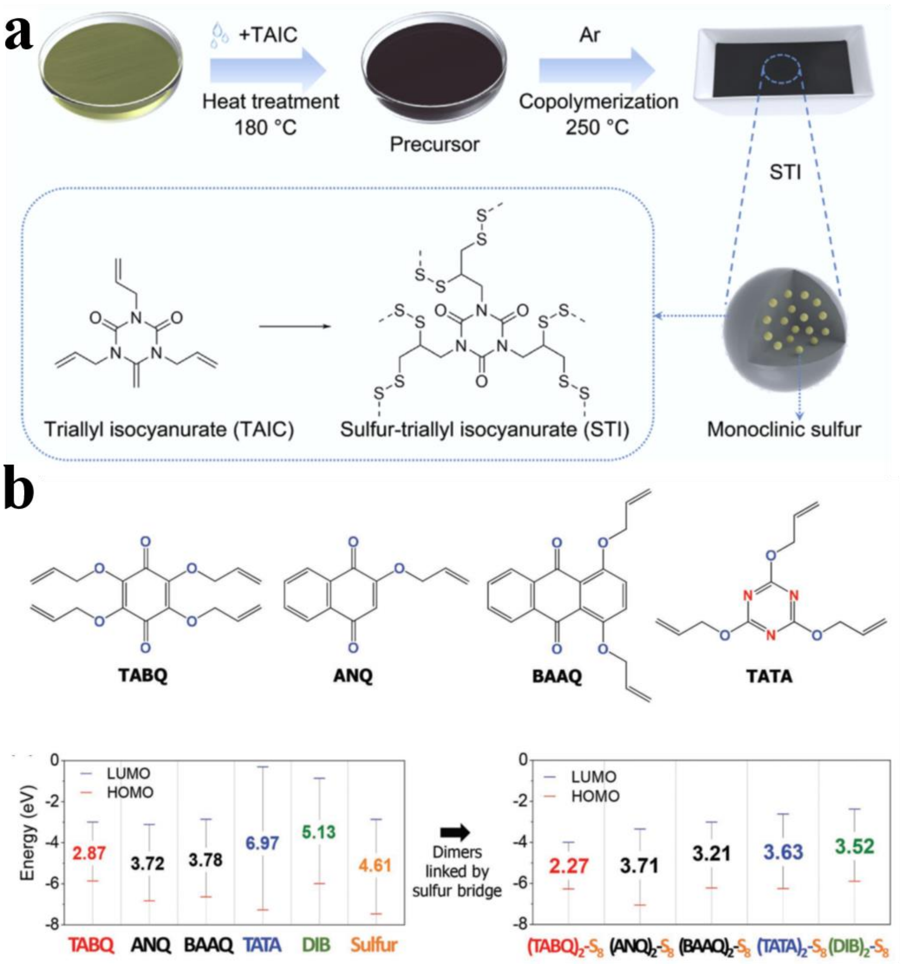

Figure 1.26. a) Schematic illustration of the synthesis process of STI and proposed chemical structure. b) Molecular structures of TABQ, ANQ, BAAQ and TATA as well as the corresponding calculated energy diagrams of these compounds and their dimers with sulfur bridge. a) Reproduced with permission.[83] Copyright 2020 Elsevier. b) Reproduced with permission.[84] Copyright 2018 Wiley-VCH.

Though high sulfur content copolymers can suppress the shuttle effect, the electrical conductivity of polymers is insufficient. Kang *et al*. studied how the structure of linkers affect the electrical conductivity and further affect the electrochemical performance of copolymers.[84] Four linker molecules based on quinone and triazine were investigated: tetra(allyloxy)-1,4-benzoquinone (TABQ), 2-allyloxy-naphthoquinone (ANQ), 1,4-bis(allyloxy)-anthraquinone (BAAQ) and triallyloxy-triazine (TATA). Density functional theory (DFT) revealed that TABQ has the lowest bandgap in both single molecules and dimers linked by sulfur, which promises a high sulfur utilization and fast redox kinetics (Figure 1.26b). This also showed the possibility of tuning the properties of high sulfur content copolymers by designing the structure of monomers. As expected, among the four synthesized copolymers, Poly(S-TABQ) with a sulfur content of 75% had the best performance. The batteries based on poly(S-TABQ) had a high initial specific capacity of 1346 mA h g^{-1} at a current density of 0.1 C (1 C = 1670 mA g^{-1}). Exceptionally, a discharge capacity of 833 mA h g^{-1} could be achieved at a high current density of 10 C. XPS tests of samples after 100 cycles showed that the change in intensity of C-S bond in poly(S-TABQ) is negligible, while in poly(S-TATA), a significant reduction of C-S content was determined. Also, poly(S-TABQ) showed lower ohmic resistance and charge transport resistance.

Selenium sulfide or Se-doped S (Se_xS_y) has been used as a substitution of elemental S to synthesize sulfur contained copolymers because of the high electrical conductivity of Se (~10^{-3} S m^{-1}). In 2017, Zhou *et al*. reported an organosulfur cathode made from SeS_2. Se-doped poly (diallyl tetrasulfide) (PDATtSSe) was synthesized by using diallyl sulphide as a monomer and SeS_2 as the source of sulphur and selenium.[85] The content of S and Se in PDATtSSe was calculated to be 71.6%. When tested, PDATtSSe delivered a specific capacity of 700 mA h g^{-1} at a current density of 200 mA g^{-1} (based on the mass of PDATtSSe). A reversible capacity of 500 mA h g^{-1} and a low decay rate of 0.02% per cycle were achieved after 400 cycles at 600 mA g^{-1}. Then *in situ* UV/vis spectroscopy test revealed that no soluble lithium polysulfides formed during discharge and charge as no peak shifting was detected. SEM images also showed that a smooth and uniform solid-electrolyte-interphase layer formed upon the lithium foil, indicating that the shuttle effect was greatly alleviated. Also, lower charge transfer resistance and faster Li^+ diffusion coefficient were found in samples with Se-doping.

In general, high sulphur content copolymers are easy to prepare and have relatively high capacities. Alkenes and alkynes are the most commonly used monomers as they are the simplest and most frequently investigated organic compounds that have unsaturated groups. Another kind of widely used monomer is thiols. Because of the instability of S-H bond, thiols react easily with S at a relatively low temperature. Furthermore the physical and chemical properties of copolymers can be adjusted by designing the structure of monomers and controlling the ratio of S/monomers.[86-87] The electrical conductivity of copolymers is lower than expected. Introducing carbon materials to improve conductivity is a possible solution. Heteroatom doping might also be a way. The doping elements have higher conductivity or increase the density of electrons to lower electron transfer resistance. What’s more, the reaction mechanism of these copolymers has not been fully understood. Models have been proposed to explain the electrochemical behaviours, but there are still debates about it. The reaction pathway is not clear. Some reported the breakage of terminal bonds at first and then the internal bonds, while others reported the opposite pathway. The breakage of C-S bonds on the ends of S chains is debatable, different final products such as R-Li and R-S-Li have been reported. Advanced characterization technology as well as simulation works are still needed to figure out the actual reactions of these copolymers.

1.3.1.3 Sulfurized polymers

Polymers with unsaturated or reactive groups can also react with sulfur to form sulfurized polymers. However, the reaction condition is more rigid than those of monomers, usually involves high temperature, inert gas protection, and solid-state milling, *etc*. Meanwhile, during the high-temperature treatment, C-H bonds may break and gases (H_2S, SO_2 *etc*.) will be released. But the improved electrical conductivity and structural stability that arise are fascinating.

Among all sulfurized polymers that have been studied in LSBs, sulfurized poly acrylonitrile (SPAN) is the most popular one ever since the first report from Wang's group in 2002.[88] The good electrochemical properties and compatibility with carbonate electrolyte is attractive. The research about revealing the reaction mechanism and the structure of SPAN as well as designing and synthesizing SPAN-based materials with high performance are advancing. The formation of C-S covalent bond has been widely characterized and accepted. Recent research showed that there might be a S-containing ring structure. There is also research using carbon materials to improve the electrical conductivity or metal oxides to improve the stability of PAN. Other sulfurized polymers such as thiourea aldehyde resin[89] and poly (acrylic acid) (PAA)[90-91] have also been investigated.

Sulfurized PAN

Ever since Wang's report, sulfurized PAN (SPAN) has attracted more and more attention. The ability to suppress the shuttle effect, compatibility with carbonate electrolyte and low self-discharge is intriguing. The research about SPAN is mainly about two aspects. First, the structure of SPAN and secondly the reaction mechanism. Although a ladder structure in SPAN is commonly accepted, some details are divergent. The formation mechanism of C-S bond is unclear, and the quantitative analysis is rare. For example, how many S atoms are bonded with C and the length of the S chain or ring have never been studied. What's more, some reports reported physically absorbed S in SPAN together with covalently bonded S. In the charge-discharge process, the C-S bond will break and form repetitively and this is not clear. Different final discharge products and reaction pathways have been reported. A rational structure is needed to explain the high initial capacity and low Coulombic efficiency at the first cycle. Second, developing new synthesis method, incorporation of other components (carbon materials, metal oxides and heteroatom doping methods) to achieve a satisfactory performance is also needed.

Structure of SPAN

When Wang *et al.* first reported the synthesis of SPAN, they proposed a structure that elemental S_8 is embedded in the framework of pyrolytic PAN. However, in 2004, Yu *et al.* reported the existence of C-S bonds in SPAN.[92] Fourier Transform Infrared (FTIR), Raman and X-ray photoelectron (XPS) spectra confirmed the existence of C-S bonds. Specifically, for samples prepared at 450 ℃, the structure with a backbone of N-containing ring structure and a side chain with two sulfur atoms was proposed. Later, Wang *et al.* reported a single electron discharge process of SPAN cathodes, and the higher specific capacity than theoretical specific capacity of S was ascribed to the intercalation between Li^+ and the local environment surrounding the nitrogen (**Figure 1.27a**).[93] Recently, Weret *et al.* comprehensively studied the synthesis mechanism, chemical structure and lithiation/delithiation pathway of SPAN.[94] During the synthesis, at above 170 ℃, the ring opening polymerization of S_8 formed diradicals, which attacked C atom in C≡N, and initiated the formation of heterocyclic structures (Figure 6b). Furthermore, at a higher temperature, dehydrogenation took place. However, the morphology changes and mass loss after CS_2 washing also indicated the existence of physically confined S_8 in SPAN. During charge and discharge processes, Raman, FTIR and solid-state nuclear magnetic resonance (NMR) tests all proved the reversible cleavage and formation of C-S and N-S bonds, and the electron donating effect of Li-C and Li-N bonds increased the electron density of conjugated structures leading to the decrease of charge/discharge voltage hysteresis after the second cycle.

Though many models have been proposed to explain the electrochemical properties of SPAN from different aspects, they are all debatable.[95-96] In some reports, the bonds between the terminal S atoms and carbon atoms broke and reform during the charge and discharge process while others did not. The formation of N-S bonds is only reported in some recent articles. It is also noteworthy that the synthesis condition including reaction time, temperature, mass ratio of S/PAN will affect the structures and the electrochemical properties of SPAN. High temperature and long reaction time will lead to less physically absorbed S as S is easy to evaporate. The chain length or size of the cycle may be affected by the mass ratio of the precursors.

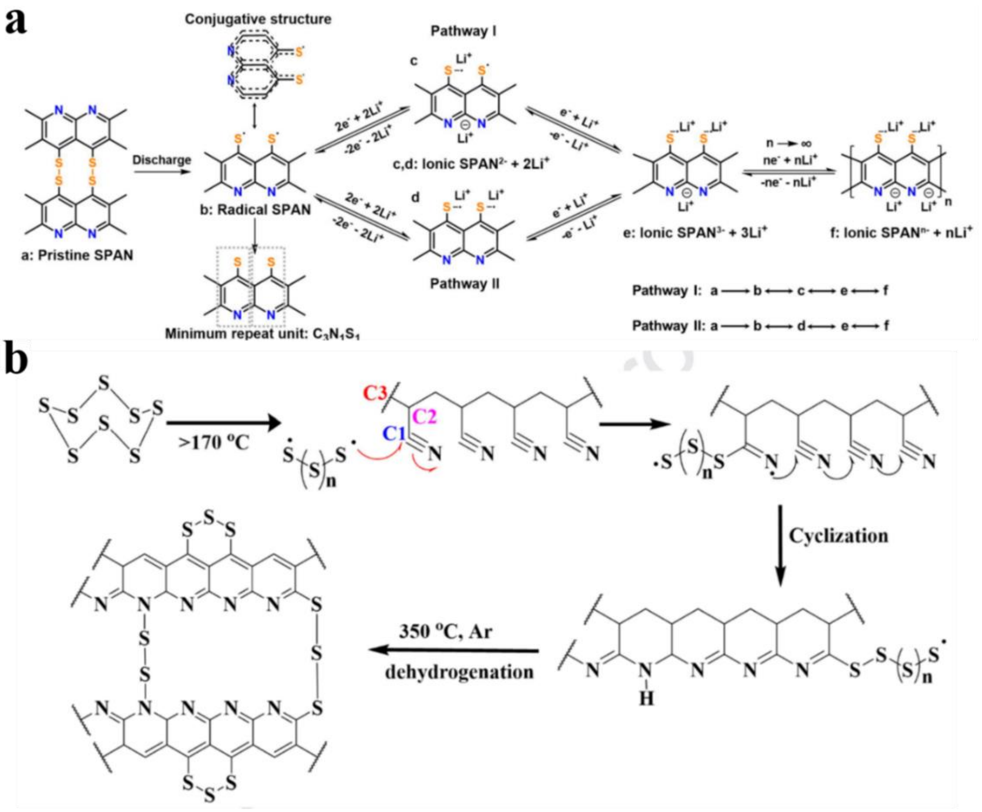

Figure 1.27. a) Possible reaction pathway of SPAN. b) Proposed reaction mechanism of synthesizing SPAN. a) Reproduced with permission.[93] Copyright 2018 American Chemical Society. b) Reproduced with permission.[94] Copyright 2020 Elsevier.

Performance of SPAN

The conjugated structure of SPAN can increase the electrical conductivity to some extent, but it is still far from satisfactory. Attempts have been made to solve these problems. Nuli's group synthesized PAN@CNT and PAN@graphene nanosheets composite materials to improve the electrical conductivity of SPAN.[97-98] Through *in situ* polymerization, PAN formed a core-shell structure with CNT or were anchored on the surface of graphene nanosheets, which provided better chemical interaction than physical mixing. As a result, the electrodes with CNT or graphene nanosheets had higher capacities than the counterparts (**Figure 1.28a** and b), especially at high current densities. Chen *et al*. used selenium sulfur composite (Se$_x$S) to synthesize Se-doped sulfurized PAN (Se$_x$SPAN).[99] The higher electrical conductivity of Se enabled the fast diffusion of Li$^+$, thus providing fast reaction kinetics and suppressing the shuttle effect (Figure 1.28c). With a small amount of Se-doping, Se$_{0.06}$SPAN exhibited a high reversible capacity of 1300 mA h g^{-1} at a current density of 0.2 A g^{-1}. This compound is compatible in both ether- and carbonate-based electrolytes. Besides the innovation of electrodes, there is research about developing electrolyte additives, binders *etc*. for SPAN-based materials. Phosphorus-rich compounds have been used to develop flame-retardant electrolytes. Yang *et al*. used triethyl phosphate and 1,1,2,2-tetrafluoroethyl-2,2,3,3-tetrafluoropropyl as the additive in electrolytes to provide flame-retardant properties and good stability. Batteries with this electrolyte were capable of operating at 60 °C.[100]

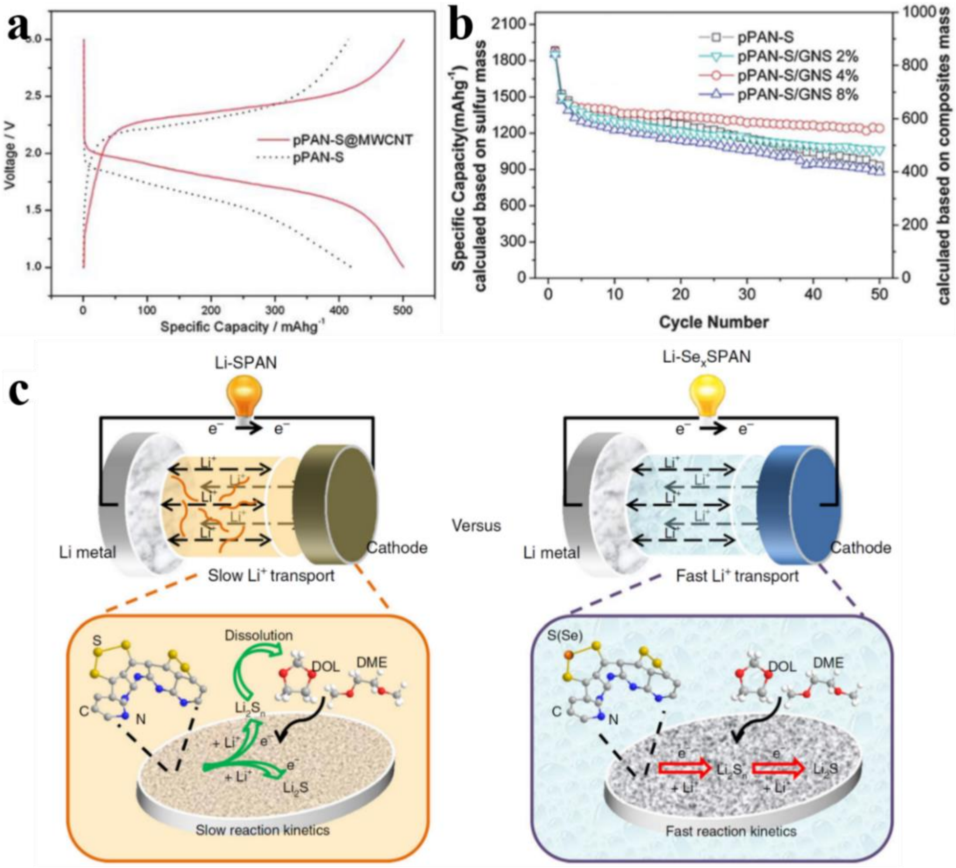

Figure 1.28. a) Charge-discharge curves of pure SPAN and SPAN@CNT tested as a current density of 1 C. b) Cyclic stability of SPAN and SPAN@GNS with different GNS content at a

current density of 0.1 C. c) Schematic diagram of proposed reaction process of Se-doped SPAN. a) Reproduced with permission.[97] Copyright 2011 Royal Society of Chemistry. b) Reproduced with permission.[98] Copyright 2012 Royal Society of Chemistry. c) Reproduced with permission.[99] Copyright Springer Nature.

Other sulfurized polymers

Liu's group has reported a series of sulfurized PAA material for LSBs. In 2019, they reported a novel 2D organic polysulfane grafted on carbon chain as the cathode material.[101] The KCl template was used to provide an ultra-thin morphology with defects to minimise Li^+ diffusion pathway. KI was used to promote the reduction of S_8 to di- or tri- sulfur radicals, which substitute the carbonyl group in PAA through a coupling reaction (**Figure 1.29a**). The sulfur content in the as-synthesized organic polysulfane nanosheets (OPNS) can be controlled by adjusting the reaction time for 1 to 24 h. OPNS-72 (72 means a weight ratio of 72% of sulfur) synthesized at 8 h had a reversible capacity of 889 mA h g^{-1} at a current density of 1 C (1 C = 1670 mA g^{-1}). High area loading (9.7 mg cm^{-2}) electrodes were tested in this work. A capacity of 594 mA h g^{-1} was maintained after 400 cycles at 1 C, with a decay rate of 0.065% per cycle. Afterwards, they further reported a flexible nanosheet with polysulfane grafted on porous graphene (pGPS), which had an excellent electrochemical performance. A high capacity of 1045 mA h g^{-1} at 1 C (1 C = 1670 mA g^{-1}) and good capacity retention of 95.3% after 100 cycles at 5 C.

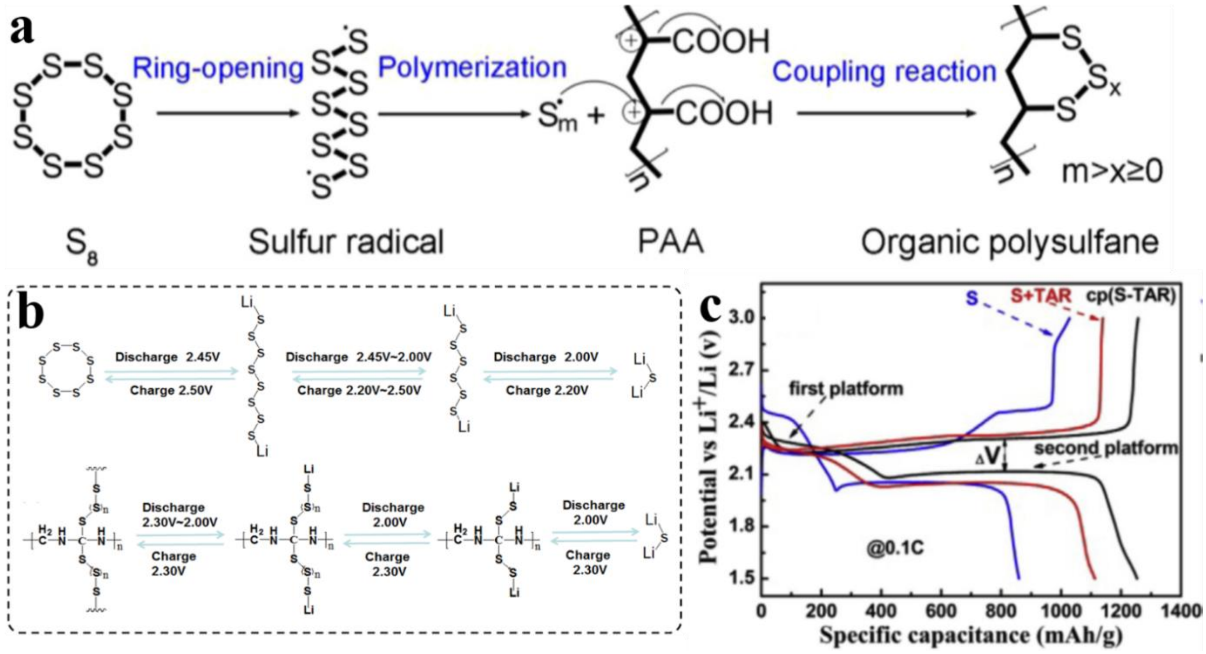

Figure 1.29. a) Proposed synthetic mechanism of organic polysulfane. b) Reaction pathways of S/C and cp(S-TAR)/C electrodes. c) Charge and discharge curves for LSBs with S/C, S+TAR/C and cp (S-TAR)/C electrodes at a current density of 0.1 C. a) Reproduced with permission.[101] Copyright 2019 Elsevier. b-c) Reproduced with permission.[89] Copyright 2018 Elsevier.

Chen's group reported several sulfurized polymers with novel structures. In 2019, a thiourea aldehyde resin (TAR) with sulfur-rich side chains was synthesized through a two-step process.[89] At first, a condensation between thiourea and formaldehyde took place, then the mixture of polymer and sulfur was kept at 170 °C for 8 hours, forming a highly cross-linked compound (S-TAR). This structure has several advantages: i) the hyper branched framework formed mesopores and provided higher electrical conductivity; ii) the combination of physical and chemical confinement suppresses the shuttle effect; iii) mesoporous structure provides abundant diffusion channels for Li^+. Importantly, ultraviolet visible (UV-vis) spectroscopy was used to quantitatively measure the content of covalently bonded sulfur in S-TAR. It turned out that 51.0 wt% of sulfur was bonded with TAR. S-TAR had a high specific capacity of 1285 mA h g^{-1} at a current density of 0.1 C (Figure 1.27b and 1.27c), and 819 mA h g^{-1} was maintained after 500 cycles at 1 C with a decay rate of 0.045% per cycle. Instead of using conductive components to improve electrical conductivity, using conductive polymers is also effective. Zeng et al. used poly(m-aminothiophenol) (PMAT), a conductive polymer with abundant thiol groups, to synthesize a highly cross-linked sulfurized polymer (S-PMAT).[100] Conductive PMAT enabled better conductivity and the reactive thiol groups reacted with sulfur to form covalent bonds, suppressing the dissolution of lithium polysulfides. As a result, S-PMAT delivered a specific capacity of 1240 mA h g^{-1} at a current density of 0.1 C (1 C = 1670 mA g^{-1} as well as a high stability of 495 mA h g^{-1} at 2 C after 1000 cycles with a decay rate of 0.04% per cycle. In summary, the electrochemical performances (including S content, specific capacity and cyclic stability) as well as test conditions of different organosulfur compounds are listed in **Table 1.1**.

Table 1.1. Electrochemical performance of organosulfur compounds

Cathode	S content (%)	Specific capacity (mA h g^{-1})	Cyclic stability (%)
DMTS[79]	76.2	720 (0.1 C 1 C = 849 mA g^{-1})	82 (50 cycles 0.1 C)
PMTT[103]	50	406 (0.2 C 1 C = 418 mA g^{-1})	87 (100 cycles 0.2 C)
PHS[77]	55.5	650 (0.5 C 1 C = 775 mA g^{-1})	80 (500 cycles 1 C)
DMTS/3DFNG[76]	63.4	822 (0.1 C 1 C = 849 mA g^{-1})	53.8 (500 cycles 1 C)
DIXPS[75]	64.6	628 (0.1 C 1 C = 672 mA g^{-1})	74 (1000 cycles 4 C)
Poly(S-r-DIB)[80]	70	1100 (0.1 C 1 C = 1672 mA g^{-1})	74.8 (100 cycles 0.1 C)
SDIB@CNT[81]	63.5	1300 (0.1 C 1 C = 1675 mA g^{-1})	98 (100 cycles 0.1 C)
PDATtSSe[104]	72.6	700 (200 mA g^{-1})	92 (400 cycles 600 mA g^{-1})

3DP-pSG[82]	75	812.8 (50 mA g^{-1})	43.4 (50 cycles 50 mA g^{-1})
Poly(S-TABQ)[84]	75	1346 (0.1 C 1 C = 1670 mA g^{-1})	74 (500 cycles 1 C)
STI[83]	90	1123 (0.2 C not mentioned)	94 (350 cycles 1 C)
BTTP[86]	~72	901.7 (901.7 mA g^{-1})	68.4 (120 cycles 901.7 mA g^{-1})
PDATtS[87]	-	700 (200 mA g^{-1})	85 (300 cycles 600 mA g^{-1})
SPAN[88]	53.4	850 (0.2 mA cm^{-2})	75 (50 cycles 0.2 mA cm^{-2})
CSM-450[92]	35.2	520 (not mentioned)	92 (240 cycles not mentioned)
SPAN@MWCNT[97]	63	697 (0.1 C not mentioned)	85 (50 cycles 0.1 C)
SPAN@GNS[98]	47	~1850 (0.1 C 1 C = 1675 mA g^{-1})	80 (100 cycles 0.1 C)
S/cPAN[105]	51	860 (100 mA g^{-1})	57 (100 cycles 100 mA g^{-1})
CoS_2/SPAN/CNT[106]	43.2	1799 (0.2 C not mentioned)	880 mA h g^{-1} (400 cycles 1 C)
Te_xS_{1-x}@pPAN[90]	47.6	1504 (0.1 A g^{-1})	87.3 (200 cycles 0.5 A g^{-1})
$Se_{0.06}$SPAN[99]	47.2	1300 (0.2 A g^{-1})	0.029/cycle (800 cycles 0.4 A g^{-1})
BP-SPAN[107]	43	2036 (0.1 C 1 C = 1675 mA g^{-1})	46.6 (200 cycles 1 C)
SPAN[108]	53.6	829 (0.2 C not mentioned)	~70% (200 cycles 1 C)

S-PPy[109]	~40	1222 (0.1 mA cm^{-2})	47 (20 cycles 0.1 mA cm^{-2})
S/T-PPy[110]	30	1157 (0.1 mA cm^{-2})	56 (80 cycles 0.1 mA cm^{-2})
cp(S-PMAT)[102]	~80	1240 (0.1 C 1 C = 1672 mA g^{-1})	66.9 (1000 cycles 2 C)
cp(S-TAR)[89]	39	1285 (0.1 C 1 C = 1672 mA g^{-1})	0.045/cycle (500 cycles 1 C)
OPNS[101]	72	891 (1 C 1 C = 1670 mA g^{-1})	0.014/cycle (620 cycles 1 C)
pGPS	71	1045 (0.5 C 1 C = 1670 mA g^{-1})	95.3 (1000 cycles 5 C)

1.3.2 Organosulfur in electrolytes for LSBs

The electrolyte plays an important role in LSBs. On one hand, the solid-liquid-solid reaction pathway enables fast reaction and high utilization of active materials. Soluble long-chain lithium polysulfides can be reduced to short-chain lithium polysulfides in the electrolyte, which is faster than solid-state reactions. The S on the surface of hosts is reduced to lithium polysulfides and dissolve in the electrolyte, the S inside is available for reaction, which is of high importance because of the insulating nature of S. On the other hand, the concentration gradient forces the soluble long-chain lithium polysulfides to diffuse between anodes and cathodes in the electrolyte. The long-chain lithium polysulfides can react with Li metal to form short-chain lithium polysulfides and Li_2S_2/Li_2S. The consumption and corrosion of Li anodes will lead to the formation of lithium dendrites and safety issues. The “dead” sulfur formed will lead to low efficiency and stability. To solve these problems, recently, organosulfur has been used as the electrolyte additive from two aspects: i) provide new reaction pathways or improve the reaction kinetics and suppress shuttle effects;[111-113] ii) change the composition and properties of solid-electrolyte-interphase (SEI) for high stability[114–117].

Xie *et al*. introduced sulfur container additives to the electrolyte to improve the performance through reversible storage and release of lithium polysulfides intermediates (**Figure 1.30a**).[112]

Di(tri)sulphide polyethylene glycol (PES_n), the sulfur container, can store and release sulfur by reversibly lengthening and shortening sulfur chains. The high reactivity of sulfur container with sulfur could be verified by the fast reaction between PES_n and Li_2S_8/Li_2S, Li_2S_8 solution turned light orange immediately and white Li_2S suspension turned yellow. Also, the PES_n facilitated a unique and uniform deposition of Li_2S, the aggregation of Li_2S will lead to low efficiency in the charge process. Consequently, batteries with PES_n exhibited an enhancement in capacity and stability by 151 mA h g^{-1} after 100 cycles at 0.5 C (Figure 1.30b). However, these highly reactive compounds may lead to severe self-discharge behaviour. Gupta *et al*. introduced an additive (methyl trifluoroacetate (CH_3TFA)) that could react with lithium polysulfides to form lithium trifluoroacetate (LiTFA) and dimethyl polysulfides, both of which enhanced the performance of LSBs.[111] The high donor number of LiTFA inhibited the clustering of the polysulfide intermediates, which lowers the amount of lithium polysulfides for further reactions, even under lean electrolyte condition. Meanwhile, the dimethyl polysulfides could alter or enhance the reaction pathways and showed high stability with lithium metal anodes. Pouch cells with CH_3TFA additive at high sulfur loading (4.8 mg cm^{-2}) under the lean electrolyte condition (4.5 μL mg^{-1}) had a capacity of around 700 mA h g^{-1} after 40 cycles.

Constructing artificial SEI through the reaction between organosulfur additives in the electrolyte and lithium metal anodes is a promising way of stabilizing lithium metal anodes for practical application in LSBs. Li *et al*. reported a flexible and tough SEI layer through adding poly(sulphur-random-triallylamine) (PST) into electrolytes as an additive (Figure 1.30c).[115] PST reacted with Li to form lithium organosulfides (RS_6Li_6), lithium organopolysulfides (RS_xLi_6), lithium polysulfides and Li_2S/Li_2S_2, the organic compounds functioned as "plasticizers" to make the hybrid SEI layer more flexible and stable. It was also found that too many PST additives in the electrolyte could result in lower stability, probably caused by increased consumption of lithium and a thicker hybrid SEI layer showing higher resistance. Finally, batteries with 8% PST additive had a Coulombic efficiency as high as 99% for 400 cycles at a current density of 2 mA cm^{-2} with a capacity of 1 mA h cm^{-2}. Wei *et al*. reported an organosulfur containing SEI as a shield to prevent lithium polysulfides from reacting with lithium metal anodes.[114] 3,5-bis(trifluoromethyl)thiophenol (BTB), which reacted with lithium to form an organosulfur-containing SEI layer, was used as an additive in the electrolyte. The visualized test showed that BTB would react with lithium foils, but the formed SEI layer protected the lithium foil from further reaction, as assessed by the colour of the lithium polysulfides solution stayed light yellow after 16 hours. It was believed that the $Ph\text{-}S^-$

component, which was formed by the reaction between sulfydryl groups in BTB and lithium metals, repelled lithium polysulfides by electrostatic repulsion. With BTB as the additive, cells with a more practical operating condition (high loading of 4.5 mg cm^{-2}, low E/S ratio of 5.0 μL mg^{-1} and an ultrathin lithium foil (50 μm)) delivered an initial capacity of 950 mA h g^{-1} and remained 700 mA h g^{-1} after 82 cycles at a current density of 0.1 C.

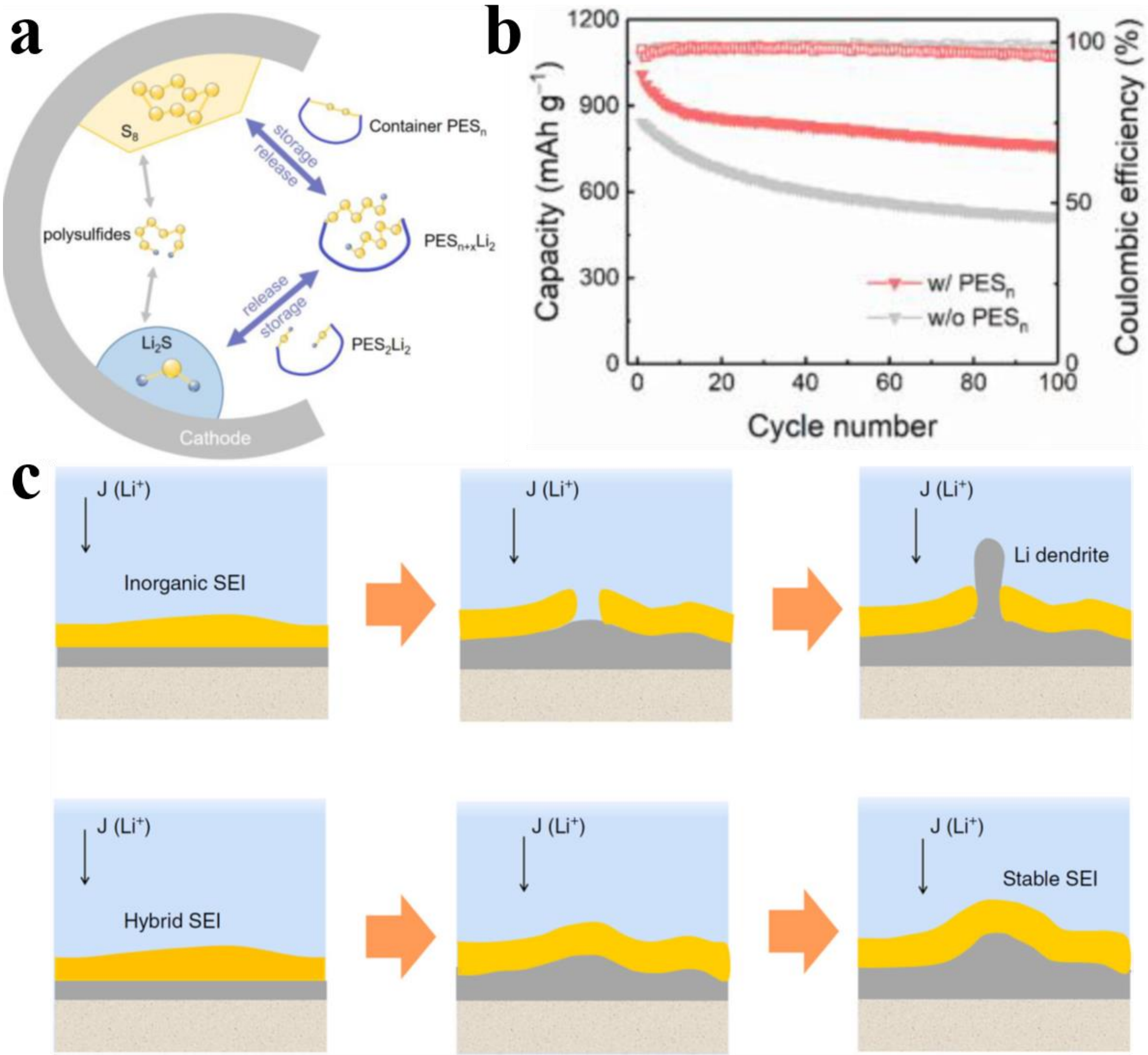

Figure 1.30. a) Working mechanism of sulphur container PES_n. b) Cyclic stability of LSBs with and without PES_n. c) Illustration of the protection of Li metal anodes by stable inorganic/organic hybrid SEI layers. a-b) Reproduced with permission.[111] Copyright 2019 Wiley-VCH. c) Reproduced with permission.[115] Copyright 2017 Springer Nature.

1.3.3 Organosulfur in interlayers and binders for LSBs

Functionalized interlayers and binders have also been applied to alleviate the shuttle effect in LSBs.[19,118–121] Adding an interlayer between cathode and separator with the ability to adsorb lithium polysulfides or accelerate the electrochemical reaction is an effective strategy to suppress shuttle effect and protect the lithium metal anodes. The interlayers should be thin, electrically conductive and flexible, and most importantly should have components with the ability to adsorb the intermediates or accelerate the electrochemical reaction. Heteroatom-doped carbon materials, metal oxides/sulfides/phosphides, metal-organic-frameworks have been studied as effective components in interlayers for LSBs. Wang *et al*. reported a SPAN-based functionalized interlayer for LSBs.[122] SPAN was synthesized by a similar process as other reports. After that, one side of the separator was coated with a slurry made from SPAN, acetylene black and carboxymethyl cellulose in a weight ratio of 8: 1: 1. It was found that this interlayer enabled higher utilization of sulfur and suppress the shuttle effect. Batteries with this interlayer had a high initial capacity of 1338 mA h g^{-1}, and 65% capacity retention after 200 cycles at 1 C. However, it is also worth mentioning that SPAN itself contributed part of the total capacity of the batteries. This interlayer was not free-standing or self-supported, instead it was coated on a Celgard separator.

Functionalized binders have been used to accommodate the volume change of electrode materials, improve the electrical conductivity and stability of batteries. For example, cross-linked binders have been used for Si anodes to accommodate the volume change and improve the structural integrity.[123–125] In LSBs, Zeng *et al*. reported a comb-like ion-conductive organo-polysulfide polymer binder to improve the electrodeposition of S and Li_2S.[124] The aggregation of insulating Li_2S and S_8 after discharge and charge processes will lead to high resistance of electrical/ionic conductivity and finally leads to poor long cycle stability. In this work, a polymer (PSPEG) was synthesized by the undiscriminated reaction between polyethylene glycol after grafting dichloro and Na_2S_x moities. It was found that the $–S_x$- bonds could act as mediator to improve the electrodeposition of Li_2S/S_8 and further suppress the aggregation and enhance the utilization of active materials and the cycling performance. The ether oxygen groups on the side chain could increase the Li^+ migration rate and improve the rate performance of LSBs. Batteries with only 1 wt% could deliver a capacity of 780 mA h g^{-1} after 100 cycles at a current density of 0.1 C (1 C = 1675 mA g^{-1}). However, when using this binder, the electrode material could easily peel off from aluminium foil current collectors and it was hard to cut into electrode disks for battery assembling.

1.4 Methods and techniques

1.4.1 X-ray diffraction (XRD)

XRD is a method that use the diffraction pattern to gain information about the chemical composition and atomic or molecular structure of materials. Once X-ray hits the sample, part of the X-ray will be scattered. At certain angle, if the travel distance of X-ray is a multiple of the wavelength, the signal will be enhanced. By using the brag equation, we can calculate the lattice distance of the sample: $n \lambda = 2 d \sin \theta$. λ is the wavelength of the X-ray, θ is the angle, d is the lattice distance and n is a constant. For an X-ray diffractometer, the wavelength is identical, and the angle can be obtained from the detector. There are also databases of XRD data that obtained from pure chemicals that can be used to find out what materials the samples may be.

1.4.2 X-ray photoelectron spectrum (XPS)

XPS has been widely used to analysis the molecular structure and valence state of compounds. The basic mechanism of XPS test is that the binding energy of inner shell electrons of atoms is unique and related to the valence state. The binding energy can be calculated from the equation: $E(b) = hv - E(k) - w$. E(b) is the binding energy of the inner shell electrons, hv is the photo energy, E(k) is the kinetic energy of electrons and w is the work function of the spectrometer. Among them, hv and w are constants for spectrometers with certain source of X-ray. E(k) can be obtained from the detectors. It is also worth noting that the only the information of the surface (about 10 nm) of the sample can be obtained. Etching process is needed before test to get information of materials thicker than10 nm.

1.4.3 Raman spectroscopy

Raman spectra is a scattering spectrum that can be used to characterize the molecular structure of compounds. The molecular energy level is quantized in a compound, including translational energy, vibrational energy, rotational energy and so on. When a light or electron magnetic wave goes through the sample, the molecules will absorb energy and jump to the virtual state from the ground state. Then some of the molecules at virtual state will go back to the ground state and emit electron magnetic wave with the same frequency, which is called Rayleigh scattering. Other molecules will go to a state between the ground state and the virtual state with electron magnetic wave about different frequency, which is called Raman scattering.

1.4.4 Scanning electronic microscope (SEM)

SEM has been widely used to characterize the morphology of materials. During the test, electron beams with certain energy will hit the surface of the sample. A variety of elastic and inelastic collision between electrons and nucleus will take place. Most of the collision will lead to the generation of heat, while in other collision, there will be stimulated or reflected electrons and X-ray with signals about the sample. By collecting the information of the electrons and X-ray, the morphology, chemical composition, and other information of the sample can be obtained. Secondary electrons are stimulated electrons from the outer layer of the atoms in the sample. Secondary electrons are generated on the surface of the sample, mostly 5-10 nm, which are sensitive to the morphology of the sample. And the number of secondary electrons depends on the morphology of the samples instead of the atomic number or atomic mass.

1.4.5 Transition electronic microscope (TEM)

TEM test is similar to SEM test, they all use electron beams to hit samples and collect the information about the samples. The difference is that in TEM test, the electrons that goes through the samples will be collected, which will tell information about the structure, depth and so on about the sample.

1.4.6 Electrochemistry tests

Cyclic voltammetry (CV)

CV test has been widely used to study the reversible process, interface absorption and mechanism of electrochemical reactions. During the test, a linear varying voltage at controlled scan rate is applied to the electrodes: $E = E_i - vt$. E_i is the initial voltage, v is the scan rate and t is the time. As the voltage changes, the corresponding current is collected. When the voltage approaches the voltage platform of the reversible reactions, the current will increase grammatically. Meanwhile, a concentration gradient will be formed as the reactants on the surface run out, and as a result the current will reach a peak (i_p).

Rate test

Rate test is aimed to test the performance of the materials at different current density, especially at high current density, which is important for fast charge and discharge technology. The current density will increase at the beginning and then goes back step by step. For a good material, the capacity should be high at high current density and a good capacity retention is also needed when the current density goes back to a low one.

Long cycle test

Long cycle test is designed to find out the life time of a battery, like how many times of charging is possible while the energy density is still satisfactory. At the beginning, a activation process, several cycles at low current density, is needed, during which electrolyte penetration SEI formation will take place. After that, the batteries will be cycled at a constant high current density.

1.5 Reference

[1] D. Vrankovic, M. Graczyk-Zajac, C. Kalcher, J. Rohrer, M. Becker, C. Stabler, G. Trykowski, K. Albe, R. Riedel, *ACS Nano* **2017**, *11*, 11409.

[2] C. Zhan, T. Wu, J. Lu, K. Amine, *Energy Environ. Sci.* **2018**, *11*, 243.

[3] H. E. Wang, X. Zhao, X. Li, Z. Wang, C. Liu, Z. Lu, W. Zhang, G. Cao, *J. Mater. Chem. A* **2017**, *5*, 25056.

[4] F. Wu, T. P. Pollard, E. Zhao, Y. Xiao, M. Olguin, O. Borodin, G. Yushin, *Energy Environ. Sci.* **2018**, 0.

[5] Y. Zuo, B. Li, N. Jiang, W. Chu, H. Zhang, R. Zou, D. Xia, *Adv. Mater.* **2018**, *30*, 2.

[6] M. R. Palacín, *Chem. Soc. Rev.* **2018**, DOI 10.1039/C7CS00889A.

[7] Y. Zhang, B. Lin, Y. Sun, X. Zhang, H. Yang, J. Wang, *RSC Adv.* **2015**, *5*, 58100.

[8] C. Chen, Y. Wen, X. Hu, X. Ji, M. Yan, L. Mai, P. Hu, B. Shan, Y. Huang, *Nat. Commun.* **2015**, *6*, 1.

[9] W. Zheng, P. Zhang, J. Chen, W. Tian, Y. Zhang, zhengming sun, *J. Mater. Chem. A* **2018**, DOI 10.1039/C7TA10394H.

[10] P. C. Tsai, B. Wen, M. Wolfman, M. J. Choe, M. S. Pan, L. Su, K. Thornton, J. Cabana, Y. M. Chiang, *Energy Environ. Sci.* **2018**, *11*, 860.

[11] X. Q. Zhang, W. C. Li, B. He, D. Yan, S. Xu, Y. Cao, A. H. Lu, *J. Mater. Chem. A* **2018**, *6*, 1397.

[12] J. Kim, H. Lee, H. Cha, M. Yoon, M. Park, J. Cho, *Adv. Energy Mater.* **2018**, *8*, 1.

[13] P. Zou, Y. Wang, S. W. Chiang, X. Wang, F. Kang, C. Yang, *Nat. Commun.* **2018**, *9*, DOI 10.1038/s41467-018-02888-8.

[14] Y. Yao, Z. Chen, A. Zhang, J. Zhu, X. Wei, J. Guo, W. D. Wu, X. D. Chen, Z. Wu, *J. Mater. Chem. A* **2017**, *5*, 25237.

[15] Y. Zhang, C. Wang, G. Pastel, Y. Kuang, H. Xie, Y. Li, B. Liu, W. Luo, C. Chen, L. Hu, *Adv. Energy Mater.* **2018**, *c*, 1.

[16] G. Wang, J. Zhang, S. Yang, F. Wang, X. Zhuang, K. Müllen, X. Feng, *Adv. Energy*

Mater. **2018**, *8*, 1.

[17] J. Zhang, H. Huang, J. Bae, S.-H. Chung, W. Zhang, A. Manthiram, G. Yu, *Small Methods* **2017**, *1700279*, 1700279.

[18] J. Coetzer, *Electrochim. Acta* **1978**, *23*, 787.

[19] C. Li, Z. Xi, D. Guo, X. Chen, L. Yin, *Small* **2018**, *14*, 1.

[20] Q. Sun, B. Xi, J. Li, H. Mao, X. Ma, J. Liang, **2018**, *1800595*, 1.

[21] M. Yu, J. Ma, M. Xie, H. Song, F. Tian, S. Xu, Y. Zhou, B. Li, D. Wu, H. Qiu, R. Wang, *Adv. Energy Mater.* **2017**, *7*, 1.

[22] Y. Hwa, H. K. Seo, J. M. Yuk, E. J. Cairns, *Nano Lett.* **2017**, *17*, 7086.

[23] Q. Pang, X. Liang, C. Y. Kwok, L. F. Nazar, *Nat. Energy* **2016**, *1*, 1.

[24] H. Kim, J. Lee, H. Ahn, O. Kim, M. J. Park, *Nat. Commun.* **2015**, *6*, DOI 10.1038/ncomms8278.

[25] Y. Liu, S. Liu, G. Li, X. Gao, *Adv.Energy Mater*. **2021**, *33*, 2003955.

[26] S. A. Abbas, J. Ding, S. H. Wu, J. Fang, K. M. Boopathi, A. Mohapatra, L. W. Lee, P. C. Wang, C. C. Chang, C. W. Chu, *ACS Nano* **2017**, *11*, 12436.

[27] Y. C. Jeong, J. H. Kim, S. H. Kwon, J. Y. Oh, J. Park, Y. Jung, S. G. Lee, S. J. Yang, C. R. Park, *J. Mater. Chem. A* **2017**, DOI 10.1039/C7TA08153G.

[28] M. Li, C. Wang, L. Miao, J. Xiang, T. Wang, K. Yuan, J. Chen, Y. Huang, *J. Mater. Chem. A* **2018**, DOI 10.1039/C8TA00459E.

[29] W. Chen, T. Lei, C. Wu, M. Deng, C. Gong, K. Hu, Y. Ma, L. Dai, W. Lv, W. He, X. Liu, J. Xiong, C. Yan, *Adv. Energy Mater.* **2018**, *8*, 1.

[30] L. Fan, S. Wei, S. Li, Q. Li, Y. Lu, **2018**, *1702657*, 1.

[31] S. Chen, D. Wang, Y. Zhao, D. Wang, **2018**, *1*, 1.

[32] T. Li, H. Bo, H. Cao, Y. Lai, Y. Liu, Z. Huang, *Int. J. Electrochem. Sci*. **2017**, *12*, 5713.

[33] X. Ji, K. T. Lee, L. F. Nazar, *Nat. Mater.* **2009**, *8*, 500.

[34] J. Z. Y. Qiu, Yongcai; Li, Wanfei; Zhan, Wen; Li, Guizhu; Hou, Yuan; Liu, Meinan;

Zhou, LIsha; Ye, Fangmin; Li, Hongfei; Wei, Zhnahua; Yang, Shihe; Duan, Wenhui; Ye, Yifan; Guo, **2014**, 4821.

[35] J. He, L. Luo, Y. Chen, A. Manthiram, *Adv. Mater.* **2017**, *29*, 1.

[36] C. Dai, J. M. Lim, M. Wang, L. Hu, Y. Chen, Z. Chen, H. Chen, S. J. Bao, B. Shen, Y. Li, G. Henkelman, M. Xu, *Adv. Funct. Mater.* **2018**, *28*, 1.

[37] Y. Zhong, L. Yin, P. He, W. Liu, Z. Wu, H. Wang, *J. Am. Chem. Soc.* **2018**, *140*, 1455.

[38] E. Environ, **2012**, 9269.

[39] A. Manuscript, **2018**, DOI 10.1039/C8TA00612A.

[39] A. Manuscript, **2017**, DOI 10.1039/C7TA09039K.

[41] N. Cheng, L. Ren, X. Xu, Y. Du, S. X. Dou, **2018**, *1801257*, 1.

[42] Y. Zhang, T. Cheng, Y. Wang, W. Lai, H. Pang, W. Huang, **2016**, 5242.

[43] S. Gadipelli, Z. Guo, **2014**, DOI 10.1021/cm502399q.

[44] V. A. Online, **2014**, 335.

[45] W. Chen, T. Lei, C. Wu, M. Deng, C. Gong, K. Hu, Y. Ma, **2018**, *1702348*, 1.

[46] L. Ge, Y. Yang, L. Wang, W. Zhou, R. De Marco, Z. Chen, **2014**, *2*, 8.

[47] J. Tang, R. R. Salunkhe, J. Liu, N. L. Torad, M. Imura, S. Furukawa, Y. Yamauchi, **2015**, DOI 10.1021/ja511539a.

[48] G. Qian, **2015**, 1.

[49] R. Demir-Cakan, M. Morcrette, F. Nouar, C. Davoisne, T. Devic, D. Gonbeau, R. Dominko, C. Serre, G. Férey, J. M. Tarascon, *J. Am. Chem. Soc.* **2011**, *133*, 16154.

[50] J. Zhou, R. Li, X. Fan, Y. Chen, R. Han, W. Li, J. Zheng, B. Wang, X. Li, *Energy Environ. Sci.* **2014**, *7*, 2715.

[51] J. Zhou, X. Yu, X. Fan, X. Wang, H. Li, Y. Zhang, W. Li, J. Zheng, B. Wang, X. Li, *J. Mater. Chem. A* **2015**, *3*, 8272.

[52] H. Park, D. J. Siegel, *Chem. Mater.* **2017**, *29*, 4932.

[53] J. Zheng, J. Tian, D. Wu, M. Gu, W. Xu, C. Wang, F. Gao, M. H. Engelhard, J. G. Zhang, J. Liu, J. Xiao, *Nano Lett.* **2014**, *14*, 2345.

[54] Z. Wang, B. Wang, Y. Yang, Y. Cui, Z. Wang, B. Chen, G. Qian, *ACS Appl. Mater. Interfaces* **2015**, *7*, 20999.

[55] D. Cai, M. Lu, L. Li, J. Cao, D. Chen, H. Tu, J. Li, W. Han, *Small* **2019**, *15*, 1.

[56] G. Xu, B. Ding, L. Shen, P. Nie, J. Han, X. Zhang, *J. Mater. Chem. A* **2013**, *1*, 4490.

[57] G. Chen, Y. Li, W. Zhong, F. Zheng, J. Hu, X. Ji, W. Liu, C. Yang, Z. Lin, M. Liu, *Energy Storage Mater.* **2020**, *25*, 547.

[58] L. Zhang, Y. Liu, Z. Zhao, P. Jiang, T. Zhang, M. Li, S. Pan, T. Tang, T. Wu, P. Liu, Y. Hou, H. Lu, **2020**.

[59] N. Zhang, Y. Yang, X. Feng, S. H. Yu, J. Seok, D. A. Muller, H. D. Abruña, *J. Mater. Chem. A* **2019**, *7*, 21128.

[60] S. Chen, J. Luo, N. Li, X. Han, J. Wang, Q. Deng, Z. Zeng, S. Deng, *Energy Storage Mater.* **2020**, *30*, 187.

[61] H. Zhang, W. Zhao, M. Zou, Y. Wang, Y. Chen, L. Xu, H. Wu, A. Cao, *Adv. Energy Mater.* **2018**, *8*, 1.

[62] H. Zhang, W. Zhao, Y. Wu, Y. Wang, M. Zou, A. Cao, *J. Mater. Chem. A* **2019**, *7*, 9195.

[63] J. Han, S. Gao, R. Wang, K. Wang, M. Jiang, J. Yan, K. Jiang, *ACS Appl. Mater. Interfaces* **2019**, *11*, 46792.

[64] J. Jin, W. Cai, J. Cai, Y. Shao, Y. Song, Z. Xia, Q. Zhang, J. Sun, *J. Mater. Chem. A* **2020**, *8*, 3027.

[65] H. Chen, Y. Xiao, C. Chen, J. Yang, C. Gao, Y. Chen, J. Wu, Y. Shen, W. Zhang, S. Li, F. Huo, B. Zheng, *ACS Appl. Mater. Interfaces* **2019**, *11*, 11459.

[66] Y. Fan, Z. Niu, F. Zhang, R. Zhang, Y. Zhao, G. Lu, *ACS Omega* **2019**, *4*, 10328.

[67] Y. He, Z. Chang, S. Wu, Y. Qiao, S. Bai, K. Jiang, P. He, H. Zhou, *Adv. Energy Mater.* **2018**, *8*, 1.

[68] S. Bai, X. Liu, K. Zhu, S. Wu, H. Zhou, *Nat. Energy* **2016**, *1*, DOI

10.1038/nenergy.2016.94.

[69] J. He, Y. Chen, A. Manthiram, *Energy Environ. Sci.* **2018**, *11*, 2560.

[70] P. Chiochan, X. Yu, M. Sawangphruk, A. Manthiram, *Adv. Energy Mater.* **2020**, *10*, 1.

[71] Z. Shadike, S. Tan, Q. C. Wang, R. Lin, E. Hu, D. Qu, X. Q. Yang, *Mater. Horizons* **2021**, *8*, 471.

[72] H. Yang, J. Chen, J. Yang, J. Wang, *Angew. Chemie - Int. Ed.* **2020**, *59*, 7306.

[73] X. Zhang, K. Chen, Z. Sun, G. Hu, R. Xiao, H. M. Cheng, F. Li, *Energy Environ. Sci.* **2020**, *13*, 1076.

[74] S. J. Visco, L. C. DeJonghe, *J. Electrochem. Soc.* **1988**, *135*, 2905.

[75] A. Bhargav, A. Manthiram, *Adv. Energy Mater.* **2020**, *10*, DOI 10.1002/aenm.202001658.

[76] J. He, A. Bhargav, A. Manthiram, *Energy Storage Mater.* **2019**, *23*, 88.

[77] A. Bhargav, M. E. Bell, J. Karty, Y. Cui, Y. Fu, *ACS Appl. Mater. Interfaces* **2018**, *10*, 21084.

[78] A. Bhargav, Y. Ma, K. Shashikala, Y. Cui, Y. Losovyj, Y. Fu, *J. Mater. Chem. A* **2017**, *5*, 25005.

[79] M. Wu, Y. Cui, A. Bhargav, Y. Losovyj, A. Siegel, M. Agarwal, Y. Ma, Y. Fu, *Angew. Chemie - Int. Ed.* **2016**, *55*, 10027.

[80] W. J. Chung, J. J. Griebel, E. T. Kim, H. Yoon, A. G. Simmonds, H. J. Ji, P. T. Dirlam, R. S. Glass, J. J. Wie, N. A. Nguyen, B. W. Guralnick, J. Park, Á. Somogyi, P. Theato, M. E. Mackay, Y. E. Sung, K. Char, J. Pyun, *Nat. Chem.* **2013**, *5*, 518.

[81] G. Hu, Z. Sun, C. Shi, R. Fang, J. Chen, P. Hou, C. Liu, H. M. Cheng, F. Li, *Adv. Mater.* **2017**, *29*, 1.

[82] K. Shen, H. Mei, B. Li, J. Ding, S. Yang, *Adv. Energy Mater.* **2018**, *8*, DOI 10.1002/aenm.201701527.

[83] X. Li, L. Yuan, D. Liu, Z. Li, J. Chen, K. Yuan, J. Xiang, Y. Huang, *Energy Storage Mater.* **2020**, *26*, 570.

[84] H. Kang, H. Kim, M. J. Park, *Adv. Energy Mater.* **2018**, *8*, DOI 10.1002/aenm.201802423.

[85] J. Zhou, T. Qian, N. Xu, M. Wang, X. Ni, X. Liu, X. Shen, C. Yan, *Adv. Mater.* **2017**, *29*, DOI 10.1002/adma.201701294.

[86] P. Sang, J. Song, W. Guo, Y. Fu, *Chem. Eng. J.* **2021**, *415*, DOI 10.1016/j.cej.2021.129043.

[87] J. Zhou, X. Zhou, Y. Sun, X. Shen, T. Qian, C. Yan, *J. Energy Chem.* **2021**, *56*, 238.

[88] J. Wang, J. Yang, J. Xie, xu naixin, *Adv. Mater.* **2002**, *50*, 963.

[89] S. Zeng, L. Li, J. Yu, N. Wang, S. Chen, *Electrochim. Acta* **2018**, *263*, 53.

[90] S. Li, Z. Han, W. Hu, L. Peng, J. Yang, L. Wang, Y. Zhang, B. Shan, J. Xie, *Nano Energy* **2019**, *60*, 153.

[91] H. Hu, Y. Hu, H. Cheng, S. Dai, K. Song, M. Liu, *J. Power Sources* **2021**, *491*, DOI 10.1016/j.jpowsour.2021.229617.

[92] X. G. Yu, J. Y. Xie, J. Yang, H. jiang Huang, K. Wang, Z. S. Wen, *J. Electroanal. Chem.* **2004**, *573*, 121.

[93] W. Wang, Z. Cao, G. A. Elia, Y. Wu, W. Wahyudi, E. Abou-Hamad, A. H. Emwas, L. Cavallo, L. J. Li, J. Ming, *ACS Energy Lett.* **2018**, *3*, 2899.

[94] M. A. Weret, C. F. Jeffrey Kuo, T. S. Zeleke, T. T. Beyene, M. C. Tsai, C. J. Huang, G. B. Berhe, W. N. Su, B. J. Hwang, *Energy Storage Mater.* **2020**, *26*, 483.

[95] X. Zhao, C. Wang, Z. Li, X. Hu, A. Abdul Razzaq, Z. Deng, *J. Mater. Chem. A* **2021**, DOI 10.1039/d1ta03300j.

[96] B. He, Z. Rao, Z. Cheng, D. Liu, D. He, J. Chen, Z. Miao, L. Yuan, Z. Li, Y. Huang, *Adv. Energy Mater.* **2021**, *11*, 1.

[97] L. Yin, J. Wang, J. Yang, Y. Nuli, *J. Mater. Chem.* **2011**, *21*, 6807.

[98] L. Yin, J. Wang, F. Lin, J. Yang, Y. Nuli, *Energy Environ. Sci.* **2012**, *5*, 6966.

[99] X. Chen, L. Peng, L. Wang, J. Yang, Z. Hao, J. Xiang, K. Yuan, Y. Huang, B. Shan, L. Yuan, J. Xie, *Nat. Commun.* **2019**, *10*, DOI 10.1038/s41467-019-08818-6.

[100] H. Yang, C. Guo, J. Chen, A. Naveed, J. Yang, Y. Nuli, J. Wang, *Angew. Chemie - Int. Ed.* **2019**, *58*, 791.

[101] H. Hu, B. Zhao, H. Cheng, S. Dai, N. Kane, Y. Yu, M. Liu, *Nano Energy* **2019**, *57*, 635.

[102] S. Zeng, L. Li, L. Xie, D. Zhao, N. Wang, S. Chen, *ChemSusChem* **2017**, *10*, 3378.

[103] A. Bhargav, Y. Ma, K. Shashikala, Y. Cui, Y. Losovyj, Y. Fu, *J. Mater. Chem. A* **2017**, *5*, 25005.

[104] J. Zhou, T. Qian, N. Xu, M. Wang, X. Ni, X. Liu, X. Shen, C. Yan, *Adv. Mater.* **2017**, *29*, 1.

[105] Y. Z. Zhang, S. Liu, G. C. Li, G. R. Li, X. P. Gao, *J. Mater. Chem. A* **2014**, *2*, 4652.

[106] A. Abdul Razzaq, X. Yuan, Y. Chen, J. Hu, Q. Mu, Y. Ma, X. Zhao, L. Miao, J. H. Ahn, Y. Peng, Z. Deng, *J. Mater. Chem. A* **2020**, *8*, 1298.

[107] S. Ma, Y. Wang, C. Fu, Y. Ma, Y. Gao, G. Yin, P. Zuo, *Chem. Commun.* **2020**, *56*, 12797.

[108] J. Lei, J. Chen, A. Naveed, H. Zhang, J. Yang, Y. Nuli, J. Wang, *ACS Appl. Energy Mater.* **2021**, *4*, 5706.

[109] M. Sun, S. Zhang, T. Jiang, L. Zhang, J. Yu, *Electrochem. commun.* **2008**, *10*, 1819.

[110] X. Liang, Y. Liu, Z. Wen, L. Huang, X. Wang, H. Zhang, *J. Power Sources* **2011**, *196*, 6951.

[111] A. Gupta, A. Bhargav, A. Manthiram, *ACS Energy Lett.* **2021**, *6*, 224.

[112] J. Xie, Y. W. Song, B. Q. Li, H. J. Peng, J. Q. Huang, Q. Zhang, *Angew. Chemie - Int. Ed.* **2020**, *59*, 22150.

[113] S. Gu, J. Jin, S. Zhuo, R. Qian, Z. Wen, *ChemElectroChem* **2018**, *5*, 1717.

[114] J. Y. Wei, X. Q. Zhang, L. P. Hou, P. Shi, B. Q. Li, Y. Xiao, C. Yan, H. Yuan, J. Q. Huang, *Adv. Mater.* **2020**, *32*, 1.

[115] G. Li, Y. Gao, X. He, Q. Huang, S. Chen, S. H. Kim, D. Wang, *Nat. Commun.* **2017**, *8*, DOI 10.1038/s41467-017-00974-x.

[116] S. Bonakala, A. D. Pathak, A. Deyko, C. Christova, I. Rudra, G. Verbist, *ACS Appl. Mater. Interfaces* **2020**, *12*, 18101.

[117] K. Chen, R. Fang, Z. Lian, X. Zhang, P. Tang, B. Li, K. He, D. wei Wang, H. M. Cheng, Z. Sun, F. Li, *Energy Storage Mater.* **2021**, *37*, 224.

[118] J. Xie, H. J. Peng, J. Q. Huang, W. T. Xu, X. Chen, Q. Zhang, *Angew. Chemie - Int. Ed.* **2017**, *56*, 16223.

[119] Y. He, Z. Chang, S. Wu, H. Zhou, *J. Mater. Chem. A* **2018**, DOI 10.1039/C8TA01115J.

[120] J. K. Huang, M. Li, Y. Wan, S. Dey, M. Ostwal, D. Zhang, C. W. Yang, C. J. Su, U. S. Jeng, J. Ming, A. Amassian, Z. Lai, Y. Han, S. Li, L. J. Li, *ACS Nano* **2018**, *12*, 836.

[121] E. Cha, M. D. Patel, J. Park, J. Hwang, V. Prasad, K. Cho, W. Choi, *Nat. Nanotechnol.* **2018**, DOI 10.1038/s41565-018-0061-y.

[122] F. Wang, X. He, *Mater. Lett.* **2019**, *256*, 126604.

[123] Q. Xu, J. K. Sun, Z. L. Yu, Y. X. Yin, S. Xin, S. H. Yu, Y. G. Guo, *Adv. Mater.* **2018**, *1707430*, 1.

[124] M. Chen, B. Li, X. Liu, L. Zhou, L. Yao, J. Zai, X. Qian, X. Yu, *J. Mater. Chem. A* **2018**, *6*, 3022.

[125] N. Kim, H. Park, N. Yoon, J. K. Lee, *ACS Nano* **2018**, *12*, 3853.

[126] F. L. Zeng, N. Li, Y. Q. Shen, X. Y. Zhou, Z. Q. Jin, N. Y. Yuan, J. N. Ding, A. B. Wang, W. K. Wang, Y. S. Yang, *Energy Storage Mater.* **2019**, *18*, 190.

Chapter 2

ZIF-8@ZIF-67 derived cobalt sulfides nanoparticles supported on N-doped carbon as host of S for high-performance lithium-sulfur batteries

2.1 Introduction

Lithium-suflur batteries (LSBs) with high theoretical capacity (1675 mA h g^{-1}) and high energy density (2600 W h kg^{-1}) have been regarded as the most promising candidate for next-generation energy storage system.[1–5] The high abundance of sulfur on earth and cheap price make the large-scale application of LSBs possible. However, the commercialization of LSBs is hindered by several obstacles. First, the isolating nature of sulfur and the discharge products Li_2S/Li_2S_2 leads to low utilization of active materials especially at high current density.[6–9] Second, the difference between sulfur and Li_2S/Li_2S_2 results in big volume change (about 80%) during charge and discharge.[10–12] The repeated volume change could cause the fragmentation of electrodes and finally the failure of the batteries. Finally, the notorious shuttle effect.[13–17] The intermediates formed during charge and discharge, long chain lithium polysulfides (LPSs), are soluble in the organic electrolyte. High order LPSs will diffuse from the surface of cathode to the surface of anode and react with lithium to form low order LPSs. The corrosion of lithium anode will lead to low efficiency and low cyclic stability.

Strategies have been proposed to solve these problems by researchers over the past decades.[18–26] Carbon materials with porous structure and high conductivity can be used as S host in LSBs. The porous structure confines LPSs in the pores can prevent them from diffusing to the anode side. Also, the pores can accommodate the volume change of sulfur during charge and discharge. However, the low polarity of carbon materials often results in low interaction between carbon materials and LPSs. Transition metal sulfides/phosphides/nitrides with high polarity can provide stronger absorption towards LPSs through Lewis acid and base interaction. Polysulfides anions with lone pair electrons act as Lewis bases while transition metal ions act as Lewis acids. Using redox mediators to accelerate the reactions and alleviate shuttle effect is another possible way. By promoting the kinetics, the reactions proceed faster and the chance that LPSs will shuttle between cathode and anode is reduced.

Zeolite Imidazole Frameworks (ZIFs), including ZIF-67 and ZIF-8, as well as their derivate have been used as S host in LSBs in many researches.[27–31] However, the low conductivity of pristine ZIFs is not favourable. Synthesizing ZIF-derived carbon material through high temperature pyrolysis is a possible way to increase the conductivity.[32–34] During the high temperature pyrolysis, the Co metal centres in ZIF-67 will catalyse the graphitization of carbon and finally results in high conductivity. But the framework is easy to collapse, and the surface area is reduced. For ZIF-8, the Zn metal centres have no catalyst activity and start evaporating from 800 °C. The evaporation of Zn results in high surface area but the low graphitization of carbon lead to low conductivity.

Herein, I have designed and synthesied cobalt sulfides nanoparticles supported on N-doped carbon framework (CSNCF) from a ZIF-8@ZIF-67 core-shell template and applied it as S host for LSBs. The ZIF-8 core prevents the collapse of ZIF-67 shell and provides higher surface area. The graphitized carbon, including carbon nanotubes (CNTs), derived from ZIF-67 shell increases the conductivity. The comparison of the two ZIFs are list in table 2.1. What's more, the cobalt sulfides show strong chemical absorption and catalyst activity. When using this material as S host, batteries showed high electrochemical performance.

Table 2.1. The comparison of ZIF-8 and ZIF-67 and their derivates.

ZIFs	ZIF-8	ZIF-67
Metal centre	Zn	Co
Metal centre boiling point	907 °C	2890 °C
Advantages of pyrolyzed sample	High surface area	High graphitization level (conductivity)
	High N content	High stability
Disadvantages of pyrolyzed sample	Amorphous carbon	Low surface area
	Low stability	Low N content

2.2 Experiment section

2.2.1 Materials

Cobalt nitrate hexahydrate, Nickel nitrate hexahydrate, 2-methyl imidazole, $LiNO_3$, sulfur, lithium bis(trifluoromethanesulfonimide) (LiTFSI), N-methyl pyrrolidone (NMP), 1,2-dimethoxyethane (DME) and 1,3-dioxolane (DOL) were purchased from Sigma-Aldrich and used directly. Carbon-coated aluminium foil, Celgard separator, Lithium metal foil and commercial electrolyte for lithium-ion batteries were purchased form MTI company.

2.2.2 Synthesis of ZIF-8@ZIF-67

ZIF-8@ZIF-67 was synthesized through epitaxial growth. ZIF-8 was firstly synthesized according to some reports. 8.1 g zinc nitrate hexahydrate was added into 400 mL methanol and stirred for half an hour to form solution A. 5.26 g 2-methy imidazole was added into 400 mL methanol and stirred for half an hour to form solution B. Then solution B was added into solution A slowly under stirring. The mixture was stirred for an hour and aged for 24 hours. Then the product was centrifuged and washed with methanol for several times and then dried at 80 ℃ overnight. 1.6 g of the as-synthesized ZIF-8 was dissolved into 200 mL methanol and sonicated for half an hour to form solution C. 3.54 g cobalt chloride hexahydrate was added into 60 mL methanol and stirred for half an hour to form solution D. 17.9 g 2-methyl imidazole was added into 60 mL methanol and stirred for half an hour to form solution E. Solution D was added into solution C slowly under stirring. After half an hour, solution E was added into the mixture slowly under stirring. Then the mixed solution was stirred for 24 hours. Then the product was centrifuged and washed with methanol for several times and then dried at 80 ℃ overnight.

2.2.3 Synthesis of cobalt sulfides nanoparticles supported on N-doped carbon framework (CSNCF)

The as-synthesized ZIF-8@ZIF-67 was firstly carbonized at different temperature to synthesis cobalt nanoparticles supported on N-doped carbon framework (CNCF-X), X is the reaction temperature. For example, in the synthesis of CNCF-1000, ZIF-8@ZIF-67 was heated at 1000 ℃ under Ar atmosphere in a tube furnace for 3 hours with a heating rate of 2 ℃/min. The product was mixed with S in a mass ratio of 1:1 through milling. The mixture was put in a porcelain boat and transferred to a tube furnace with Ar atmosphere. Then the mixture was firstly heated to 300 ℃ at a heating rate of 2 ℃/min and kept for 1 hour, followed by heating to 650 ℃ at a heating rate of 2 ℃/min and kept for 2 hours. The product was collected after cool down to room temperature and named as CSNCF-1000.

2.2.4 Synthesis of CSNCF/S composite

CSNCF-X was mix with S through ball milling at a mass ratio of 1:2. Then the mixture was transferred into a small glass bottle and place into a Taflon reactor. The reactor was sealed under Ar atmosphere to eliminate the reaction between S and air. Then the mixture was heated at 155 ℃ for 24 hours. The product was collected after cool down to room temperature.

2.2.5 Material characterization

Scanning electron microscopic (SEM) images were taken by a field emission scanning electron microscope (Jeol JSM 6701). Transition electron microscopic (TEM) and energy dispersive spectra (EDS) characterizations were performed on a probe-corrected (CEOS) JEM ARM 200CF (JEOL Japan) operated at 200 keV. X-ray diffraction (XRD) was carried out in a Bruker-Axs D8 X-ray diffractometer. FTIR test was carried out by using a Bruker ALPHA

FTIR spectrometer (Platinum-ATR). Raman spectrums were characterized by using a Raman spectrometer (514.5 nm laser Renishaw). X-ray photoemmision spectrum (XPS) were carried out by Al-K-α, Thermos Fisher scientific.

2.2.6 Electrochemical test

The electrochemical performance of samples was tested by assembling 2032 coin cells in an argon-filled glove box. Cathodes were made through a typical process. Samples, super P and Polyvinylidene Fluoride (PVDF) were mixed in a mass ratio of 8:1:1, with N-methyl pyrrolidone (NMP) as dispersion solution. The slurry was then coated on carbon coated aluminium foil and dried at 60 ℃ under vacuum overnight. The coated foil was then cut into disks with a diameter of 16 mm. The area sulfur loading is 0.9-1.3 mg cm^{-2} if not specifically mentioned. The electrolyte was prepared according to some reports. 1 mol L^{-1} Lithium bistrifluoromethane sulfonimide (LiTFSI) was dissolved in a mix solution of 1,2-dimethoxyethane (DME) and 1,3-dioxolane (DOL) (1:1 v/v) with 2 wt% $LiNO_3$ as addictive. And the dosage of electrolyte was controlled at 10 μL mg^{-1}(s). Lithium foil and Celgard separator were used as anode and separator. Arbin and Neware battery test system were used to test the electrochemical performance of these coin cells.

2.2.7 Absorption test

Li_2S_6 catholyte was prepared in an argon protected glove box. 0.1 mol Li_2S and 0.5 mol S were dissolved in a mix solution of 10 mL DOL and 10 mL DME. The solution was stirred for 24 hours for complete reaction. Then 2 mL of the as-prepared Li_2S_6 catholyte was added into a glass bottle with 5 mg of samples.

2.3 Results and discussion

2.3.1 Morphology and structure

To prepare CSNCF-1000, ZIF-8@ZIF-67 template was synthesized through epitaxial growth as shown in **Figure 2.1** (details in experimental section).

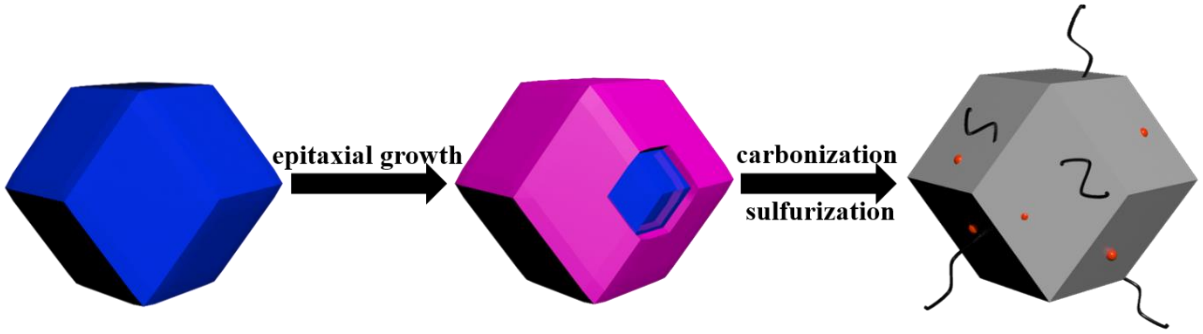

Figure 2.1. Schematic illustration of the synthesis process cobalt sulphides supported on N-doped carbon framework (CSNCF).

The X-ray diffraction (XRD) patterns **(Figure 2.2a**) of ZIF-8, ZIF-67 and ZIF-8@ZIF-67 matched well with the stimulated data of ZIF-8/ZIF-67. The XRD patterns of ZIF-8 and ZIF-67 indicate the similar structure of ZIF-8 ($[Zn(MeIm)_2]_n$) (MeIm = 2-methyl imidazole) and ZIF-67 ($[Co(MeIm)_2]_n$), which enables the epitaxial growth of ZIF-67 on the surface on ZIF-8. Fourier transform infrared (FTIR) spectrums (**Figure 2.2b**) of samples also showed overlapped patterns, manifested the similar structure of samples. Raman spectrums (**Figure 2.2c**) of ZIF-8@ZIF-67 showed an integration of those of ZIF-8@ZIF-67, verifying the successful epitaxial growth of ZIF-67. The peaks of Raman and FTIR were assigned as shown in **Table 2.2** and **Table 2.3**.

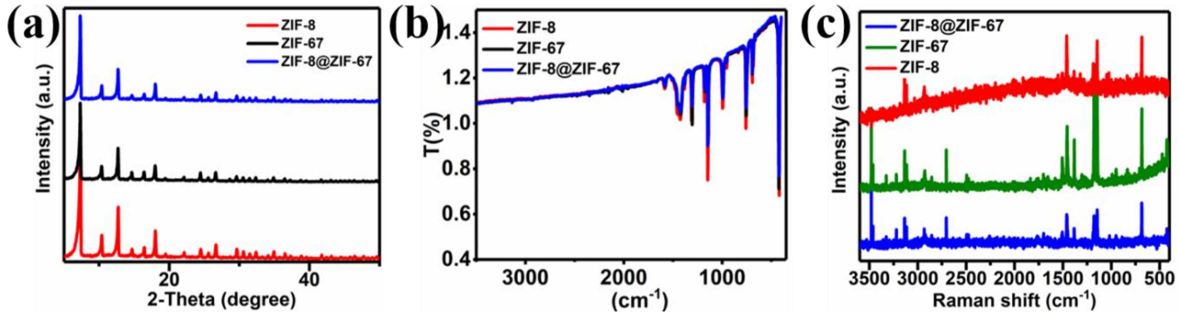

Figure 2.2. a) X-ray diffraction (XRD) patterns of ZIFs. b) Fourier transform infrared (FTIR) spectrums of ZIFs. c) Raman spectrums of ZIFs.

Table 2.2. Assignment of peaks in FTIR spectrum.

wavenumber (cm^{-1})	assignment

694	C-H bending
762	C-H bending
995	=C-H in-plane bend
1147	=C-H in-plane deformation vibration
1179	=C-H in-plane deformation vibration
1313	CH$_2$ wagging
1384	CH$_3$ asymmetric bend
1427	CH$_2$ asymmetric bend
1456	C=C stretch
1585	C=N stretch
2931	C-H symmetric stretch
3137	=C-H stretch

Table 2.3. Assignment of peaks in Raman spectrum.

Raman shift (cm^{-1})	assignment
683	Imidazolium ring puckering
1143/1182	C-H bending
1312	C-N stretch
1385	N-H wagging
1460	CH$_3$ bending
1507	C-N stretch
2932	C-H stretch (methyl)
3111/3136	C-H stretch (imidazolium ring)
3250-2200 broad band	H-N---H hydrogen bridge

Scanning electron microscope (SEM) images (**Figure 2.3a-c**) and transition electron microscope (TEM) images (Figure 2.3d-f) of samples showed typical dodecahedron structure. ZIF-8 has a size of ~500 nm while ZIF-8@ZIF-67 had a slightly larger size.

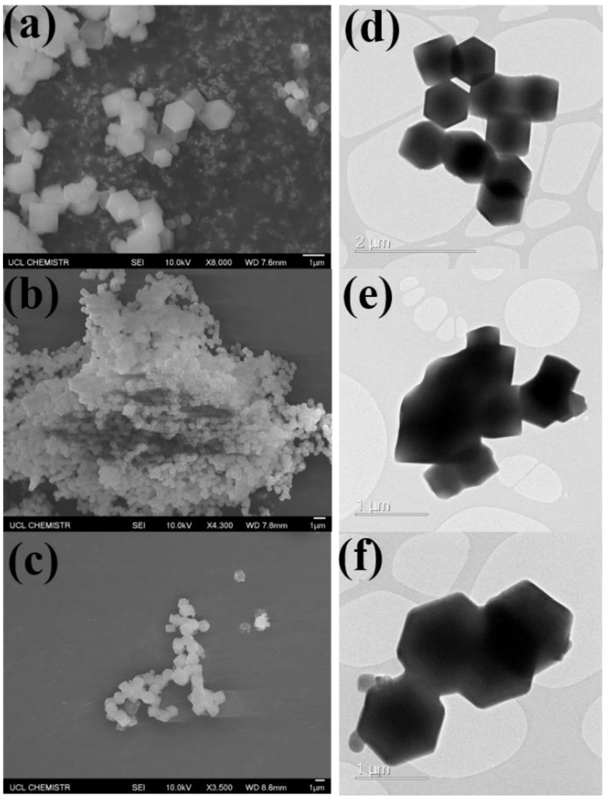

Figure 2.3. Scan electron microscope (SEM) images of ZIFs. a) ZIF-8, b) ZIF-67 and c) ZIF-8@ZIF-67. Transition electron microscope (TEM) images of ZIFs. d) ZIF-8, e) ZIF-67 and f) ZIF-8@ZIF-67.

The distribution of the particle size of ZIF-8 and ZIF-8@ZIF-67 core-shell structure were shown in the histogram as shown in **Figure 2.4**. The particle size increased from 0.91 μm to 1.14 μm after the growth of ZIF-67 shell.

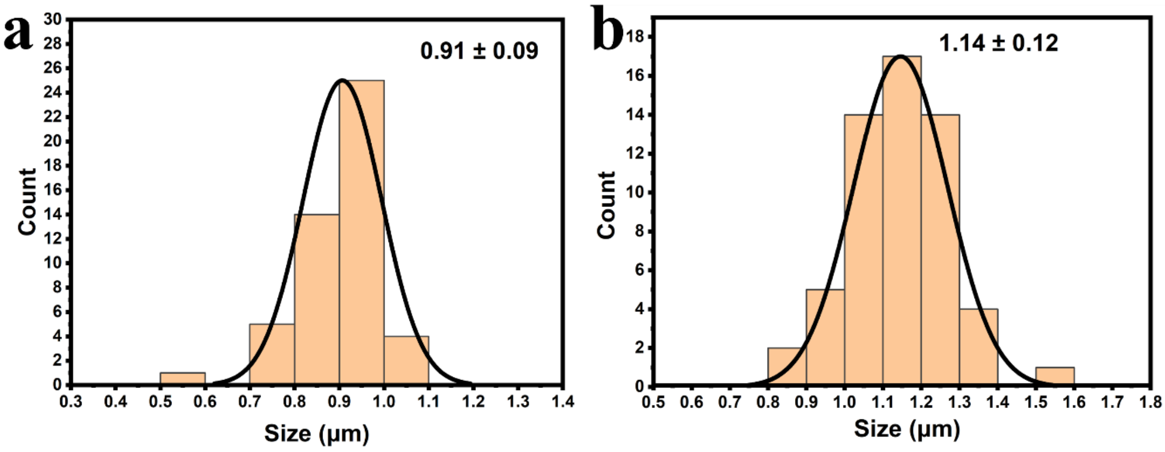

Figure 2.4. Particle size distribution of a) ZIF-8 and b) ZIF-8@ZIF-67.

Energy dispersion spectrum (EDS) of ZIF-8@ZIF-67 showed a core-shell structure as shown in **Figure 2.5**. Co and Zn uniformly dispersed in the sample, while Co had a larger range than Zn, indicating that ZIF-8 formed the core and ZIF-67 grew on the out surface to form the shell.

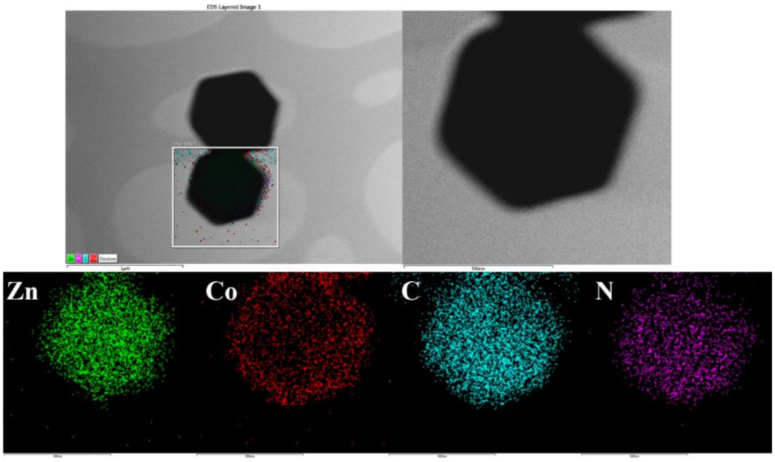

Figure 2.5. Element dispersion (EDS) mapping of ZIF-8@ZIF-67.

ZIF-8@ZIF-67 was then carbonized under argon atmosphere at 1000 °C to synthesis cobalt nanoparticles supported on N-doped carbon framework (CNCF-1000). Pristine ZIF-8 and ZIF-67 were also carbonized at the same condition to synthesis N-doped carbon framework (NCF-1000) and graphitized carbon framework (GCF-1000). The morphology of the as-prepared samples was characterized by SEM (**Figure 2.6**) and TEM (**Figure 2.7**).

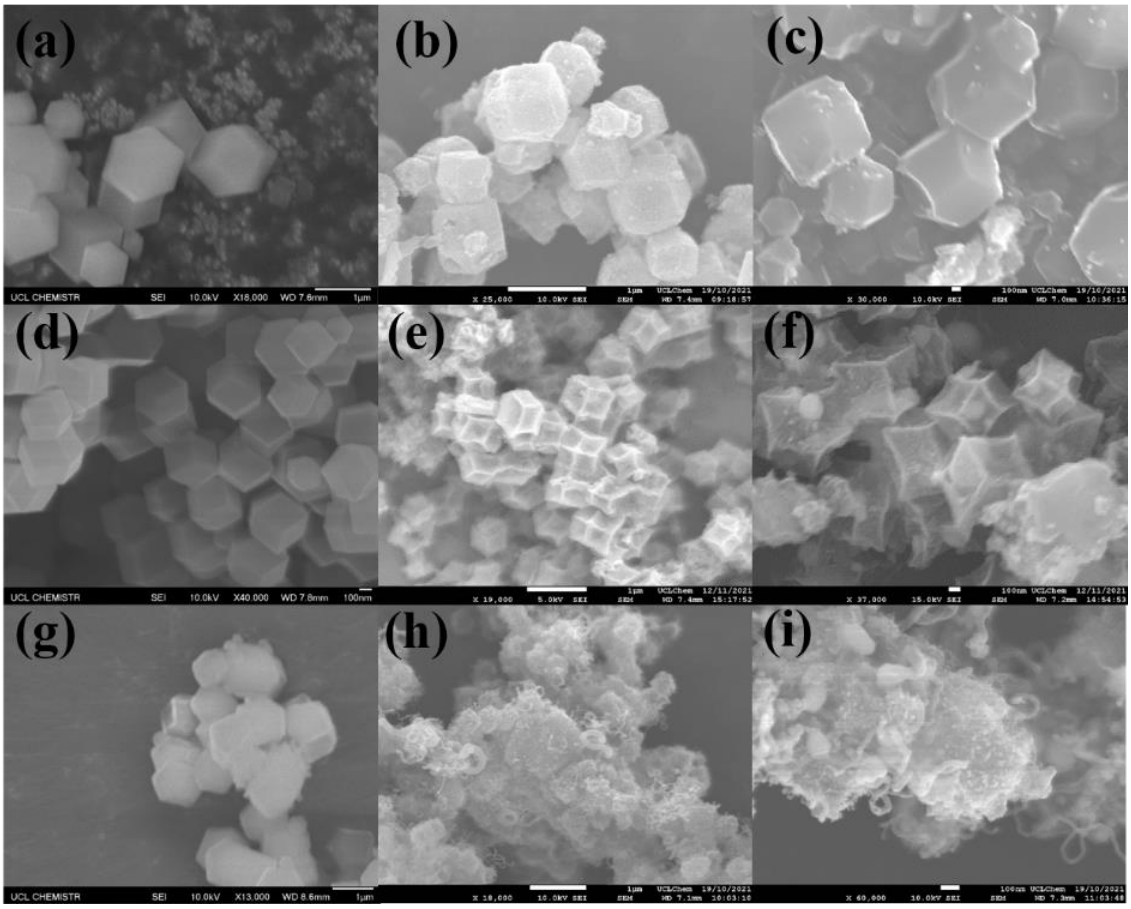

Figure 2.6. SEM images of samples. a) ZIF-8, b) NCF-1000, c) SNCF-1000, d) ZIF-67, e) GCF-1000, f) SGCF-1000, g) ZIF-8@ZIF-67, h) CNCF-1000, and i) CSNCF-1000.

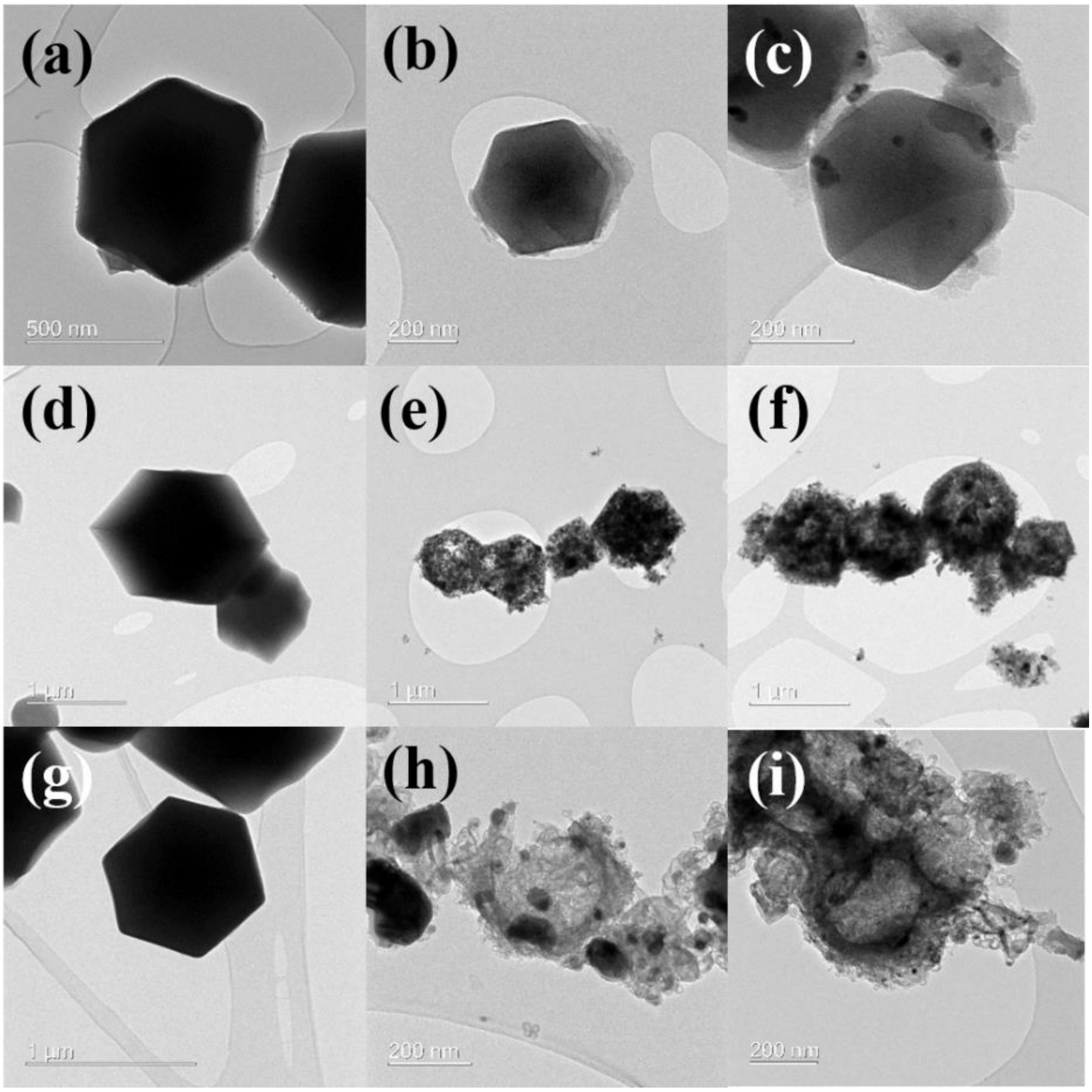

Figure 2.7. TEM images of samples. a) ZIF-8, b) NCF-1000, c) SNCF-1000, d) ZIF-67, e) GCF-1000, f) SGCF-1000, g) ZIF-8@ZIF-67, h) CNCF-1000, and i) CSNCF-1000.

After carbonization, NCF-1000 inherited the dodecahedron structure of ZIF-8 and the surface of NCF-1000 became fuzzy. The Zn (boiling point 907 ℃) metal cores in ZIF-8 evaporated at 1000 ℃ and resulted in amorphous and porous N-doped carbon framework. Low resolution TEM image (Figure 2.7b) and high-resolution TEM image (**Figure 2.8**) showed the amorphous structure of NCF.

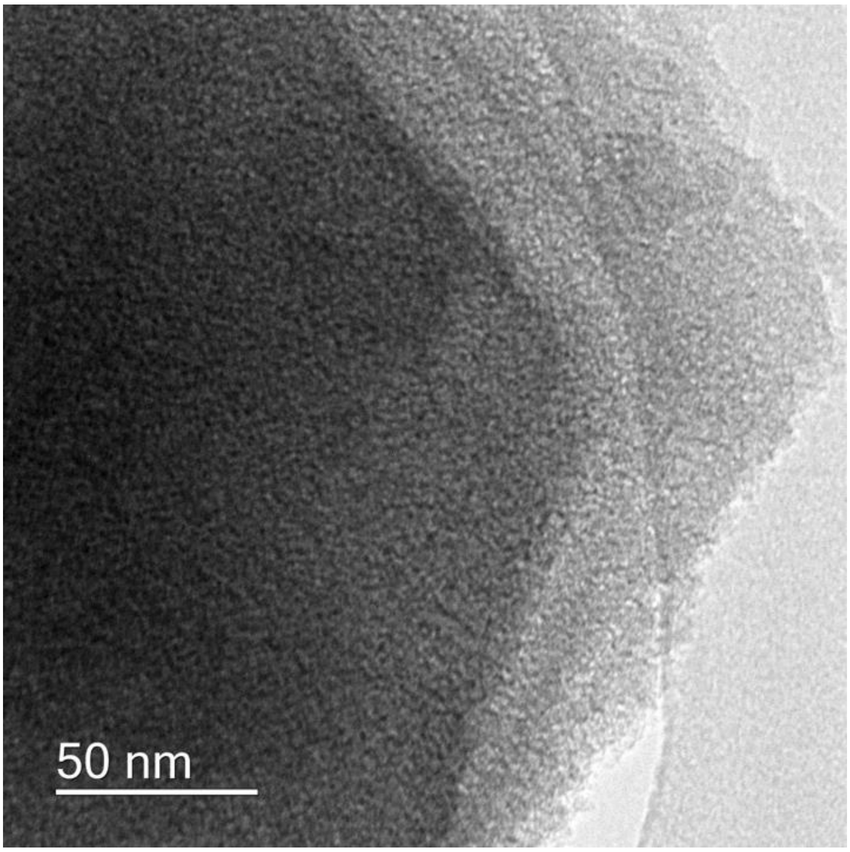

Figure 2.8. High-resolution TEM image of NCF-1000.

Though Zn evaporated at 1000 ℃, after carbonization there was still some small Zn nanoparticles on the surface of NCF-1000. As for ZIF-67, the boiling point of Co metal cores is 2870 ℃, much higher than 1000 ℃, so that after carbonization, the Co metal core aggregated to form nanoparticles (Figure 2.6e and 2.7e). Though the dodecahedron structure of ZIF-67 was maintained after carbonization, the large particle size leads to low specific surface area and pore structure, which is not suitable to be used as S host. But at high temperature Co could catalyst the graphitization of carbon materials through forming Co/C alloy to improve the conductivity of the product (**Figure 2.9**).

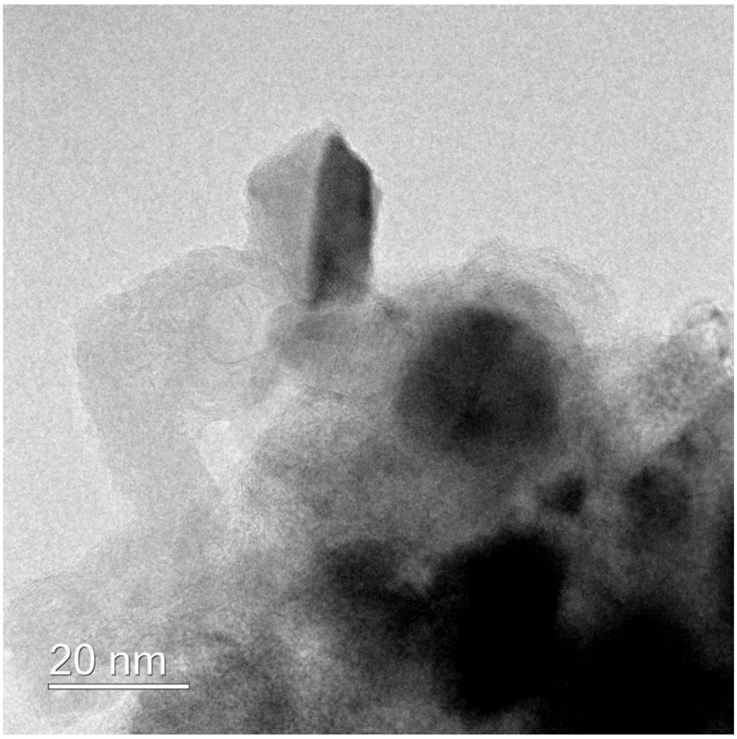

Figure 2.9. High-resolution TEM image of GCF-1000.

For ZIF-8@ZIF-67, after carbonization a core-shell structure was formed. ZIF-8 in the core transformed into porous N-doped carbon and ZIF-67 on the surface transformed into Co nanoparticles supported on graphitized carbon and carbon nanotubes (CNTs) (Figure 2.7h and **Figure 2.10**). EDS mapping of CNCF-1000 (**Figure 2.11**) clearly showed the uniform dispersion of C and Co in the sample, while the signal of Zn is rather low, which could be ignored. The as-prepared samples were than mixed with S and heated at 650 °C for 2 hours to synthesis sulfurized products. As can be seen from both SEM and TEM images, the morphology of samples didn’t change after sulfurization.

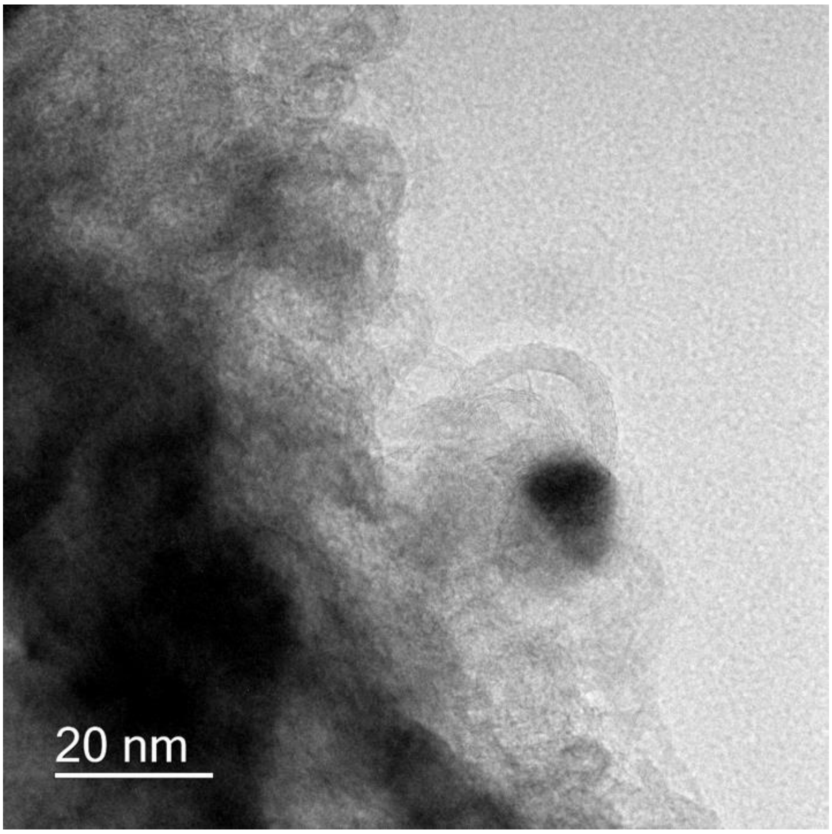

Figure 2.10. High resolution TEM image of CNCF-1000.

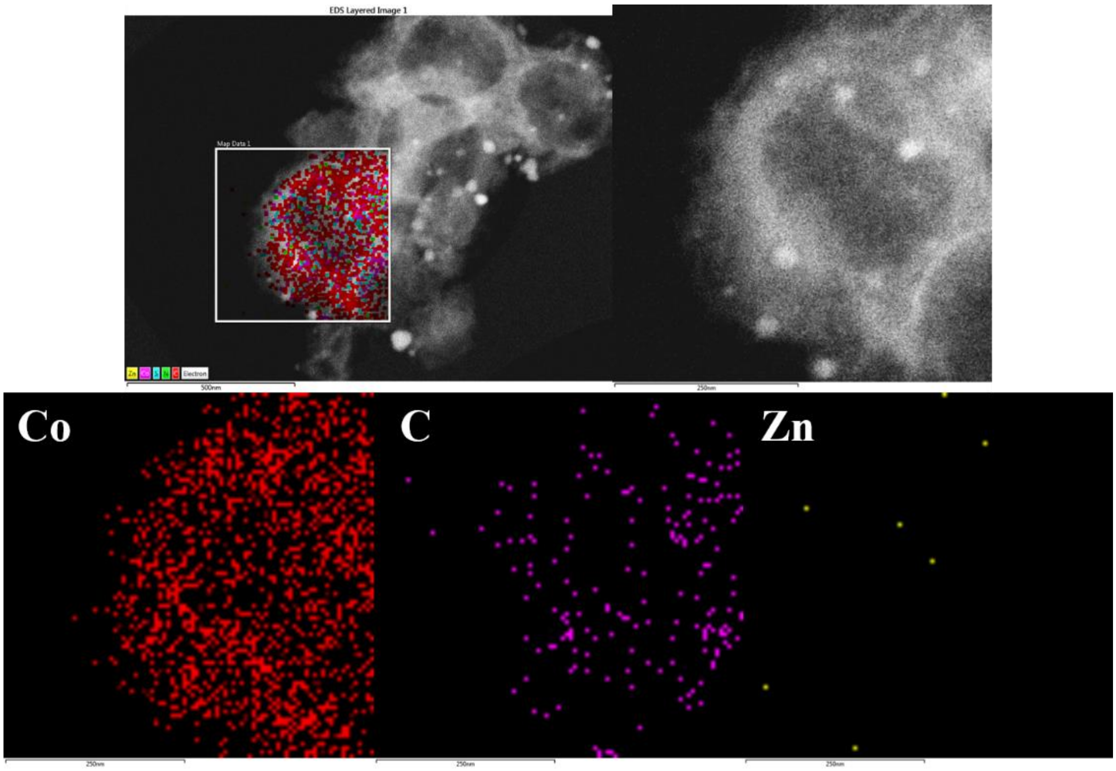

Figure 2.11. EDS mapping of CNCF-1000.

The chemical structure of the products was characterized by XRD, Raman X-ray photoelectron spectroscopy (XPS) and Fourier Transform Infrared Spectroscopy (FTIR). XRD patterns (**Figure 2.12**) showed that after carbonization at 1000 °C for 3 hours, ZIF-8 transformed into amorphous carbon material (NCF-1000), ZIF-67 and ZIF-8@ZIF-67 transformed into graphitized carbon and metal Co (GCF-1000 and CNCF-1000). The peak at around 26 degrees is the characteristic peak of graphitized carbon materials. This also agrees with the TEM results that CNTs were formed in CNCF-1000.

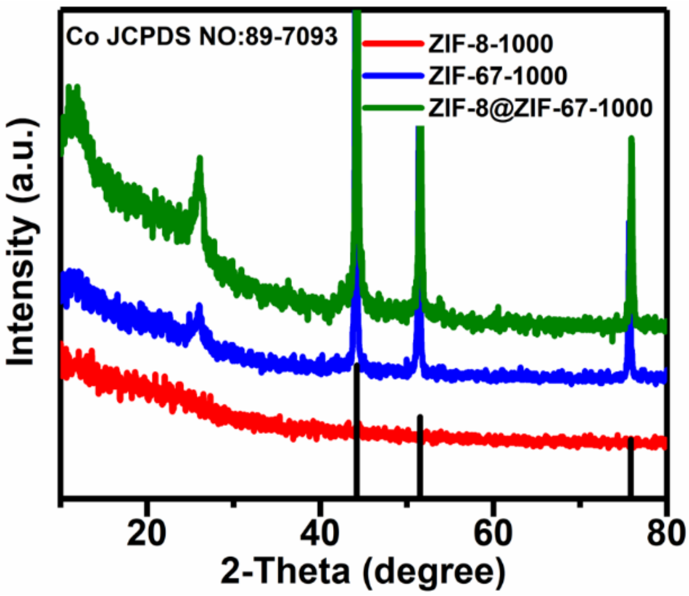

Figure 2.12. XRD patterns of samples carbonized at 1000 degrees for 3 hours.

After sulfurization, the Co nanoparticles in GCF-1000 and CNCF-1000 turned into a mixture of Co, CoS and Co_9S_8 as indicated by XRD patterns (**Figure 2.13a**). The high-resolution TEM image (Figure 2.13b) showed a Co_9S_8 nanoparticle wrapped by graphitized carbon. The interplanar spacing is 0.191 nm same with the 511 lattice plane of Co_9S_8.

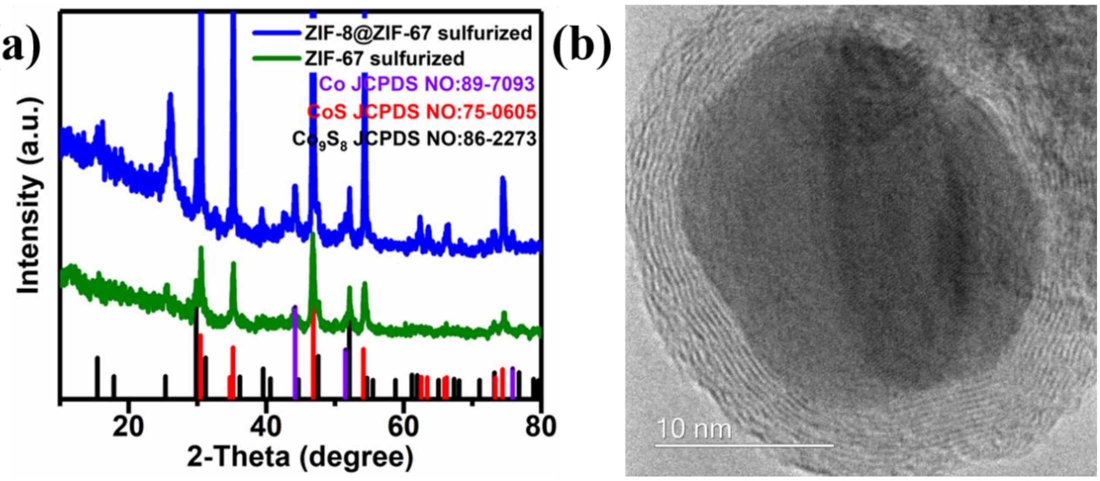

Figure 2.13.a) XRD patterns of samples after sulfurization. b) High resolution TEM image of CSNCF-1000.

For sulfurized NCF-1000 (SNCF-1000), after sulfurization s weak signal of ZnS was detected in XRD pattern as shown in **Figure 2.14**. This could be ascribed to the sulfurization of small Zn particles on the surface of NCF-1000 as shown in the TEM images.

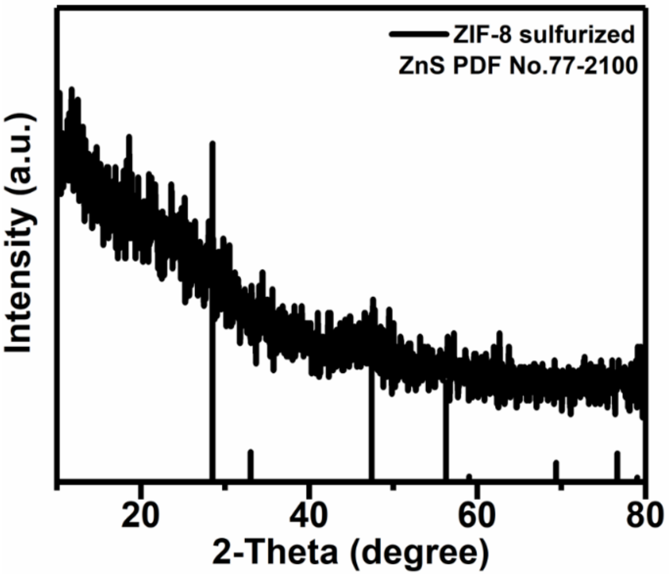

Figure 2.14. XRD pattern of SNCF-1000.

Raman tests also showed that CNCF-1000 had a higher graphitization level as the G bond at around 1580 cm^{-1} became sharper and the intensity increased (**Figure 2.15**). For NCF-1000, the intensity of D bond is higher than that of G bond, indicating an amorphous structure of NCF-1000.

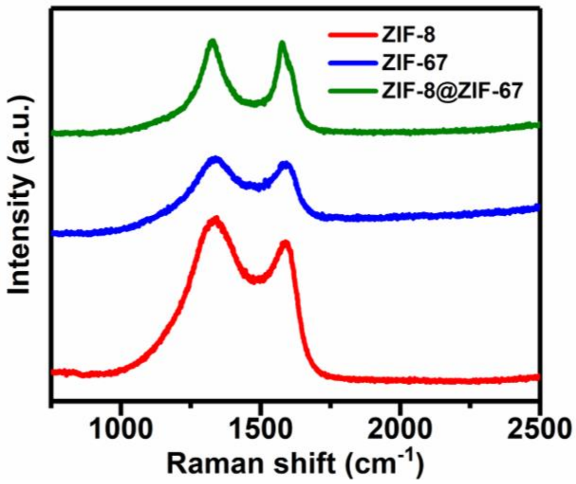

Figure 2.15. Raman spectrums of samples carbonized at 1000 degrees for 3 hours.

The chemical structure of samples was further characterized by XPS. As shown in **Figure 2.16a-b**, no signal of Zn was detected in CSNCF-1000 in constant with XRD and TEM results. The O content in the samples shown in Figure 2.15 could come from three aspects. First, physically absorbed O_2 on the surface of the samples. Though there was vacuum process before the XPS test, there might still be some absorbed O_2. Second, some oxidized carbon on the surface of the samples during the synthesis process. Though Ar was used to provide an inert atmosphere, H_2 was not used during the synthesis process. There might be some leak in the connections of the tubes. Third, the surface of the samples might be oxidized as they were not stored in an inert atmosphere like the glove box. The XPS in chemistry department has been down for quite a long time last year, the samples have been stored for too long before XPS test. Structures like Co=S=O might be formed on the surface. For SNCF-1000, Zn signal was detected (Figure 2.16c). The high resolution XPS spectrum (Figure 2.16d) showed that Zn existed in the form of ZnS, same as the results of XRD test.

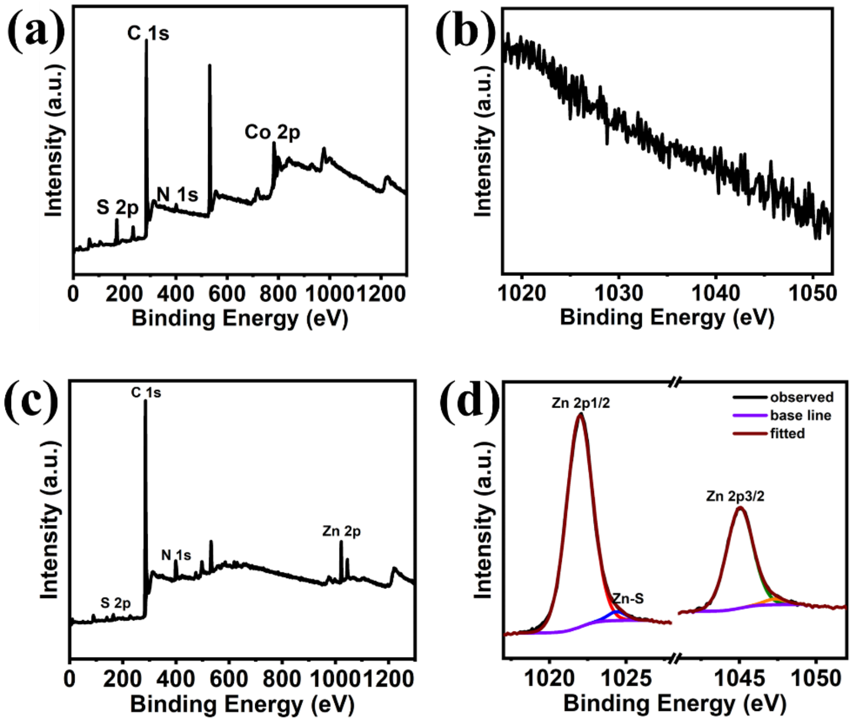

Figure 2.16. XPS spectrum of samples. a) CSNCF-1000, b) high resolution spectrum of Zn in CSNCF-1000, c) SNCF-1000 and d) high resolution spectrum of Zn in SNCF-1000.

The N atoms from the linker (2-methyl imidazole) resulted in N-doped carbon as indicated by the high resolution XPS spectrum of N (**Figure 2.17a**). Pyridinic, pyrronic and graphitic N were formed in CSNCF-1000. The S spectrum (Figure 2.17b), peaks at 163.5 eV and 164,9 eV originated from the S 2p3/2 and S 2p1/2 of S, respectively. The peaks at around 170 eV could be ascribed to the chemical bonds between S and Co.

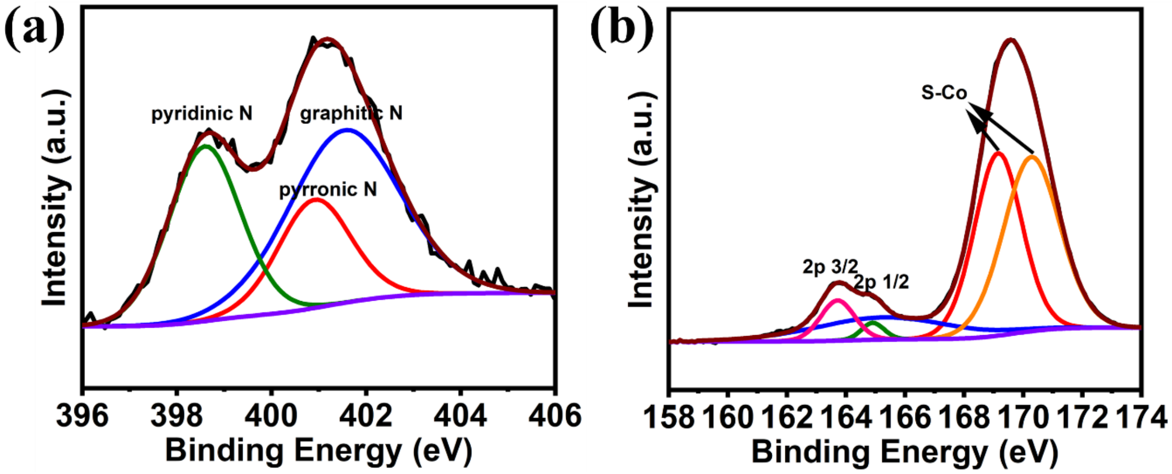

Figure 2.17. High resolution XPS spectrum of a) N and b) S in CSNCF-1000.

The high resolution XPS spectrum (**Figure 2.18**) of Co revealed that Co existed in three different valences: Co^0, Co^+ and Co^{2+}. The peak at 773.7 eV stemmed from Co^0. XRD test also showed that part of the Co particles cannot be sulfurized. The peak at 779.1 eV and 780.3 eV originated from Co^+ and Co^{2+}, respectively. Co in CoS and Co_9S_8 existed in two valences: +1 and +2. The peak at 786.0 eV was the satellite peak of Co.

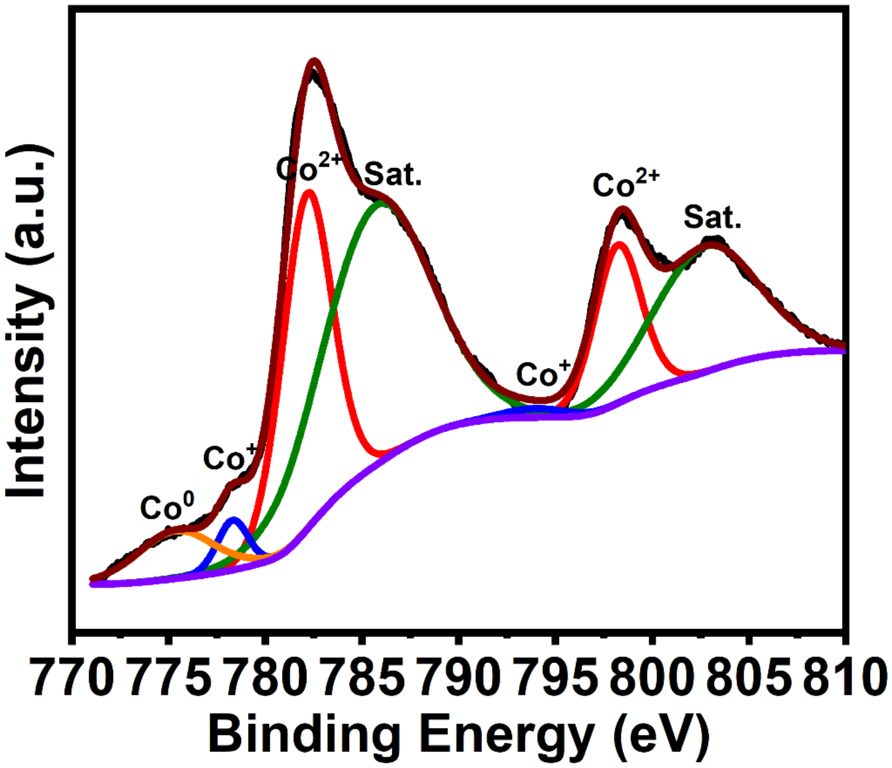

Figure 2.18. High resolution XPS spectrum of Co in CSNCF-1000.

FTIR spectrum (**Figure 2.19**) also confirmed the existence of Co=S bond in CSNCF-1000 as indicated by the peak at around 1100 cm^{-1}. No obvious peak at this region can be observed in SNCF-1000 sample. The peak at around 2100 cm^{-1} stemmed from C≡C/C≡N.

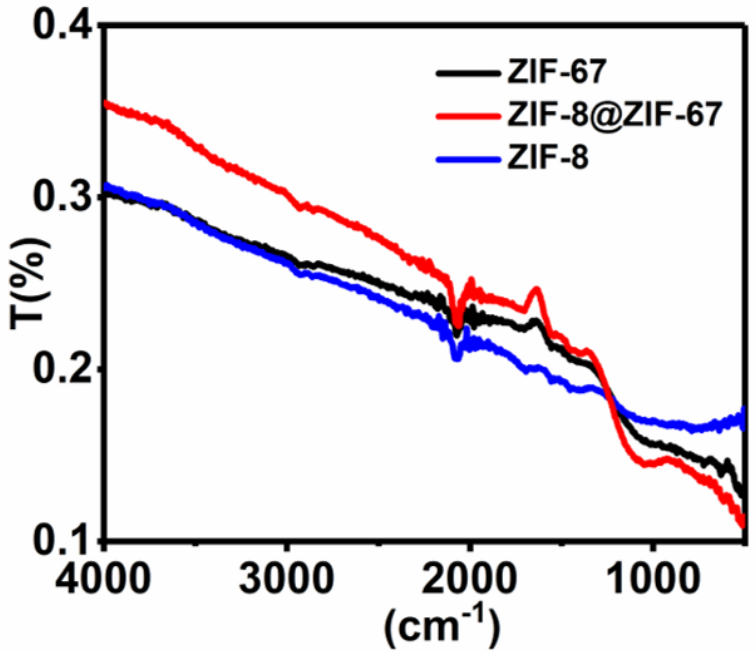

Figure 2.19. FTIR spectrum of samples after sulfurization.

The porous structure of samples was then tested by Brunauer-Emmett-Teller (BET) surface area measurement as shown in **Figure 2.20**. SNCF-1000, synthesized for ZIF-8 template had a super high specific surface area of 1490 m^2 g^{-1}. While SGCF-1000, synthesized form ZIF-67 template, had the lowest specific surface area of 210 m^2 g^{-1}. With ZIF-8 as core, the specific surface area of CSNCF-1000 increased to 240 m^2 g^{-1}, indicating that the core-shell structure successfully alleviated the collapse of ZIF-67 during carbonization at high temperature.

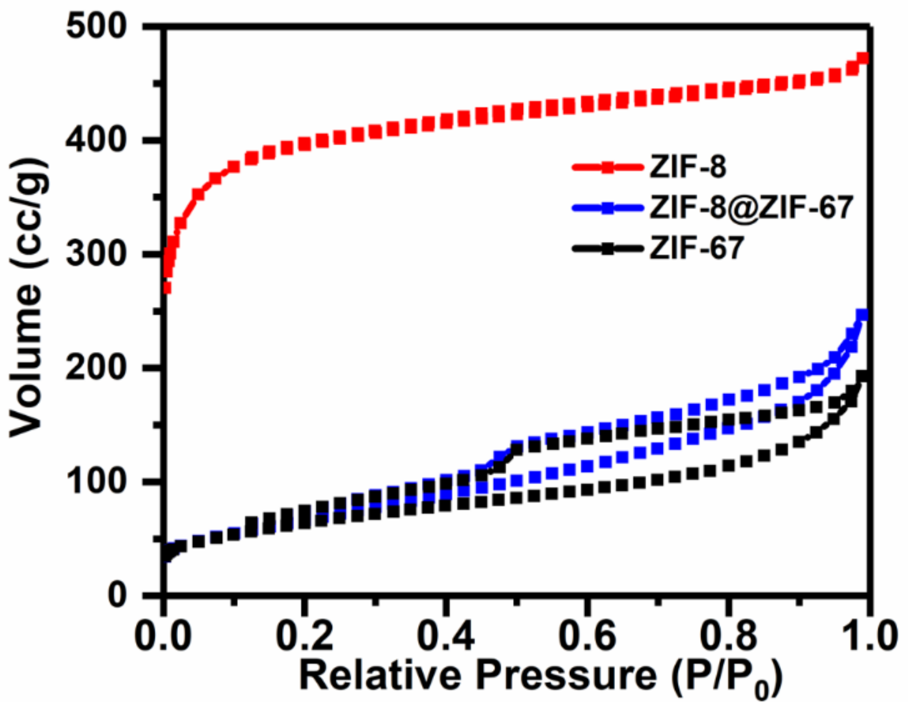

Figure 2.20. Brunauer-Emmett-Teller (BET) surface area measurement of samples after sulfurization.

3.3.2 Electrochemical tests

The electrochemical performance of CSNCF-1000 was tested by assembling coin cells using CSNCF-1000 as S host and lithium foil as anode. CSNCF-1000/S composite was prepared through a melt-diffusion process at first. The S content of the as-prepared CSNCF-1000/S composite was tested to be around 55 % by thermo gravimetric analyser (TGA) as shown in **Figure 2.21**. The mass lose at low temperature might be ascribed to the evaporation of H_2O and other components that were absorbed in the sample.

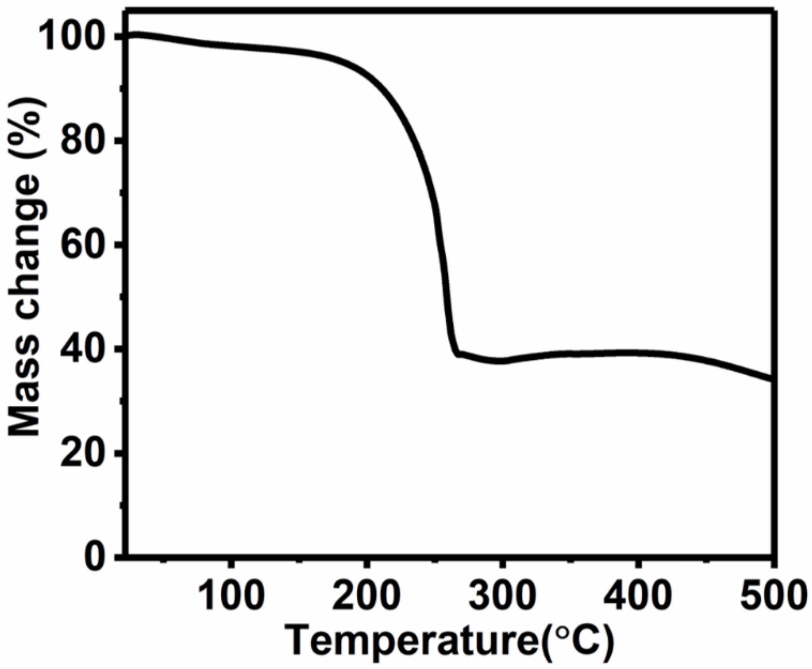

Figure 2.21. Thermo gravimetric analyser (TGA) curves of CSNCF-1000/S composite.

The CSNCF-1000/S composite was then made into an electrode through a slurry coating process, the area loading of S in the electrode was 0.9-1.4 mg cm^{-2}, and the electrolyte usage when assembling coin cells was kept at 10 µL mg^{-1}(based on the mass of S) if not specially mentioned in the following discussion. The cyclic voltammetric curves are shown in **Figure 2.22**. The two cathodic peaks at 2.26 and 2.03 V correspond to the transform from S_8 to long chain LPSs and then further to short chain LPSs. The anodic peak at 2.45 V correspond to the transform from Li_2S to S_8. As the scan rate increased, the peaks shifted to both sides as the polarization increased.

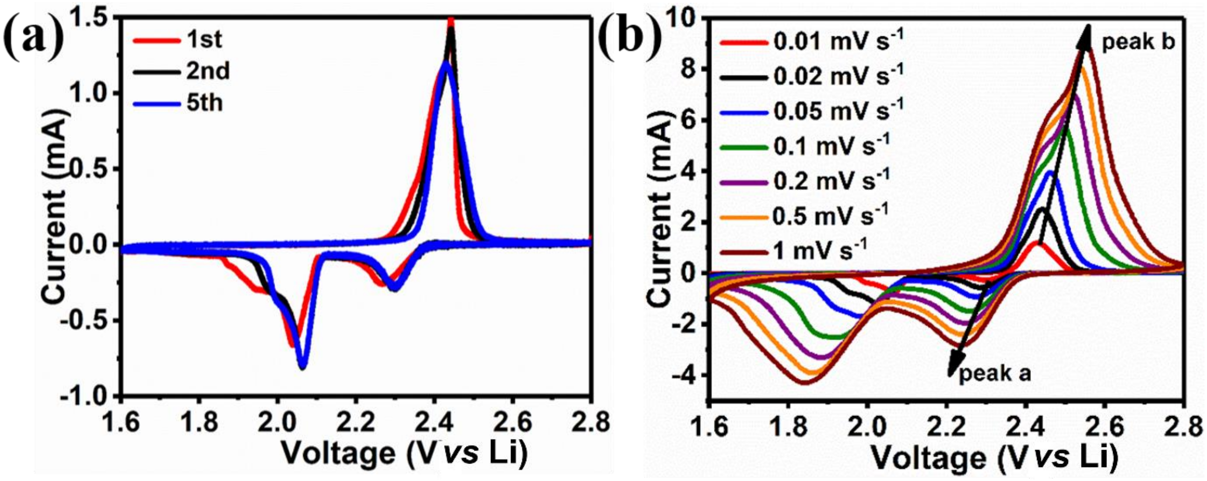

Figure 2.22. a) Cyclic voltammetry (CV) curves the first 5 cycles, b) CV curves at different scan rate increase from 0.01 mV s^{-1} to 0.02, 0.05, 0.1, 0.2, 0.5 and 1 mV s^{-1}.

The relation between the peak current and the scan rate was shown in **Figure 2.23**. In both cathodic peak (peak a) and anodic peak (peak b), the peak current and the square root of scan rate showed good linear relation, indicating both the discharge and charge process are diffusion limited instead of capacitive contributed.

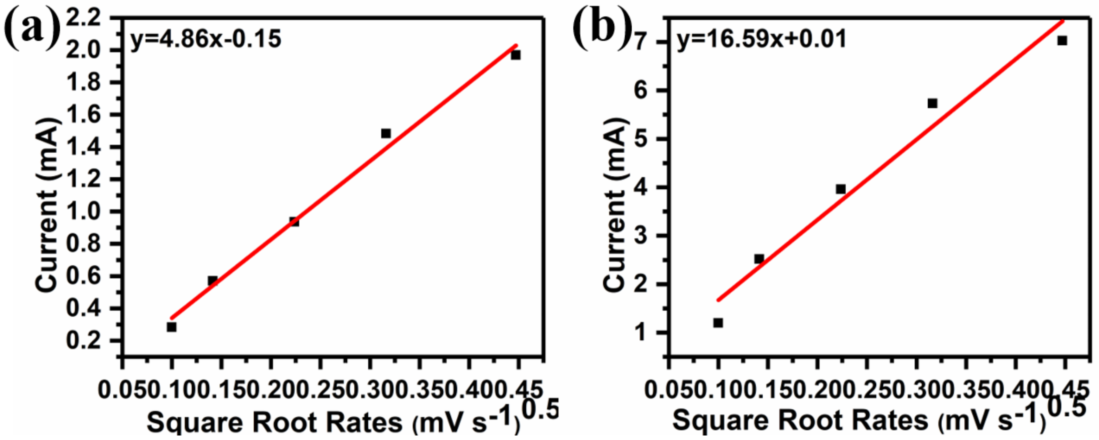

Figure 2.23. Linear relation between the peak current and the square root of scan rate.

The charge-discharge curves showed two discharge voltage platforms at 2.09 and 2.31 V, which are close to the CV results. A high initial specific capacity of 1313 mA h g^{-1} was reached at the first cycle at a current density of 0.1 C (1 C = 1675 mA g^{-1}). A reversible specific capacity of 1272 mA h g^{-1} was maintained after charging. Among all the samples, CSNCF-1000 had the highest specific capacity as shown in **Figure 2.24**. SNCF-1000 had the lowest initial specific capacity of 930 mA h g^{-1}, while SGCF-1000 delivered a specific capacity of 1088 mA g^{-1} at the first cycle. The voltage difference of discharge and charge at half of the capacity (Δ_V) was measured to compare the polarization. CSNCF-1000, GCF-1000 and NCF-1000 showed Δ_V of 138 mV, 146 mV and 160 mV, respectively (Figure 2.23d). The lowest Δ_V of CSNCF-1000 indicated a catalyst activity of cobalt CSNCF-1000 and good efficiency.

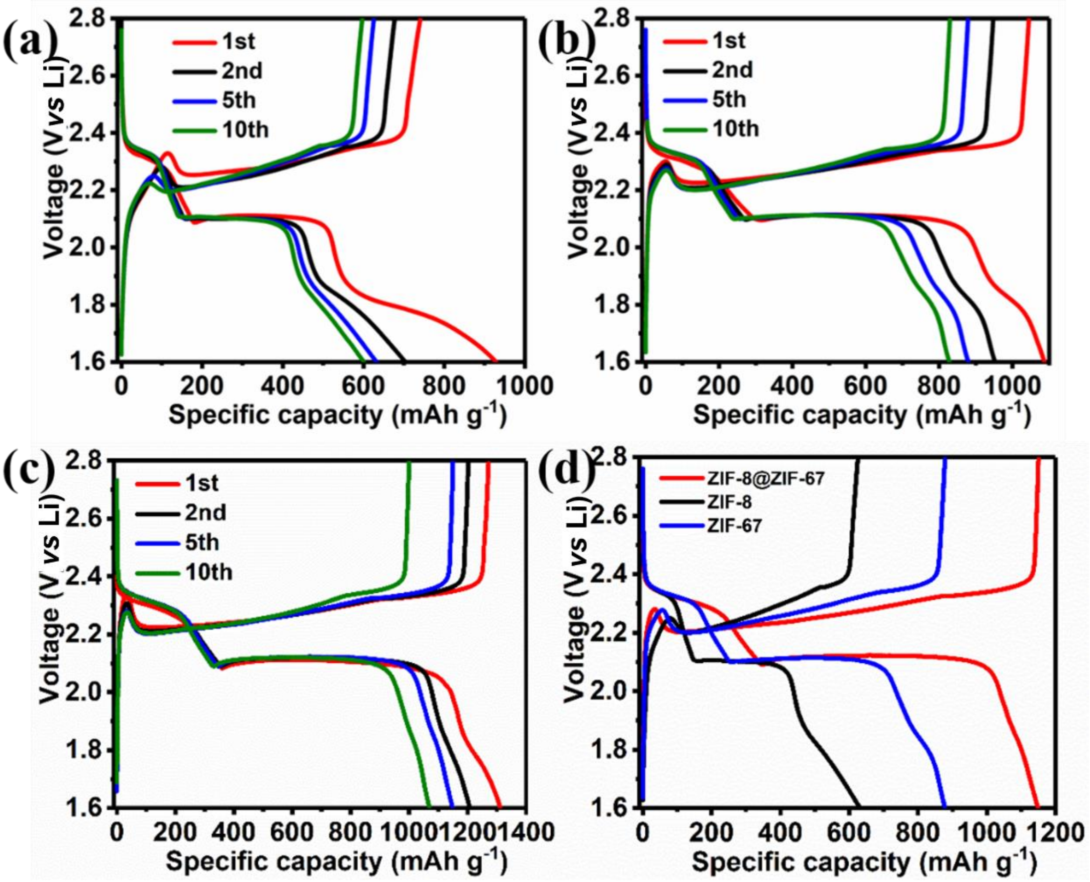

Figure 2.24. Charge-discharge curves of samples at a current density of 0.1 C (1 C = 1675 mA g^{-1}): a) SNCF-1000, b) SGCF-1000 and c) CSNCF-1000. d) charge-discharge curves of samples at the 5th cycle.

The rate performance (**Figure 2.25**) was then tested at different current density: increased from 0.1 C to 2 C step by step and then decreased back to 0.1 C. CSNCF-1000 maintained a specific capacity of 584 mA h g^{-1} at 2 C, which recovered to 995 mA h g^{-1} when the current density went back to 0.1 C, showing good capacity retention. However, for SNCF-1000, only 271 mA h g^{-1} was maintained at 2 C, and 537 mA h g^{-1} was recovered, the lowest among all three samples. The difference in rate performance mainly resulted from the difference in conductivity of samples. As proved by XRD, Raman and TEM, CSNCF-1000 sample had the highest graphitization level with CNTs formed, and SNCF-1000 was amorphous carbon.

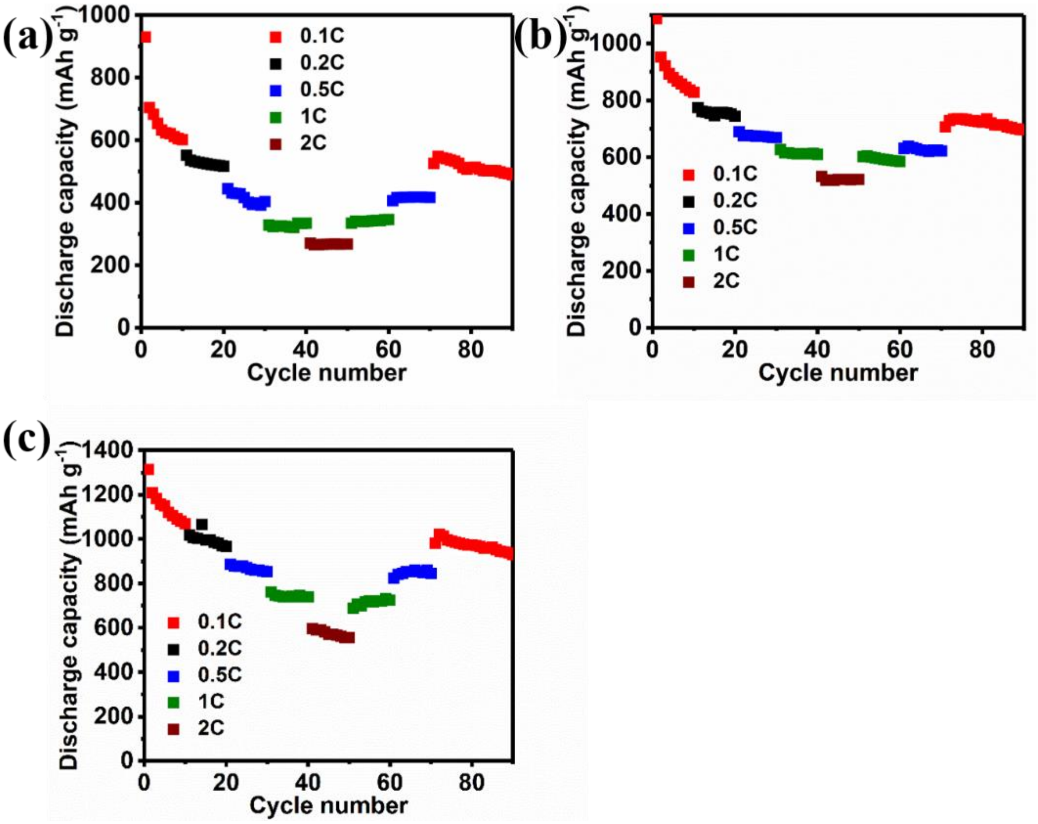

Figure 2.25. Rate performance of samples: a) SNCF-1000, b) SGCF-1000 and c) CSNCF-1000. The current density increased from 0.1 C to 0.2, 0.5, 1 and 2 C and then decreased to 1, 0.5 and 0.1 C step by step.

The cyclic stability of samples is shown in **Figure 2.26**. After 5 cycles of activation process at a current density of 0.1 C, CSNCF-1000 showed a specific capacity of 880 mA h g^{-1} at 1 C, which kept stable in the following 170 cycles and reached 620 mA h g^{-1}. However, the capacity dropped dramatically in the following test with only 470 mA h g^{-1} left after 200 cycles. During this process the Coulombic efficiency is higher than 100%, indicating the occurrence of shuttle effect. For SNCF-1000 and SGCF-1000, more stable performance was observed but the specific capacity is much lower than that of CSNCF-1000. High area S loading electrode is essential for the practical application of LSBs. Thus, coin cells with high area S loading of 4 mg cm^{-2} were assembled and tested with low electrolyte usage of 7 μL mg^{-1}. A specific capacity of 120 mA h g^{-1} was achieved after the activation process, and 84 mA h g^{-1} was maintained after 200 cycles. And the Coulombic efficiency was about 100%, showing good stability.

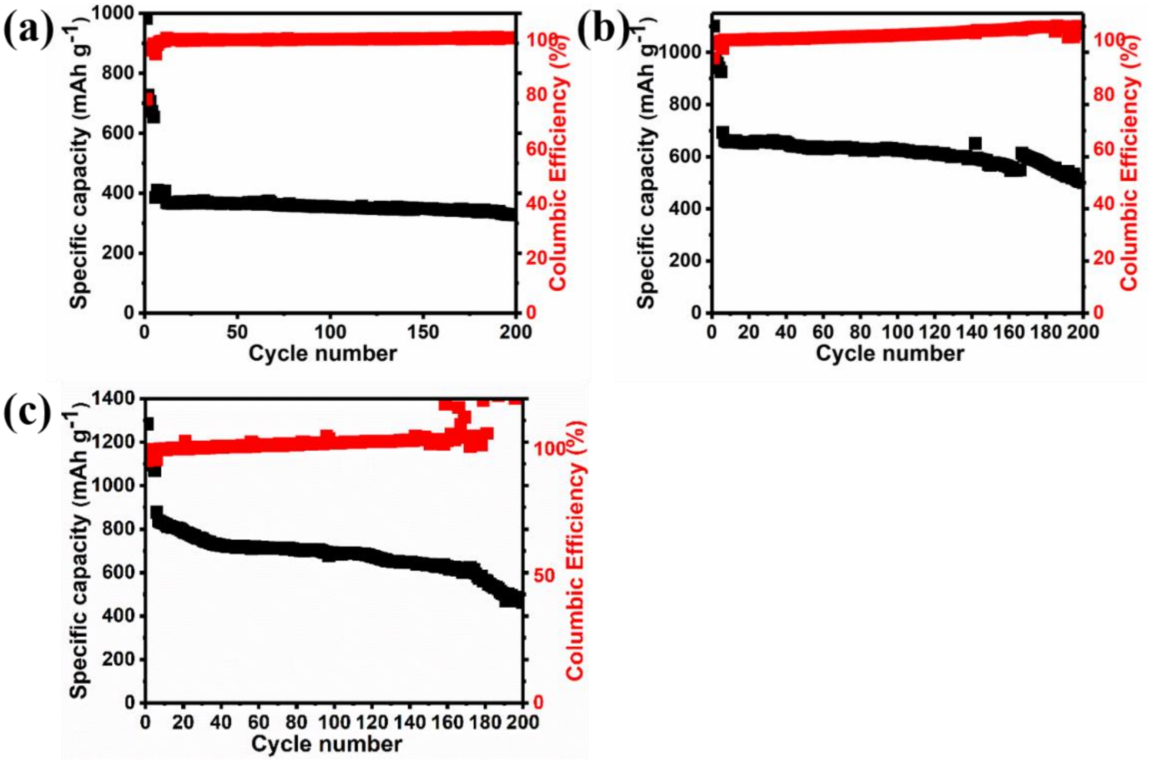

Figure 2.26. Cyclic performance of samples at a current density of 1 C: a) SNCF-1000, b) SGCF-1000 and c) CSNCF-1000.

The absorption test and the XPS test of samples after absorption were performed to gain some insight into the mechanism of CSNCF-1000. As shown in **Figure 2.27**, the Li_2S_6 solution in CSNCF-1000 and GCF-1000 became clear after 24 hours, while that in NCF-1000 stayed light yellow. The cobalt sulphides and Co atoms in CSNCF-1000 and GCF-1000 had strong absorption ability toward LPSs with high polarity. The high porosity and high level of N doping also favoured the absorption of LPSs as reported, but the low polarity restricted it.

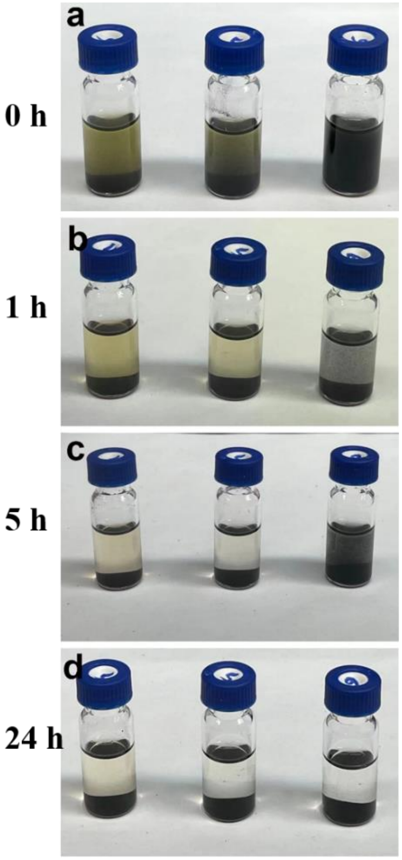

Figure 2.27. Photographs of samples immersed in Li_2S_6 solution for certain time, from left to right: SNCF-1000, SGCF-1000 and CSNCF-1000.

The Ultraviolet-visible spectrums of solution after absorption tests is shown in **Figure 2.28**. No significant peak could be observed, indicating that Li_2S_6 was absorbed by CSNCF-1000.

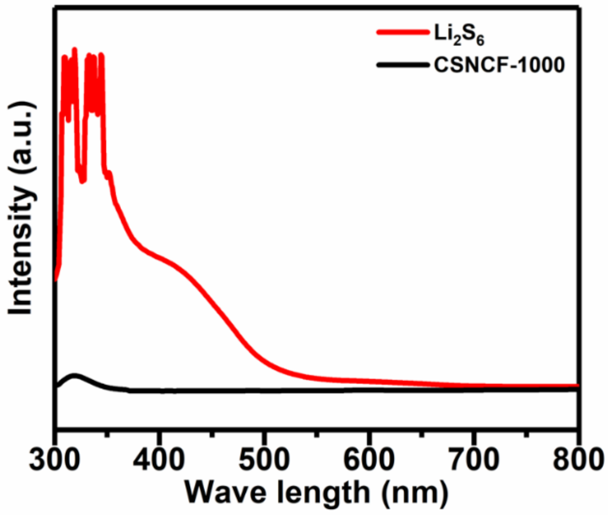

Figure 2.28. UV-vis spectrum before and after absorption test.

The high resolution XPS spectrum of CSNCF-1000 revealed the strong interaction between CSNCF and LPSs (**Figure 2.29**). The intensity of Co^+ peak increased significantly, as the intensity of Co^{2+} peak decreased, indicating that Co^{2+} in CSNCF-1000 was reduced to Co^+ by LPSs. The peaks shifted to lower energy, which could be ascribed to the absorption of LPSs on the surface of LPSs as reported by other research. The S spectrum is much different from that of CSNCF-1000. The peaks between 161 eV and 165 eV could be ascribed to the bridging S (S_B) and the terminal S (S_T) of polysulfides. The peak at 166.7 eV represents the thiosulfate on the surface of CSNCF-1000, which came from the oxidization of S in polysulfides. The peaks at 169.2 eV and 170.5 eV represent the polythionate and sulfate that formed from the further reaction between thiosulfate and polysulfides. The Zn spectrum of NCF-1000 was similar with that before Li_2S_6 absorption (Figure 2.29c). Except for a peak of Zn-S bond that comes from zinc sulfide formed on the surface of NCF-1000, no other interaction between Zn and S was detected. In the S spectrum (Figure 2.29d), the signal of bridging S and terminal S were also detected as LPSs were physically absorbed on the surface on NCF-1000, which had high specific surface area. The thiosulfate and polytionate signal could be ascribed to the interaction between LPSs and N atoms in NCF-1000. However, no signal of sulfate was detected indicating the limitation of catalyst ability of N doping.

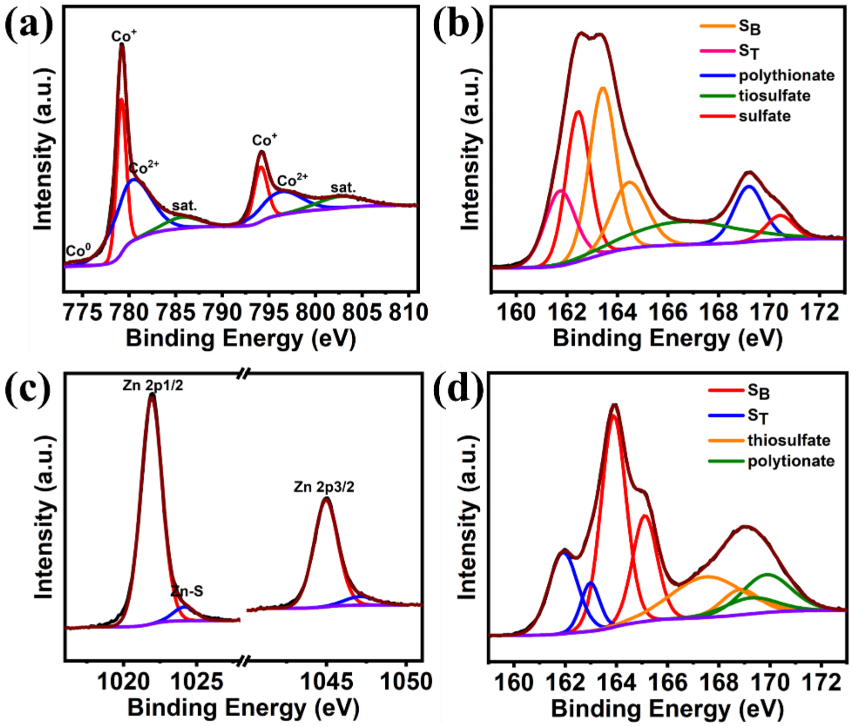

Figure 2.29. High resolution XPS spectrum of a) Co, b) S in CSNCF-1000 and c) Zn, d) S in SNCF-1000 after absorption test.

The effect of carbonization temperature on the performance was studied by synthesizing samples at different temperature: CSNCF-800 and CSNCF-900. The EDS results showed that in samples synthesized at 800 °C, intensive signal of Zn was detected (**Figure 2.30**). The residual Zn added up to the total mass of electrode and thus resulted in lower specific capacity. Besides, after Zn was evaporated, more pore volume will be available for S host. For CSNCF-900, weak signal of Zn was detected (**Figure 2.31**), indicating that most of Zn from the precursor evaporated during the carbonization process.

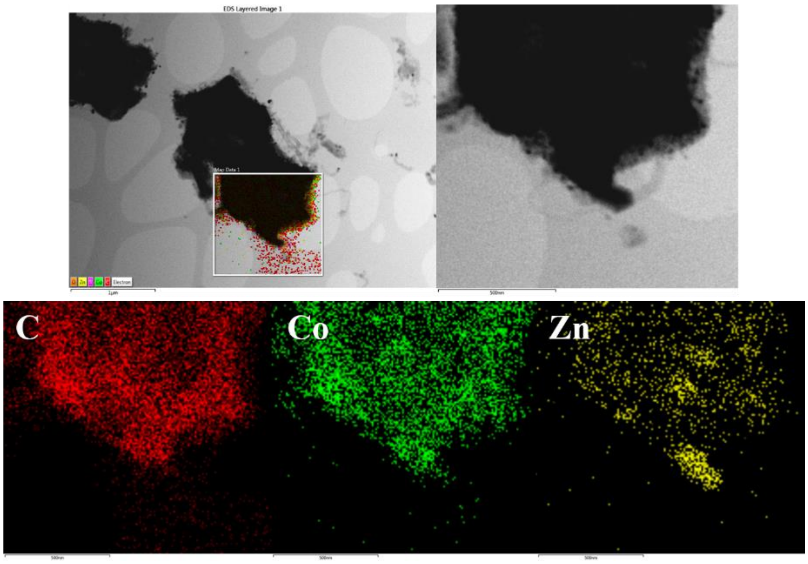

Figure 2.30. EDS mapping of CSNCF-800.

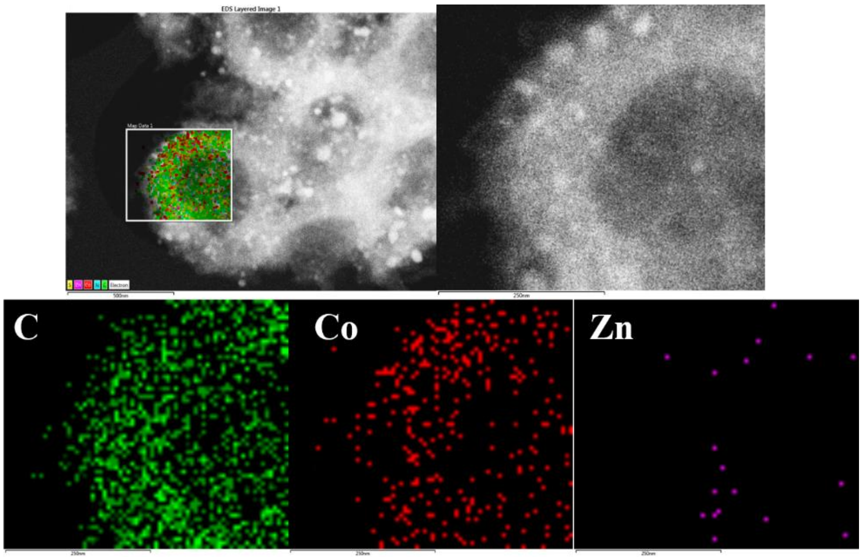

Figure 2.31. EDS mapping of CSNCF-900.

The effect of temperature on the morphology was characterized by SEM and TEM (**Figure 2.32**). The dodecahedron structure of ZIF-8@ZIF-67 template was inherited in all the samples synthesized at different temperature. But in those synthesized at 800 ℃, no obvious CNT was synthesized while in CSNCF-900 and CSNCF-1000, CNTs can be observed on the surface.

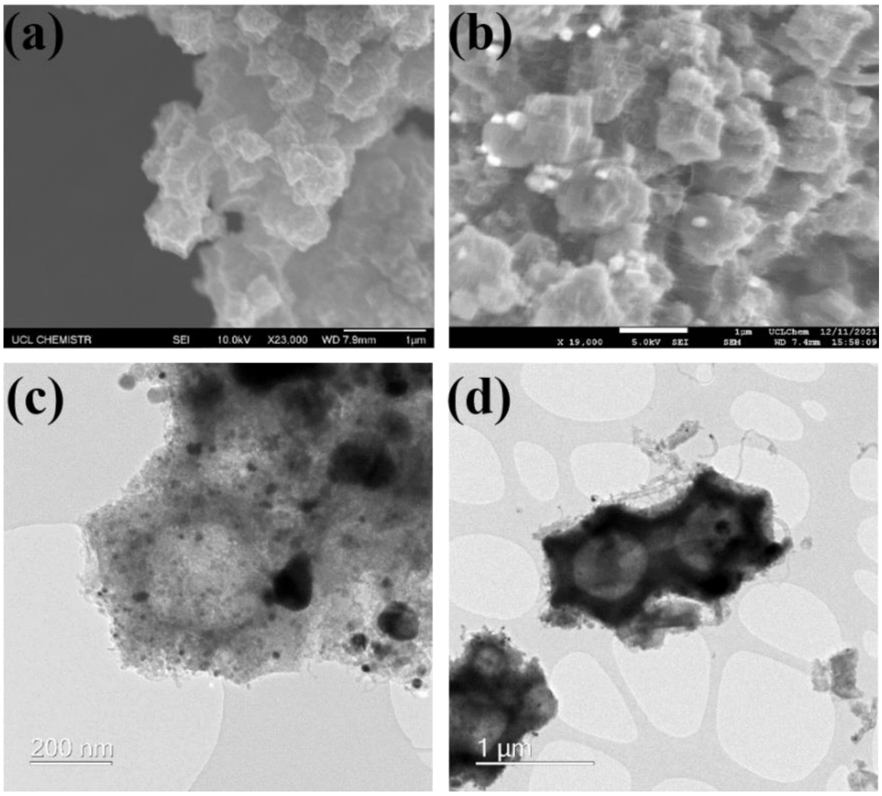

Figure 2.32. a) SEM image of CSNCF-800, b) SEM image of CSNCF-900, c) TEM image of CSNCF-800 and d) TEM image of CSNCF-900.

The XRD results of samples (**Figure 2.33a**) sulfurization agreed with the SEM and TEM results as the peak at around 26 degrees became sharp and the intensity increased as the carbonization temperature increased. Furthermore, the Raman spectrums (Figure 2.33b) showed an increase in the intensity of G bond as the carbonization temperature increased, confirming the increase of graphitization level.

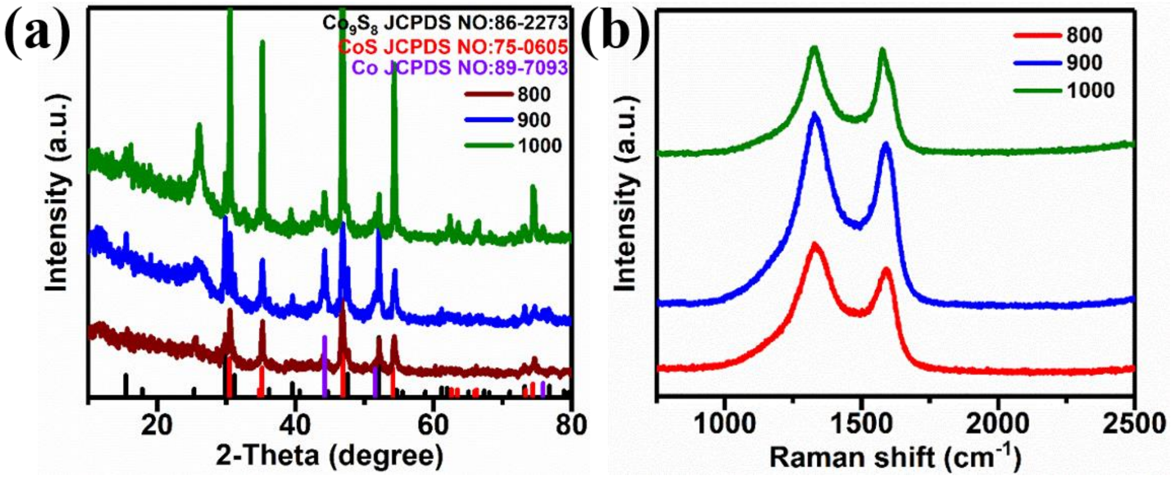

Figure 2.33. a) XRD patterns and b) Raman spectrum of samples prepared at different temperatures.

The electrochemical performance of CSNCF-800 and CSNCF-900 were then tested (**Figure 2.34**). CSNCF-900 had an initial specific capacity of 1281 mA h g^{-1}, 130 mA h g^{-1} than that of CSNCF-800. When the current density increased to 2 C, a specific capacity of 617 mA h g^{-1} was maintained, while CSNCF-800 only delivered a specific capacity of 450 mA h g^{-1} at 2 C. The higher initial specific capacity and better rate performance of CSNCF-900 could be ascribed to the higher conductivity result from the higher level of graphitization at higher temperature. When the current density went back to 0.1 C, a high specific capacity of 813 mA h g^{-1} could be delivered by CSNCF-900.

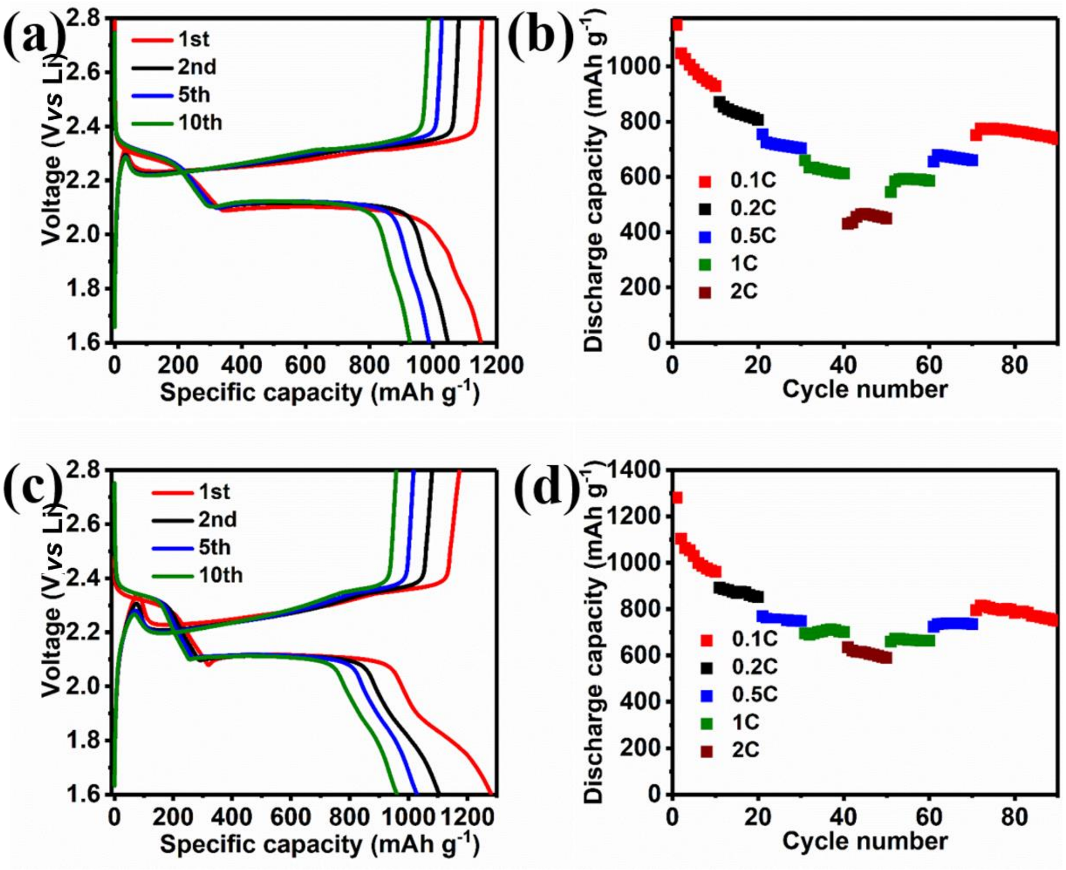

Figure 2.34. a) Charge-discharge curves of CSNCF-800 at a current density of 0.1 C, b) Rate performance of CSNCF-800, The current density increased from 0.1 C to 0.2, 0.5, 1 and 2 C and then decreased to 1, 0.5 and 0.1 C step by step. c) charge-discharge curves of CSNCF-900 at a current density of 0.1 C and d) Rate performance of CSNCF-900 The current density increased from 0.1 C to 0.2, 0.5, 1 and 2 C and then decreased to 1, 0.5 and 0.1 C step by step.

To verify the function of cobalt sulphides, samples were immersed in acid for 24 hours to get rid of Co before sulfurization (CSNCF-X-aw, aw means acid wash). The SEM images (**Figure 2.35**) of samples prepared after acid wash showed similar morphology with those prepared without acid wash, indicating that the carbon framework is stable in acid. However, in the TEM images less Co particles could be observed as shown in Figure 2.35d-f. Especially for CSNCF-1000-aw, very few Co particles could be observed in the carbon framework. However, because Co particles were etched, more pore structure was formed (Figure 2.35f).

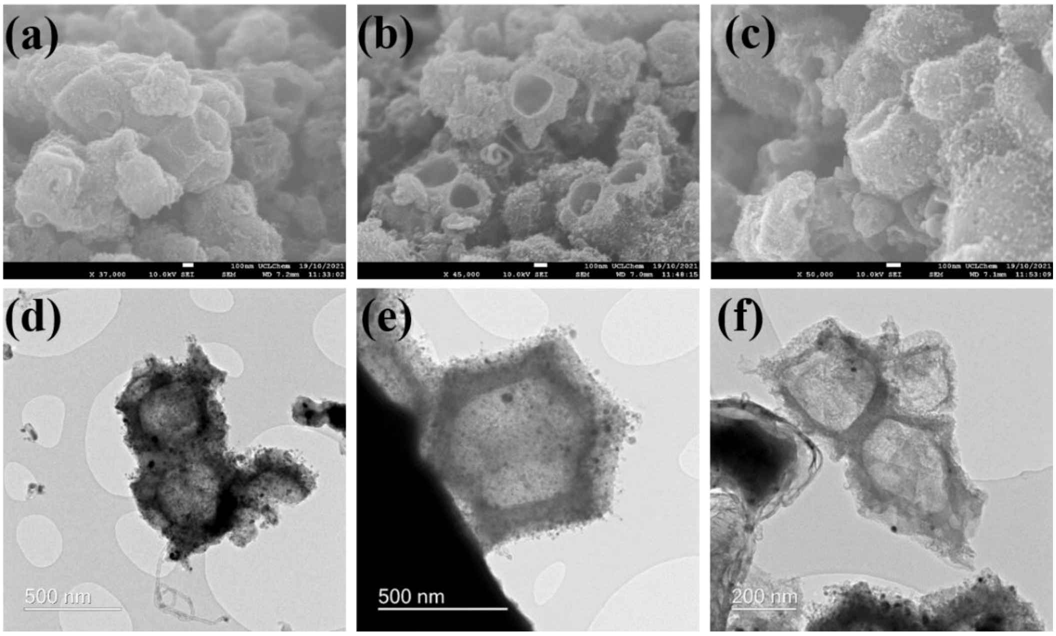

Figure 2.35. SEM images of a) CSNCF-800-aw, b) CSNCF-900-aw and c) CSNCF-1000-aw. TEM images of d) CSNCF-800-aw, e) CSNCF-900-aw and f) CSNCF-1000-aw.

Peaks of Co could still be observed from XRD patterns of samples after acid wash (**Figure 2.36a**), indicating that same Co particles could not be etched by acid. These particles could be deep inside the carbon framework or covered by thick carbon layers that were very stable in acid. This also agrees with the results of sulfurized samples prepared without acid wash as mentioned before. Co^0 signal could be observed in both XRD pattern and XPS spectra. The XRD patterns of sulfurized samples after acid wash is quite different (Figure 2.36b). The peaks of Co_9S_8 could be observed in XRD pattern of CSNCF-800-aw. This could be explained that some pore structure or active sites were exposed after acid wash. However, no peaks of Co_9S_8 could be observed in XRD patterns of CSNCF-900/1000-aw. This also agrees with TEM results that at higher temperature, less Co particles could be remained after acid wash.

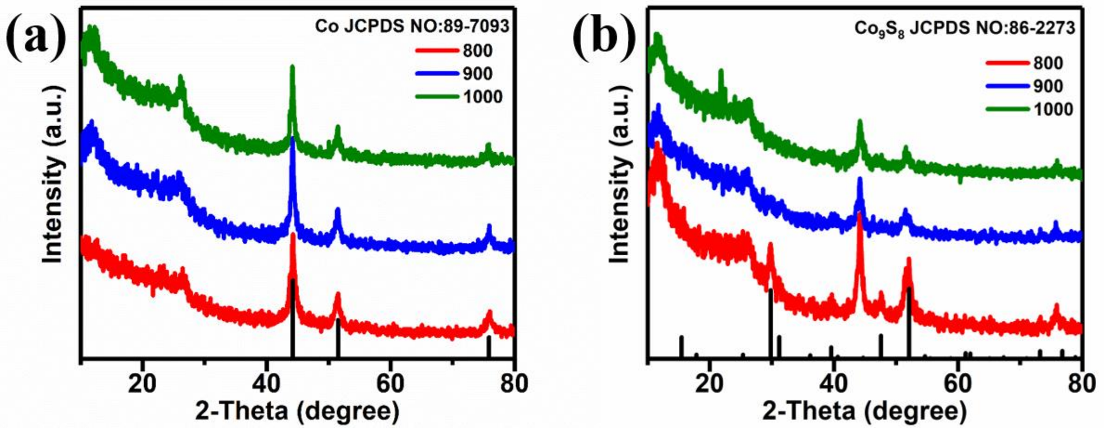

Figure 2.36. a) XRD patterns of samples after acid wash. b) XRD patterns of sulfurized samples after acid wash.

The electrochemical performance of CSNCF-X-aw was tested (**Figure 2.37**). Among all the samples, CSNCF-900-aw delivered the highest initial specific capacity of 1090 mA h g^{-1}. Others only had an initial specific capacity of around 800 mA h g^{-1}. The high specific capacity of CSNCF-900-aw could result from a compromise of higher conductivity at higher temperature and more residual Co, which has also been reported to have absorption ability towards LPSs, after acid wash at lower temperature. A specific capacity of 478 mA h g^{-1} could be maintained when the current density increased to 2 C (Figure 2.37e). After 200 cycles at 1 C, CSNCF-900-aw delivered a specific capacity of 378 mA h g^{-1} (Figure 2.37f), which is also the highest among all three samples.

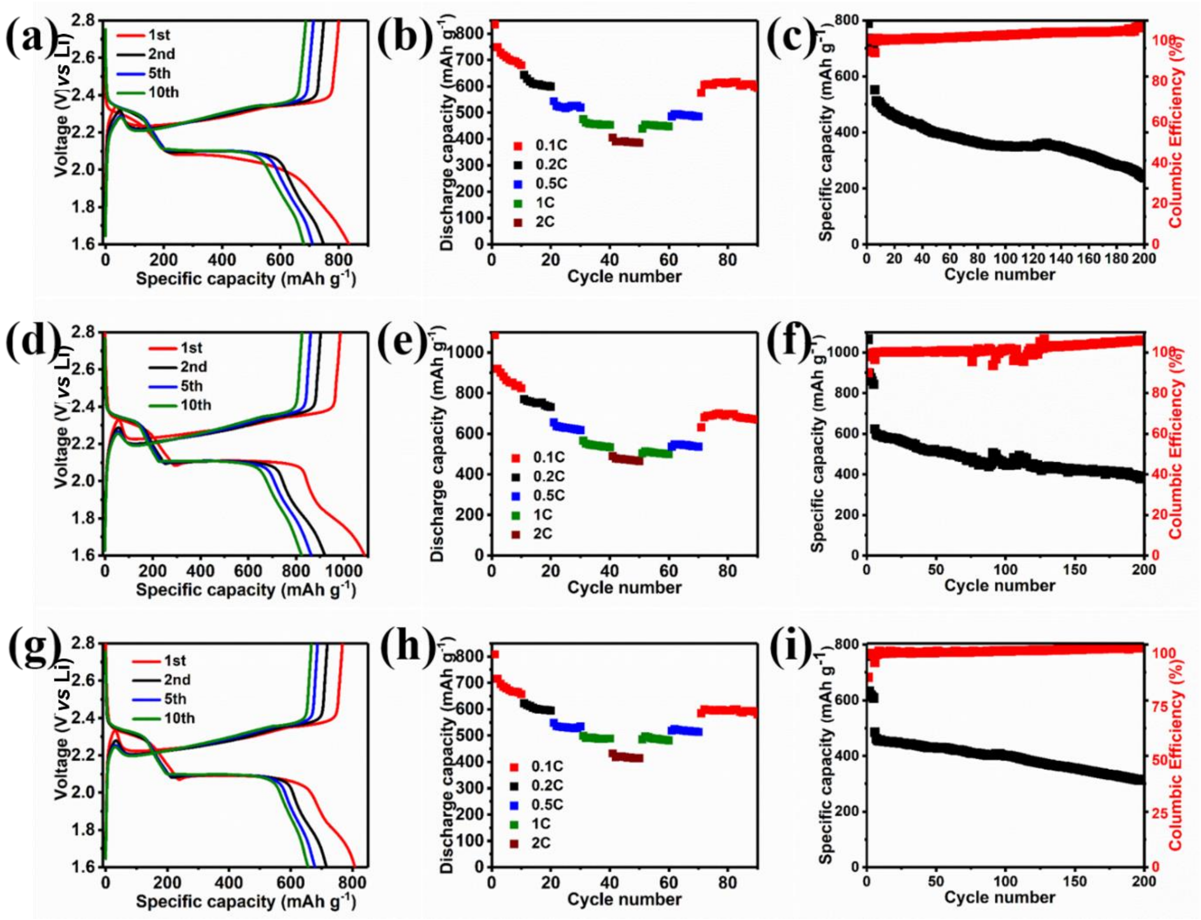

Figure 2.37. Charge-discharge curves at a current density of 0.1 C, rate performance (the current density increased from 0.1 C to 0.2, 0.5, 1 and 2 C and then decreased to 1, 0.5 and 0.1 C step by step) and long cycle stability performance at a current density of 1 C of a-c) CSNCF-800-aw, d-f) CSNCF-900-aw and g-i) CSNCF-1000-aw.

Symmetric cells were assembled with Li_2S_6 catholyte to reveal the reaction process (**Figure 2.38**). For CSNCF-1000 without Li_2S_6 catholyte, no peaks could be observed as no reaction took place. And for CSNCF-1000-aw and NCF-1000, no obvious peak could be observed with Li_2S_6 catholyte. However, for CSNCF-1000 with Li_2S_6 catholyte, a high current of 2 mA could be reached, indicating that cobalt sulphides have high catalyst activity and accelerate the reactions.

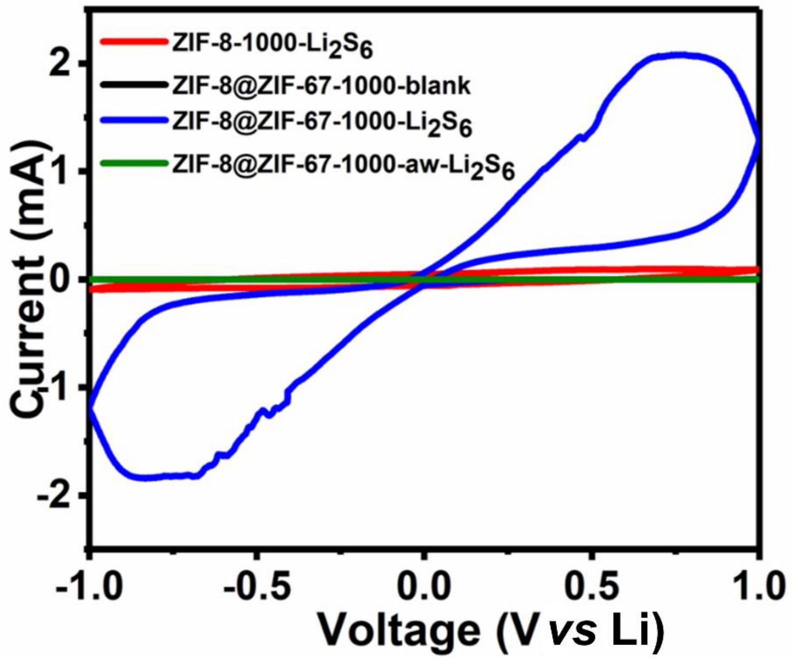

Figure 2.38. CV curves of symmetric cells with Li_2S_6 catholyte.

3.4 Conclusion

This chapter presents the design and synthesis of a hierarchical structure of cobalt sulphides supported on N-doped carbon framework. The ZIF-8 core in ZIF-8@ZIF-67 template prevented ZIF-67 from collapsing and provided higher specific surface area. Graphitized carbon including CNTs formed at high temperature endows high conductivity of the electrode. Cobalt sulphides have strong absorption and catalyst ability to alleviate the shuttle effect. Coin cells with CSNCF-1000 as S host had a high specific capacity of 1313 mA h g^{-1} and a good cyclic stability with 620 mA h g^{-1} maintained after 170 cycles at a current density of 1 C.

3.5 Reference

[1] H. Jiang, X. C. Liu, Y. Wu, Y. Shu, X. Gong, F. S. Ke, H. Deng, *Angew. Chemie - Int. Ed.* **2018**, *57*, 3916.

[2] E. Cha, M. D. Patel, J. Park, J. Hwang, V. Prasad, K. Cho, W. Choi, *Nat. Nanotechnol.* **2018**, DOI 10.1038/s41565-018-0061-y.

[3] S. Liu, J. Li, X. Yan, Q. Su, Y. Lu, J. Qiu, Z. Wang, X. Lin, J. Huang, R. Liu, B. Zheng, L. Chen, R. Fu, D. Wu, *Adv. Mater.* **2018**, *30*, DOI 10.1002/adma.201706895.

[4] S. Liu, J. Li, X. Yan, Q. Su, Y. Lu, J. Qiu, Z. Wang, X. Lin, J. Huang, R. Liu, B. Zheng, L. Chen, R. Fu, D. Wu, *Adv. Mater.* **2018**, *30*, 1.

[5] G. Li, S. Wang, Y. Zhang, M. Li, Z. Chen, J. Lu, *Adv. Mater.* **2018**, *1705590*, 1.

[6] H. Yang, Q. Li, C. Guo, A. Naveed, J. Yang, Y. NuLi, J. Wang, *Chem. Commun.* **2018**, DOI 10.1039/C7CC09942H.

[7] S.-H. Yu, X. Huang, K. Schwarz, R. Huang, T. Arias, J. Brock, H. D. Abruna, *Energy Environ. Sci.* **2017**, DOI 10.1039/C7EE02874A.

[8] B. Li, S. Zhang, B. Wang, Z. Xia, *Energy Environ. Sci.* **2018**, 0.

[9] G. Hu, Z. Sun, C. Shi, R. Fang, J. Chen, P. Hou, C. Liu, H. M. Cheng, F. Li, *Adv. Mater.* **2017**, *29*, 1.

[10] J. Zhou, T. Qian, N. Xu, M. Wang, X. Ni, X. Liu, X. Shen, C. Yan, *Adv. Mater.* **2017**, *29*, 1.

[11] Y. Yamada, O. Kimizuka, K. MacHida, S. Suematsu, K. Tamamitsu, S. Saeki, Y. Yamada, N. Yoshizawa, O. Tanaike, J. Yamashita, F. Don, K. Hata, H. Hatori, *Energy and Fuels* **2010**, *24*, 3373.

[12] H. Kim, J. Lee, H. Ahn, O. Kim, M. J. Park, *Nat. Commun.* **2015**, *6*, DOI 10.1038/ncomms8278.

[13] Y. Liang, Z. Tao, J. Chen, *Adv. Energy Mater.* **2012**, *2*, 742.

[14] J. Schuster, G. He, B. Mandlmeier, T. Yim, K. T. Lee, T. Bein, L. F. Nazar, *Angew. Chemie - Int. Ed.* **2012**, *51*, 3591.

[15] Z. Xiao, Z. Yang, H. Nie, Y. Lu, K. Yang, S. Huang, *J. Mater. Chem. A* **2014**, *2*, 8683.

[16] X. Ji, K. T. Lee, L. F. Nazar, *Nat. Mater.* **2009**, *8*, 500.

[17] W. Xia, V. Hagen, S. Kundu, Y. Wang, C. Somsen, G. Eggeler, G. Sun, G. Grundmeier, M. Stratmann, M. Muhler, *Adv. Mater.* **2007**, *19*, 3648.

[18] M. Li, H. Zhou, W. Yang, L. Chen, Z. Huang, N. Zhang, C. Fu, Y. Kuang, *J. Mater. Chem. A* **2017**, *5*, 1014.

[19] N. Huang, G. Li, H. Huang, P. Sun, T. Xiong, Z. Xia, F. Zheng, J. Xu, X. Sun, *Appl. Surf. Sci.* **2016**, *390*, 847.

[20] C. Li, Z. Xi, D. Guo, X. Chen, L. Yin, *Small* **2018**, *14*, 1.

[21] W. Hou, B. Tang, L. Lu, J. Sun, J. Wang, C. Qin, L. Dai, *RSC Adv.* **2014**, *4*, 4848.

[22] N. Wang, L. Li, D. Zhao, X. Kang, Z. Tang, S. Chen, *Small* **2017**, *13*, 1.

[23] J. Liu, D. Zhu, T. Ling, A. Vasileff, S. Z. Qiao, *Nano Energy* **2017**, *40*, 264.

[24] X. Yao, N. Huang, F. Han, Q. Zhang, H. Wan, J. P. Mwizerwa, C. Wang, X. Xu, *Adv. Energy Mater.* **2017**, *7*, 1.

[25] X. Fang, W. Weng, J. Ren, H. Peng, *Adv. Mater.* **2016**, *28*, 491.

[26] J. Zhang, H. Hu, Z. Li, X. W. Lou, *Angew. Chemie - Int. Ed.* **2016**, *55*, 3982.

[27] G. K. Gao, Y. R. Wang, S. B. Wang, R. X. Yang, Y. Chen, Y. Zhang, C. Jiang, M. J. Wei, H. Ma, Y. Q. Lan, *Angew. Chemie - Int. Ed.* **2021**, *60*, 10147.

[28] X. F. Liu, X. Q. Guo, R. Wang, Q. C. Liu, Z. J. Li, S. Q. Zang, T. C. W. Mak, *J. Mater. Chem. A* **2019**, *7*, 2838.

[29] S. Li, J. Lin, Y. Ding, P. Xu, X. Guo, W. Xiong, D. Y. Wu, Q. Dong, J. Chen, L. Zhang, *ACS Nano* **2021**, *15*, 13803.

[30] P. Chiochan, X. Yu, M. Sawangphruk, A. Manthiram, *Adv. Energy Mater.* **2020**, *10*, 1.

[31] S. Bai, X. Liu, K. Zhu, S. Wu, H. Zhou, *Nat. Energy* **2016**, *1*, DOI 10.1038/nenergy.2016.94.

[32] J. Tang, R. R. Salunkhe, J. Liu, N. L. Torad, M. Imura, **n.d.**, 1.

[33] H. Pang, W. Huang, **2016**, DOI 10.1002/adma.201600319.

Chapter 3

ZIF-derived CoP/Ni_2P supported on N-doped carbon framework as S host for lithium-sulfur batteries

3.1 Introduction

In the last chapter, a core-shell ZIF-8@ZIF-67 template was used to synthesis NCFCS as S host for LSBs. The unique core-shell structure takes the advantages of both ZIF-8 and ZIF-67. The ZIF-8 core provided high surface area and alleviate the collapse of ZIF-67, which is beneficial for S host. [1–6] The ZIF-67 shell provided high conductivity of the material by improving the graphitization level of carbon materials.[7–11] As a result, cells using the as-synthesized NCFCS as S host showed improved electrochemical performance compared with samples prepared from ZIF-8 and ZIF-67. However, the complicated synthesis process and ultrahigh temperature is an obstacle stand in the possible practical application of this material. There are also facile ways to synthesis porous structure from ZIF templates, like water bath, hydrothermal and so on. Meanwhile, there are a variety of other transition metal-based compounds, like transition metal phosphides, that have been used as catalyst in energy related areas including LSBs.[12–15]

In this chapter, CoP/Ni_2P supported on N-doped carbon framework was synthesized from ZIF-67 template through a facile strategy and applied as S host for LSBs. At first, layered-double-hydroxide (LDH) structure was synthesized through alcoholysis of ZIF-67, then the as-synthesized LDHs were phosphating to generate a variety of metal phosphides supported on N-doped carbon frameworks. The metal ions will affect the morphology as well as electrochemical properties of the final products. When used as host of S for LSBs, the MPNCs showed good performance. A high initial specific capacity of over 1200 mA h g^{-1} could be reached at a current density of 0.1 C (1 C = 1675 mA g^{-1}). A good capacity retention could be maintained at high current density of 2 C for 50 cycles with a capacity of 560 mA g^{-1} maintained.

3.2 Experimental section

3.2.1 Materials

Cobalt nitrate hexahydrate, Nickel nitrate hexahydrate, 2-methyl imidazole, $LiNO_3$, sulfur, lithium bis(trifluoromethanesulfonimide) (LiTFSI), N-methyl pyrrolidone (NMP), 1,2-dimethoxyethane (DME) and 1,3-dioxolane (DOL) were purchased from Sigma-Aldrich and used directly. Carbon-coated aluminium foil, Celgard separator, Lithium metal foil and commercial electrolyte for lithium-ion batteries were purchased form MTI company.

3.2.2 Synthesis of ZIF-67

ZIF-67 template was synthesized according to some reports. 5.84 g cobalt nitrate hexahydrate was added into 500 mL methanol and stirred for 30 min to form solution A. 6.40 g 2-metyl imidazole was added into 500 mL methanol and stirred for 30 min to form solution B. Then solution B was added into solution A slowly. After that the mixture was stirred for another 1 hour and aged for 24 hours. Then the solution was centrifuged and washed with methanol for several times to obtain the product, which was then dried at 80 ℃ overnight to obtain ZIF-67 powders.

3.2.3 Synthesis of layered-double-hydroxides (LDHs)

LDHs were synthesized through the alcoholysis of ZIF-67 template. Typically, 400 mg ZIF-67 template was added into 240 mL ethanol and sonicated for half an hour to form a homogeneous solution. A total amount of 1296 mg metal nitrate hexahydrates were added into 120 mL ethanol and stirred for half an hour. Then the solutions were mixed and heated to 85 ℃ under stirring. For sample Co_xNi_{1-x}LDH, x means the mass ratio of cobalt nitrate hexahydrate and 1-x means the mass ratio of nickel nitrate hexahydrate. After refluxing for 1 hour, the solution was centrifuged and washed with ethanol for several times until the color stopped changing. Then the product was dried at 80 ℃ overnight to obtain LDHs powders.

3.2.4 Synthesis of metal phosphides supported on N-doped carbon frameworks

50 mg of the as obtained LDHs were place in a tube furnace with 500 mg sodium hypophosphite was placed in the upstream. The tube was heated to 350 ℃ with a heating rate of 2 ℃/min and kept for 2 hours with argon gas as protecting gas. After cooling down to room temperature, MPNCs could be collected. The tail gas was introduced into $FeCl_3$ aqueous solution to oxidize the PH_3 gas, which is dangerous.

3.2.5 Preparation of electrodes

Co_xP/S composites were first prepared before preparing electrodes. Co_xP s and S were mixed through ball milling in a mass ratio of 1:2. After that, the mixture was transferred into a glass tube and sealed under argon protected atmosphere. Finally, the mixture was heated to 155 ℃ and kept for 24 hours. After cooling down to room temperature, the mixture can be collected for electrode preparation.

Co_xP/S composite, PvDF and Super P were mixed in a mass ratio of 8:1:1 and methyl-2-pyrrolidone (NMP) was used as dispersion solution to prepare a slurry through milling. Then the slurry was coated on carbon-coated aluminium foil through blade coating. The samples were dried at 60 ℃ for hours and then further vacuum dried at 60 ℃ overnight. Finally, the as-prepared electrode was cut into disks with a diameter of 16 mm and transferred into an argon protected glove box for battery assembling.

3.2.6 Characterization

Scanning electron microscopic (SEM) images were taken by a field emission scanning electron microscope (Jeol JSM 6701). Transition electron microscopic (TEM) and energy dispersive spectra (EDS) characterizations were performed on a probe-corrected (CEOS) JEM ARM 200CF (JEOL Japan) operated at 200 keV. X-ray diffraction (XRD) was carried out in a Bruker-Axs D8 X-ray diffractometer. FTIR test was carried out by using a Bruker ALPHA FTIR spectrometer (Platinum-ATR). Raman spectrums were characterized by using a Raman spectrometer (514.5 nm laser Renishaw). X-ray photoemmision spectrum (XPS) were carried out by Al-K-α, thermos fisher scientific.

3.2.7 Electrochemical tests

The electrolyte was prepared by dissolving 1 M lithium bis trifluoromethane sulfonimide (LiTFSI) in a mix solution of 1,2-dimethoxyethane (DME) and 1,3-dioxolane (DOL) (1:1 v/v) with 2 wt% $LiNO_3$ as addictive. The usage of electrolyte was kept at 10 μL/mg (based on S) for all the cells. Lithium foil and Celgard separator were used as anode and separator. Arbin and Neware battery test system were used to test the electrochemical performance of these coin cells.

3.2.8 Absorption test

Li_2S_6 catholyte was prepared in an argon protected glove box. 0.1 mol Li_2S and 0.5 mol S were dissolved in a mix solution of 10 mL DOL and 10 mL DME. The solution was stirred for 24 hours for complete reaction. Then 2 mL of the as-prepared Li_2S_6 catholyte was added into a glass bottle with 5 mg of sample.

3.3 Results and discussion

3.3.1 Morphology and structure of ZIF-67

The morphology of the as-synthesized ZIF-67 nanocrystals was characterized by scanning electron microscope (SEM) and transition electron microscope (TEM). As shown in **Figure 3.1a**, ZIF-67 nanocrystals have a typical rhombic dodecahedron structure. The diameter of the nanocrystals is ~400 nm as can be seen in the high-resolution SEM image (Figure 3.1b).

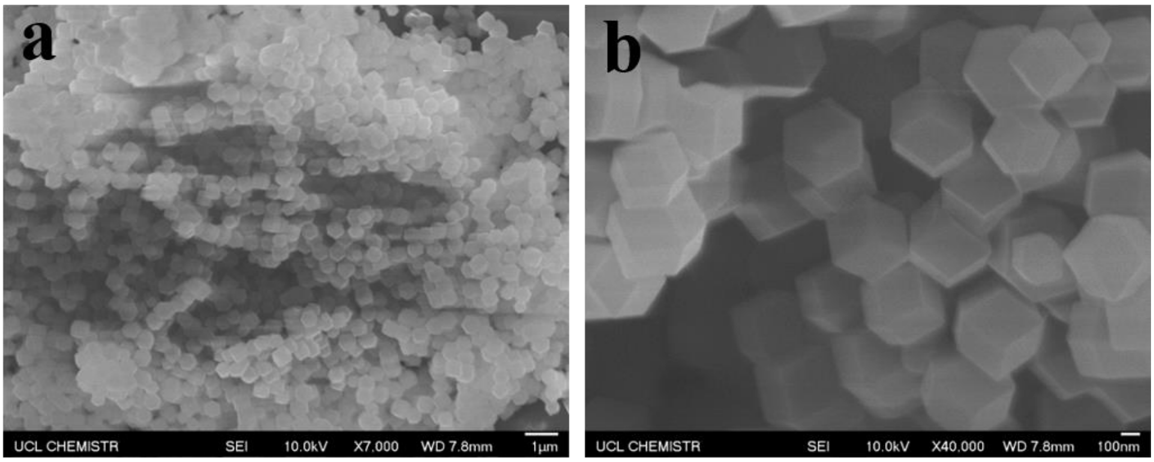

Figure 3.1. Low (a) and high (b) magnification scanning electron microscope (SEM) images of the as-synthesized ZIF-67 nanocrystals.

The micro structure of ZIF-67 nanocrystals was further characterized by TEM (**Figure 3.2**). The size of ZIF-67 nanocrystals was the same as indicated by SEM test, and no mesopores and hollow structure can be seen from the TEM image, indicating that the pristine ZIF-67 nanocrystals was not suitable as host of S in lithium-sulfur batteries.

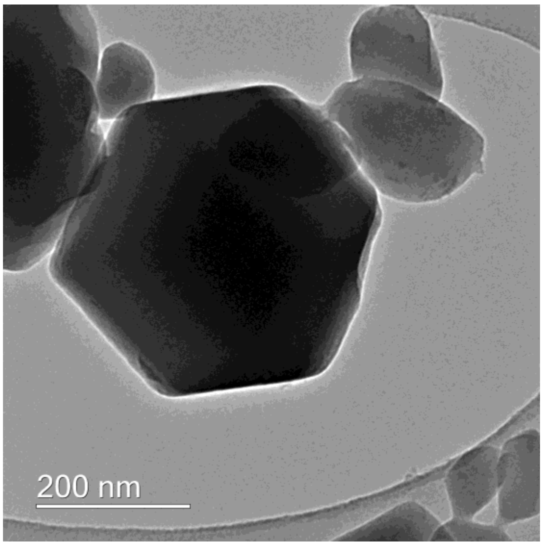

Figure 3.2. Transition electron microscope (TEM) image of the as-synthesized ZIF-67 nanocrystals.

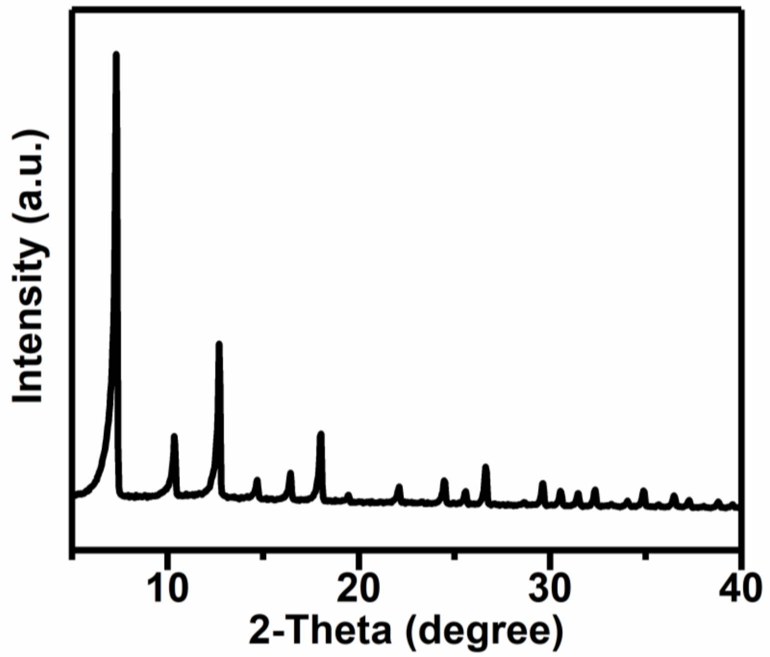

Figure 3.3. X-ray diffraction pattern (XRD) of the as-synthesized ZIF-67 nanocrystals.

The successful synthesis of ZIF-67 nanocrystals was also confirmed by the X-ray diffraction pattern (XRD) as shown in **Figure 3.3**. The peaks at the small angle, which is the characteristic peaks of ZIF materials, indicates the ordered long-range metal ion-linker structure. The asymmetry of the XRD pattern. The lower the peak angle, the higher the asymmetry will be.

It’s because the diffraction cone diameter reduces to zero at zero degree and the smaller the cone, the greater the distortion is at the detector. It’s a function of powder diffraction geometry. Meanwhile, Mo source was used in the XRD test, which means shorter wavelength at lower angle compared with that use Cu source.

After synthesis, ZIF-67 nanocrystals were transferred to Co LDH. ZIF-67 nanocrystals were firstly transferred to Co LDH by mixing ZIF-67 nanocrystals with cobalt nitrate in ethanol solution. During the reaction, the core was etched as the Co^{2+} will alcoholysis and release H^+ in ethanol solution, meanwhile, formed layered cobalt hydroxide will precipitate. At the end, the hollowed Co LDH was synthesized, which can be confirmed by the XRD pattern (**Figure 3.4**). The diffraction peaks at 12.5°, 24.9°, 32.7° and 58.3° correspond to the (003), (006), (012) and (110) crystal planes of typical layered double hydroxide materials.

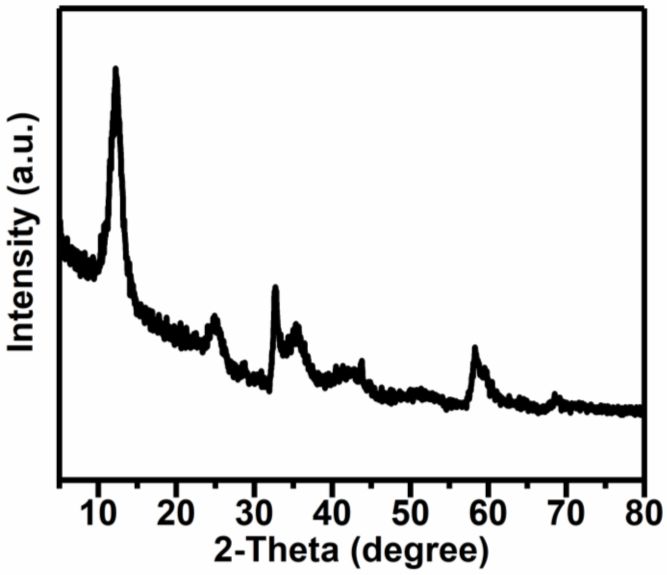

Figure 3.4. XRD pattern of the as-synthesized Co LDH.

The microstructure of Co LDH was characterized by SEM and TEM. SEM images (**Figure 3.5**) showed that the rhombic dodecahedron structure from the ZIF-67 template was kept in Co LDH. However, different from the ZIF-67 nanocrystals, Co LDH has a porous structure. Cobalt hydroxide layers randomly stacked to form the walls of the nano cages, and the core of ZIF-67 nanocrystals was totally removed. The nano cage structure was further confirmed by TEM images (**Figure 3.6**). As seen from the high-resolution TEM image (Figure 3.6b), there are many micro pores in the layer.

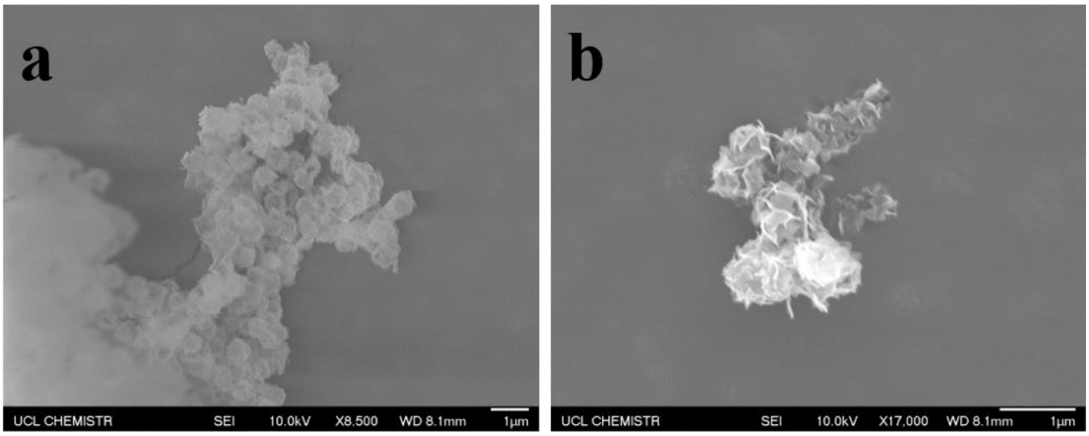

Figure 3.5. Low- and high-resolution SEM images of Co LDH.

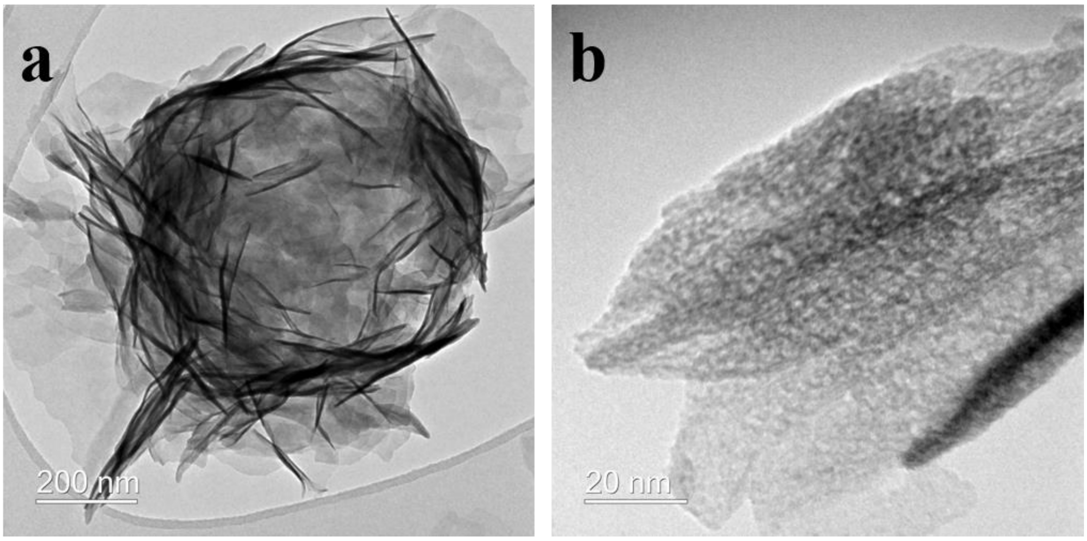

Figure 3.6. Low- and high-resolution TEM images of Co LDH.

The chemical composition of Co LDH was studied by X-ray photoelectron spectroscopy (XPS). As can be seen from **Figure 3.7**, the peaks of Co and O at around 782 and 532 eV should be from the cobalt hydroxide, while the peaks of C and N at around 285 and 406 eV should be from linkers of ZIF-67 template. This indicates that not all the linkers of ZIF-67 are removed during the synthesis.

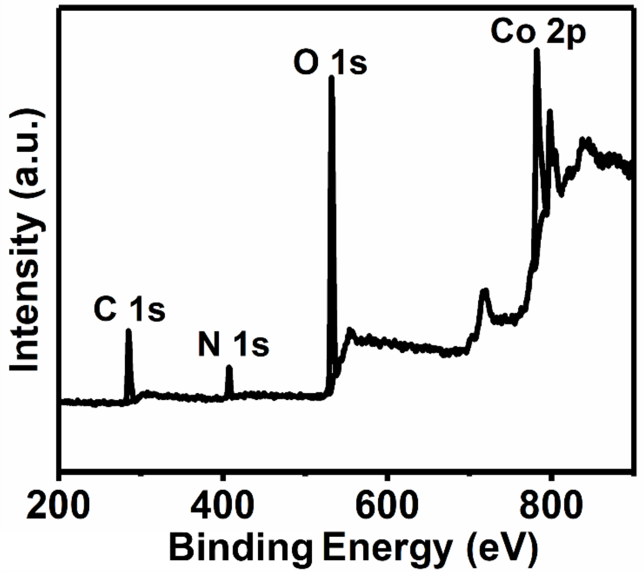

Figure 3.7. X-ray photoelectron spectroscopy (XPS) of Co LDH.

Finally, CoP was synthesized by heating Co LDH with NaH_2PO_2 under N_2 atmosphere. PH_3 derived from NaH_2PO_2 at high temperature will react with Co LDH to form CoP, while the nano cage structure of Co LDH will be maintained.

At first, the morphology and structure of the as-synthesized CoP nano cages was characterized by SEM. The rhombic dodecahedron structure of the ZIF-67 template was still kept, while the walls of the nano cage are made of CoP nanoparticles (**Figure 3.8**), the size of these CoP nano cages are also ~400 nm. And as can be seen from the high-resolution SEM image, the walls are like wrinkled papers, which should enable high surface area.

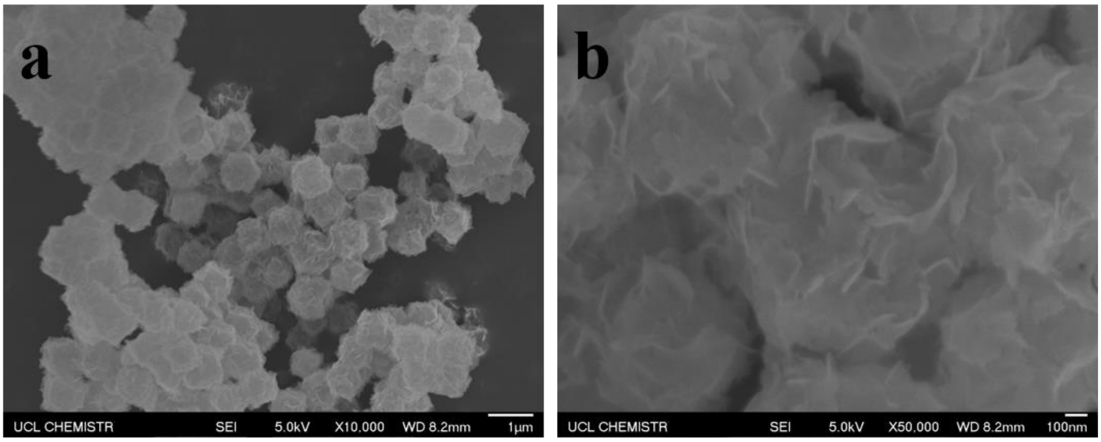

Figure 3.8. Low (a) and high (b) resolution SEM images of CoP nano cages.

TEM images (**Figure 3.9**) further revealed the microstructure of CoP nano cages. As can be seen, small CoP nanoparticle firstly formed thin sheets, which has lots of in plane pores. Then these sheets stack to form the walls of the nano cages with hollow structure. This structure has several advantages over the pristine ZIF-67 template. First, the hollow structure derived from Co LDH is suitable for hosting S and accommodating the volume change of S during charge and discharge, which is extremely different from the ZIF-67 template. Second, CoP nanoparticles uniformly distributed on the walls with a size of tens of nanometers. These CoP nanoparticles provide plenty of absorption sites of lithium polysulfide. Further, the porous structure will provide channels for electrolyte and ions diffusion, which is beneficial for lithium-sulfur batteries.

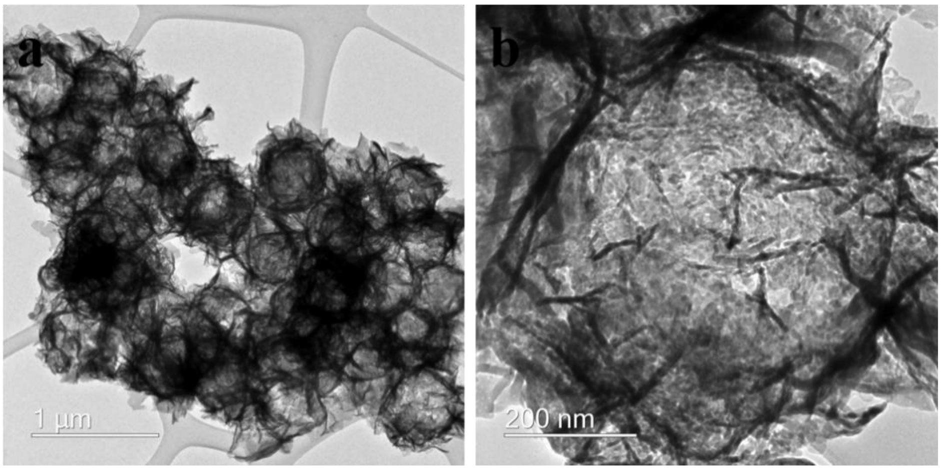

Figure 3.9. Low (a) and high (b) resolution TEM images of CoP nano cages.

XRD pattern (**Figure 3.10**) also confirmed the successful synthesis of CoP. The diffraction peaks at 31.6°, 36.3°, 46.2°, 48.1° and 56.0° corresponding to the (011), (111), (112), (211) and

(020) crystal planes of CoP. It is worth mentioning that the broad peak at around 10° indicates the existence of carbon in this material.

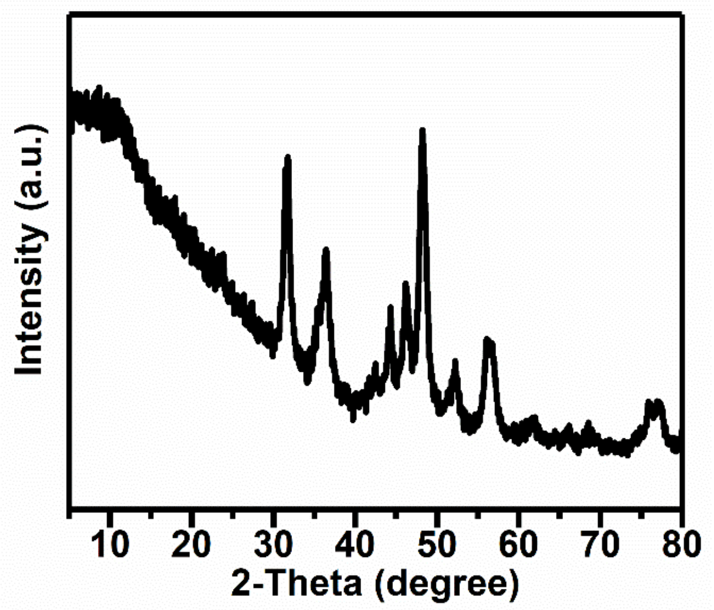

Figure 3.10. XRD pattern of CoP nano cages.

XPS test was conducted to further reveal the chemical composition of CoP nano cages (**Figure 3.11**). Except from carbon cobalt and phosphite, oxygen and nitrogen were also detected from this sample. Nitrogen should be derived from the linkers (2-methyl imidazole) of ZIF-67 template, while oxygen may have two resources. First, there should be a lot of oxygen in Co LDH, which may still exist in CoP nano cages. Second, CoP may be oxidized when exposed to air during the experiment, which is very common in transition metal phosphide materials.

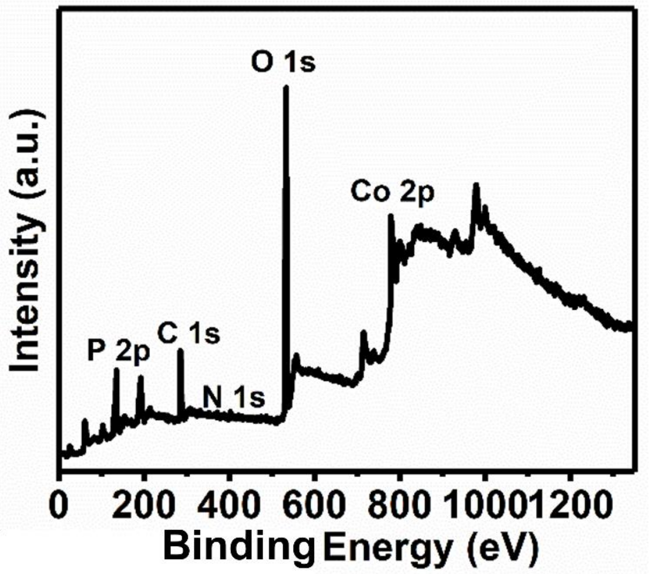

Figure 3.11. XPS spectrum of CoP nano cages.

High resolution spectrum of Co and P are further studied to study the composition of this material. As shown in **Figure 3.12a**, the peak at around 130 eV is ascribed to the P 2p in CoP, while the peaks at around 134.5 eV indicates the existence of phosphorus species with higher valence, or to put it another way, oxidized phosphorus. The high-resolution Co 2p can be deconvoluted into several peaks at around 789 and 782 eV, corresponding to CoP and oxidized cobalt, respectively. Above all, the oxidization of CoP nano cages was confirmed, and the oxidized surface should enhance the performance of this material according to earlier research. As reported, when exposed to lithium polysulfide, the Co-O-P bond will break, then Co-S-S-Li and Li-O-P bond will form, resulting in strong chemical absorption.

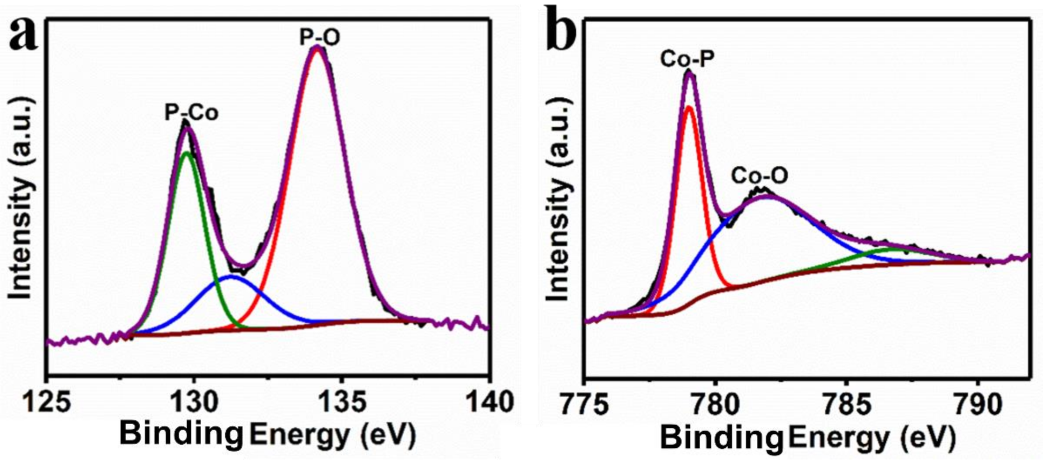

Figure 3.12. High resolution XPS spectrum of P (a) and Co (b) of CoP nano cages.

Finally, S/CoP was prepared through a melt-diffusion process. At 155 ^{o}C, sulfur has the lowest viscosity, thus will infiltrate into the pores by capillarity. The successful loading of S was confirmed by TEM image (**Figure 3.13**) of S/CoP composite. As shown, the surface of S/CoP composite is rough, and the gap between the CoP sheets is filled with sulfur. However, in some cases, the structure of CoP nano cages was broken, only sulfur covering the CoP sheets was detected (Figure 3.13b). This may be ascribed to the low mechanical strength of CoP nano cages. The nano cages could be destroyed during the hand milling or the heating process when preparing S/CoP composite.

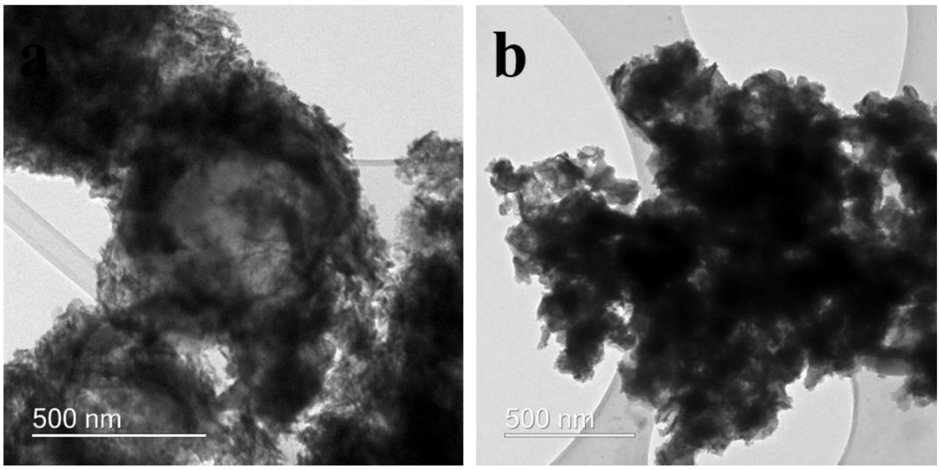

Figure 3.13. TEM images of S/CoP composite.

Before testing the electrochemical properties of S/CoP composite, the sulfur content in this composite was tested by thermogravimetry analysis (TGA). As testing in Ar atmosphere, only S evaporate at high temperature and carbon framework and CoP will maintain. As shown in **Figure 3.14**, the weight percentage of S in S/CoP composite is around 67%.

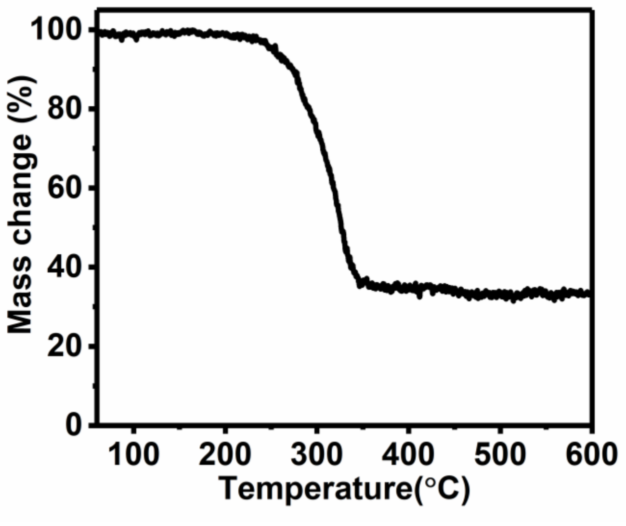

Figure 3.14. Thermogravimetry curves of S/CoP composite.

3.3.2 Electrochemical tests

The electrochemical properties were tested by assembling coin cells using S/CoP and lithium foil as working electrode and counter electrode, respectively. The cyclic voltammetry (CV) curves of S/CoP (**Figure 3.15**) show typical peaks of lithium-sulfur batteries. The two reduction peaks at 2.04 and 2.31 V are known for the electrochemical transformation of soluble long-chain lithium polysulfide to short-chain lithium polysulfide and further to insoluble lithium sulfide (Li_2S_2 and Li_2S). While in the charge process, the oxidation peak at 2.40 V arises from the conversion of Li_2S_2 and Li_2S to Li_2S_8 and then to S. It is also worth mentioning that the potential of the lower reduction peak is relatively higher than that of the pure sulfur sample, which indicates that CoP may have some catalyst activity towards lithium-sulfur batteries. The higher reduction voltage results in a lower over potential during charge and discharge, which means a higher efficiency of the whole battery.

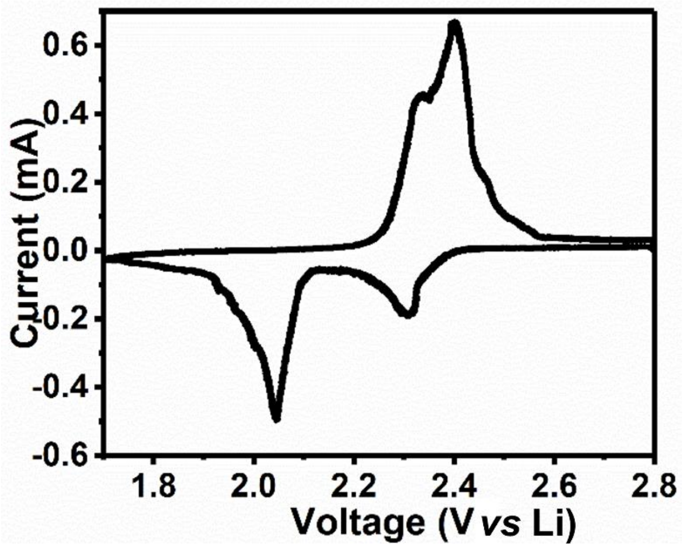

Figure 3.15. Cyclic voltammetry (CV) curve of S/CoP composite.

The charge-discharge properties were tested as shown in **Figure 3.16**. The S/CoP composite was tested at a current density of 0.1 C (1 C = 1675 mA h g^{-1}) at the beginning. The two discharge voltage platform at 2.35 and 2.09 V match well with the two reduction peaks of CV test. The capacity of the higher discharge platform is 300 mA h g^{-1}, which is lower than the theoretical capacity of 419 mA h g^{-1}. Since the second cycle, the discharge and charge curves become stable.

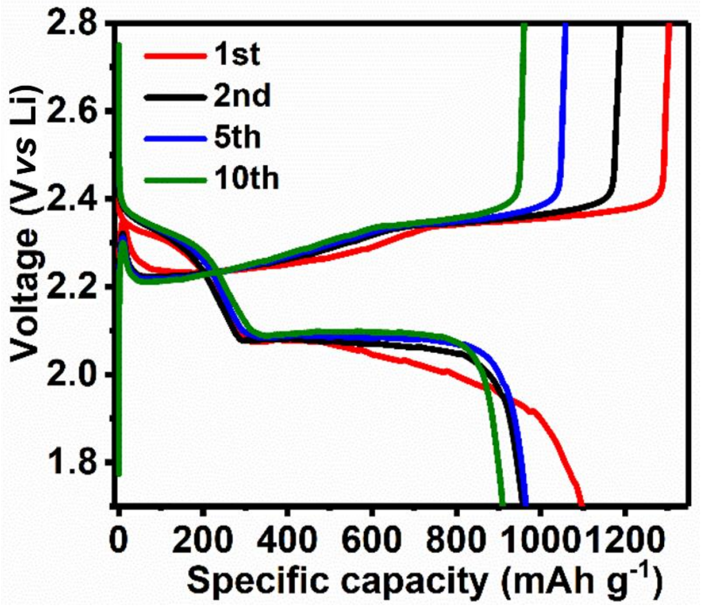

Figure 3.16. Charge-discharge curves of S/CoP composite at a current density of 0.1 C.

The rate performance of S/CoP composite was tested at different current density (**Figure 3.17**). The current density first rose from 0.1 C to 0.2, 0.5, 1, 2 and 5 C, and then went back to 0.1 C. As the current density rise, the discharge capacity goes down to 995, 808, 558, 392, 270 and 90 mA h g^{-1} at 0.1, 0.2, 0.5, 1, 2 and 5 C, respectively. When the current density goes back to 0.1 C, a discharge capacity of 735 mA h g^{-1} was maintained, resulting in a capacity retention of 74%.

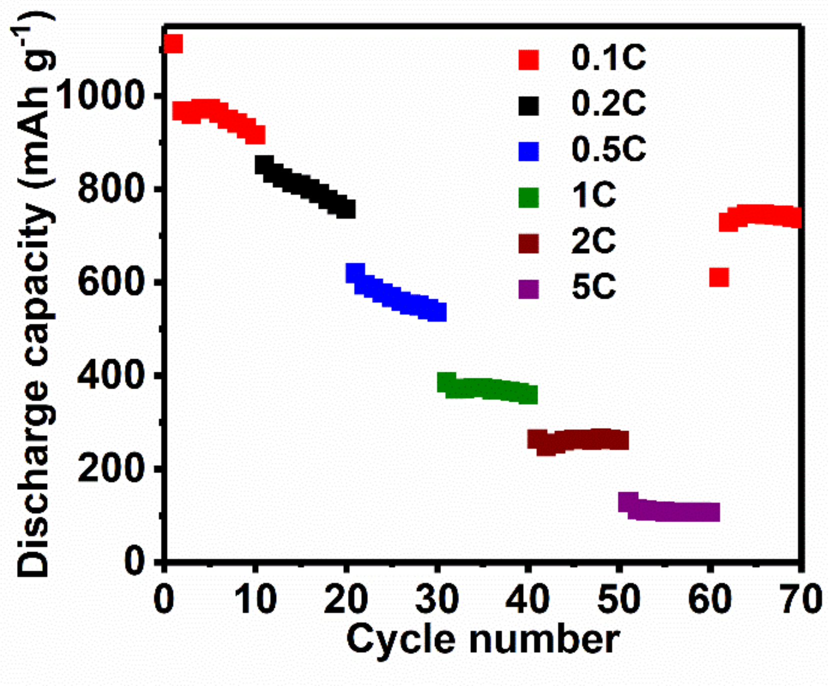

Figure 3.17. Rate performance of S/CoP composite. The current density increased from 0.1 C to 0.2, 0.5, 1 and 2 C and then decreased to 1, 0.5 and 0.1 C step by step.

Furthermore, the cyclic stability of S/CoP composite was tested at a high current density of 5 C as shown in **Figure 3.18**. After the first cycle, the discharge capacity slowly drops from 130 mA h g^{-1} to about 100 mA h g^{-1} in the first 100 cycles. After the first 100 cycles, the discharge capacity becomes stable in the following 200 cycles. However, after 300 cycles, the discharge capacity drops dramatically to lower than 20 mA h g^{-1} over 1000 cycles. This could be explained by the fact that many CoP nano cages were broken during the hand milling process to prepare S/CoP composite, which can be seen from TEM images of Figure 23. As the CoP nano cages broke, the host of sulfur and the physical confinement of lithium polysulfide may be gone. As a result, more lithium polysulfide will dissolve in the electrolyte, and react with sulfur or lithium to form long or short-chain lithium polysulfide, resulting in a worse shuttle effect.

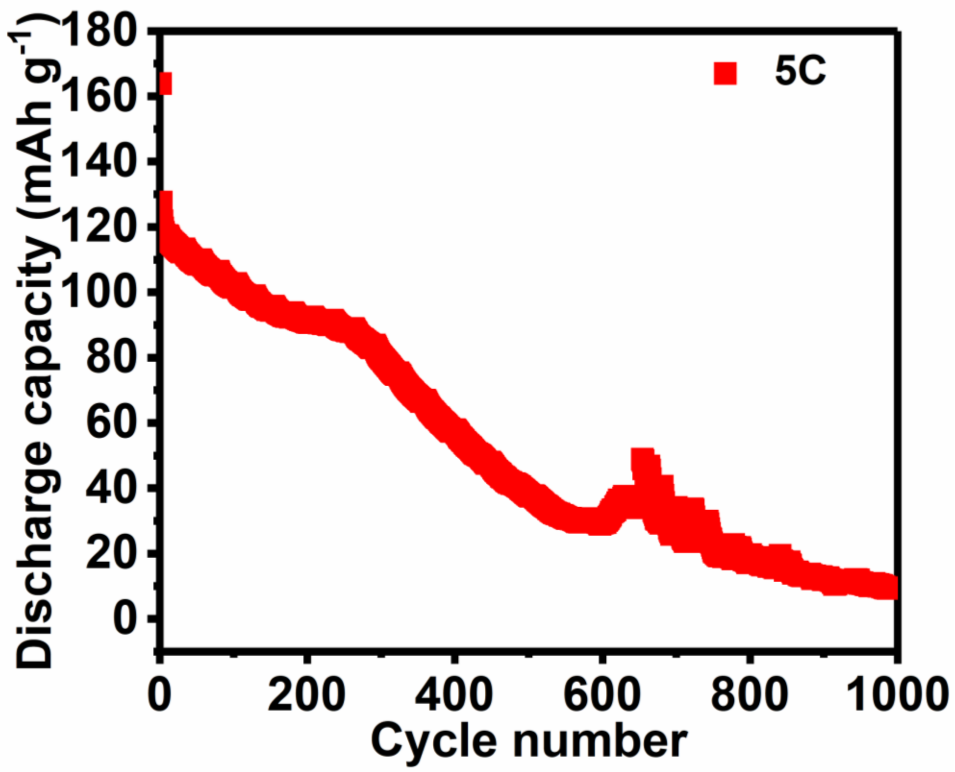

Figure 3.18. Cyclic stability of S/CoP composite tested at high current density of 5 C.

An absorption test was conducted to confirm the chemical absorption of lithium polysulfide by CoP. At first, Li_2S_6, one kind of lithium polysulfide formed in lithium-sulfur batteries, solution at a concentration of 5 mM was prepared by dissolving Li_2S and S in DOL/DME mixture in the glove box, then CoP nano cages was added to this solution and rested for 24 hours. As can be seen from **Figure 3.19**, the as-prepared Li_2S_6 solution showed a pale-yellow colour at the beginning and became more and more clear after adding CoP nano cages. After one day, the solution became almost colourless. This test indicates that the as-synthesized CoP nano cages have a good chemical absorption of lithium polysulfide. Pure carbon materials like carbon black have very limited absorption ability towards LPSs (**Figure 3.20**) as reported by Ji *et al*.[16]

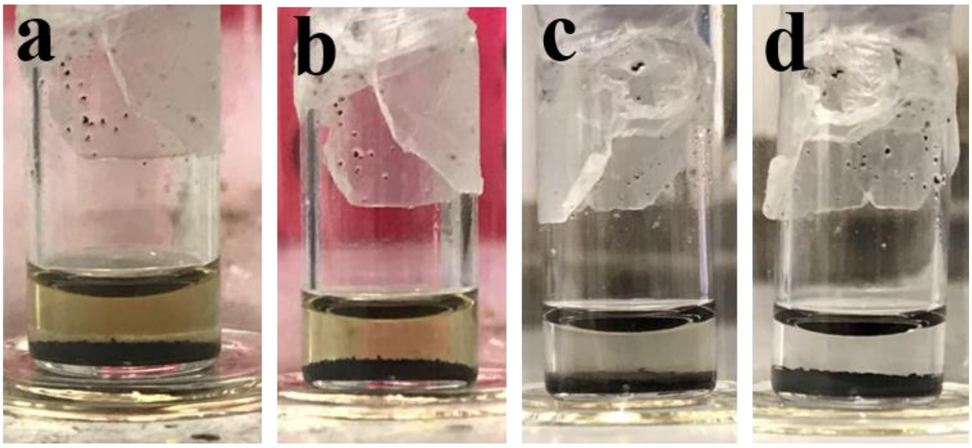

Figure 3.19. Optical photographs of Li_2S_6 after adding CoP nano cages for (a) 0 hour, (b) 1 hour, (c) 5 hours and (d) one day.

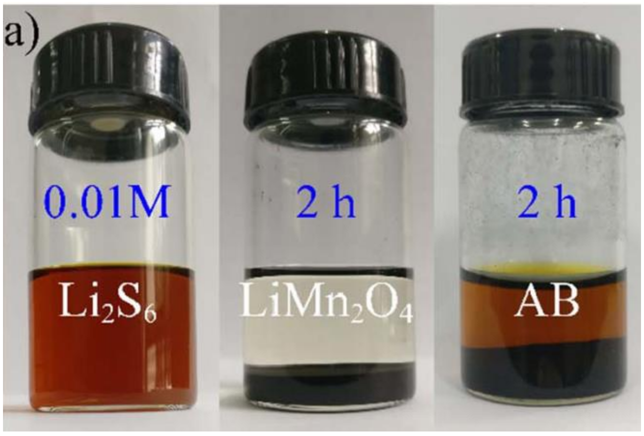

Figure 3.20. Photograph of Li_2S_6 solution with $LiMn_2O_4$ and acetylene black.[16]

Above all, CoP nano cages have been successfully synthesized and applied as host of S in lithium-sulfur batteries. The nano cage structure is able to provide physical confinement of lithium polysulfide and accommodate the volume change of sulfur during charge and discharge. The CoP nano particles on the walls of the nano cage provide abundant chemical absorption sites for lithium polysulfide. However, the stability of this material is not good enough, which can be ascribed to the weak mechanical strength of CoP nano cages. These nano cages may break down in the handing milling process of preparing S/CoP composite.

Two strategies are proposed to prepare a much more stable structure for better performance. First, lower the temperature in synthesizing the CoP nano cages, as high temperature may break the structure. Second, introducing Ni ion in Co LDH to synthesis a more stable structure.

At first, Co LDH and NaH_2PO_2 were heated at different temperature from 200 ℃ to 250 ℃, 275 ℃ and 300 ℃. As proved by XRD patterns (**Figure 3.21**), at a temperature higher than 275 ℃, CoP was successfully synthesized, while at a temperature lower than 275 ℃, Co_3O_4 was the final product. As can be seen in Figure 3.20a, the peaks of the sample prepared at 200 ℃ matches well with those of Co_3O_4, with peaks at 19.0^o, 32.3^o, 38.8^o. 44.8^o, 59.4^o and 65.2^o correspond to the (111), (220), (311), (400), (511) and (440) crystal planes of Co_3O_4. When the temperature rose to 250 ℃, the peaks do not shift, which indicates the same product, but the intensity increases, and the peaks become narrower and sharper. For the sample prepared at 275 ℃, the peaks at 31.6^o, 36.3^o, 46.2^o. 48.1^o, 52.3^o and 56.8^o correspond to the (011), (111), (112), (211), (103) and (301) crystal planes of CoP. The same peaks were detected when the temperature went up to 300 ℃ suggesting that CoP could be synthesized when the temperature is higher than 275 ℃.

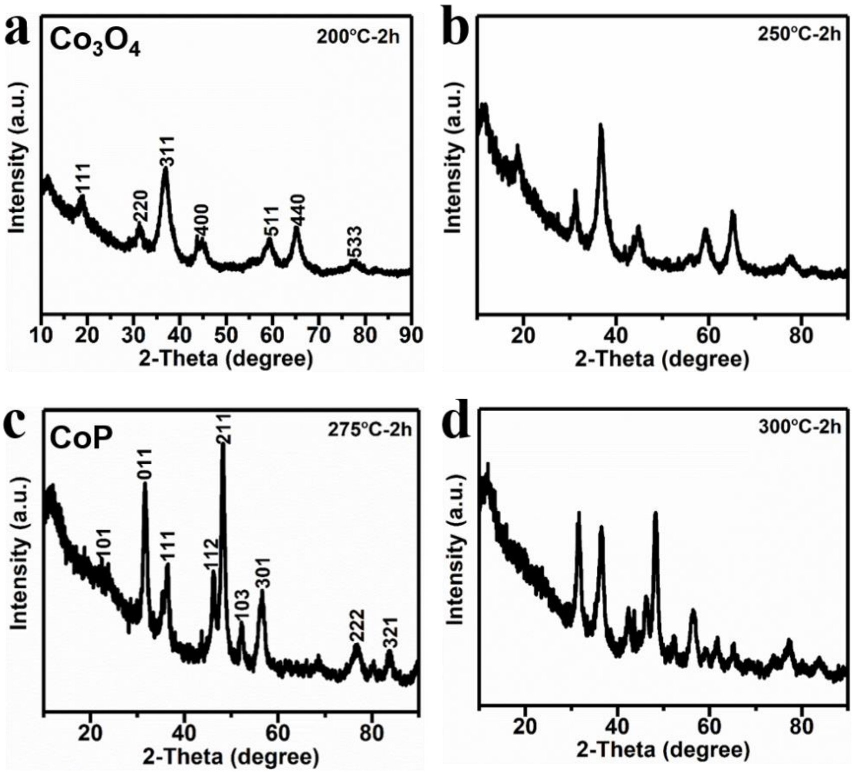

Figure 3.21. XRD patterns of samples prepared at different temperatures: (a) 200 ^oC, (b) 250 ^oC, (c) 275 ^oC and (d) 300 ^oC.

After that, Co Ni LDH with different ratios of Co and Ni were synthesized. During the synthesis, different mass ratio of cobalt nitrate hexahydrate and nickel nitrate hexahydrate were added, while the total mass of the metal nitrate was kept at 540 mg, for example, to synthesize $Co_{0.25}Ni_{0.75}$ LDH, 135 mg cobalt nitrate hexahydrate and 405 mg nickel hexahydrate were added. In total, Co, $Co_{0.75}Ni_{0.25}$, $Co_{0.5}Ni_{0.5}$, $Co_{0.25}Ni_{0.75}$, and Ni LDH were synthesized. However, in the following discussion, $Co_{0.25}Ni_{0.75}$ LDH is used as a representative sample. Same as Co LDH, in the XRD pattern of $Co_{0.25}Ni_{0.75}$ LDH (**Figure 3.22**), the diffraction peaks at 12.5°, 32.7° and 58.3° correspond to the (003), (012) and (110) crystal planes of typical layered double hydroxide materials.

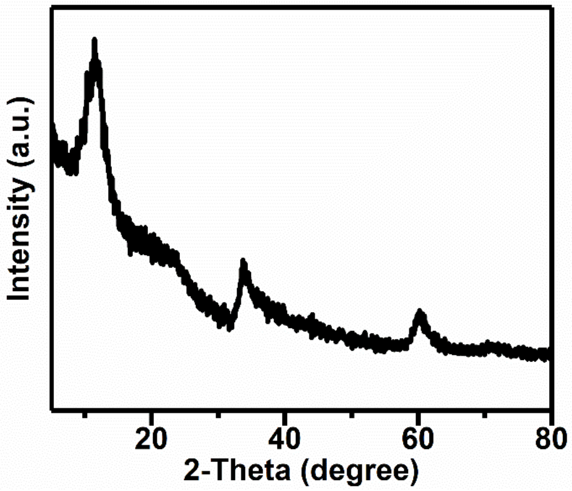

Figure 3.22. XRD patterns of $Co_{0.25}Ni_{0.75}$ LDH.

The microstructure of as-synthesized Co_xNi_{1-x} ($0 \leq x \leq 1$) LDH was characterized by SEM (Figure **3.23**). As can be seen, all the samples showed a polyhedron cage structure with lots of nano sheets stacked to form the walls. As the mass ratio of nickel nitrate increases, more and more nano sheets were synthesized. This can be explained that nickel nitrate has high alcoholysis rate and provides more nucleation site that more nano sheets will form.

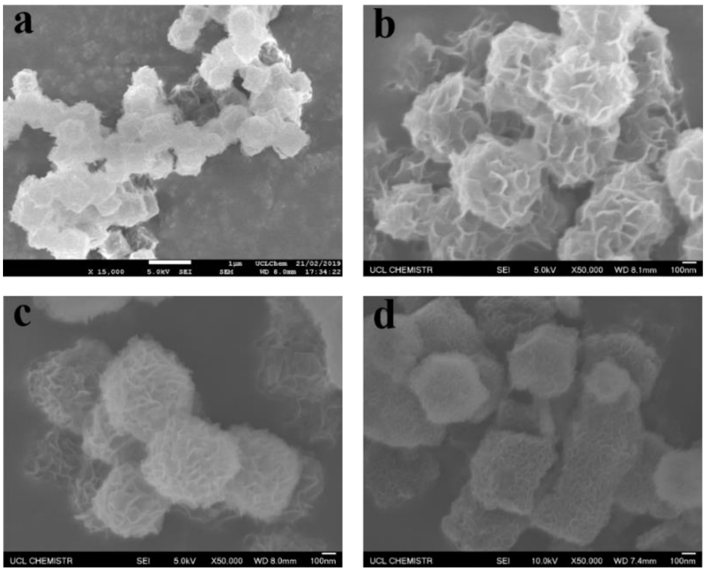

Figure 3.23. SEM images of the as-synthesized Co_xNi_{1-x} ($0 \leq x \leq 1$) LDH sample. (a) $Co_{0.75}Ni_{0.25}$ LDH, (b) $Co_{0.5}Ni_{0.5}$ LDH, (c) $Co_{0.25}Ni_{0.75}$ LDH, (d) Co_0 LDH.

The microstructure of the as-synthesized Co_xNi_{1-x} LDH was further characterized by TEM (**Figure 3.24**). The contrast between the walls and the inner space clearly shows the nano cage structure. The high-resolution TEM image (**Figure 3.25**) shows that the walls are made of wrinkled nano sheets, which may provide high specific surface area of this material.

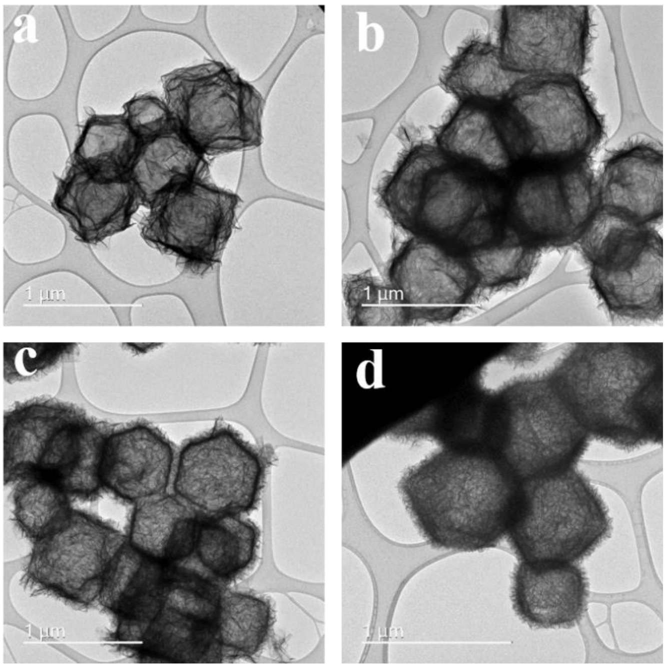

Figure 3.24. Low resolution TEM images of the as-synthesized Co_xNi_{1-x} ($0 \leq x \leq 1$) LDH sample. (a) $Co_{0.75}Ni_{0.25}$ LDH, (b) $Co_{0.5}Ni_{0.5}$ LDH, (c) $Co_{0.25}Ni_{0.75}$ LDH, (d) Co_0 LDH.

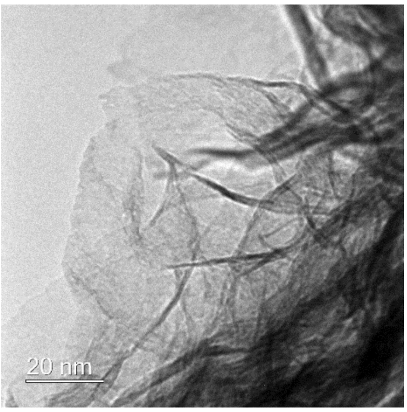

Figure 3.25. High resolution TEM image $Co_{0.25}Ni_{0.75}$ LDH.

After synthesizing Co_xNi_{1-x} ($0 \le x \le 1$) LDH, $Co_xNi_{1-x}P$ samples were prepared by the same procedure as mentioned above, except that the temperature was set at 275 ^{o}C instead of 350 ^{o}C. The morphology of CoP nano cages prepared at 275 ^{o}C (**Figure 3.26**) shows no obvious difference with that prepared at 350 ^{o}C. While in the case of $Co_{0.25}Ni_{0.75}P$ prepared at 275 ^{o}C, the morphology is much different. More nano sheets are formed compared with CoP, which is the same as $Co_{0.25}Ni_{0.75}$ LDH and Co LDH. As mentioned above, the introduction of Ni^{2+} in Co LDH results in more nano sheets, which convert to $Co_xNi_{1-x}P$ nano sheets in the $Co_xNi_{1-x}P$ nano cages. More nano sheets assembled into thicker walls of the nano cages, and a much more stable polyhedrons structure was maintained.

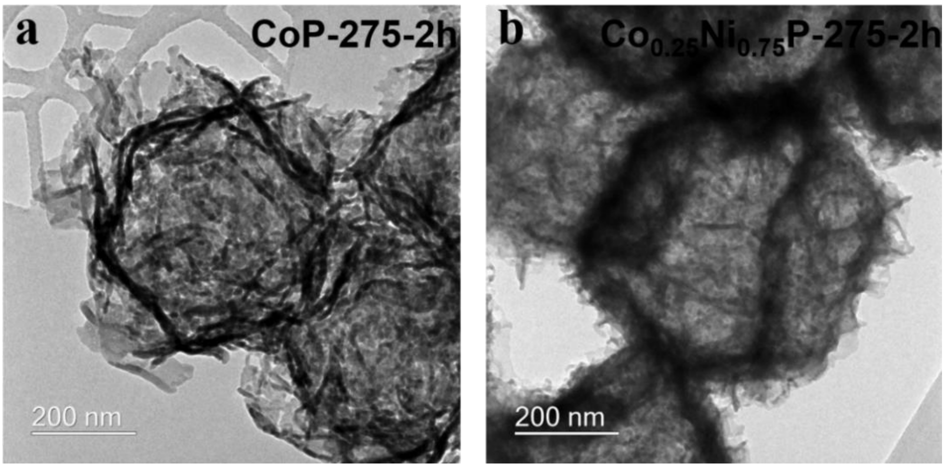

Figure 3.26. TEM images of the as-synthesized (a) CoP and (b) $Co_{0.25}Ni_{0.75}P$.

Samples prepared with different ratio of Ni^{2+} were all characterized by TEM (**Figure 3.27**) to see how Ni^{2+} affected the morphology of the products. As shown in Figure 3.26, with the increase of Ni^{2+}, the shell became thicker and thicker. For $Co_{0.75}Ni_{0.25}P$, $Co_{0.5}Ni_{0.5}P$, and $Co_{0.25}Ni_{0.75}P$, the surface of the shell is porous similar to those LDHs structure. However, for Co_0P, the no porous or layer structure could be seen, which leads to lower surface area. The BET tests of these samples also reveal the same results (**Figure 3.28**). With the increase in Ni ratio, LDHs showed an increase in the specific surface area from 113.6 m^2/g for Co LDH to 183.5 m^2/g for Ni LDH. However, in $Co_xNi_{1-x}P$, the specific surface area decreased (64.6 m^2/g for CoP and 6.5 m^2/g for Co_oP) as the ratio of Ni increased.

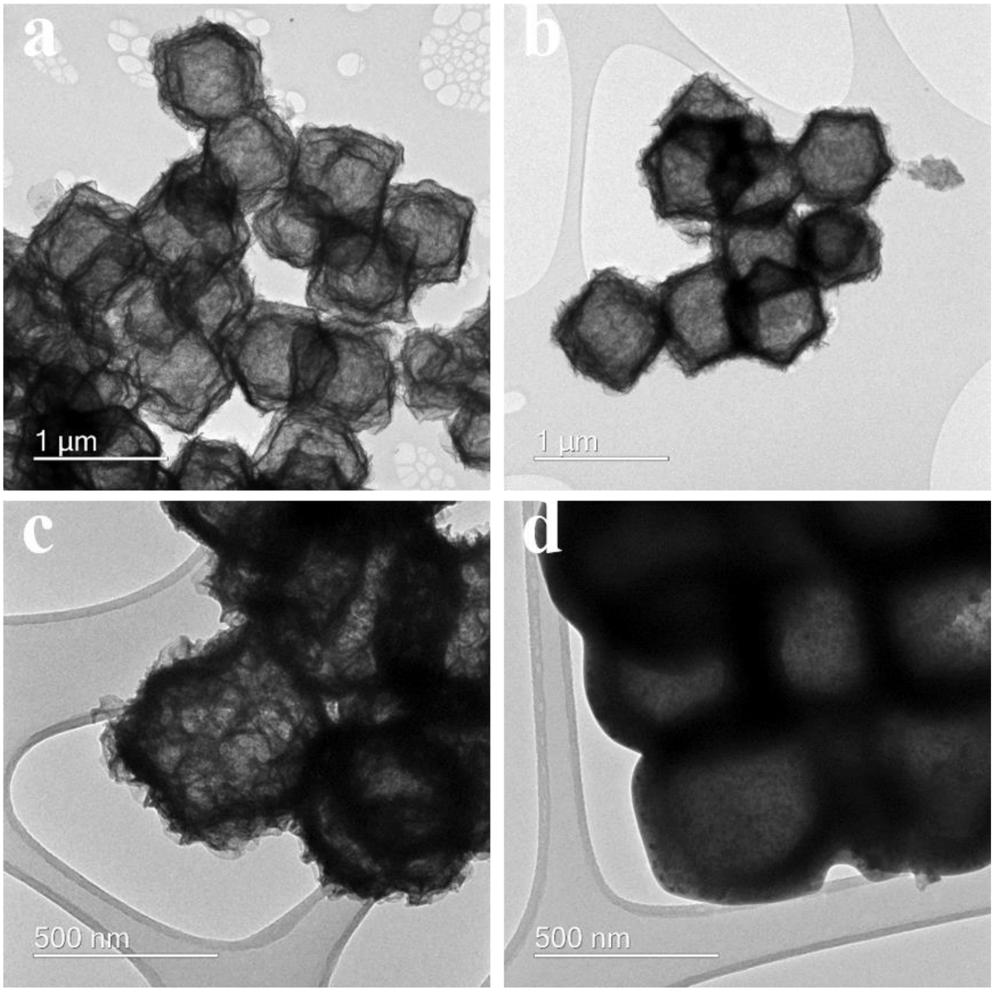

Figure 3.27. TEM images of the as-synthesized $Co_xNi_{1-x}P$ ($0 \le x \le 1$). (a) $Co_{0.75}Ni_{0.25}P$, (b) $Co_{0.5}Ni_{0.5}P$, (c) $Co_{0.25}Ni_{0.75}P$, (d) Co_0P.

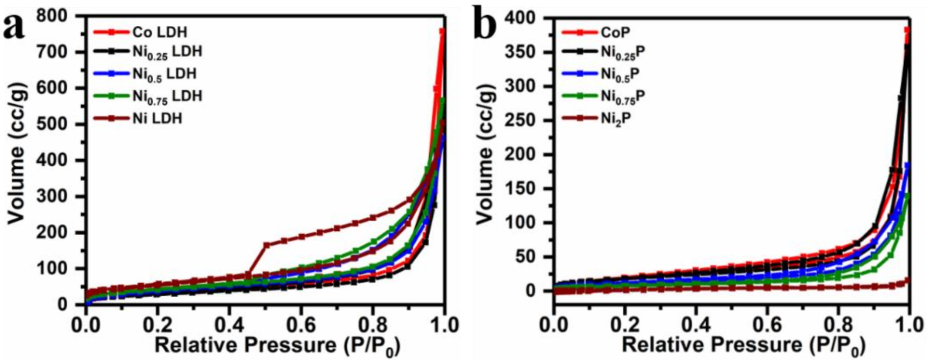

Figure 3.28. BET results of Co_xNi_{1-x} LDHs and $Co_xNi_{1-x}P$ ($0 \leq x \leq 1$).

XPS spectrum (**Figure 3.29**) also confirms the successful introduce of Ni^{2+} into Co LDH, and the more nickel nitrate used in the synthesis process, the higher ratio of Ni/Co obtained. The XRD patterns (**Figure 3.30**) of the as-synthesized $Co_xNi_{1-x}P$ nano cages also show an increase in the content of Ni_2P with more nickel nitrate. As more nickel nitrate was added, the peaks at 31.6° and 36.3°, corresponding to the (011) and (111) crystal planes of CoP, become more and more broad and weak, while the peaks at 40.8°, 44.6° and 54.2°, corresponding to the (111), (201) and (300) crystal planes of Ni_2P, become more and more sharp and strong.

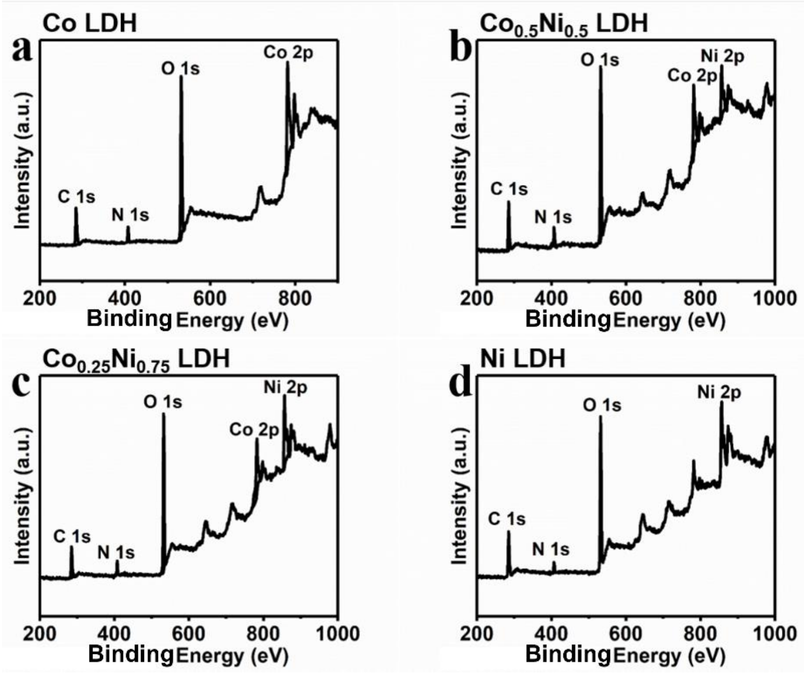

Figure 3.29. XPS spectrum of the as-prepared Co_xNi_{1-x} LDH: (a) Co LDH, (b) $Co_{0.5}Ni_{0.5}$ LDH, (c) $Co_{0.25}Ni_{0.75}$ LDH and (d) Co_0 LDH (or Ni LDH).

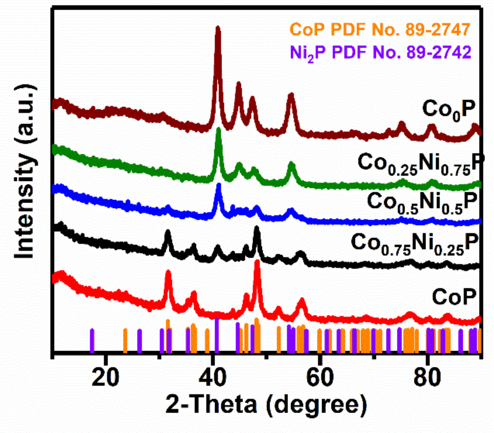

Figure 3.30. XRD patterns of the as-prepared Co$_x$Ni$_{1-x}$P nano cages.

Coin cells using the as-synthesized Co$_x$Ni$_{1-x}$P nano cages and Li foil as S host and anode were assembled to find out the relationship between Ni content and the electrochemical performance. CV curves of samples with different level of Ni content showed similar peaks as shown in **Figure 3.31**. All the samples showed typical peaks of LSBs: two distinguish peaks during the discharge process and one peak during the charge process; notably as the scan rate increased, the peaks shifted to both sides due to polarization.

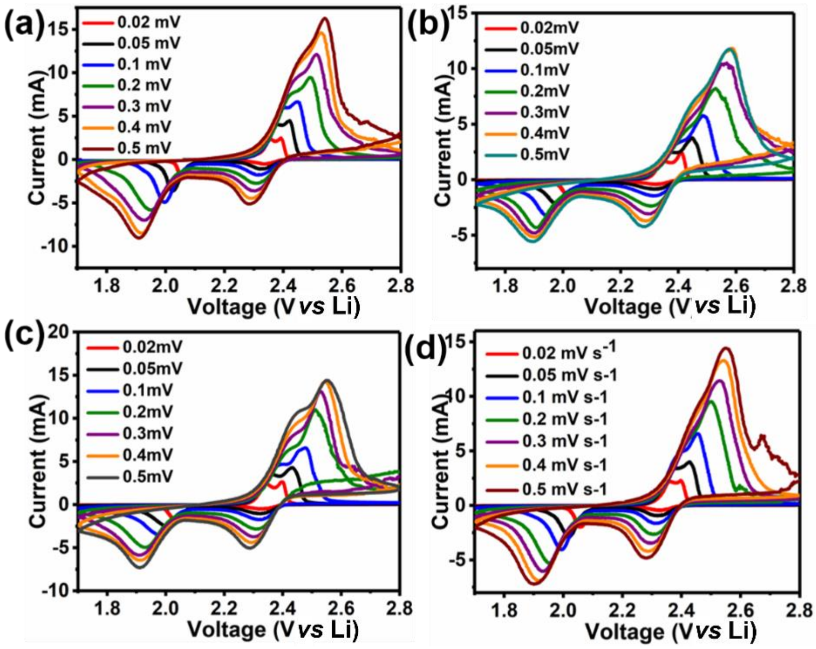

Figure 3.31. CV curves of samples. (a) Co$_{0.75}$P, (b) Co$_{0.5}$P, (c) Co$_{0.25}$P and (d) Co$_0$P.The scan rate increased from 0.02 mV s^{-1} to 0.05, 0.1, 0.2, 0.3, 0.4 and 0.5 mV s^{-1}.

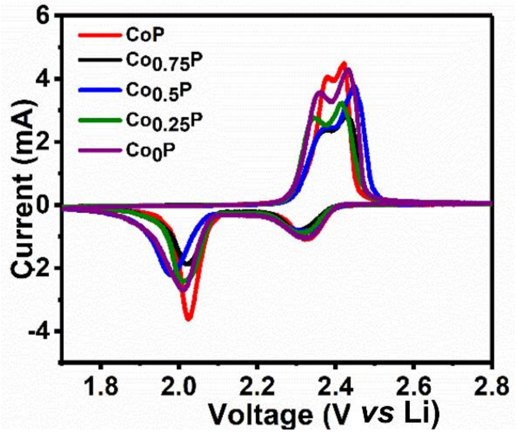

Figure 3.32. CV curves of samples at 0.05 mV s^{-1} at the 5th cycle.

The CV curves of samples at a scan rate of 0.05 mV s^{-1} at the 5th cycle were similar and overlapped with each other, indicating that the introduction of Ni in the samples did not change the electrochemical behaviours (**Figure 3.32**). According to the power law, there is a relationship between the peak current and the scan rate: $I = a V^b$, among which I is the peak current, V is the scan rate, a and b are constants. For capacitive contribution process, b is close to 1. For diffusion limited process, b is close to 0.5. As shown in **Figure 3.33**, the peak current and square root of scan rate of $Co_{0.25}P$ have a linear relation, confirming that it's a diffusion limited process.

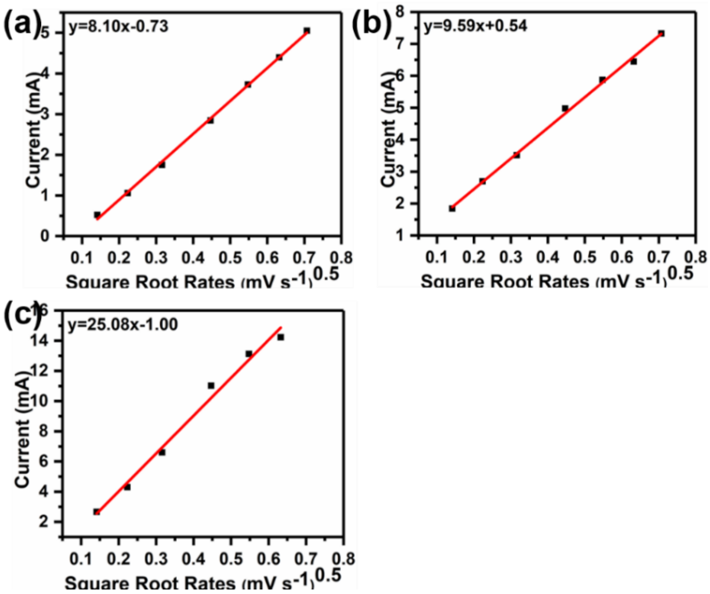

Figure 3.33. Relation between peak current and square root of scan rate of $Co_{0.25}P$.

The charge-discharge curves of samples are shown in **Figure 3.34**. They all showed two discharge voltage platform at around 2.3 and 2.1 V and one charge voltage platform at around 2.3 V, same as CoP. The initial discharge specific capacity increased as the content of Ni increased at the beginning and reached the highest at $Co_{0.25}P$ and then decreased. This could be ascribed to the increased surface area and more exposed active sites at higher Ni content as shown in SEM and TEM images. However, for Co_0P sample, the layered structure was destroyed, and the surface area decreased.

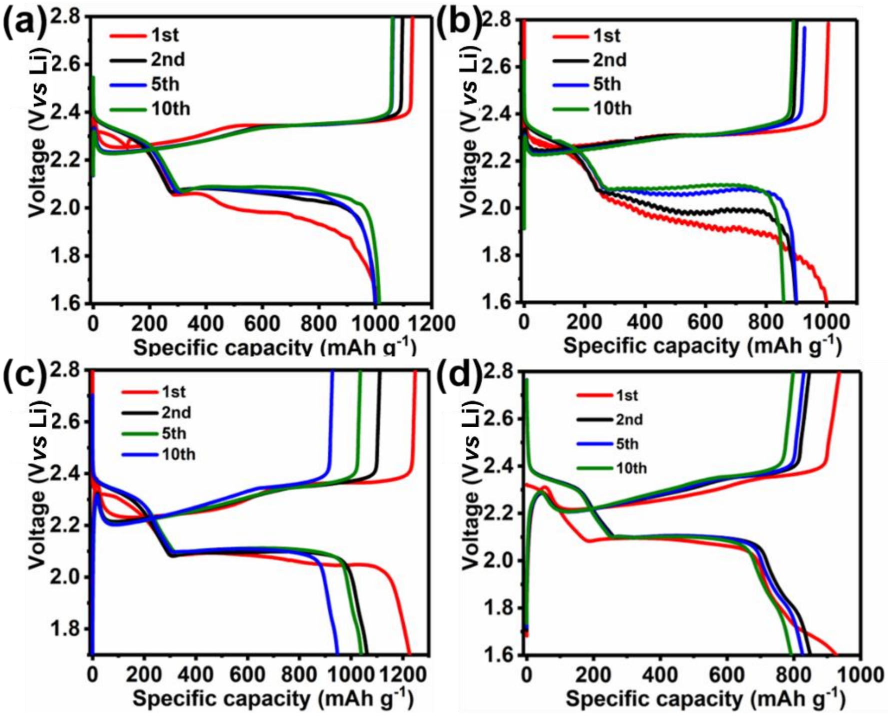

Figure 3.34. Charge-discharge curves of samples at a current density of 0.1 C. (a) $Co_{0.75}P$, (b) $Co_{0.5}P$, (c) $Co_{0.25}P$ and (d) Co_0P.

The rate performance and cyclic stability of $Co_{0.25}P$ were further tested as shown in **Figure 3.35**. As the current density increased from 0.1 C to 2 C, the specific capacity of $Co_{0.25}P$ decreased from over 1200 mA h g^{-1} to about 600 mA h g^{-1}. As the current density recovered to 0.1 C, the specific capacity increased a little bit but not as high as the initial one. The cyclic stability of $Co_{0.25}P$ was tested at a current density of 2 C. In the first 50 cycles, the specific capacity of $Co_{0.25}P$ stayed stable, with only a decrease from 655 mA h g^{-1} to 560 mA h g^{-1}.

However, after 50 cycles, the specific capacity decreased dramatically with only 120 mA h g^{-1} left after 200 cycles.

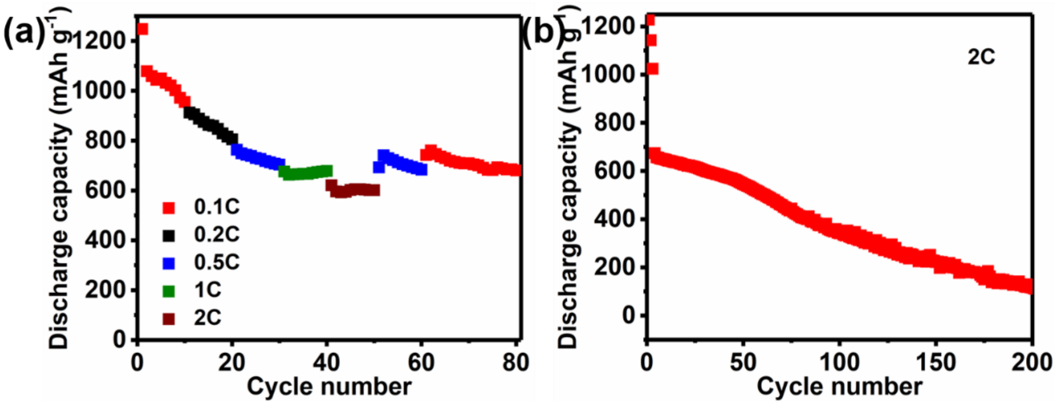

Figure 3.35. Rate performance (a), the current density increased from 0.1 C to 0.2, 0.5, 1 and 2 C and then decreased to 1, 0.5 and 0.1 C step by step. And long cycle stability (b) of $Co_{0.25}P$.

3.4 Conclusion

In summary, this chapter reports on the development of a method to synthesis Co_xP supported on N-doped carbon framework from ZIF-67 template and used it as a S host for LSBs. The impact of Ni content on the morphology and electrochemical performance of samples was studied. It was found that $Co_{0.25}P$ has the best electrochemical properties, with the highest initial specific capacity of over 1200 mA h g^{-1} and 560 mA h g^{-1} after 50 cycles at a high current density of 2 C.

3.5 Reference

[1] P. Geng, S. Zheng, H. Tang, R. Zhu, L. Zhang, S. Cao, H. Xue, H. Pang, *Adv. Energy Mater.* **2018**, *1703259*, 1.

[2] J. Xie, H. J. Peng, J. Q. Huang, W. T. Xu, X. Chen, Q. Zhang, *Angew. Chemie - Int. Ed.* **2017**, *56*, 16223.

[3] K. Long, L. Bo-Quan, P. Hong-Jie, Z. Rui, X. Jin, H. Jia-Qi, Z. Qiang, *Adv. Energy Mater.* **2018**, *0*, 1800849.

[4] Y. Zhong, D. Chao, S. Deng, J. Zhan, R. Fang, Y. Xia, Y. Wang, X. Wang, X. Xia, J. Tu, *Adv. Funct. Mater.* **2018**, *1706391*, 1.

[5] J. Xu, T. Lawson, H. Fan, D. Su, G. Wang, *Adv. Energy Mater.* **2018**, *8*, 1.

[6] Z. Wang, R. Tan, H. Wang, L. Yang, J. Hu, H. Chen, F. Pan, *Adv. Mater.* **2018**, *30*, 1.

[7] F. Zou, Y. Chen, K. Liu, Z. Yu, W. Liang, S. M. Bhaway, M. Gao, Y. Zhu, **2016**, DOI 10.1021/acsnano.5b05041.

[8] H. Pang, W. Huang, **2016**, DOI 10.1002/adma.201600319.

[9] L. Ge, Y. Yang, L. Wang, W. Zhou, R. De Marco, Z. Chen, J. Zou, **1867**, 1.

[10] J. Tang, R. R. Salunkhe, J. Liu, N. L. Torad, M. Imura, **n.d.**, 1.

[11] G. Qian, **2015**, 1.

[12] G. Chen, Y. Li, W. Zhong, F. Zheng, J. Hu, X. Ji, W. Liu, C. Yang, Z. Lin, M. Liu, *Energy Storage Mater.* **2020**, *25*, 547.

[13] K. Chen, Z. Sun, R. Fang, Y. Shi, H. M. Cheng, F. Li, *Adv. Funct. Mater.* **2018**, *28*, 1.

[14] J. Zheng, J. Tian, D. Wu, M. Gu, W. Xu, C. Wang, F. Gao, M. H. Engelhard, J. G. Zhang, J. Liu, J. Xiao, *Nano Lett.* **2014**, *14*, 2345.

[15] X. F. Lu, Y. Fang, D. Luan, X. W. D. Lou, *Nano Lett.* **2021**, *21*, 1555.

[16] P. Ji, T. Zeng, X. Hu, Y. Xu, G. Zhou, *Solid State Ionics* **2018**, *315*, 52.

Chapter 4

High performance sulfurized poly-acrylonitrile and carbon nanotube composite cathode via Se-doping

4.1 Introduction

In the last two chapters, the strategy of constructing porous carbon structure to serve as S host in LSB to alleviate the shuttle effect [1–5] has been studied. Though the electrochemical performance of LSBs was improved by using the as-synthesized compounds as S host with reduced shuttle effect, the soluble intermediates, LPSs, were still formed and the solid-liquid-solid reaction pathway took place. However, recently a new family of cathode material with C-S covalent bonds was developed as source of S for LSBs, because of the solid-solid reaction pathway without the formation of soluble LPSs.[6–11] Among all the reported compounds with C-S covalent bonds, SPAN is the most promising one. Ever since the first report of Wang's group in 2002,[24] the good electrochemical properties, facial synthesis process and compatibility with carbonate electrolyte of SPAN have attracted worldwide attention. But, the structure and mechanism of SPAN are not fully understood, and the electrochemical performance can be further improved.[10,12–18] The formation of covalent C-S bond has been reported by many researchers, but the detailed structure is still controversial. Though SPAN has high initial capacity, the rate performance and stability is impeded by the low conductivity of SPAN. Carbon materials like graphene nanosheet and carbon nanotube (CNT) have been applied to improve the conductivity.[19-20] Recently, Se-doping has also been reported as an effective strategy to improve the performance of LSBs.[21] Thus, a Se-doped SPAN incorporated with CNT was designed and synthesized as high performance cathode for LSB.

4.2 Experimental section

4.2.1 Materials

CNT (110-170 nm * 5-9 μm), $NaNO_3$, $KMnO_4$, 2,2-azobisisobutyronitrile (AIBN) Acrylonitrile, $LiNO_3$, sulfur, selenium, lithium bis(trifluoromethanesulfonimide) (LiTFSI), N-methyl pyrrolidone (NMP), 1,2-dimethoxyethane (DME) and 1,3-dioxolane (DOL) were purchased from Sigma-Aldrich and used directly. Carbon-coated aluminium foil, Celgard separator, Lithium metal foil and commercial electrolyte for lithium-ion batteries were purchased form MTI company.

4.2.2 Synthesis of mildly oxidized carbon nanotube (moCNT)

Mildly oxidized carbon nanotube (moCNT) was synthesized through a modified method. 80 mg pristine CNT and 5 mL concentrated sulphuric acid were added into a round-bottom flask and stirred overnight. Then the solution was heated to 40 °C in oil bath, at which 40 mg $NaNO_3$ was added. After that, 80 mg $KMnO_4$ was added slowly under stirring with the temperature adjusted to be under 45 °C. The mixture was then stirred for 1 hour, during which CNT was oxidized. The flask was transferred to an ice bath, and 0.3 mL, 0.3 mL and 4 mL of deionized waster were added into the flask with a time interval of 5 min, and another 14 mL of deionized water was added after 15 min. After stirring for another hour, 1 mL hydrogen peroxide (30 %) was added to react with extra $KMnO_4$ in the solution. Then, the product was washed with vast amount of deionized water through repeated centrifuge and dissolution, until pH value of the supernatant reached 7. Finally, moCNT was freeze-dried before using.

4.2.3 Synthesis of poly(acrylonitrile)@moCNT (PAN@moCNT)

PAN@moCNT was synthesized through an *in-situ* polymerization process.

2.55 g of the as synthesized moCNT was dissolved in 1000 mL deionized water and sonicated for certain time until the solution became homogeneous. Then 75 mL of the as-prepared solution was added to a flask followed by 7 mL acrylonitrile monomer and 56 mg 2,2-azobisisobutyronitrile (AIBN) under stirring. Ar gas was purged into the solution to get rid of oxygen and provide an inert atmosphere. After 30 min, the solution was heated to 65 °C and kept for 3 hours. The product was achieved through repeated centrifuge and washing with water. Finally, the product was dried at 80 °C overnight. Pure PAN sample was prepared in the same method except that deionized water instead of moCNT solution was added.

4.2.4 Synthesis of Se-doped sulfurized PAN@moCNT ($Se_xSPAN@moCNT$)

Sulfur selenium composite was synthesized first. 2 g S and certain mass of Se ($Se_{0.05}S$ with 100 mg Se and $Se_{0.1}S$ with 200 mg Se) was mixed through a liquid phase ball milling process with 5 mL ethanol as dispersion solution. The speed of ball milling was set at 200 rpm and the total time was 3 hours. The mixture was vacuum dried at 80 °C overnight and then transferred into a Teflon-lined stainless-steel autoclave and heated at 250 °C for 12 hours.

Sulfur selenium composite and PAN@moCNT was mixed through solid state ball milling before heat treatment. The mass ratio of the composite and PAN@moCNT was set at 3:1. After that, the mixture was transferred into a tube furnace, and heated to 300 °C for 2.5 hours under Ar atmosphere. Sulfurized PAN@moCNT (SPAN@moCNT) was synthesized as the same process by using sublimed sulfur.

4.2.5 Material characterization

Scanning electron microscopic (SEM) images were taken by a field emission scanning electron microscope (Jeol JSM 6701). Transition electron microscopic (TEM) and energy dispersive spectra (EDS) characterizations were performed on a probe corrected (CEOS) JEM ARM 200CF (JEOL Japan) operated at 200 keV. X-ray diffraction (XRD) was carried out in a Bruker-Axs D8 X-ray diffractometer. FTIR test was carried out by using a Bruker ALPHA FTIR spectrometer (Platinum-ATR). Raman spectrums were characterized by using a Raman spectrometer (514.5 nm laser Renishaw). X-ray photoemmision spectrum (XPS) were carried out by Al-K-α, Thermos Fisher scientific.

4.2.6 Electrochemical measurements

The electrochemical performance of samples was tested by assembling 2032 coin cells in an argon-filled glove box. Cathodes were made through a typical process. Samples, super P and Polyvinylidene Fluoride (PVDF) were mixed in a mass ratio of 8:1:1, with N-methyl pyrrolidone (NMP) as dispersion solution. The slurry was then coated on carbon coated aluminium foil and dried at 60 ℃ under vacuum overnight. The coated foil was then cut into disks with a diameter of 16 mm. The area sulfur loading is 0.9-1.3 mg cm^{-2} if not specifically mentioned. Two kinds of electrolytes were used. Commercialized carbonate electrolyte for lithium-ion batteries and self-made ether-based electrolyte. For ether electrolyte, 1 mol L^{-1} Lithium bistrifluoromethane sulfonimide (LiTFSI) was dissolved in a mix solution of 1,2-dimethoxyethane (DME) and 1,3-dioxolane (DOL) (1:1 v/v) with 2 wt% $LiNO_3$ as addictive. And the dosage of electrolyte was controlled at 10 μL mg^{-1}(s). Lithium foil and Celgard separator were used as anode and separator. Arbin and Neware battery test system were used to test the electrochemical performance of these coin cells.

4.3 Results and discussion

Se-doped SPAN incorporated with mildly oxidized CNT (Se_xSPAN@moCNT) was synthesized and applied as a cathode material for LSBs. PAN@moCNT was firstly synthesized through an *in-situ* polymerization process (**Figure 4.1a**), after which Se_xSPAN was synthesized through a pyrolysis process of a mixture of Se_xS and PAN@moCNT at 300 ℃ for 2.5 hours under Ar atmosphere (Figure 4.1b). Typically, moCNT was embedded in PAN nanoparticles to improve the conductivity of the products. Covalent C-S bonds were formed to suppress the formation of lithium polysulfides and thus eliminate the shuttle effect.

Furthermore, the introduction of Se further increases the conductivity and accelerated the reaction pathway, which enabled higher capacity at high current density (837 mA h g^{-1} at a current density of 2 C, 1 C = 1675 mA g^{-1}) and better cyclic stability (772 mA h g^{-1} after 100 cycles at 0.5 C).

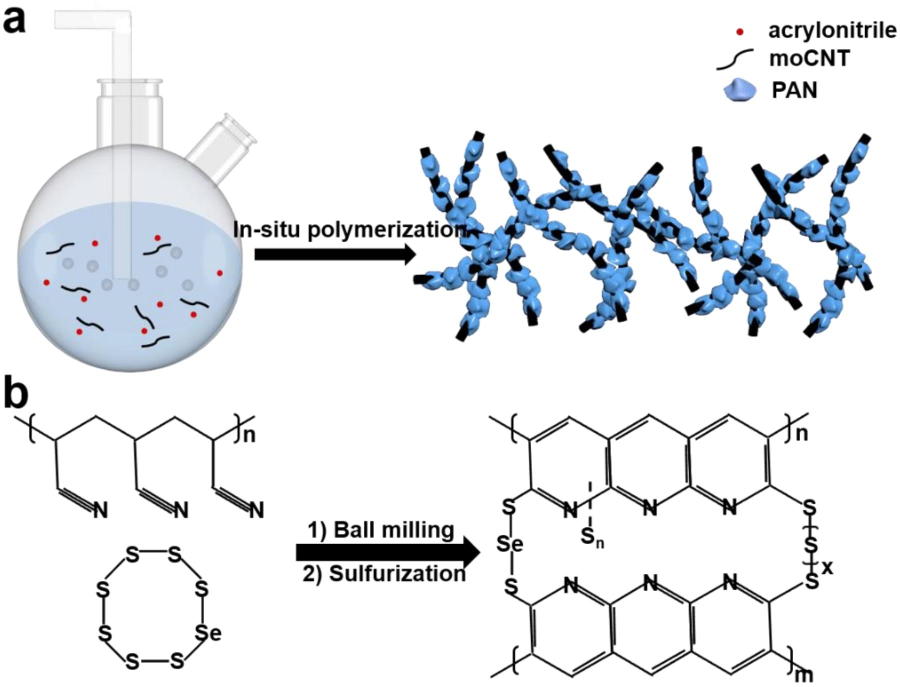

Figure 4.1. a) Schematic diagrams of *in-situ* polymerization process of poly-acrylonitrile on mildly oxidized carbon nanotube (PAN@moCNT). b) Synthesis method of Se-doped sulfurized PAN@moCNT (Se_xSPAN@moCNT) and proposed structure of the as-synthesized compound.

Se_xSPAN@moCNT was synthesized through a two-step process: the synthesis of PAN@moCNT and Se-doped S precursors and the sulfurization process. PAN@moCNT was synthesized through an *in-situ* polymerization process. At first, CNT was oxidized into moCNT through a modified Hummers method to improve the hydrophilicity and post-processing ability. After oxidization carbonyl, carboxyl and other oxygen containing groups were introduced on the surface of moCNT as indicated by X-ray photoelectron spectroscopy (XPS) results (**Figure 4.2**).

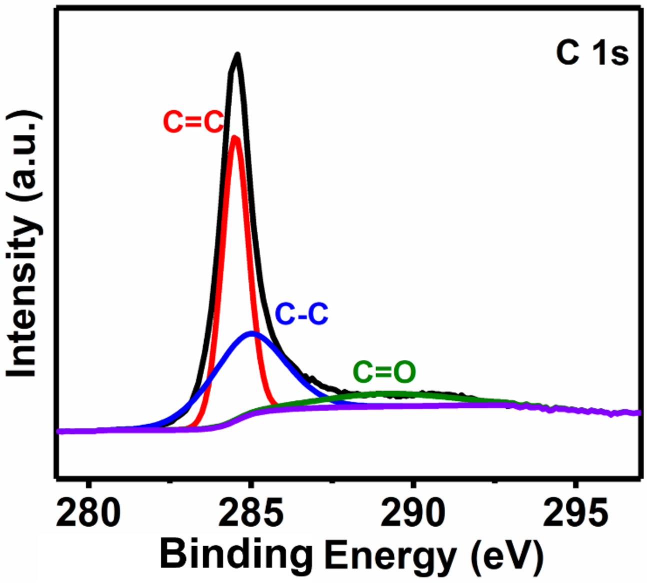

Figure 4.2. X-ray photoelectron spectra (XPS) result of mildly oxidized carbon nanotube (moCNT).

A homogeneous solution was formed by dissolving moCNT in deionized water followed by sonication for several hours. Then a certain volume of the as-prepared solution, acrylonitrile monomer and 2,2-azobisisobutyronitrile (AIBN) were added into a flask step by step under stirring. Ar was purged into the solution to provide an inert atmosphere. The mixture was then heated to 65 ℃ and kept for 3 hours. Finally, the product was collected through centrifuging, washing and vacuum drying overnight. The introduction of moCNT also affected the morphology of the samples (**Figure 4.3**). For pristine PAN sample without moCNT, irregular spheres with diameter of about 500 nm were formed as showed in scanning electron microscope (SEM) images (Figure 2a). While for PAN@moCNT, the size of the spheres decreased to about 100 nm (Figure 2b). Furthermore, transition electron microscope (TEM) images revealed more details about the morphology of samples. The irregular spheres of PAN were formed of smaller particles (Figure 2d). For PAN@moCNT, smaller PAN particles are connected by moCNT like a necklace (Figure 2e). The smaller size of PAN particles could be explained by the existence of moCNT which prevents aggregation.

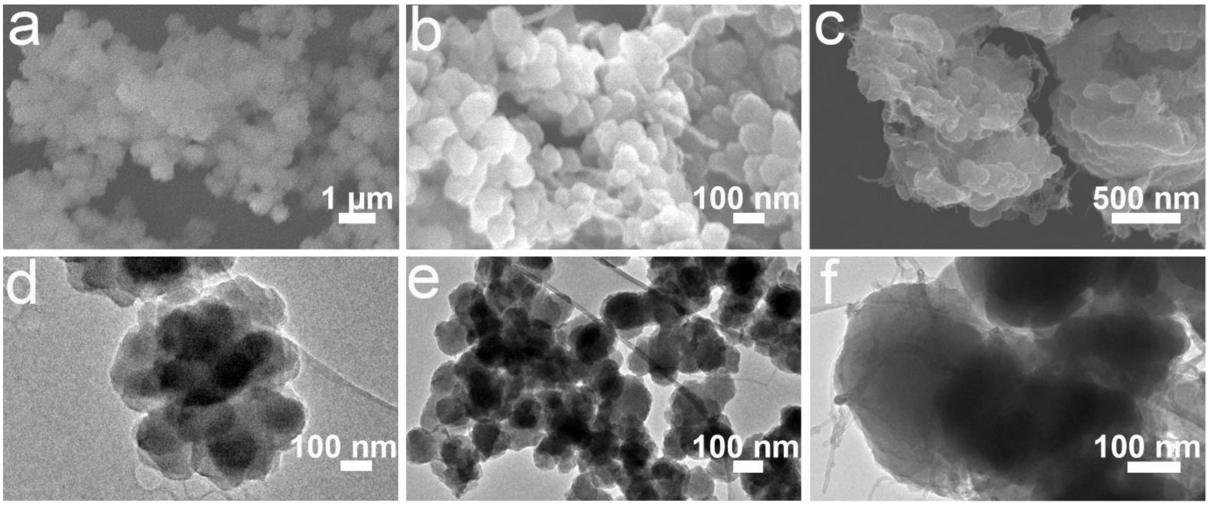

Figure 4.3. a-c) Scanning electron microscope (SEM) and d-f) transition electron microscope (TEM) images of samples. a and d) poly-acrylonitrile (PAN). b and e) PAN incorporated with mildly oxidized carbon nanotube (PAN@moCNT). c and f) Se-doped sulfurized PAN@moCNT ($Se_{0.1}$SPAN@moCNT).

Except for pristine S, Se-doped S was used as a precursor to synthesis Se_xSPAN@moCNT. S and Se were mixed through liquid phase ball milling with ethanol as dispersion solution. The mixture was then vacuum dried overnight and transferred into a Teflon-lined stainless-steel autoclave and heated at 250 °C for 12 hours. Samples with different mass ratio of Se-doping were synthesized: $Se_{0.05}S$ and $Se_{0.1}S$ (Se_nS, n means the mass ratio of Se/S before ball milling). The X-ray diffraction (XRD) pattern showed that the peaks of Se-doped S matched well with pristine S (**Figure 4.4**), indicating that Se-doping didn't break the structure of S.

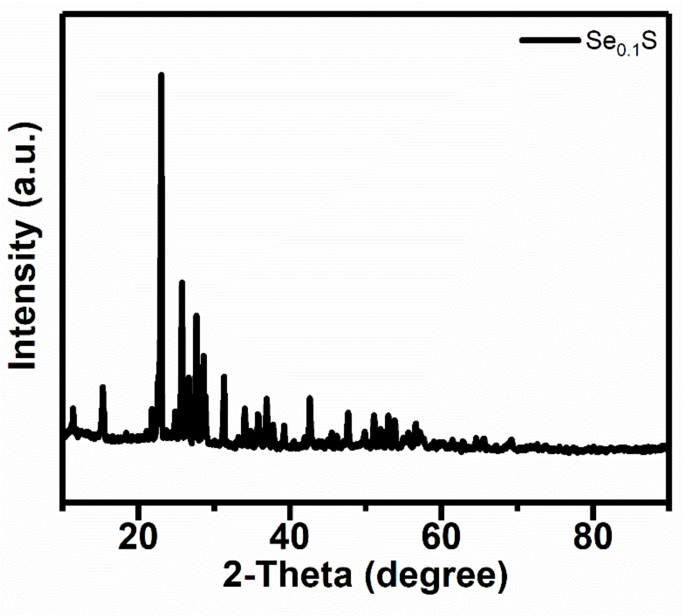

Figure 4.4. X-ray diffraction (XRD) pattern of Se-doped S (Se$_{0.1}$S).

Then the as-synthesized precursors were mixed through ball milling and then heated to 300 °C for 2.5 hours under an Ar atmosphere in a tube furnace. After sulfurization, the size of Se$_{0.1}$SPAN@moCNT particles grew up to several hundreds of nanometre with embedded moCNT (Figure 2c and 2f). For pure SPAN, the particle size was even bigger after sulfurization (**Figure 4.5**).

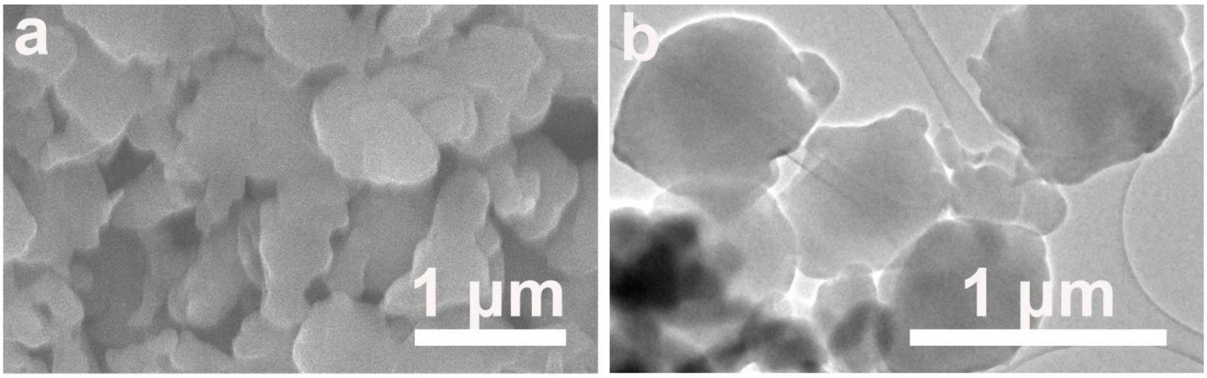

Figure 4.5. a) Scanning electron microscope (SEM) image of Sulfurized poly(acrylonitrile) (SPAN). b) Transition electron microscope (TEM) image of SPAN.

Samples with different ratio of Se-doping (SPAN@moCNT, $Se_{0.05}$SPAN@moCNT and $Se_{0.1}$SPAN@moCNT) were prepared. The content of Se-doping didn't affect the morphology of the final products (**Figure 4.6 and 4.7**).

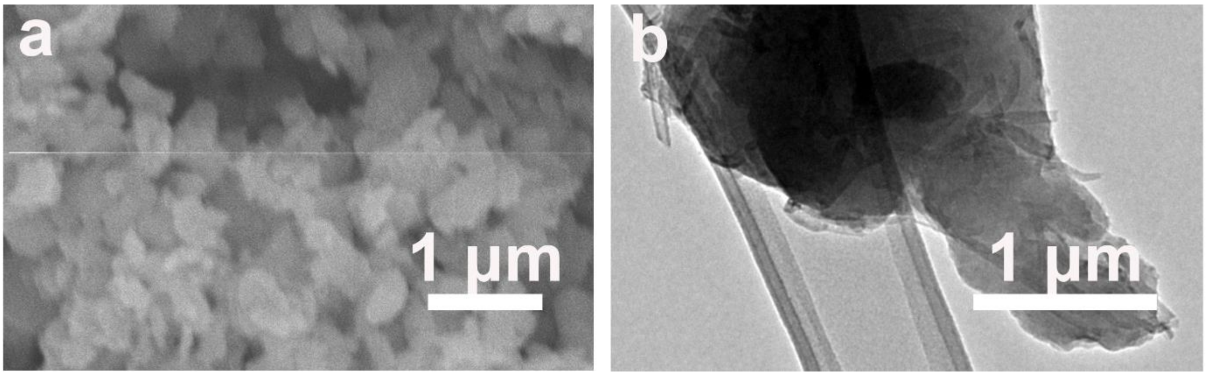

Figure 4.6. a) SEM image of SPAN@moCNT. b) TEM image of SPAN@moCNT.

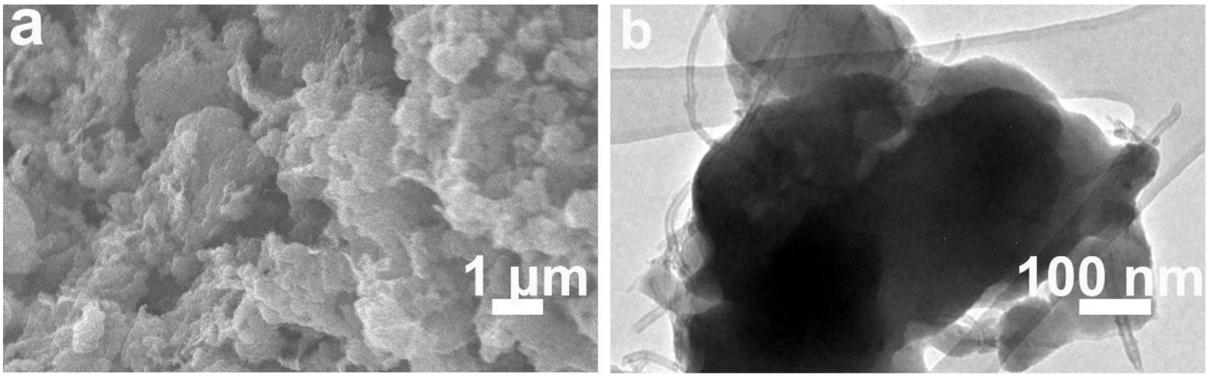

Figure 4.7. a) SEM image of $Se_{0.05}$SPAN@moCNT. b) TEM image of $Se_{0.05}$SPAN@moCNT.

X-ray energy dispersive spectroscopy (EDS) mapping of SPAN showed that after sulfurization, S uniformly dispersed in the sample (**Figure 4.8**). For $Se_{0.05}$SPAN@moCNT, Se was also uniformly dispersed in the sample, indicating the successful doping (**Figure 4.9**).

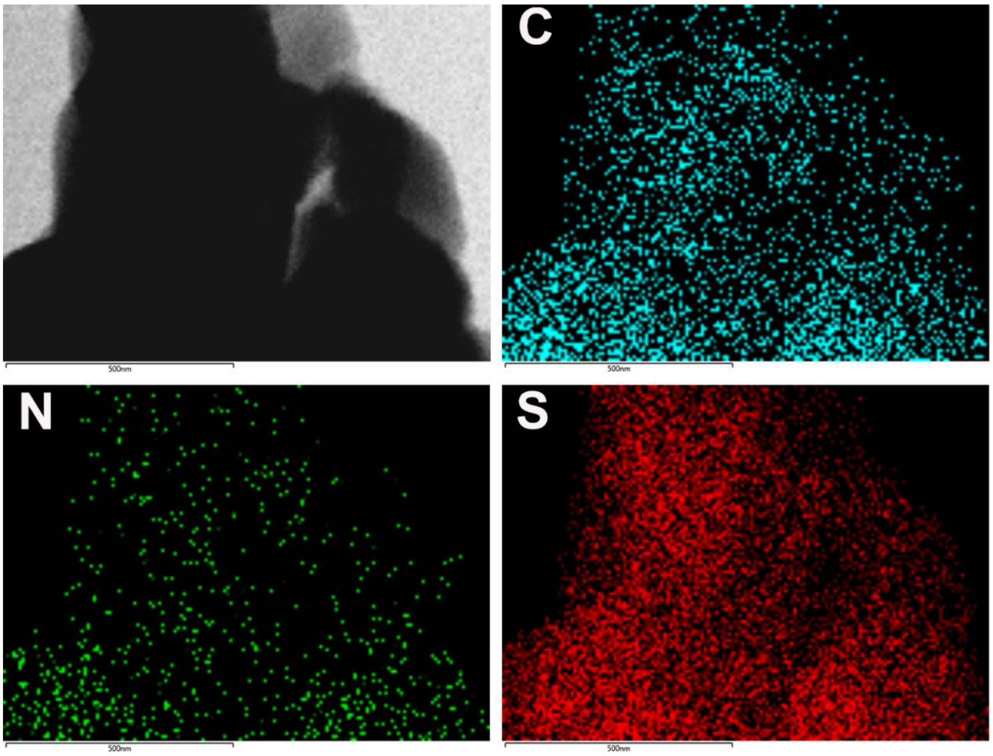

Figure 4.8. X-ray energy dispersive spectroscopy (EDS) mapping of SPAN.

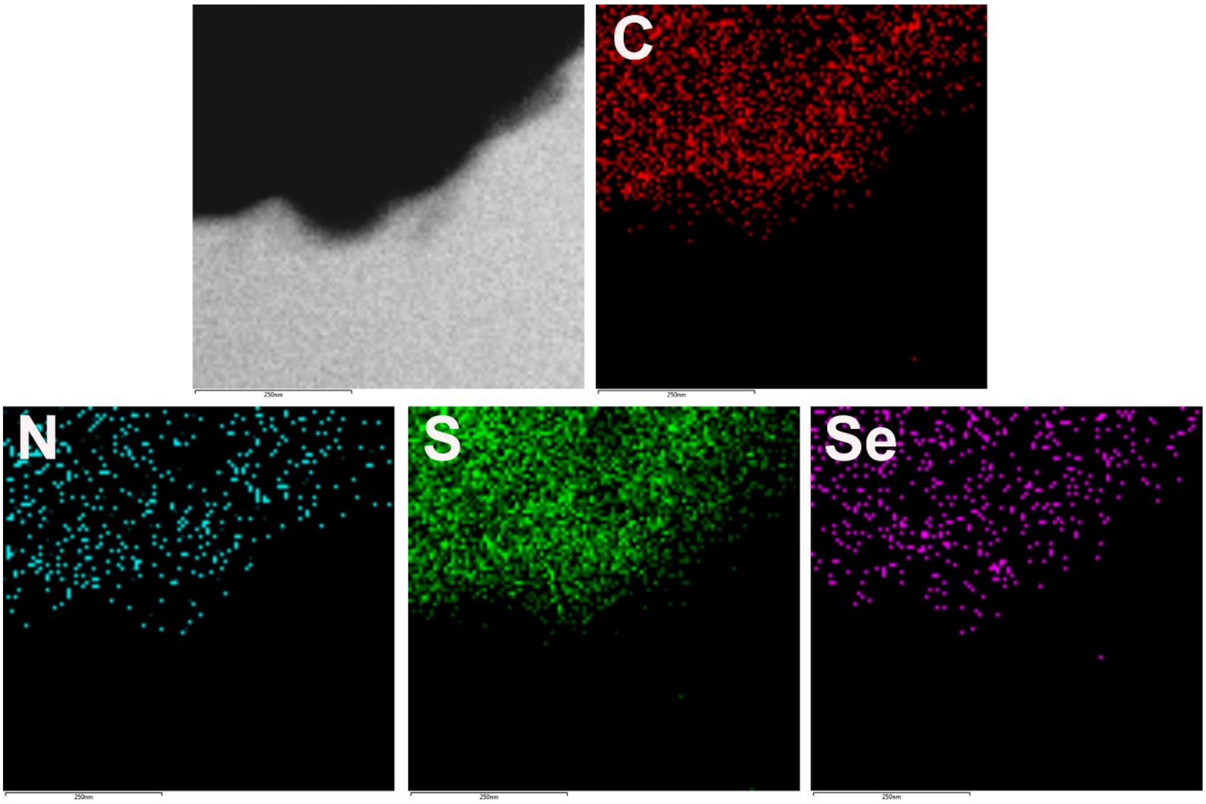

Figure 4.9. EDS mapping of $Se_{0.05}$SPAN@moCNT.

The chemical structure of Se_xSPAN@moCNT was characterized by XRD, Fourier Transform Infrared (FTIR), Raman and X-ray photoelectron spectroscopy (XPS) (**Figure 4.10**). XRD patterns (Figure 4.10a) showed no obvious peaks of S or Se_nS in all sulfurized samples. The peak at around 26 degrees could be ascribed to the (002) plane of amorphous carbon formed during the sulfurization process. For samples with different levels of Se-doping, the XRD patterns were similar. While in pure PAN sample, the peak at around 17 degrees corresponded to the (001) plane of PAN crystalline structure.

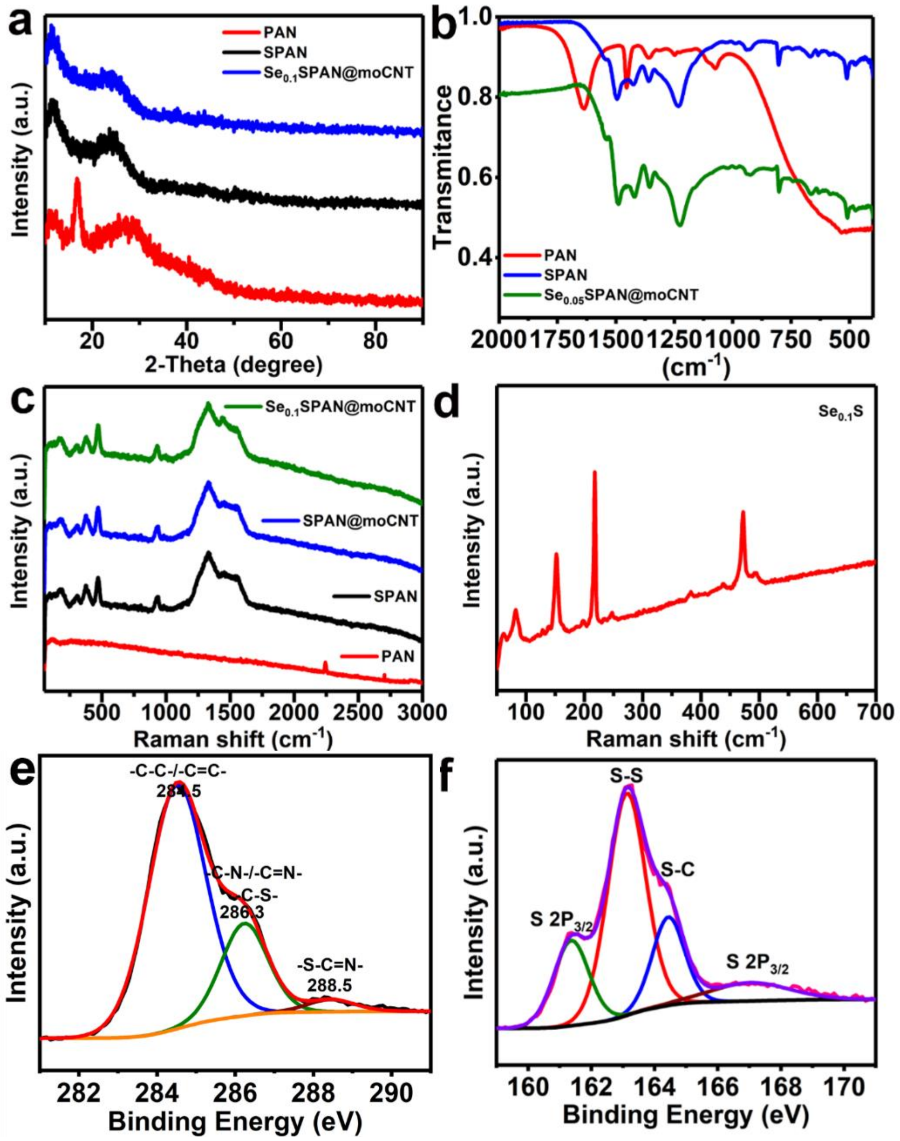

Figure 4.10. a) X-ray diffraction (XRD) spectra of samples. b) Fourier Transform Infrared (FTIR) spectra of samples. c) Raman spectra of samples. d) Raman spectra of $Se_{0.1}S$. e) High resolution X-ray photoelectron spectra (XPS) of C in $Se_{0.1}SPAN$@moCNT. f) High resolution XPS spectra of S in $Se_{0.1}SPAN$@moCNT.

FTIR patterns of samples showed the formation of C-S covalent bond and ring structure after sulfurization (Figure 4.10b). Peaks at 511 cm^{-1} derived from S-S bond stretching, while peak at 668 cm^{-1} corresponded to C-S bond stretching. Ring breathing of the C-S bond containing structure caused the peaks at 801 cm^{-1} and 940 cm^{-1}. The newly occuring peaks at 1237 cm^{-1} and 1498 cm^{-1} correspond to the existence of C=N and C=C bonds, respectively. All these indicate the breakage of C≡N bond in the side chain of PAN structure, and the formation of sulfur-containing ring structure. For comparison, PAN@moCNT was synthesized and pyrolysis at the same condition. No peaks of C-S bond (511 cm^{-1} and 668 cm^{-1}) was detected in the as-prepared pPAN@moCNT sample (**Figure 4.11)**. It is also worth mentioning that despite the difference in content of Se-doping, peaks detected from sulfurized samples were at the same frequency.

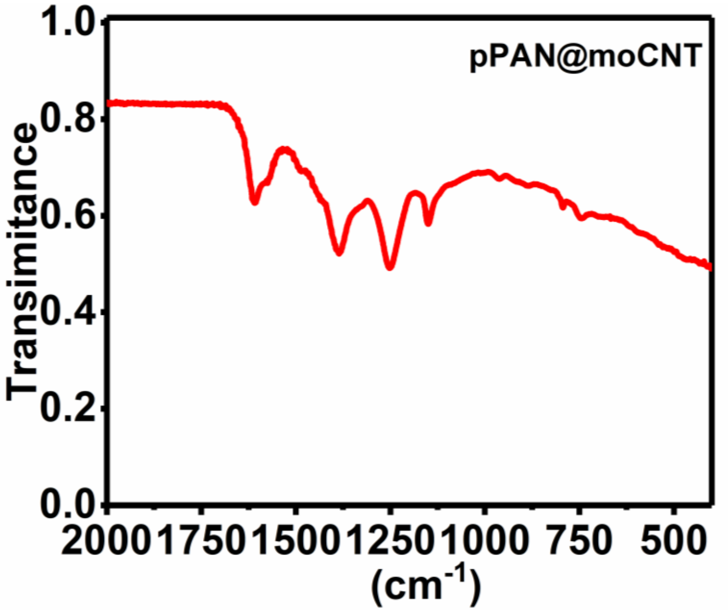

Figure 4.11. Fourier Transform Infrared (FTIR) pattern of pPAN@moCNT.

Raman spectra also confirmed the formation of C-S covalent bonds in the sulfurized samples (Figure 4.10c). After sulfurization, the peaks at 1325 cm^{-1} and 1532 cm^{-1} arose, which could be ascribed to D and G bands of carbon framework formed during the sulfurization process, which is in agreement with the XRD patterns. The peaks at lower frequency region (<1000 cm^{-1}) were mainly caused by covalent bonds between C, S and Se (Figure 4.10d). The peak at 926 cm^{-1} and 307 cm^{-1} corresponded to S-S and C-S bonds, respectively. Furthermore, XPS was applied to study the structure of sulfurized samples (**Figure 4.12**). After sulfurization, the peak of S and Se arose, indicating the existence of S and Se in the final products. In high resolution spectrum of C (Figure 4.10e), apart from the peak at 284.5 eV from –C-C-/-C=C- bonds, two new peaks were detected. The peak at 286.3 eV corresponded to –C-N-/-C=N-/-C-S- bonds, and peak at 288.5 eV corresponded to –S-C=N- bond. In high resolution spectrum of S (Figure 4.10f), except for the peak at 163.28 eV, which corresponded to –S-S- bond, the peak corresponding to a –C-S- bond at 164.48 eV was also detected. Based on these spectra, XPS also revealed the breakage of the C≡N bond and the formation of C-S bond during the sulfurization process. Above all, it can be concluded that in SPAN the C≡N bond is destroyed and a ring structure containing C-S bond is formed as shown in Figure 1. Se-doping did not change the structure, Se_xSPAN@moCNT with different content of Se-doping had similar structure with SPAN.

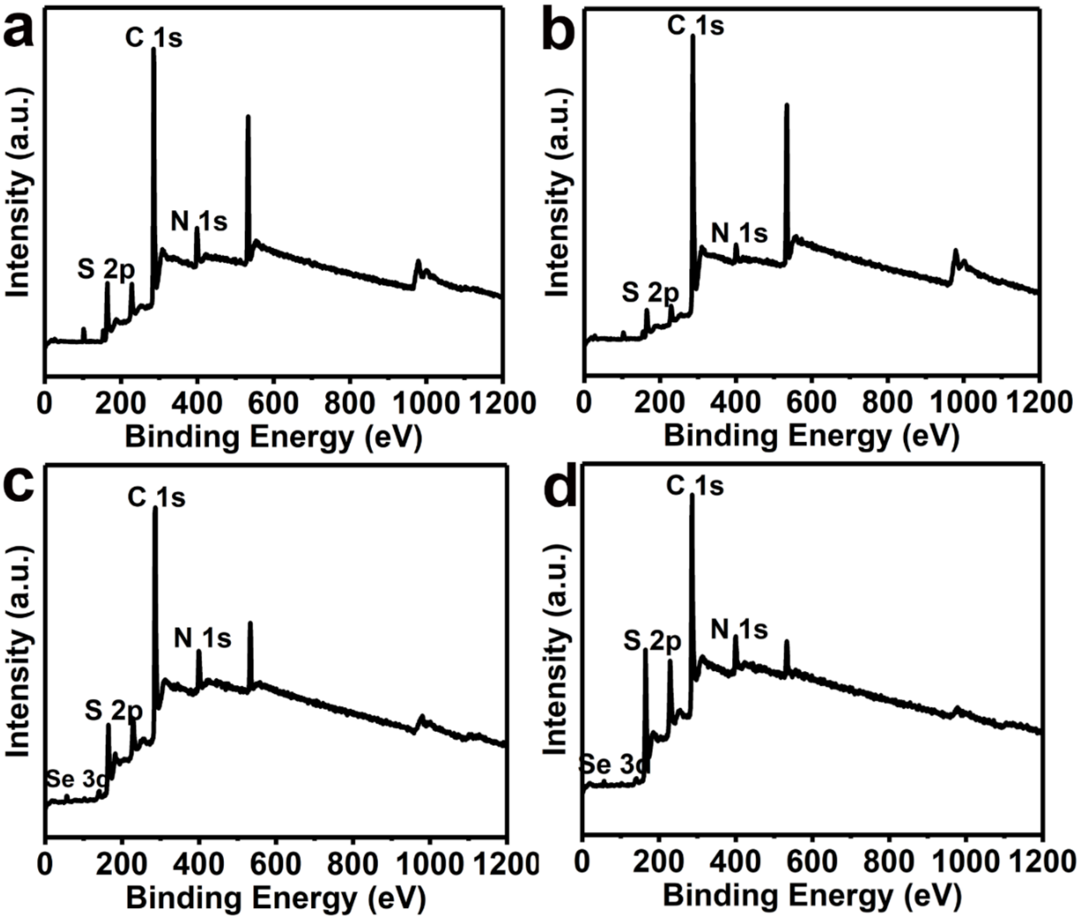

Figure 4.12. X-ray photoelectron spectra (XPS) results of samples: a) SPAN; b) SPAN@moCNT; c) $Se_{0.05}$SPAN@moCNT; d) $Se_{0.1}$SPAN@moCNT.

The electrochemical performance of $Se_xSPAN@moCNT$ was examined by assembling coin cells with $Se_xSPAN@moCNT$ and Li foil as cathode and anode, respectively. The content of S and Se in the as-prepared samples were quantitatively analysed though XPS as shown in supporting information and **Table 4.1 and Table 4.2**. In SPAN, the S content was 48.1%, while in SPAN@moCNT the S content was 47.2%. In $Se_{0.05}SPAN@moCNT$ and $Se_{0.1}SPAN@moCNT$ the total mass content of S and Se was calculated to be 55.9% and 58.9%, respectively.

Table 4.1. XPS data of different samples.

Sample	SPAN (eV)	SPAN@moCNT (eV)	$Se_{0.05}SPAN@moCNT$ (eV)	$Se_{0.1}SPAN@moCNT$ (eV)	Peak assigned
C 1s	285.63	284.43	284.61	284.83	C 1s
	286.78	285.68	285.46	285.77	
	290.30	287.41	286.01	286.29	
		289.45	290.22	290.86	
N 1s	399.20	398.62	398.89	398.63	N 1s
	400.94	400.41	400.61	399.21	
	402.12	401.98	401.83	400.81	
S 2p	162.59	162.25	162.44	162.45	S 2p1/2
	164.27	163.87	164.44	164.09	S 2p3/2
	165.55	165.058	165.75	165.29	S 2p1/2
	167.98	166.13	166.68	168.00	S 2p3/2
Se 3d			56.48	56.25	Se 3d
			58.73	57.15	

Quantitative analysis of S and Se content in different samples.

The surface composition of the samples could be calculated from the de-convoluted peaks areas of each element based on the equation below:

$$\boldsymbol{Cx} = \frac{\boldsymbol{Ix}/_{\boldsymbol{Sx}}}{\sum_{i} \boldsymbol{Ii}/_{\boldsymbol{Si}}}$$

In which C_x is the ratio of element X, I_x is the fitted area of element X, S_x is the relative sensitivity factor of element X.

Table 4.2. The relative sensitivity factor (RSF) of elements, I_x/S_x and atomic ratio of $Se_{0.05}$SPAN@moCNT (eV).

Element	State	RSF	I_x/S_x	Atomic ratio
C	1s	0.296	307483.1	8.2
N	1s	0.477	37160.8	1
S	2p1/2	0.223	103287.0	4.3
	2p3/2	0.445	57013.3	
Se	3d	0.853	2331.7	0.063

Based on the atomic ratio of elements, the total mass content of S and Se in $Se_{0.05}$SPAN@moCNT was calculated to be 55.9%. The mass ratio of Se and S (m_{Se}/m_S) was 3.6%. The mass content of S and Se in other samples were calculated by using the same method. In SPAN, the S content was 48.1%, in SPAN@moCNT the S content was 47.2% and in $Se_{0.1}$SPAN@moCNT the total mass content of S and Se was 58.9% with a mass ratio of Se and S (m_{Se}/m_S) of 5.3%.

The high content could be ascribed to the higher melting point of Se. EDS tests also showed similar results as shown in **Figure 4.13**.

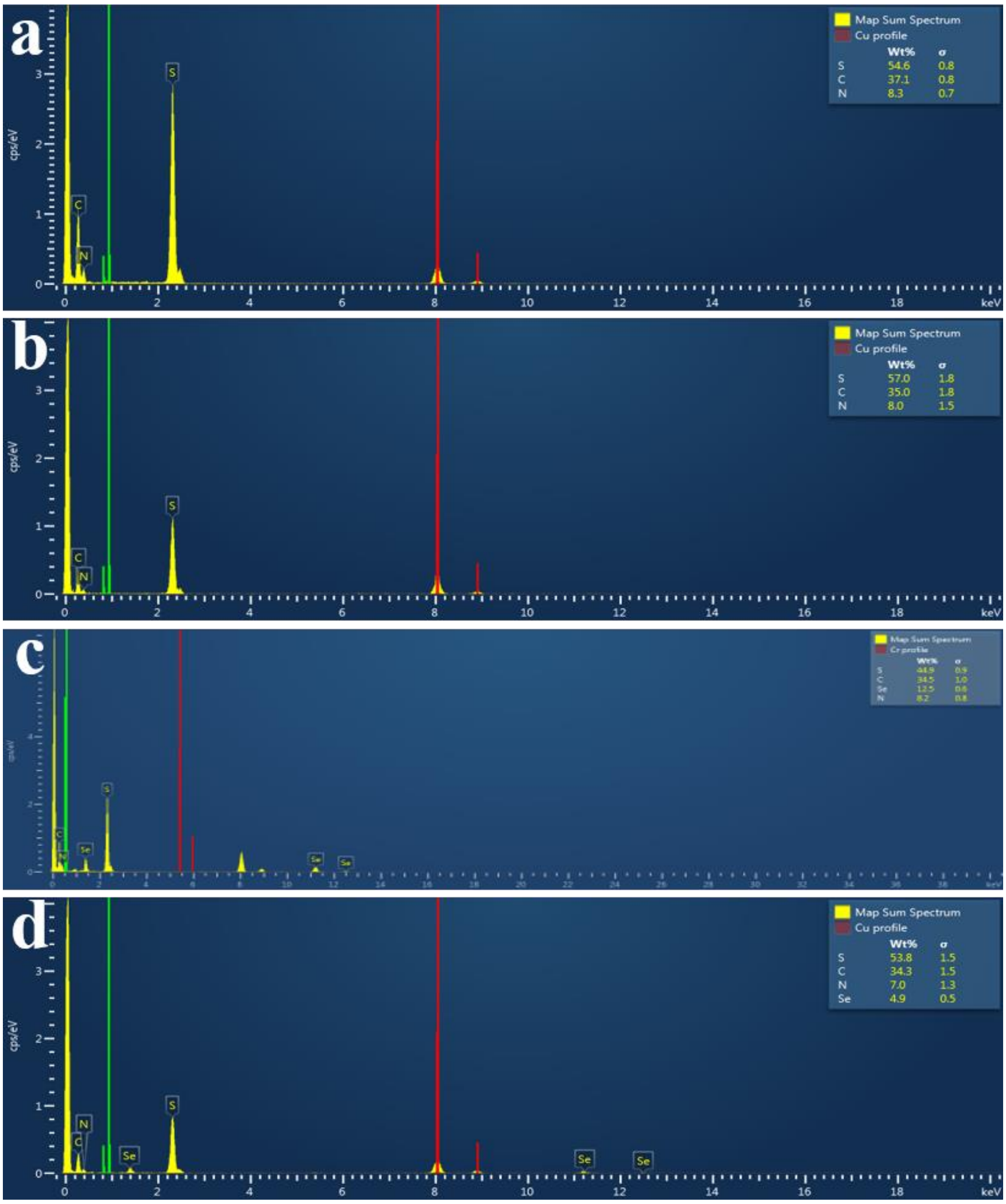

Figure 4.13. EDS elemental analysis of samples a) SPAN, b) SPAN@moCNT, c) $Se_{0.05}$SPAN@moCNT, d) $Se_{0.1}$SPAN@moCNT.

Galvanostatic charge-discharge measurement were conducted to measure the capacity of samples with different level of Se-doping (**Figure 4.14**). The specific capacity of Se_xSPAN@moCNT increased with the introduction of Se-doping at first and then decreased with further increase in the level of Se-doping, as Se has higher relative atomic mass and lower theoretical specific capacity than those of S. $Se_{0.05}$SPAN@moCNT has the highest specific capacity and cycling stability. Carbonate and ether-based electrolytes were used in the tests. It was reported that LiPSs had lower solubility in carbonate-based electrolyte and a stable solid-electrolyte-interphase (SEI) would be formed and mitigated against the shuttle effect. However, ether-based electrolyte had better compatibility than with the Li metal anode.

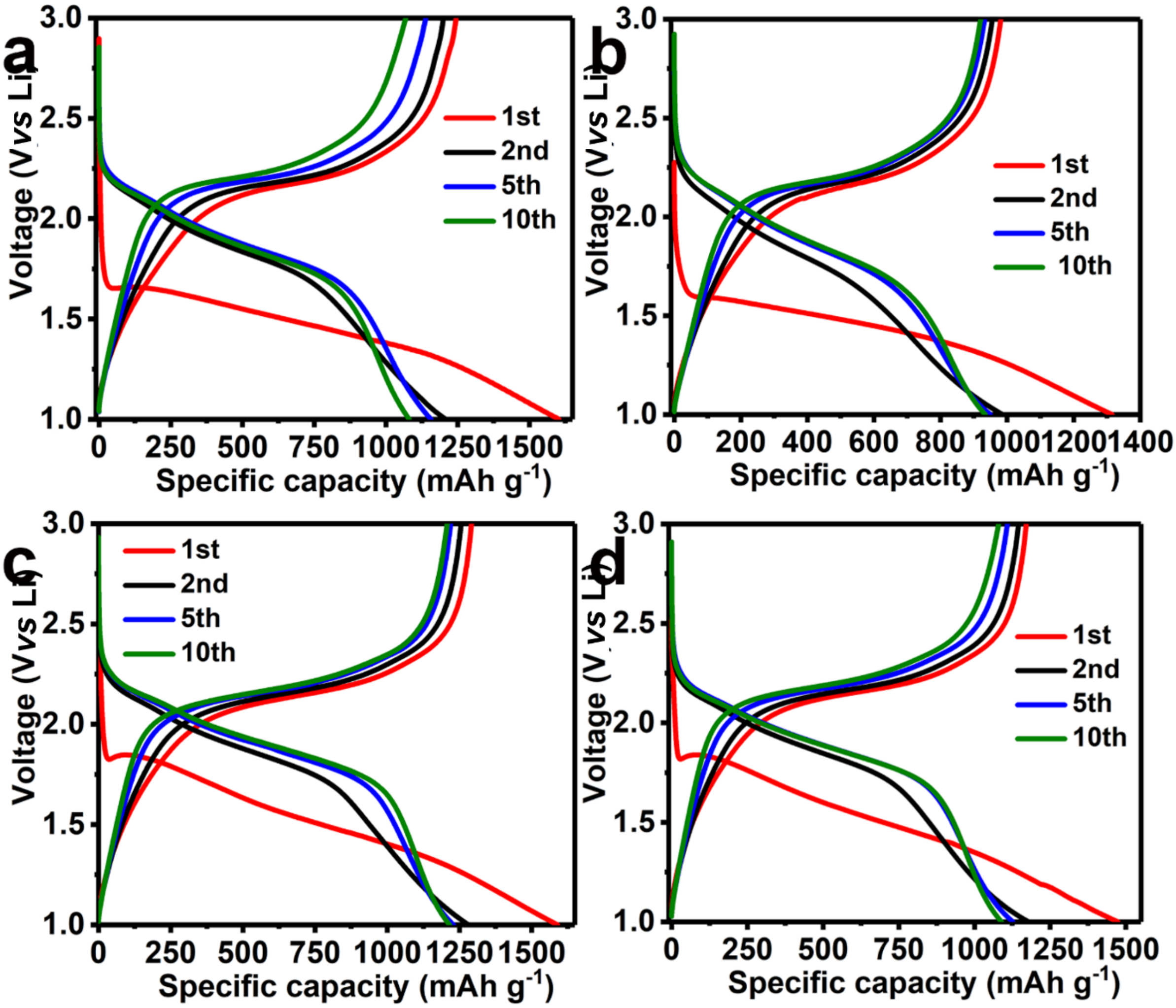

Figure 4.14. Charge-discharge curves of samples in carbonate-based electrolyte at a current density of 0.1 C. a) SPAN; b) SPAN@moCNT; c) $Se_{0.05}$SPAN@moCNT; d) $Se_{0.1}$SPAN@moCNT.

Cyclic voltammogram (CVs) tests revealed that, in carbonate-based electrolyte, there was only one voltage platform during the discharge or charge process (**Figure 4.15**). The cathodic peak at about 1.2 V moved to about 1.6 V after the first cycle, while the anodic peak about 2.3 V was stable. After the second cycle, the CV curves overlapped with each other, indicating good stability.

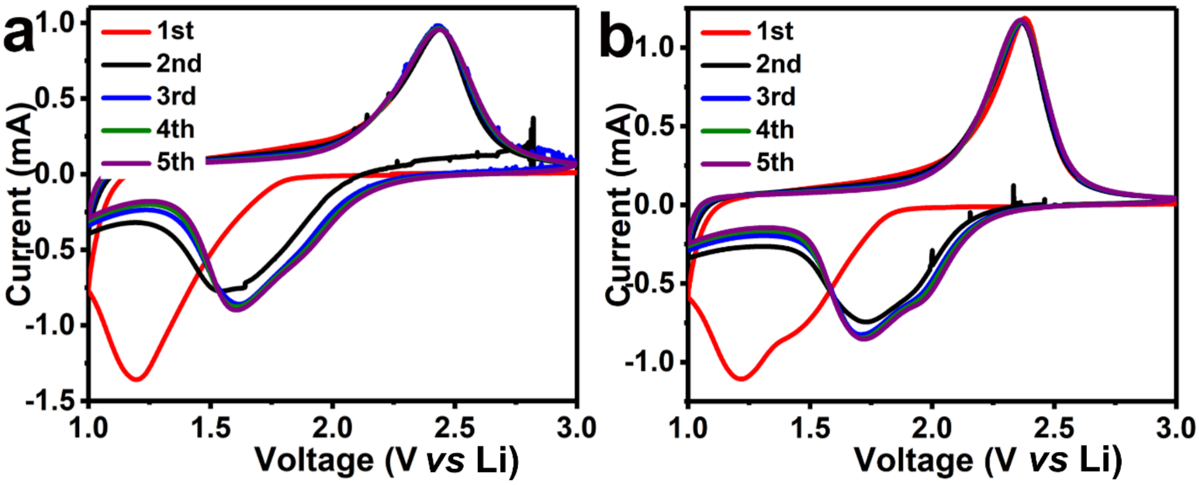

Figure 4.15. Cyclic voltammograms (CVs) curves of samples in carbonate-based electrolyte at a scan rate of 0.2 mV s^{-1}: a) $Se_{0.05}$SPAN@moCNT; b) $Se_{0.1}$SPAN@moCNT.

With an increase in scan rate from 0.2 mV s^{-1} to 2 mV s^{-1}, the position of the peak current shifted to both sides and the peak current increased from about 1 mA to over 4 mA as the polarization became greater at higher current density (**Figure 4.16a**). The charge-discharge curves tested at a current density of 0.1 C (1 C = 1675 mA g^{-1}) also show a long voltage platform at about 1.7 V in the first cycle, which shifted to about 2.0 V in the second cycle and became stabilized in the following cycles (Figure 4.16b). These agree with the current peak shift in the CV measurements. For $Se_{0.05}$SPAN@moCNT sample, an initial specific discharge capacity of 1591 mA h g^{-1} could be reached with a Coulombic efficiency of 81%. After the first cycle, a reversible specific capacity of 1283 mA h g^{-1} was maintained and the Coulombic efficiency reached over 98%, which showed good stability compared with those without Se-doping. The charge-discharge curves of samples with different levels of Se-doping were compared in Figure 4.16c to find out how Se-doping affected the specific capacity of samples. The fifth cycle at 0.1 C was chosen for comparison as the performance becomes relatively stable. The specific capacity of samples increased from 1157 mA h g^{-1} to 1230 mA h g^{-1} with the first introduction of Se-doping. It is recognised that the high conductivity of Se-doping could accelerate the reaction and mitigate the shuttle effect. However, with a further increase in the Se-content, the specific capacity decreased to 1128 mA h g^{-1}. Though Se could go through a multi-electron reaction the same as S, the higher atomic mass (79 g mol^{-1}) results in lower theoretical specific capacity (679 mA h g^{-1}). Thus, there is a compromise between accelerating reaction and lowering specific capacity.

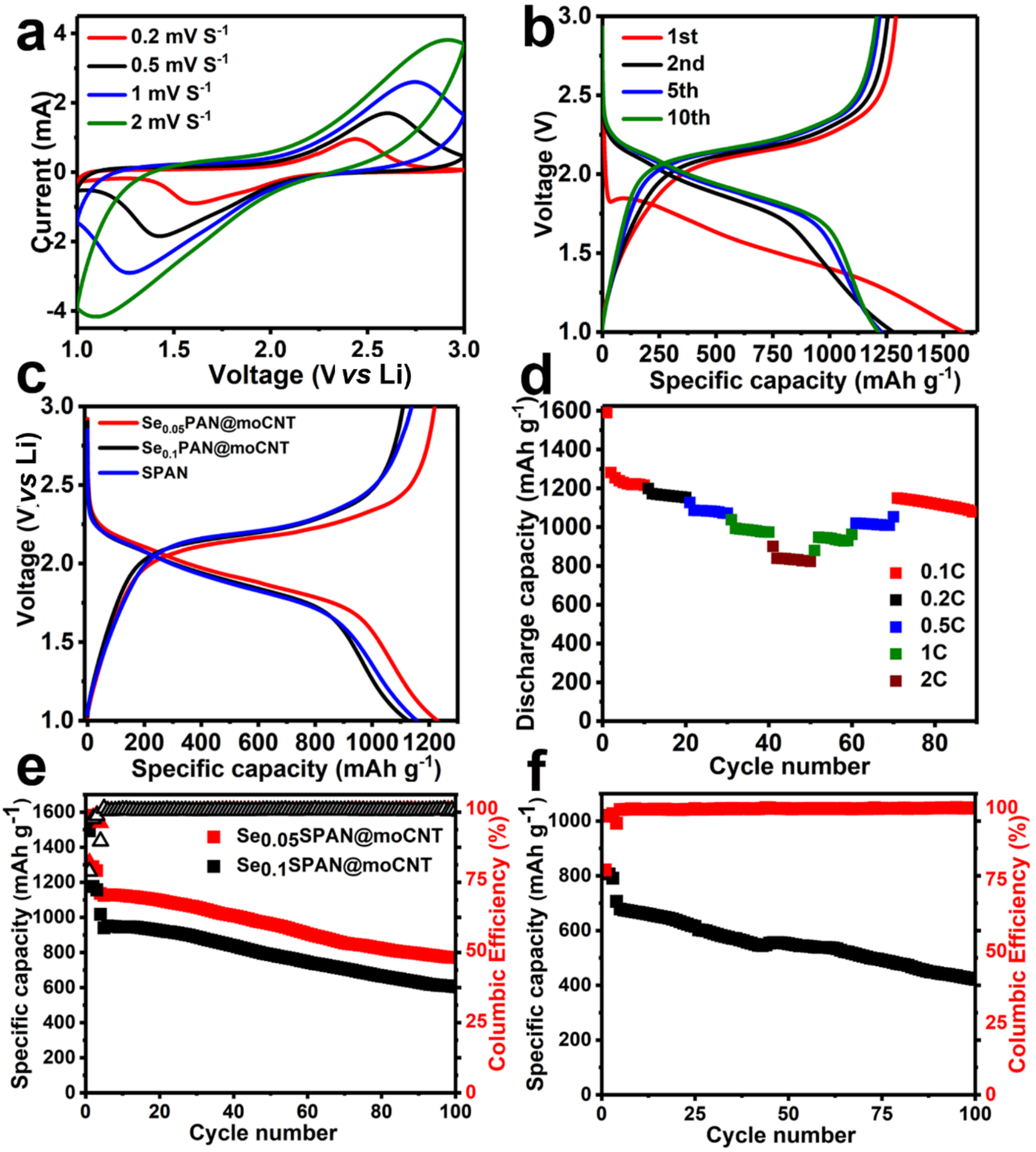

Figure 4.16. Electrochemical performance of samples tested in carbonate-based electrolyte a) Cyclic voltammograms (CV) curves of $Se_{0.05}$SPAN@moCNT tested at different scan rates, from 0.2 mV S^{-1} to 2 mV S^{-1}. b) Charge-discharge curves of $Se_{0.05}$SPAN@moCNT at a current density of 0.1 C (1 C = 1675 mA g^{-1}). c) Fifth cycle of charge-discharge curves of different samples. d) Rate performance of $Se_{0.05}$SPAN@moCNT tested at different current density, increased from 0.1 C to 2 C and then went back to 0.1 C. e) Cyclic stability of samples tested at a current density of 0.5 C. f) Cyclic performance of $Se_{0.05}$SPAN@moCNT under high area loading condition (3 mg cm^{-2}) at a current density of 0.5 C.

The rate capacities of samples were tested (Figure 4.16d and **Figure 4.17**). For $Se_{0.05}$SPAN@moCNT, when the current density increased from 0.1, 0.2, 0.5 and 1 to 2 C, the specific capacities decreased from 1230 mA h g^{-1} to 838 mA h g^{-1} because of high polarization at high current density. Among all the samples, $Se_{0.05}$SPAN@moCNT showed the highest specific capacities at all current densities, as the compromised content of Se-doping mitigated the shuttle effect and provided high theoretical specific capacity. The high conductivity of Se also enabled a high rate capacity retention of 69%, which was only 46% in the SPAN sample. When the current density decreased back to 0.1 C, $Se_{0.05}$SPAN@moCNT had a specific capacity of 1141 mA h g^{-1}, 93% of the initial specific capacity, showing good ability to recover.

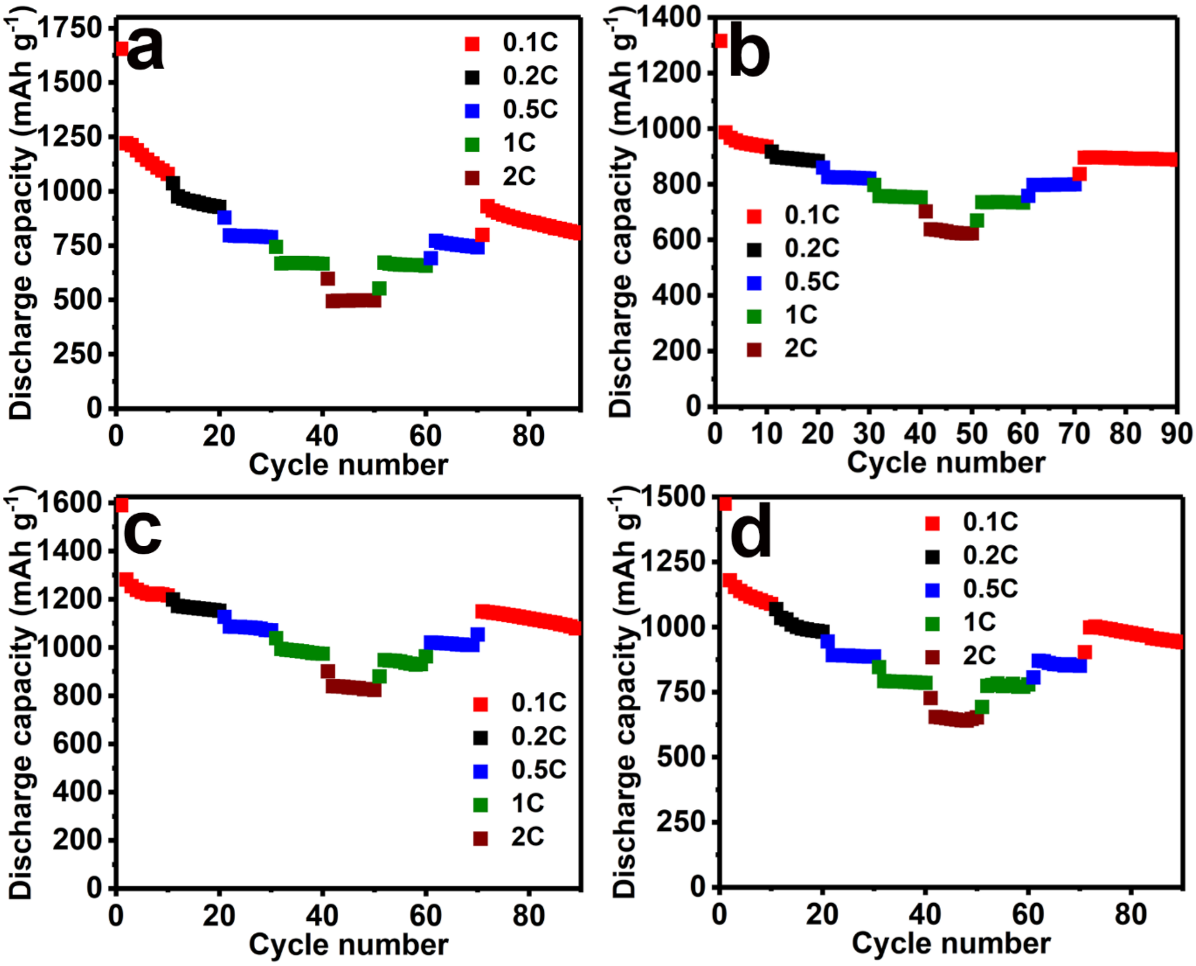

Figure 4.17. Rate performance of different samples in carbonate-based electrolyte. The current density increased from 0.1 C to 0.2, 0.5, 1 and 2 C and then decreased to 1, 0.5 and 0.1 C step by step. a) SPAN; b) SPAN@moCNT; c) $Se_{0.05}$SPAN@moCNT; d) $Se_{0.1}$SPAN@moCNT.

The cyclic stability of samples was tested at 0.5 C (Figure 4.16e and **Figure 4.18**). $Se_{0.05}$SPAN@moCNT showed a high reversible specific capacity of 1136 mA h g^{-1} after the activation process in the first three cycles, during which the Coulombic efficiency was lower than 98%. After activation, the Coulombic efficiency was higher than 99% and 772 mA h g^{-1} was maintained after 100 cycles of test with a capacity decay rate of 0.385% per cycle. The same phenomenon could be observed from $Se_{0.1}$SPAN@moCNT, except for a lower specific capacity. After activation, $Se_{0.1}$SPAN@moCNT had an initial specific capacity of 1172 mA h g^{-1}, after 100 cycles, 606 mA h g^{-1} was maintained with a capacity decay rate of 0.652%. Besides, a high area loading of S is important for the practical application of LSBs. Electrodes with an area mass loading of 3 mg cm^{-2} were prepared and tested. A high initial specific capacity of 1020 mA h g^{-1} could be achieved at a current density of 0.1 C. After the activation process, the specific capacity decreased to 707 mA h g^{-1} as the current density increased to 0.5 C. After 100 cycles, a specific capacity of 425 mA h g^{-1} was maintained, with a capacity decay rate of 0.493% per cycle. For the sample without Se-doping (SPAN@moCNT), the cells delivered an initial specific capacity of about 1000 mA h g^{-1} but failed after 60 cycles, a severe shuttle effect took place resulting in a Coulombic efficiency higher than 100%.

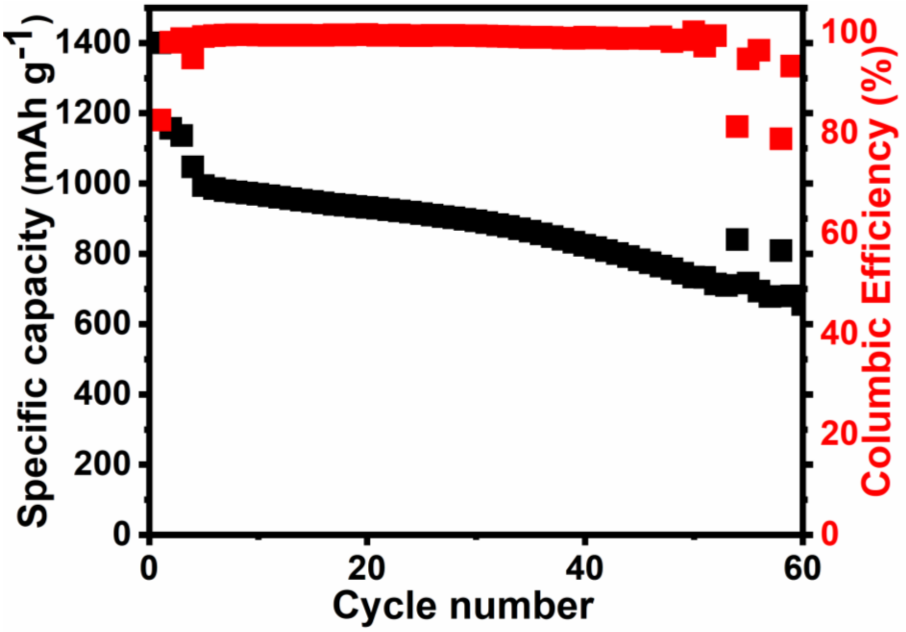

Figure 4.18. Cyclic performance of SPAN@moCNT in carbonate-based electrolyte.

Though carbonate-based electrolyte with low solubility of LPSs endows a high performance with an eliminated shuttle effect, ether-based electrolyte is more favourable for Li metal anode.

To find the difference between these two electrolyte systems, the electrochemical performance of the as-synthesized samples under ether-based electrolyte were tested by assembling coin cells with Se_xSPAN@moCNT and Li foil as cathode and anode, respectively. CV curves were different from those in carbonate-based electrolyte (**Figure 4.19**). Except for the cathodic peak at about 1.6 V, there were two more peaks at about 2.1 V and 2.4 V, which is common in C/S composite cathode materials in LSBs. High solubility of LPSs in ether-based electrolyte enabled a step by step solid-liquid-solid reaction pathway. Though C-S covalent bonds were characterized by Raman, FTIR, XPS tests, the length of the S chain or ring was not quantitively clarified. For example, if a chain with four S atoms was formed: -C-S-S-S-S-C-. During the discharge process, -C-S-Li and Li-S-S-Li (Li_2S_2) were formed, no soluble lithium polysulfides were formed. However, during the following charging process, chains with only two S atoms might by formed (-C-S-S-C-) and Li_2S_2 was oxidized to S_8. In the following tests, the formed S_8 molecules would undergo the solid-liquid-solid reaction pathway like the C/S composite cathode, thus the peaks arose.

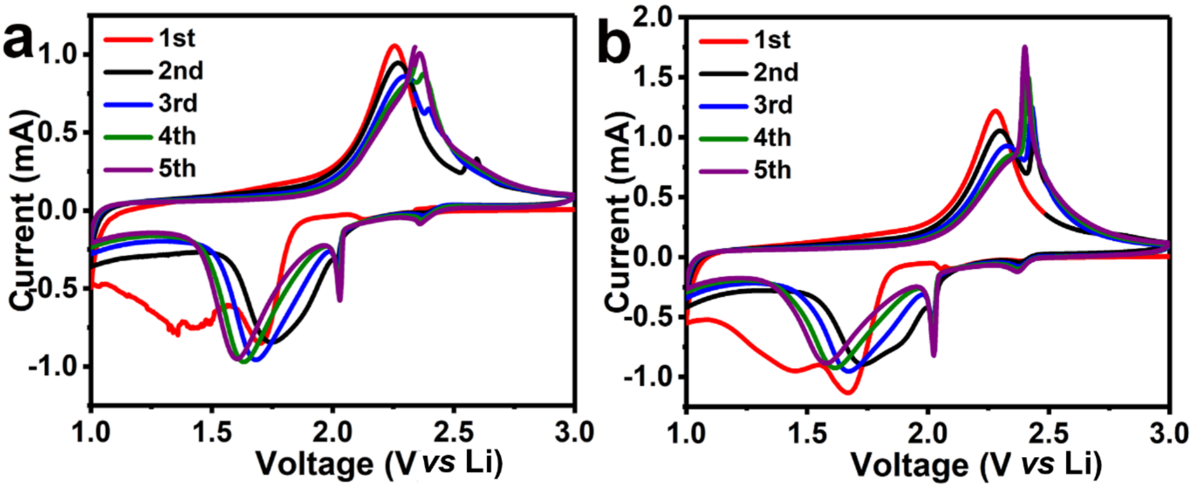

Figure 4.19. CV curves of samples in ether-based electrolyte at a scan rate of 0.2 mV s^{-1}: a) $Se_{0.05}SPAN$@moCNT; b) $Se_{0.1}SPAN$@moCNT.

When the scan rate increased, the peak positions shifted to both sides, the same as that in carbonate-based electrolyte (**Figure 4.20a**). The charge-discharge curves showed that the discharge voltage platform shifted from about 1.7 V to about 2.0 V after the first cycle (Figure 4.20b), in agreement with the CV results.

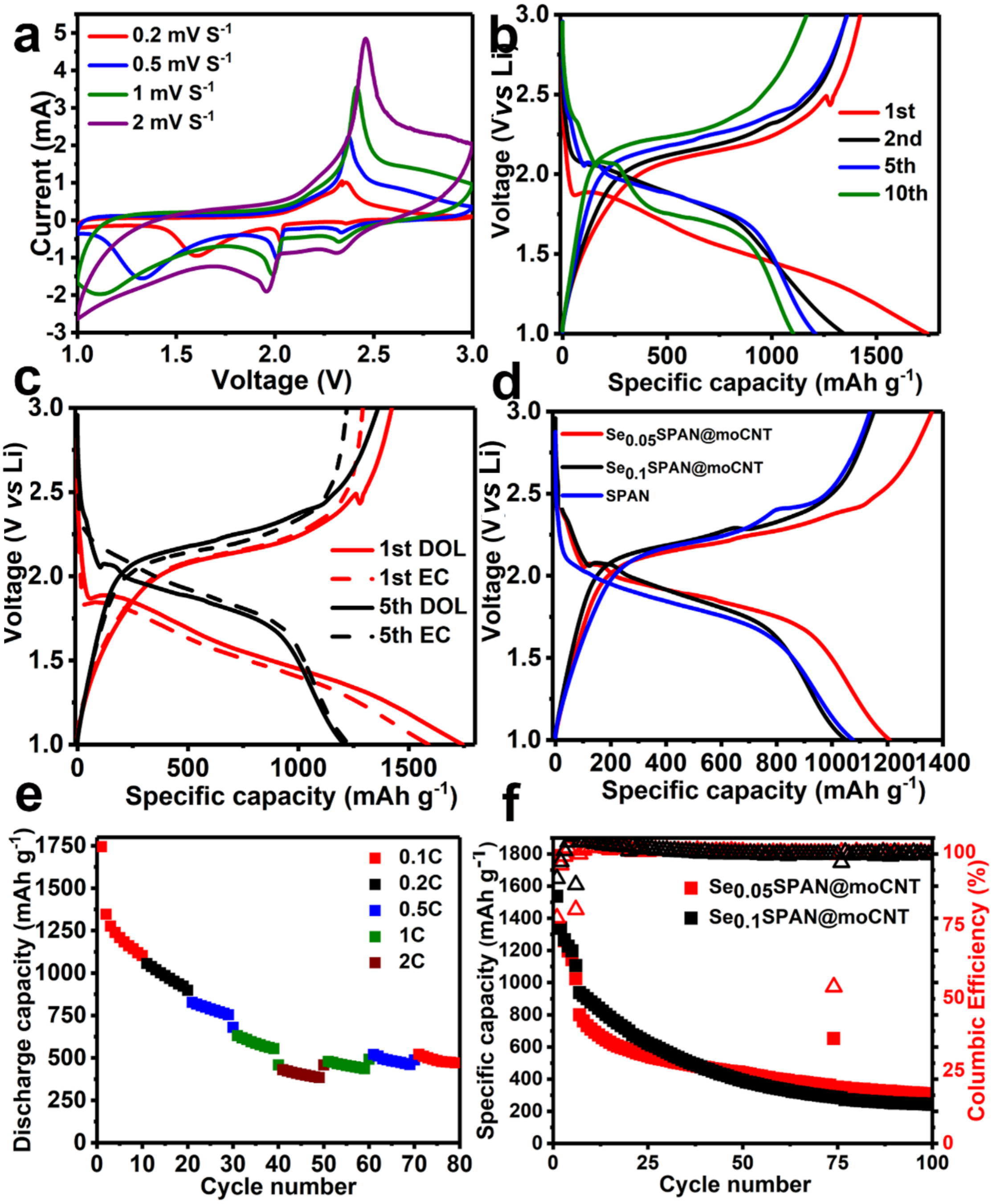

Figure 4.20. Electrochemical performance of samples tested in ether-based electrolyte. a) CV curves of $Se_{0.05}$SPAN@moCNT tested at different scan rates, from 0.2 mV S^{-1} to 2 mV S^{-1}. b) Charge-discharge curves of $Se_{0.05}$SPAN@moCNT at a current density of 0.1 C. c) charge-discharge curves of $Se_{0.05}$SPAN@moCNT tested in carbonate and ether-based electrolyte systems. d) Fifth cycle of charge-discharge curves of different samples. e) Rate performance of $Se_{0.05}$SPAN@moCNT tested at different current density, increased from 0.1 C to 2 C and then went back to 0.1 C. f) Cyclic stability of samples tested at a current density of 0.5 C.

Despite the difference in the content of Se-doping, all samples showed similar charge-discharge curves (**Figure 4.21**)

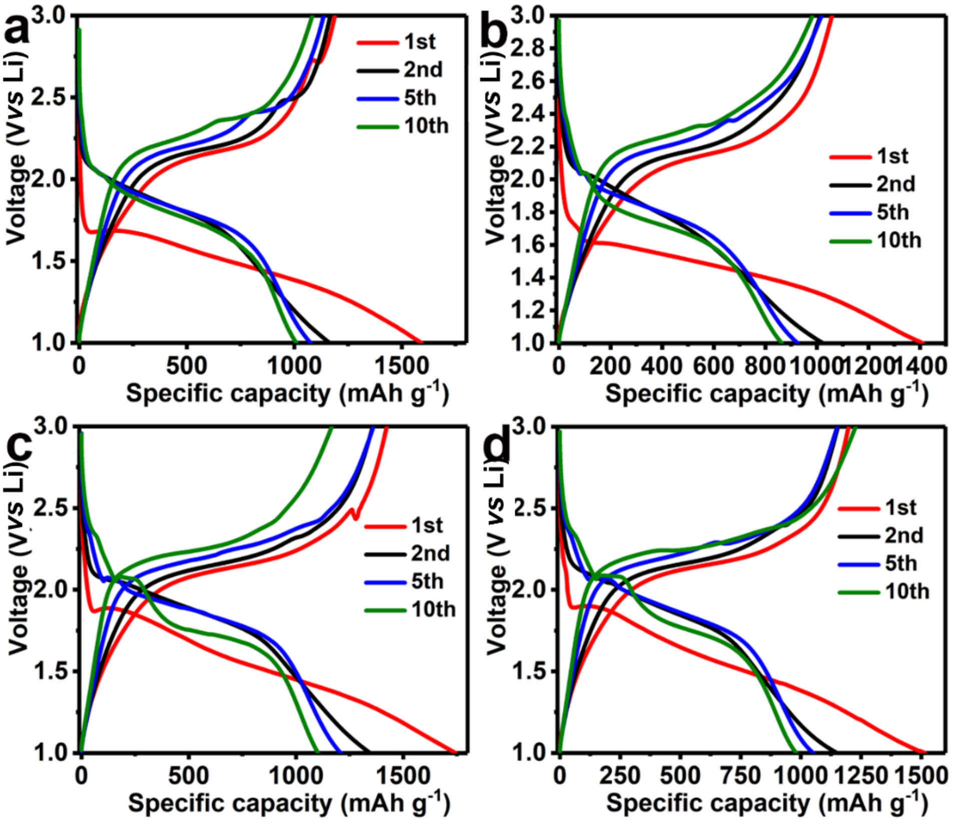

Figure 4.21. Charge-discharge curves of samples in ether-based electrolyte at a current density of 0.1 C. a) SPAN; b) SPAN@moCNT; c) Se$_{0.05}$SPAN@moCNT; d) Se$_{0.1}$SPAN@moCNT.

The charge-discharge curves of Se$_{0.05}$SPAN@moCNT in different electrolyte systems were compared as shown in Figure 4.20c. In ether-based electrolyte, samples delivered a higher specific capacity in the first cycle. This might be caused by the difference in the formation of SEI in different electrolyte system. After the first cycle, the difference in specific capacities narrowed down. However, in ether-based electrolyte, the charge specific capacity was higher than the discharge specific capacity, which could be ascribed to shuttle effect in ether-based electrolyte. Except for covalently bonded S, there might be some physically absorbed S in the carbon framework. During the charge process, long chain LPSs would be formed through the oxidization of Li$_2$S. Long chain LPSs would diffuse to the surface of a Li anode and react with Li to form short chain LPSs, which could be electrochemically oxidized again. This would lead to a higher charge specific capacity than expected. Samples with different content of Se-doping were tested. Se$_{0.05}$SPAN@moCNT showed the highest specific capacity, 1209 mA h g^{-1} at a current density of 0.1 C (Figure 4.20d). The rate performance in ether-based electrolyte was tested (Figure 4.21e and **Figure 4.22**). Because of the shuttle effect, the specific capacity decreased dramatically from 1208 mA h g^{-1} to 410 mA h g^{-1} when the current density increased from 0.1 C to 2 C. When the current density went back to 0.1 C, only 493 mA h g^{-1} capacity was maintained, with a low capacity retention of 41%.

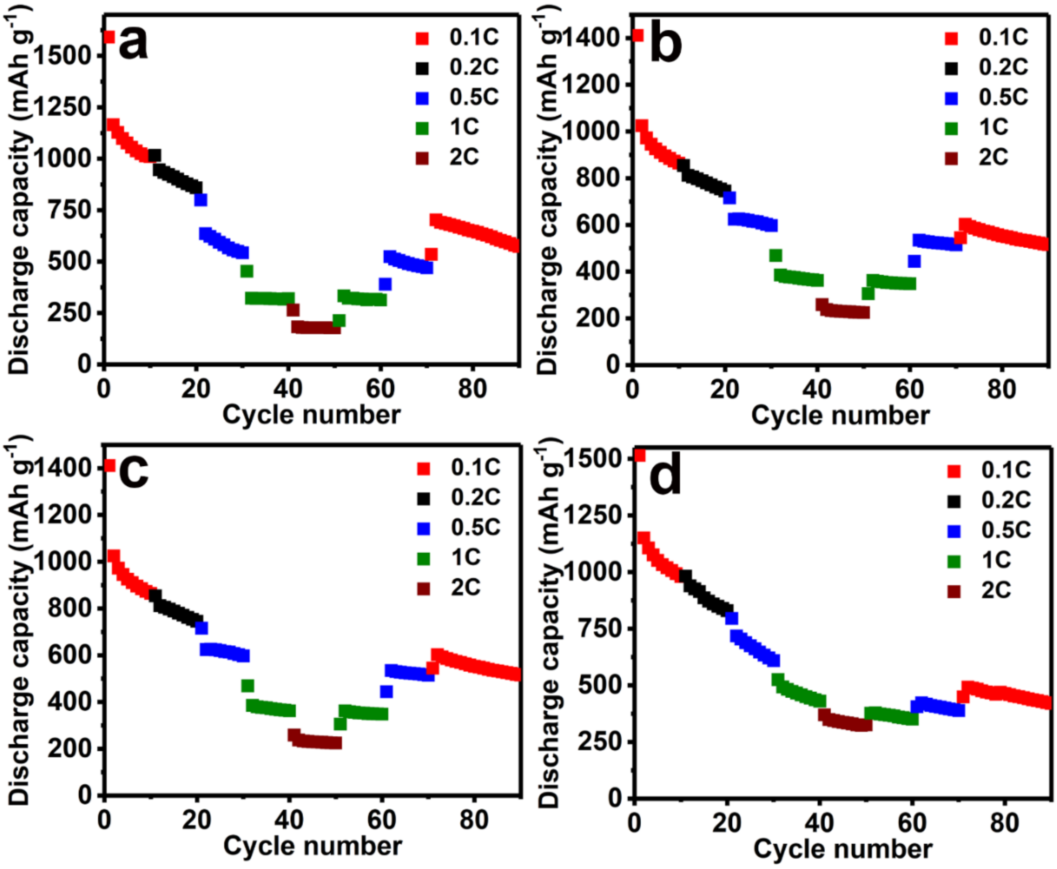

Figure 4.22. Rate performance of different samples in ether-based electrolyte. The current density increased from 0.1 C to 0.2, 0.5, 1 and 2 C and then decreased to 1, 0.5 and 0.1 C step by step. a) SPAN; b) SPAN@moCNT; c) $Se_{0.05}$SPAN@moCNT; d) $Se_{0.1}$SPAN@moCNT.

The cyclic stability of samples in ether-based electrolyte is worse than those in carbonate-based electrolyte (Figure 4.20f and **Figure 4.23**). The capacity decreased quickly after the activation process, with only 310 mA h g^{-1} after 100 cycle at a current density of 0.5 C. The Coulumbic efficiency was about 102%, higher than 100%, indicating the occurrence of shuttle effect.

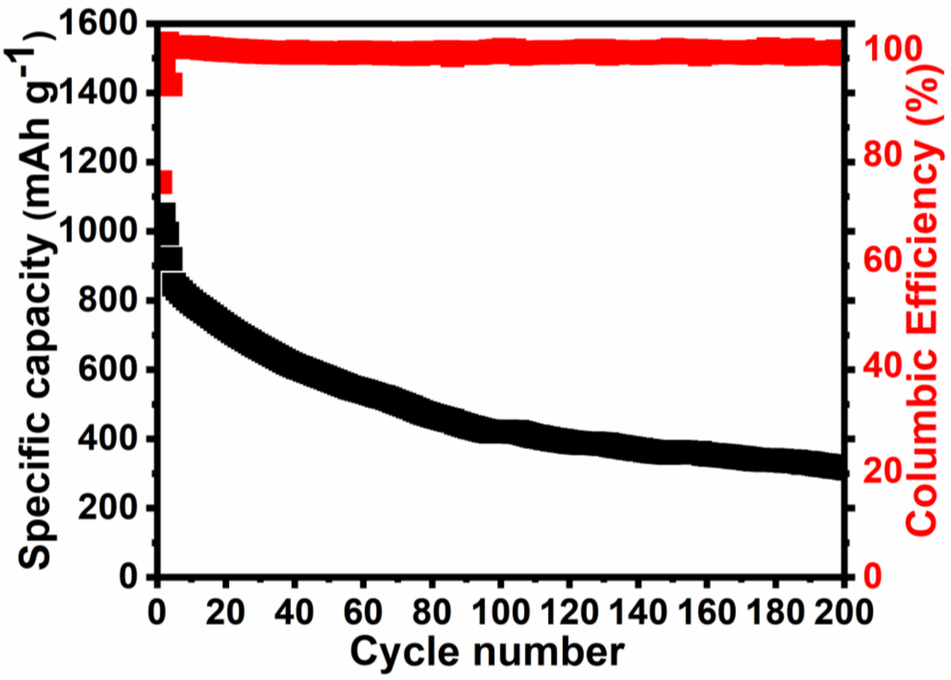

Figure 4.23. Cyclic performance of SPAN@moCNT in ether-based electrolyte.

To further analyse the reaction mechanism of samples in different electrolyte systems, electrochemical impedance spectrum (EIS) was applied to study the resistance of cells before and after CV tests. Before the CV test, the Nyquist plot showed one semi cycle at high frequency region and a sloping line in the low frequency region (**Figure 4.24a** and 4.24b). The semi cycle in the high frequency region showed the charge transfer resistance (Rc) in the cathodes. The intercept of the sloping lines represented the Warburg impedance (W_0). As the content of Se-doping increased, the charge transfer resistance decreased in both ether and carbonate-based electrolyte. About 580 Ω and 180 Ω for $Se_{0.05}$SPAN@moCNT in ether and carbonate-based electrolyte, respectively. Further about 450 Ω and 120 Ω for $Se_{0.1}$SPAN@moCNT in ether and carbonate-based electrolyte, respectively. These EIS results indicated that the introduction of Se-doping successfully improved the conductivity of Se_xSPAN@moCNT cathode. Also, for the same sample, the resistance in ether-based electrolyte is lower than that of carbonate-based electrolyte, which might be the reason for higher initial specific capacity in ether-based electrolyte. After the CV test, there were two depressed semi-cycles in the high and medium frequency region and one short sloping line at low frequency region in carbonate-based electrolyte (Figure 4.25c and 4.25d), while there is only one semi cycle in the high frequency region in ether-based electrolyte. The semi cycle in the medium frequency region might be ascribed to the resistance of the deposited discharge products (R_d). After the CV test, the resistance in all tested samples decreased, which could be explained by the activation process. Same as those before CV test, samples with higher content of Se-doping had lower resistance.

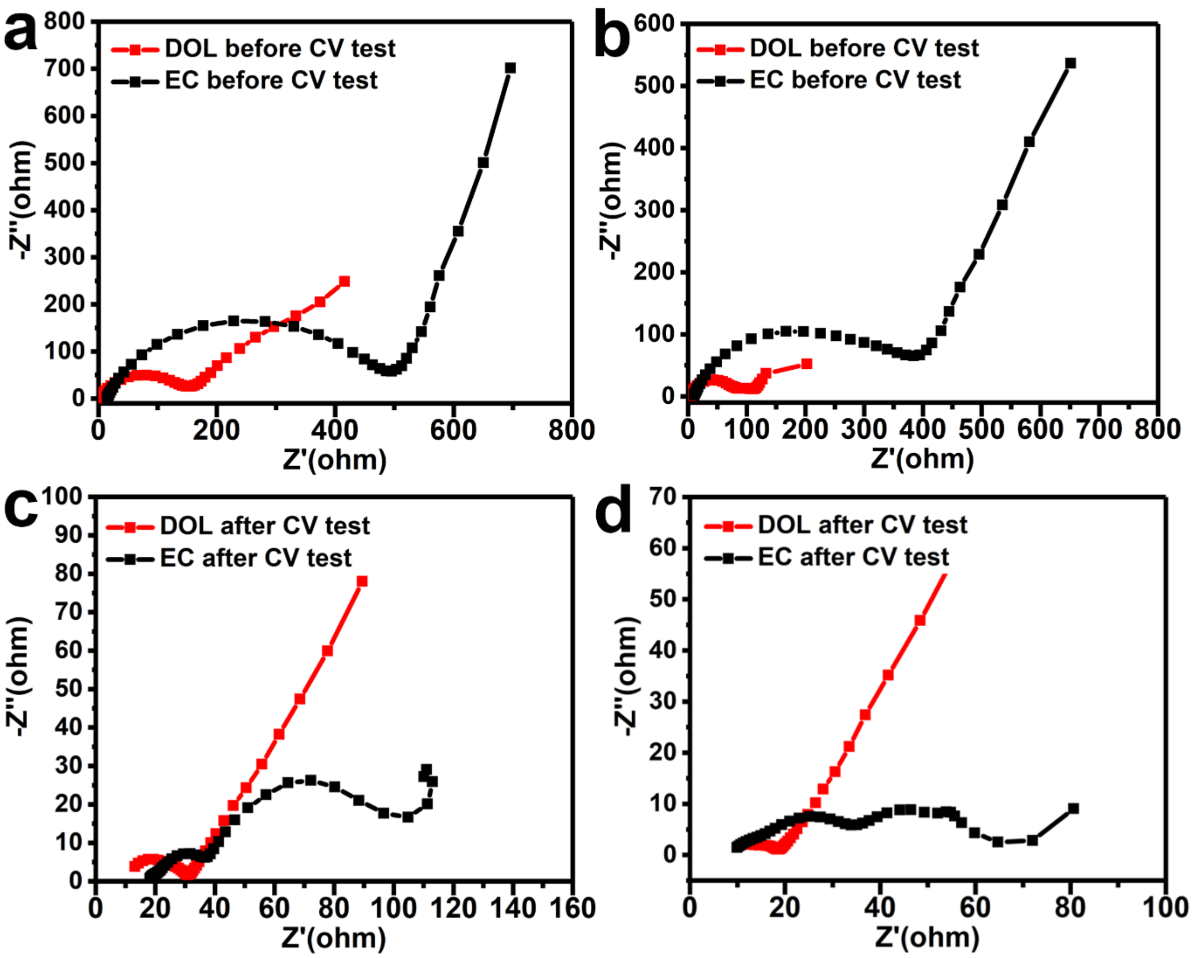

Figure 4.24. Electrochemical impedance spectrum (EIS) of samples. a) $Se_{0.05}$SPAN@moCNT before CV test. b) $Se_{0.1}$SPAN@moCNT before CV test. c) $Se_{0.05}$SPAN@moCNT after CV test. d) $Se_{0.1}$SPAN@moCNT after CV test.

4.4 Conclusion

A new type of Se_xSPAN@moCNT was designed and synthesized through a two-step process: *in situ* polymerization and sulfurization. The incorporation of moCNT and introduction of Se-doping improved the conductivity. The structure of Se_xSPAN@moCNT was similar with SPAN, with C-S covalent bond and ring structure with C, S and Se formed.

Se-doping could also accelerate the reaction and mitigated against the shuttle effect. A high electrochemical performance could be achieved in carbonate-based electrolyte. High capacity at high current density (837 mA h g^{-1} at a current density of 2 C, 1 C = 1675 mA g^{-1}) and better cyclic stability (772 mA h g^{-1} after 100 cycles at 0.5 C). However, the poor performance in ether-based electrolyte indicates that there should also be physically absorbed S in the products, which caused severe shuttle effect.

4.5 Reference

[1] X. Yao, N. Huang, F. Han, Q. Zhang, H. Wan, J. P. Mwizerwa, C. Wang, X. Xu, *Adv. Energy Mater.* **2017**, *7*, 1.

[2] J. Zhang, H. Hu, Z. Li, X. W. Lou, *Angew. Chemie - Int. Ed.* **2016**, *55*, 3982.

[3] B.-Q. Li, S.-Y. Zhang, L. Kong, H.-J. Peng, Q. Zhang, *Adv. Mater.* **2018**, 1707483.

[4] F. Wu, T. P. Pollard, E. Zhao, Y. Xiao, M. Olguin, O. Borodin, G. Yushin, *Energy Environ. Sci.* **2018**, 0.

[5] Z. W. Seh, J. H. Yu, W. Li, P. C. Hsu, H. Wang, Y. Sun, H. Yao, Q. Zhang, Y. Cui, *Nat. Commun.* **2014**, *5*, 1.

[6] J. Zhou, R. Li, X. Fan, Y. Chen, R. Han, W. Li, J. Zheng, B. Wang, X. Li, *Energy Environ. Sci.* **2014**, *7*, 2715.

[7] Q. Liu, J. Tian, W. Cui, P. Jiang, N. Cheng, A. M. Asiri, X. Sun, *Angew. Chemie - Int. Ed.* **2014**, *53*, 6710.

[8] C. Zhang, H. Bin Wu, C. Yuan, Z. Guo, X. W. Lou, *Angew. Chemie - Int. Ed.* **2012**, *51*, 9592.

[9] P. Sang, J. Song, W. Guo, Y. Fu, *Chem. Eng. J.* **2021**, *415*, DOI 10.1016/j.cej.2021.129043.

[10] J. Zhou, X. Zhou, Y. Sun, X. Shen, T. Qian, C. Yan, *J. Energy Chem.* **2021**, *56*, 238.

[11] S. J. Visco, C. C. Mailhe, L. C. De Jonghe, M. B. Armand, *J. Electrochem. Soc.* **1989**, *136*, 661.

[12] J. Wang, J. Yang, J. Xie, xu naixin, *Adv. Mater.* **2002**, *50*, 963.

[13] A. Manthiram, Y. Fu, S. H. Chung, C. Zu, Y. S. Su, *Chem. Rev.* **2014**, *114*, 11751.

[14] W. J. Chung, J. J. Griebel, E. T. Kim, H. Yoon, A. G. Simmonds, H. J. Ji, P. T. Dirlam, R. S. Glass, J. J. Wie, N. A. Nguyen, B. W. Guralnick, J. Park, Á. Somogyi, P. Theato, M. E. Mackay, Y. E. Sung, K. Char, J. Pyun, *Nat. Chem.* **2013**, *5*, 518.

[15] Q. Pang, X. Liang, C. Y. Kwok, L. F. Nazar, *Nat. Energy* **2016**, *1*, 1.

[16] G. Hu, Z. Sun, C. Shi, R. Fang, J. Chen, P. Hou, C. Liu, H. M. Cheng, F. Li, *Adv. Mater.* **2017**, *29*, 1.

[17] J. Liu, M. Wang, N. Xu, T. Qian, C. Yan, *Energy Storage Mater.* **2018**, *15*, 53.

[18] M. A. Weret, C. F. Jeffrey Kuo, T. S. Zeleke, T. T. Beyene, M. C. Tsai, C. J. Huang, G. B. Berhe, W. N. Su, B. J. Hwang, *Energy Storage Mater.* **2020**, *26*, 483.

[19] K. Shen, H. Mei, B. Li, J. Ding, S. Yang, *Adv. Energy Mater.* **2018**, *8*, DOI 10.1002/aenm.201701527.

[20] L. Yin, J. Wang, J. Yang, Y. Nuli, *J. Mater. Chem.* **2011**, *21*, 6807.

[21] X. Wang, Y. Qian, L. Wang, H. Yang, H. Li, Y. Zhao, T. Liu, *Adv. Funct. Mater.* **2019**, *29*, DOI 10.1002/adfm.201902929.

Chapter 5

Outlook and perspective

Two different strategies have been applied in the PhD project to solve the challenges and problems faced by lithium-sulfur batteries (LSBs). First, ZIF derived materials have been used as S host for LSBs. The porous structure provided enough space for S host and accommodate the volume change during charge and discharge. The carbon framework synthesized through carbonization at high temperature had higher conductivity compared with pristine ZIF materials. Cobalt sulphides/phosphides derived from the Co centres of ZIFs had strong chemical absorption toward lithium polysulfides, which alleviated the shuttle effect. Second, sulfurized poly acrylonitrile (SPAN) with covalent C-S bonds have been used as source of S for LSBs. The covalent C-S bonds reduced the formation of lithium polysulfides thus mitigate the shuttle effect.

The project has brought some implications for both academia and industry. A core-shell structured ZIF-8@ZIF-67 template was designed and synthesized to fabricate porous carbon framework as S host for the first time. This provides a new direction of using ZIF-based materials as S host for LSBs. Besides, a facile process without high temperature treatment was used to synthesis CoP nano cage. The facile process enables large scale production of this material as S host for LSBs. SPAN has been widely studied as S source for LSBs because of the C-S covalent bonds. The existence of C-S covalent bonds was also confirmed in this project, but it was also found that there was also physically absorbed sulfur, which has rarely been reported. Meanwhile, using different strategies to improve the performance of SPAN could promote the practical application of SPAN in LSBs.

In the second chapter, ZIF-8@ZIF-67 template was used to synthesis cobalt sulphides supported on N-doped carbon framework (CSNCF) and used as a S host for LSBs. The core-shell structure alleviates the collapse of ZIF-67 during high temperature carbonization and provide higher specific surface area, which is beneficial for S hosts. The cobalt sulphides derived from the Co centres of ZIF-67 had strong absorption ability and catalyst activity as evidenced by the visual absorption test, XPS test and electrochemical tests of samples after acid wash, which has no cobalt sulphides. It was also found that higher carbonization temperature enabled higher conductivity and thus better electrochemical performance The particle size of ZIF-8@ZIF-67 in this experiment was around 500 nm. It has been reported that the size of ZIFs affect the electrochemical performance. A proper size should be able to provide enough space for S host, electrolyte diffusion and shorter charge diffusion length. Thus, it is worth synthesizing ZIF-8@ZIF-67 template with different particle size and find out how the particle size affect the electrochemical performance of CSNCF.

In the third chapter, $Co_xNi_{1-x}P$ nano cages were synthesized from ZIF-67 template. Samples with different content of Ni had different morphology and electrochemical performance. Higher content of Ni provided higher specific surface area of layer double hydroxide (LDH) precursors. But the phosphorization process damaged the morphology of LDHs. It was found that $Co_{0.25}P$ had the best electrochemical performance. However, the rate performance of $Co_xNi_{1-x}P$ was not satisfactory. This could result from the relatively low conductivity at low phosphorization temperature. Using conductive carbon materials like carbon nanotube (CNT), graphene and so on to improve the conductivity of the electrode is a promising way. Besides, LDHs precursors can be used to synthesized metal nitrides, metal sulphides and so on, which has also been reported as S host.

In the fourth chapter, Se-doped SPAN was used a cathode for LSBs. The introduce of Se-doping improved the electrochemical performance of SPAN by providing higher conductivity. Samples with different level of Se doping were synthesised and tested. Though Se has higher conductivity than S, the higher atomic mass of Se enables lower specific capacity. Samples with a compromised level of Se doping ($Se_{0.05}S$) had the best performance. Besides, the structure of Se_xSPAN was characterized by a variety of methods. The formation of C-S bonds as well as a N containing ring structure was confirmed. However, it was also found that there was still physically absorbed S in the as-synthesized SPAN samples, which affected the electrochemical performance. To get rid of the physically absorbed S, higher sulfurization temperature and longer sulfurization time should be helpful. Besides, immersing the as-synthesized SPAN samples in CS_2 solution, in which S has a high solubility, is another possible way.

This research was mainly focused on the design and synthesis of cathode material for LSBs. However, using a functional separator to eliminate the shuttle effect, applying solid state electrolyte to protect the Li metal anode and so on are also possible ways to the commercialization of LSBs and also the hot research topics recently. Besides, all the batteries that were tested in this project were in coin cell configuration, which is different from the practical conditions, like less lithium anode, less electrolyte usage, thicker electrode, high area loading and so on. To promote the industrialization of LSBs, materials or electrodes must by tested in pouch cell configuration at more practical conditions to find out the possible candidates. What’s more, this project only focused on the gravimetric energy density of LSBs, while volumetric energy density of LSBs is also of great importance for the industrialization of LSBs. Improving the volumetric energy density from the material or electrode level and cell design might be two possible ways.